

University of Alberta

DUCTILE STEEL PLATE SHEAR WALLS WITH PEC COLUMNS

by

Mehdi Dastfan

A thesis submitted to the Faculty of Graduate Studies and Research

in partial fulfillment of the requirements for the degree of

Doctor of Philosophy

in

Structural Engineering

Department of Civil and Environmental Engineering

©Mehdi Dastfan

Fall 2011

Edmonton, Alberta

Permission is hereby granted to the University of Alberta Libraries to reproduce single copies of this thesis and to lend or sell such copies for private, scholarly or scientific research purposes only. Where the thesis is converted to, or otherwise made available in digital form, the University of Alberta will advise potential users of the thesis of these terms.

The author reserves all other publication and other rights in association with the copyright in the thesis and, except as herein before provided, neither the thesis nor any substantial portion thereof may be printed or otherwise reproduced in any material form whatsoever without the author's prior written permission.

ABSTRACT

The behavior of steel plate shear walls under the effects of lateral loads depends on the stiffness of the surrounding frame members. Previous research has quantified the minimum required stiffness of columns in the middle stories of steel plate shear wall systems. As the columns of the steel plate shear wall system are subjected to both large axial forces and bending moments, use of composite columns is a viable option in this system. Among the different types of composite columns, the recently developed partially encased composite columns with built-up steel sections have some advantages over other types of composite columns and thus their performance as columns in steel plate shear wall systems needs to be studied.

In the first part of this research, a numerical and analytical study has developed a new design parameter and determined the minimum required stiffness of end beams in end panels of the steel plate shear wall system. The effect of the rigidity of the frame connections on the uniformity of the tension field has also been studied in this part.

The second part of this research includes two large-scale tests on steel plate shear walls with built-up partially encased composite (PEC) columns. One of the test specimens was modular and the other one used reduced beam sections in the frame. The results of the tests show that the columns were stiff enough to anchor the infill plate. The PEC columns in these tests performed in a ductile manner. The overall system behavior was ductile, stable and the specimens showed good seismic behavior and redundancy. Based on the results and observations of this research, design recommendations for PEC columns used as the vertical boundary members of steel plate shear walls are provided.

ACKNOWLEDGEMENTS

I would like to take this opportunity to express my sincere gratitude to those who have contributed to the fulfillment of this work by their support, encouragement, help or remarks.

I would like to acknowledge the assistance of the Natural Sciences and Engineering Research Council of Canada by providing the hardware for this study. Personal financial assistance in the form of scholarships from Alberta Innovates (Alberta Ingenuity Graduate Scholarship), the Faculty of Graduate Studies and Research (Entrance award and Killam Scholarship) and the Graduate Student Association (travel fund) are greatly appreciated. I would also like to say thank you to Canam Group for providing the test specimens and Lehigh Inland Cement Limited for providing the required concrete for this project.

I would like to thank Dr. Robert G. Driver for giving me the opportunity to do my Ph.D. studies under his supervision at the University of Alberta; it was great working with you, not just academically. The assistance of other graduate students- Adel, Amir, Hadi, Mehrdad, Sadegh, Xiaoyan- who helped me in casting concrete and/or during the test is also appreciated.

In addition, I would like to say a big thank you to my family in Iran. My parents' foresight to provide everything for me to get the best education is truly the foundation of all my advancements. I will be eternally grateful for all their support.

Last, but not least, I would like to extend my sincere gratitude and love to my dear wife, Elham, for her kindness and support all the way to this achievement and whom this thesis is dedicated to.

TABLE OF CONTENTS

1. INTRODUCTION	1
1.1 General	1
1.2 Objectives and scope	3
1.3 Thesis overview	5
2. BACKGROUND AND LITERATURE REVIEW	9
2.1 Introduction	9
2.2 Partially encased composite columns	10
2.2.1 <i>Experimental studies on PEC columns</i>	11
2.2.2 <i>Numerical studies on PEC columns</i>	16
2.2.3 <i>Prediction of the strength of the PEC columns</i>	19
2.3 Reduced Beam Section (RBS) connections	23
2.4 Steel plate shear walls	25
2.4.1 <i>Analytical studies on the column flexibility parameter</i>	26
2.4.2 <i>Experimental studies on steel plate shear walls</i>	30
2.5 Test of a steel plate shear wall with PEC columns	35
3. FLEXURAL PARAMETERS FOR BOUNDARY FRAME MEMBERS IN STEEL PLATE SHEAR WALL SYSTEMS	48
3.1 Introduction	48
3.2 End-panel flexibility parameter	49
3.3 Limit analysis for the end-panel flexibility parameter	52
3.4 Effect of beam-to-column connection rigidity on flexural parameters	55
3.4.1 <i>Effect of connection rigidity on column flexibility parameter (ω_r)</i>	56
3.4.2 <i>Effect of connection rigidity on end-panel flexibility parameter (ω_L)</i>	57
3.5 Summary	59

4. TEST SPECIMENS, PROTOCOLS, PREPARATIONS AND

MATERIAL PROPERTIES	71
4.1 Introduction	71
4.2 Description of test specimens	72
4.2.1 Modular test specimen	72
4.2.2 RBS test specimen	75
4.3 Test set-up	77
4.4 Loading regime	79
4.5 Instrumentation and data collection	80
4.6 Concrete placement	82
4.7 Ancillary tests	84
4.8 Material properties	85

5. MODULAR STEEL PLATE SHEAR WALL TEST RESULTS

5.1 Introduction	110
5.2 General observations	111
5.2.1 Gravity load application	111
5.2.2 "Force control" cycles	111
5.2.3 "Displacement control" cycles	112
5.3 Hysteretic behavior	117
5.3.1 Hysteretic loops of the first and second stories	117
5.3.2 Rotation of the frame connections	119
5.4 Energy dissipation capacity, stiffness and ductility	120
5.4.1 Energy dissipation capacity	120
5.4.2 Stiffness and ductility	121
5.5 Strain gauge data	122

6. TEST RESULTS OF STEEL PLATE SHEAR WALL

WITH RBS CONNECTIONS	142
6.1 Introduction	142
6.2 General observations	143
6.2.1 Gravity load application	143
6.2.2 "Force control" cycles	143
6.2.3 "Displacement control" cycles	144
6.3 Hysteretic behavior	150
6.3.1 Hysteretic loops of the first and second stories	150
6.3.2 Rotation of the frame connections	151
6.4 Energy dissipation capacity, stiffness and ductility	152
6.4.1 Energy dissipation capacity	152
6.4.2 Stiffness and ductility	153
6.5 Strain gauge output data	154
6.5.1 Strain data obtained from columns	154
6.5.2 Strain data obtained from the infill plate of the first story	156
6.5.3 Strain data obtained from RBS cut region	156
6.6 3D camera system output	157
7. COMPARISONS AND DISCUSSION OF TEST RESULTS	180
7.1 Introduction	180
7.2 Typical hysteretic loops	180
7.3 Envelope of the hysteretic loops and ductility	182
7.4 First floor beam-to-column connection rotations	185
7.5 Energy dissipation capacity	186
7.6 Effective moment of inertia of PEC columns	187
7.7 Combination of axial compression and bending	189

8. SUMMARY, CONCLUSIONS AND RECOMMENDATIONS	200
8.1 Summary	200
8.2 Conclusions	201
8.2.1 Flexibility parameters in steel plate shear wall systems	201
8.2.2 Tests of shear walls with PEC columns	202
8.3 Recommendations	205
8.3.1 Design	205
8.3.2 Future research	207
LIST OF REFERENCES	209
APPENDIX A. SHOP DRAWINGS OF TEST SPECIMENS	215
APPENDIX B. ANCILLARY TEST RESULTS	224
B.1 Steel	225
B.2 Concrete	232

LIST OF TABLES

Table 3.1: Hot-rolled wide-flange sections for top beams ($\omega_h = \omega_L = 2.5$)	61
Table 3.2: The effect of the frame connection rigidity on the parameter C_2 for different values of ω_h and panel aspect ratios	61
Table 3.3: The effect of the frame connection rigidity on the parameter C_3 for proposed maximum values of ω_L and panel aspect ratios	62
Table 4.1: Targeted base shear and first floor displacement values in different cycles of the modular test	88
Table 4.2: Targeted base shear and first floor displacement values in different cycles of the RBS test	88
Table 4.3: Tension test results of all the coupons, related to the modular test specimen	89
Table 4.4: Tension test results of all the coupons, related to the RBS test specimen	90
Table 4.5: Concrete cylinder properties on associated test dates	91
Table 7.1: Displacement ductility (R) of the first story of the test specimens in different load levels at the post-peak stage	190
Table 7.2: Effective moment of inertia of PEC columns of the modular and RBS test specimens and corresponding flexibility parameters	190
Table B.1: Material properties of concrete in first story of PEC columns in the modular and RBS test specimens	232
Table B.2: Material properties of concrete in second story of PEC columns in the modular and RBS test specimens	233

LIST OF FIGURES

Figure 1.1: Typical steel plate shear wall (Photo courtesy of Canam Group)	7
Figure 1.2: Development of tension field in post-buckling stage in steel plate shear wall	7
Figure 1.3: Typical cross section of PEC column	8
Figure 2.1: Concrete-filled tubes (left) and fully encased composite column (right)	38
Figure 2.2: Partially encased composite columns with a) Standard steel section; b) Built-up steel section	38
Figure 2.3: Sequence of construction of PEC column (Vincent and Tremblay 2001) ..	39
Figure 2.4: a) Typical radius RBS cut; b) Dimensions of radius RBS cut (Moore et al. 1999)	39
Figure 2.5: Hysteretic loops of a moment frame (left) and a steel plate shear wall (right) (Elgaaly et al. 1993)	40
Figure 2.6: Exact and approximate curves to find the maximum stress in a non-uniform tension field (Wagner 1931)	40
Figure 2.7: Parameter C_2 as a function of the parameter ω_h	41
Figure 2.8: Method to define yield deformation and elastic stiffness (ATC 1992)	41
Figure 2.9: Four-story steel plate shear wall tested by Driver et al. (1997)	42
Figure 2.10: Envelope of hysteretic loops of the first story (Driver et al. 1997)	43
Figure 2.11: Steel plate shear walls tested by Astaneh-Asl and Zhao (2002)	43
Figure 2.12: Specimen tested by Qu et al. (2008)	44
Figure 2.13: a) Offset of plastic hinge center toward column face; b) Dimensions of a typical radius RBS cut and offset of the plastic hinge (Qu and Bruneau 2010)	44
Figure 2.14: Lateral load transfer system designed by Deng and Driver (2007)	45

Figure 2.15: Un-deformed (left) and deformed (right) meshed model in numerical study conducted by Deng and Driver (2007)	45
Figure 2.16: Lateral displacement versus lateral reaction (Deng and Driver 2007)	46
Figure 2.17: Test specimen before concrete was cast (Deng et al. 2008)	46
Figure 2.18: Hysteretic loops of story shear versus story deflection of first story (Deng et al. 2008)	47
Figure 3.1: Tension strips anchored to surrounding frame members	62
Figure 3.2: Distributed load along column applied by anchored tension strips	63
Figure 3.3: Distributed load along boundary members applied by anchored tension strips	63
Figure 3.4: Stress distribution along the diagonal of the end panel with $L / h = 0.5$...	64
Figure 3.5: Stress distribution along the diagonal of the end panel with $L / h = 1.0$...	64
Figure 3.6: Stress distribution along the diagonal of the end panel with $L / h = 1.5$...	65
Figure 3.7: Non-uniformity of tension field stress as a function of ω_L and ω_h	65
Figure 3.8: Non-uniformity of tension field stress as a function of ω_L and L / h	66
Figure 3.9: Comparison of the finite element analysis results and analytical study result	66
Figure 3.10: Parameter C_2 as a function of ω_h in panels with $L / h = 0.5$	67
Figure 3.11: Parameter C_2 as a function of ω_h in panels with $L / h = 1.0$	67
Figure 3.12: Parameter C_2 as a function of ω_h in panels with $L / h = 1.5$	68
Figure 3.13: The deformed shape of panels in middle stories with pinned (left) or fixed (right) beam-to-column connections	68
Figure 3.14: Effect of the frame connection rigidity on parameter C_3 for different values of ω_L in panels with $L / h = 0.5$ and infill plates with 3 mm thickness	69
Figure 3.15: Effect of the frame connection rigidity on parameter C_3 for different values of ω_L in panels with $L / h = 1.0$ and infill plates with 3 mm thickness	69

Figure 3.16: Effect of the frame connection rigidity on parameter C_3 for different values of ω_L in panels with $L / h = 1.0$ and infill plates with 6 mm thickness	70
Figure 3.17: Effect of the frame connection rigidity on parameter C_3 for different values of ω_L in panels with $L / h = 1.5$ and infill plates with 3 mm thickness	70
Figure 4.1: Exploded (left) and assembled (right) view of the modular test specimen	92
Figure 4.2: Cross-section of PEC columns with longitudinal rebars at the base (left) and without longitudinal rebars at other levels (right)	93
Figure 4.3: Modular steel plate shear wall test specimen	94
Figure 4.4: Additional fish plate in the first floor beam-to-column connection of the modular test specimen	95
Figure 4.5: Steel plate shear wall test specimen with RBS connections in the first story	96
Figure 4.6: Detail of the first floor frame connection in the RBS specimen	97
Figure 4.7: RBS cut surface condition; before grinding (top) and after grinding (bottom)	97
Figure 4.8: East elevation of the modular test set-up	98
Figure 4.9: East elevation of the RBS test set-up	99
Figure 4.10: Applied cyclic lateral load history to the modular and RBS test specimens	100
Figure 4.11: Gravity load application mechanism	100
Figure 4.12: Instrumentation layout for the modular test specimen	101
Figure 4.13: Instrumentation layout for the RBS test specimen	102
Figure 4.14: One set of cameras, monitoring the concrete face of PEC column at base	103
Figure 4.15: Hand-made formwork clamps	103
Figure 4.16: Formwork before the first cast of concrete in columns	104

Figure 4.17: Second lift of the concrete cast in the PEC columns in the first story	104
Figure 4.18: Grouting of the remaining gap under the cap plate	105
Figure 4.19: Dimensions of the tension coupons, taken from plate material	105
Figure 4.20: Remaining material after the coupons were removed	106
Figure 4.21: Tension test of the coupons taken from the 25M rebar (left) and the column plate (right)	106
Figure 4.22: “Split and cone” type of failure of the concrete cylinder in compression test	107
Figure 4.23: The concrete split cylinder test to determine the tensile strength of concrete	107
Figure 4.24: Compression test to obtain the stress vs. strain material properties of the concrete cylinder	108
Figure 4.25: Typical stress vs. strain curve for the infill plates (coupon: PR1)	109
Figure 4.26: Typical stress vs. strain curve for the column plates (coupon: PAA1)	109
Figure 5.1: Cracks in concrete of the north PEC column in cycle 9	126
Figure 5.2: First story infill plate fold due to rotation of the frame connection	126
Figure 5.3: Yield lines in the infill plate of the first story during cycle 15	127
Figure 5.4: Base of the south column during cycle 17	127
Figure 5.5: Local buckling of the outer flange just above the side plate at the base of the north column during cycle 20	128
Figure 5.6: Buckling of the flange between side plates at the base of south column in cycle 20	128
Figure 5.7: Outer flange of the south column at the base in cycle 24	129
Figure 5.8: First story of the specimen at the end of the test	129
Figure 5.9: Location of first story infill plate tears at the end of the test (East view) ..	130
Figure 5.10: Base shear versus first story deflection in the modular test	131
Figure 5.11: Base shear versus second floor displacement in the modular test	132

Figure 5.12: Shear force in the second story versus second story deflection in the modular test	133
Figure 5.13: Hysteretic loops of cycles 17 and 27	134
Figure 5.14: Rotation history of the side plate of column and end of the beam in the first floor of the modular test specimen	135
Figure 5.15: Rotation history of the frame connection in the first floor during the modular test	135
Figure 5.16: Rotation history of the side plate of column and end of the beam in the second floor of the modular test specimen	136
Figure 5.17: Rotation history of the frame connection in the second floor during the modular test	136
Figure 5.18: Dissipated energy in the first and second stories of the modular specimen in each cycle	137
Figure 5.19: Total dissipated energy in the modular specimen versus first floor displacement	138
Figure 5.20: Envelope of the hysteretic loops of base shear versus first story deformation in the modular test	139
Figure 5.21: Curvature of the north column at four sections in cycles 1 to 13	140
Figure 5.22: Strain readings on both sides of the outer flange at section A1	141
Figure 5.23: Strain readings on both sides of the outer flange at section D1	141
Figure 6.1: East face of north column in cycle 4	159
Figure 6.2: Buckling of the infill plates in cycle 9	159
Figure 6.3: Cracks in concrete on the east face of north column in cycle 9	160
Figure 6.4: Bottom part of east face of the north column in cycle 19	160
Figure 6.5: Diagonal crack close to top of the north column on west side in the first story during cycle 22	161
Figure 6.6: Buckling of inner flange and local crushing of the adjacent concrete under the side plate of fist floor in cycle 22	161

Figure 6.7: Buckled infill plate of the first story in cycle 23.....	162
Figure 6.8: Effect of the vertical tear in the infill plate, adjacent to south column, on the buckled shape of the infill plate of the first story during cycle 25 (from north)	162
Figure 6.9: Buckling of the inner flange of the south column in cycle 25 ⁻ (west face)	163
Figure 6.10: Buckling of the outer flange of the north column in cycle 25 ⁻ (west face)	163
Figure 6.11: Plastic hinge at top of the north column in cycle 26	164
Figure 6.12: Base of the north column and adjacent infill plate at the end of the test ..	164
Figure 6.13: Base of the south column and adjacent infill plate, separated from the column, at the end of the test	165
Figure 6.14: Tears in the infill plate of first story at the end of the RBS test.....	165
Figure 6.15: Base shear versus first story deflection in the RBS test	166
Figure 6.16: Base shear versus second floor displacement in the RBS test	167
Figure 6.17: Shear force in the second story versus second story deflection in the RBS test	168
Figure 6.18: Hysteretic loops of cycles 17 and 27 of the RBS test	169
Figure 6.19: Rotation history of the side plate of column and end of the beam in the first floor of the RBS test specimen.....	170
Figure 6.20: Rotation history of the frame connection in the first floor during the RBS test	170
Figure 6.21: Rotation history of the side plate of column in the second floor of the RBS test specimen.....	171
Figure 6.22: Amount of the dissipated energy in each cycle of the RBS test in the first and second stories.....	172
Figure 6.23: Total dissipated energy versus first floor displacement in the RBS test ..	173
Figure 6.24: Figure 6.24: Envelope of the hysteretic loops of base shear versus first story deformation in the RBS test	174
Figure 6.25: The curvature of the north column at four sections in cycles 1 to 16	175

Figure 6.26: Base of north column in cycle 16+ and initiation of new cracks, adjacent to the inner flange of column	176
Figure 6.27: out of flatness deformation of outer flange of north column in cycle 18 ⁺	176
Figure 6.28: Vertical strain distribution in outer flange of the north column in cycle 18 ⁺	177
Figure 6.29: Maximum principal strain distribution in concrete at the base of the north column in cycle 4 ⁻	177
Figure 6.30: Maximum principal strain distribution in cycle 13 ⁺ , showing the locations of the flexural cracks adjacent to the inner flange of column	178
Figure 6.31: Maximum principal strain distribution in cycle 19 ⁺	178
Figure 6.32: Maximum principal strain distribution in cycle 21 ⁺	179
Figure 6.33: Maximum principal strain distribution in cycle 23 ⁺	179
Figure 7.1: Hysteretic loops of cycles with story deformations of close 50 mm	191
Figure 7.2: Hysteretic loops of cycles with the peak base shear	192
Figure 7.3: Envelope of hysteretic loops of first story of three test specimens	193
Figure 7.4: Hysteretic loop of cycle 3 of the modular test (left) and RBS test (right)	194
Figure 7.5: Envelope of the hysteretic loops of the second story of the modular and RBS tests	195
Figure 7.6: Rotation of the frame connection in the first floor during the modular and RBS tests	196
Figure 7.7: Total amount of the dissipated energy in each cycle during the benchmark, modular and RBS tests	197
Figure 7.8: Total dissipated energy versus first floor displacement in the benchmark, modular and RBS tests	198
Figure 7.9: . P-M interaction diagram for strong-axis bending of PEC column at top of the first story.....	199

Figure A.1: Details of the assembled modular test specimen	216
Figure A.2: Details of individual modules, PEC columns, fish plate and splice plates in the modular test specimen	217
Figure A.3: Details of the first-floor beam in the modular test specimen	218
Figure A.4: Details of the second-floor beam in the modular test specimen	219
Figure A.5: Details of the cut plan to fabricate the modular test specimen	220
Figure A.6: Elevation view and details of the RBS test specimen	221
Figure A.7: Details of the frame connections and RBS cut dimensions in the RBS test specimen	222
Figure A.8: Details of the cut plan to fabricate the RBS test specimen	223
Figure B.1: Stress vs. strain curves of coupons from the infill plate of the modular test specimen	225
Figure B.2: Stress vs. strain curves of coupons from the column plates of the modular test specimen	226
Figure B.3: Stress vs. strain curves of coupons from the flanges of the first floor beam of the modular test specimen	226
Figure B.4: Stress vs. strain curves of coupons from the web of the first floor beam of the modular test specimen	227
Figure B.5: Stress vs. strain curves of coupons from the flanges of the second floor beam of the modular test specimen	227
Figure B.6: Stress vs. strain curves of coupons from the web of the second floor beam of the modular test specimen	228
Figure B.7: Stress vs. strain curves of coupons from the infill plate in the first story of the RBS test specimen	228
Figure B.8: Stress vs. strain curves of coupons from the infill plate in the second story of the RBS test specimen	229
Figure B.9: Stress vs. strain curves of coupons from the column plates of the RBS test specimen	229

Figure B.10: Stress vs. strain curves of coupons from the flanges of the first floor beam of the RBS test specimen	230
Figure B.11: Stress vs. strain curves of coupons from the web of the first floor beam of the RBS test specimen	230
Figure B.12: Stress vs. strain curves of coupons from the flanges of the second floor beam of the RBS test specimen	231
Figure B.13: Stress vs. strain curves of coupons from the web of the second floor beam of the RBS test specimen	231

LIST OF ABBREVIATIONS AND SYMBOLS

ABBREVIATIONS

ASTM	American Society for Testing and Materials
ATC	Applied Technology Council
CSA	Canadian Standard Association
LVDT	Linear Variable Displacement Transformer
PEC	Partially Encased Composite
RBS	Reduced Beam Section

SYMBOLS

A_c	cross sectional area of the concrete
A_r	the cross-sectional area of the longitudinal rebars
A_{se}	effective area of the built-up steel section
A_{st}	Area of steel in the tension part of the PEC column
a	depth of the compression part of PEC column; distance from the face of column to the starting point of the RBS cut
b	half-flange width of PEC column; length of the RBS cut; dimension of PEC column parallel to the bending axis
b_e	effective half-flange width of PEC column
b_f	total flange width of PEC column; beam flange width
C_2	parameter representing the difference between maximum stress and mean stress in a non-uniform tension field
C_3	percentage decrease in the average tensile stress in the portion of the tension field anchored to the beam compared to the average tensile stress across the full tension field

C_{ec}	Euler buckling load
C_r	factored compressive resistance of steel in the compression part of the PEC column; cross sectional axial strength of PEC column
C_{rc}	factored compressive resistance of PEC column
C_r'	factored compressive resistance of concrete in the compression part of the PEC column
c	RBS cut depth
D / T	ratio of the dead load to total axial load
d	depth of the cross section of PEC column; beam depth
E	Young's modulus of the steel plate in PEC column
E_c	Young's modulus of concrete
E_{ce}	effective elastic modulus of concrete
EI_e	effective stiffness of the PEC column
e	lever arm between C_r and T_r
e'	lever arm between C_r' and T_r
F_y	nominal yield stress of steel
F_{yr}	nominal yield stress of the longitudinal rebars
f_{ce}	effective compressive strength of concrete
f_c	concrete cylinder strength
h	story height in steel plate shear wall
I_b	moment of inertia of end beam in steel plate shear wall
I_c	moment of inertia of concrete portion of PEC column; moment of inertia of column in steel plate shear wall
I_L	moments of inertia of left column of steel plate shear wall
I_R	moments of inertia of right column of steel plate shear wall
I_s	moment of inertia of steel portion of PEC column
KL	effective PEC column length
K_e	elastic stiffness

k	plate buckling coefficient for flanges of PEC column
L	width of the wall between column centerlines in steel plate shear wall
L_{strip}	length of the tension strip in steel plate shear wall
M_{rc}	factored bending resistance of PEC column
Q	force control parameter
Q_1	base shear in first half of cycles in cyclic test
Q_2	base shear in second half of cycles in cyclic test
Q_p	peak base shear
Q_y	yield value of force control parameter
q_b	component of anchoring force, perpendicular to end beam
q_c	component of anchoring force, perpendicular to column
R	radius of RBS cut; force modification factor
s	longitudinal link spacing in PEC column
T_r	factored tensile resistance of the steel in the tension part of the PEC column
t	steel plate thickness of PEC column; flange thickness of PEC column
t_f	the flange thickness of beam
V	shear force of story in steel plate shear wall
w	infill plate thickness in steel plate shear wall
Z	plastic modulus of the full section of the beam
Z_{RBS}	plastic modulus of the section where plastic hinge forms
α	factor to account for flange imperfections and residual stresses in PEC columns; angle of inclination of tension field diagonals from vertical in steel plate shear wall
α_1	parameter to account for the effect of concrete strength
Δx	offset of plastic hinge from the center of the RBS cut toward the column face
δ	deformation control parameter
δ_1	in-plane displacement in first half of cycles in cyclic test
δ_2	in-plane displacement in second half of cycles in cyclic test
δ_b	flexural deflection of end beam due to anchoring force of the infill plate

δ_c	flexural deflection of column due to anchoring force of the infill plate
δ_{c_L}	inward deflection of left column in steel plate shear wall
δ_{c_R}	inward deflection of right column in steel plate shear wall
δ_{strip}	shortening of tension strip due to the inward deflection of the anchoring columns in steel plate shear wall
$\bar{\delta}_y$	yield value of deformation control parameter
ϵ_{max}	maximum strain in the tension diagonals in steel plate shear wall
η	plastic modulus reduction ratio at the center of the RBS cut
η_L	flexural deflections of left column of steel plate shear wall within story height
η_R	flexural deflections of right column of steel plate shear wall within story height
φ	resistance factor for structural steel
φ_c	resistance factor for concrete
φ_r	resistance factor for rebars
λ	global slenderness of PEC column
λ_p	flange slenderness of PEC column
σ_t	tensile stress in the tension field
$\sigma_{t\ max}$	maximum stress in a non-uniform tension field
$\sigma_{t\ mean}$	uniform tension field stress
u	Poisson's ratio of steel plate in PEC column
ω_h	column flexibility parameter
ω_L	end-panel flexibility parameter
Ψ	reduction parameter for size effect in PEC column

1. INTRODUCTION

1.1 General

The steel plate shear wall system has been known as one of the most effective means of resisting lateral loads, particularly forces applied to a structure during seismic events. It consists of a vertical steel infill plate connected to a surrounding frame of beams and columns to transfer lateral loads to the foundation. A typical steel plate shear wall is shown in Figure 1.1. The behavior of conventional steel plate shear walls has been studied in many numerical and experimental research projects and the general behavior of these walls is now reasonably well understood.

Columns of steel plate shear walls in mid- to high-rise buildings usually require a large compressive capacity, as they carry both the gravity loads and axial loads introduced by the overturning moment from lateral loads. Since the infill plate is commonly very thin and unstiffened, due to labor cost and foundation design concerns, it buckles in the early stages of loading and, thus, most of its shear capacity comes from tension field action in the post-buckling stage, as depicted in Figure 1.2. For the efficient use of steel in the infill plate, as well to achieve good overall seismic performance by the wall, the developed tension field should be fairly uniform, which requires proper anchorage from the surrounding frame members. As such, the boundary members should possess a flexural stiffness sufficient to achieve this. Based on the similarity of steel plate shear walls and plate girders, the North American steel design standards have defined a column flexibility parameter, ω_h , to help design engineers define the minimum required column stiffness in the middle stories of buildings. The definition of the column flexibility parameter is based on Wagner's (1931) study on plate girders. However, for the top and bottom stories, where the infill plate is anchored by end beams and columns, no feasible method existed to define the required minimum stiffnesses of the surrounding members.

The requirement of columns with high axial strength and flexural stiffness makes the composite column an attractive option for steel plate shear wall systems. In addition to strength and stiffness advantages, they typically occupy less plan area than equivalent bare steel columns and they commonly provide better fire resistance. A new type of composite column, the partially encased composite (PEC) column, was introduced and patented by the Canam Group Inc. to facilitate erection and reduce the overall cost of construction. A typical PEC column is depicted in Figure 1.3. It consists of a welded H-shaped steel section, made of thin plates, with transverse links that are welded between the flanges, close to the flange tips, to increase the local buckling capacity of the flanges. The same plate thickness is used for both the flanges and web to minimize cost. The steel skeleton erection speed is high and a smaller crane capacity is required because only the steel part of the column needs to be lifted by the crane. The formwork is simple and the concrete is cast at the same time as the concrete for the floor slab above.

Several experimental and numerical research projects have been conducted to investigate the behavior of PEC columns under concentric and eccentric axial loads. The important design parameters and failure mode have been well defined and an equation has been developed to calculate the axial strength of this type of composite column. To take advantage of the high axial strength and flexural stiffness of the PEC column in the steel plate shear wall system, an experimental research project consisting of three large-scale tests has been conducted at the University of Alberta. Deng et al. (2008) designed and tested the first test specimen (benchmark test) in which the infill plate was surrounded by a frame with rigid frame connections. The PEC columns in this test specimen were detailed according to the observations from previous experimental tests on this type of column under axial loads.

The research described herein consists of two parts. The first part includes an analytical and numerical study to develop a new flexibility parameter for end panels and to define the upper and lower limits of the new parameter in order to determine the minimum

flexural stiffness required for end (top and bottom) beams. As the beam-to-column connection in steel plate shear wall system is more rigid compared to the connection between the stiffeners and flanges of plate girders, a numerical study has been conducted to determine the effect of the connection rigidity on the minimum required stiffness of the surrounding members and the results have been presented. The second part includes the design and test of two large-scale steel plate shear wall specimens with PEC columns under quasi-static cyclic loads. A proposed modular construction method has been examined in one of the tests and in the other test specimen; a modified frame connection has been included.

1.2 Objectives and scope

Most of the diagonal tension field in the top and bottom stories of the steel plate shear wall system is anchored to a column at one end and the end beam at the other end; thus, some of the assumptions that Wagner (1931) made to develop the column flexibility parameter are not valid. To develop a feasible method to define the minimum flexural stiffness of the end beams, it is necessary to develop a new parameter for end panels and define appropriate limits for it. The main objective of the first part of this research is to develop a flexibility parameter for the end panels. To achieve the end panel flexibility parameter, ω_L , some new assumptions are made and the philosophy behind the equation of the column flexibility parameter, ω_h , developed by Wagner (1931), is utilized. The maximum and minimum values of the end panel flexibility parameter, ω_L , are proposed based on the results of an extensive numerical study. The other objective of the first part of this research is to investigate the effect of the beam-to-column connection rigidity on the stress distribution in the tension field of the middle, top and bottom stories.

Following the experimental study on the first steel plate shear wall with PEC columns (benchmark test specimen), conducted by Deng et al. (2008), two more test experiments are designed, fabricated, and tested as the second part of this research. The primary

objective of these experiments is to increase the database of the test results of steel plate shear walls with PEC columns under extreme cyclic loading, such as would be expected in a severe earthquake. One of the main interests is to observe the behavior of the PEC column in a steel plate shear wall system, where columns are subjected to axial forces, as well as bending moments due to transverse loads from anchored infill plates. The details of the PEC columns in the test specimens are modified based on lessons learned from the benchmark test (Deng et al. 2008).

The use of a modular construction method in the fabrication of one of the test specimens has been proposed by industry. In the proposed method, all parts of the steel plate shear wall system are prefabricated in the shop and assembled at the construction site using bolted connections. The main advantage of this method is the elimination of field welding, which tends to have both higher cost and lower quality as compared to shop welding. The frame connections will only transfer shear in this method. One of the objectives of the second part of this research is to study the behavior of the specimen built using the modular construction method. Some of the design concerns are discussed in this research and the test results of the modular specimen is presented.

To reduce the demand on the beam-to-column connections, reduced beam section (RBS) connections, one of the post-Northridge moment frame connections, was used in one of the specimens. The use of this type of connection has not been widely studied in previous research on steel plate shear walls. The objective of the experimental study of the specimen with RBS connections was to increase the understanding of the behavior of the RBS connection in the steel plate shear wall system. Following the observations of Qu and Bruneau (2010), the location of the plastic hinge was closely monitored by instrumentation of the RBS cut region.

1.3 Thesis overview

This thesis consists of eight chapters. An overview of the remaining chapters follows.

In Chapter 2, an overview of the previous experimental and numerical studies on partially encased composite columns is presented to provide a better understanding of the important design parameters and failure modes. The current design equations in the Canadian steel design standard, CSA S16-09 (CSA 2009), and their background are also presented. Previous studies on RBS connections and associated design parameters are briefly reviewed. A detailed background review of the column flexibility parameter is presented and, finally, a discussion of some large-scale tests on steel plate shear walls is presented. The first experimental study on a steel plate shear wall with PEC columns (Deng et al. 2008) has also been reviewed to put the test specimens in this research into context.

Chapter 3 includes the development of the end-panel flexibility parameter and the determination of its proposed upper and lower limits. The effect of the frame connection rigidity on the uniformity of tension field stresses is also studied in this chapter.

In Chapter 4, the details and some design concerns of the modular and RBS test specimens are discussed. The test set-up and cyclic load regime are defined and details of the instrumentation of the specimens are also shown in this chapter. The details of the concrete placement and the ancillary tests to define the material properties are described and a summary of the material properties is provided at the end of this chapter.

Observations during the test and the results of the modular steel plate shear wall specimen test are presented in Chapter 5. The overall modular test specimen behavior is discussed and some related key parameters like initial stiffness, ductility and energy dissipation capacity have been evaluated in this chapter.

Chapter 6 mainly deals with the test results of the test specimen with RBS connections. The observations during the test and hysteretic loops are provided in this chapter. Some related important parameters like initial stiffness, ductility and energy dissipation capacity are studied. The strain data in the RBS cut region has been evaluated. Some results of the 3D camera system in the form of the strain contours are presented to show the failure mode of the PEC column at its base.

In Chapter 7, the results of the steel plate shear wall tests are compared to the results of the test conducted by Deng et al. (2008). The reasons for the differences between test results are discussed in this chapter.

In Chapter 8, the summary of the methodology and conclusions are presented. Design and research recommendations are also included in this chapter.



Figure 1.1: Typical steel plate shear wall (Photo courtesy of Canam Group)



Figure 1.2: Development of tension field in post-buckling stage in steel plate shear wall

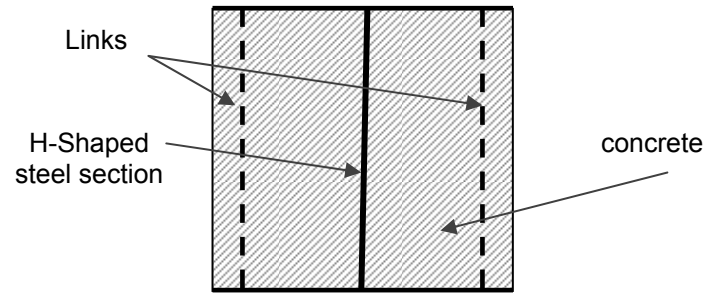


Figure 1.3: Typical cross section of PEC column

2. BACKGROUND AND LITERATURE REVIEW

2.1 Introduction

The behavior of steel plate shear walls with unstiffened infill plates is highly dependent on the post-buckling strength of the infill plates, as the infill plates are very thin and will buckle in the early stages of loading. The presence of boundary frame members with high flexural stiffness is crucial for the development of a fairly uniform tension field and, thus, efficient use of steel.

Partially encased composite columns with a built-up steel section was introduced by the Canam Group Inc. as a viable option for columns in the steel plate shear wall system, as it provides several structural and construction advantages.

In this chapter, first partially encased composite columns are introduced and the experimental and numerical studies on this type of column are reviewed. The focus of this review is on the axial strength and several parameters affecting the ductility of these columns as part of an earthquake resisting system. The proposed equations to predict the axial strength and their background are also provided in this part to provide a better understanding of the behavior of these columns.

As one of the test specimens in this study includes reduced beam section connections, a brief background of this connection type and its design concerns are provided in this chapter. The concept of steel plate shear walls is discussed and several studies that include large-scale tests of multi-story steel shear wall specimens are reviewed to identify important design issues and observations during those tests. Finally, the details of the numerical and experimental studies on the first steel plate shear wall with partially encased composite columns are explained to outline the lessons learned from that test that led to some modifications in the design of the test specimens in the current study.

2.2 Partially encased composite columns

Composite columns are constructed by using different combinations of steel and concrete to make use of their beneficial properties, such as high tensile strength and ductility of steel and high compressive strength and fire resistance of concrete, in an efficient way, depending on the required performance of the member. Concrete-filled tubes and fully encased columns are two common types of composite columns in use and are shown in Figure 2.1.

Composite columns are well known to possess high axial strength and flexural stiffness. The confinement of concrete by steel increases its compressive strength and ductility. It is beneficial to have the steel part surround and confine all the concrete. This arrangement will also help in connecting the steel beams to the column. The size of concrete-filled tubes and partially encased composite columns with standard steel sections, as shown in Figure 2.2a, are limited to available standard sections. Partially encased composite columns can also be built using built-up H-shaped steel sections to eliminate the discrete size restrictions.

The concept of partially encased composite columns fabricated with built-up steel sections, hereafter referred to as “PEC” columns in this manuscript, was in the mid-1990s. This type of column consists of a welded H-shaped steel section with transverse links that are welded between the flanges, close to the flange tips, and spaced at regular intervals to increase the local buckling capacity of the thin flanges (Vincent and Tremblay 2001). Figure 2.2b shows the cross-section of a PEC column. Concrete is cast between the flanges at the same time as the floor slab above is cast. In order to provide a means for connecting the perpendicular beams into the column at each floor level, side plates are welded to the column flange tips. The major advantage of PEC columns over partially encased composite columns with standard steel columns is that there is no limitation on the size of column. PEC columns can be sized to meet exactly the construction and

service condition requirements. As the flanges and web of the H-shaped steel section are relatively thin, the weight of the column at the time of erection is low, which reduces the size of the crane required on site. The steel flanges and web have the same thickness, so they may be cut from the same plate. The simple formwork also makes this type of composite column more economical. Figure 2.3 shows the sequence of construction of PEC column.

2.2.1 Experimental studies on PEC columns

The first series of tests on PEC columns was done by Tremblay et al. (1998). Transverse links were required to postpone the local buckling of the column flanges. All the PEC columns in this research were short, with lengths equal to five times the overall cross section dimensions, in order to preclude global buckling of test specimens during the test. A total of six PEC columns were tested under concentric axial load. The specimens had square cross sections of either 300 mm × 300 mm or 450 mm × 450 mm. The yield stress of the steel material, which was used to fabricate the H-shaped steel section, was 370 to 374 MPa. The concrete in the column had a compressive strength of 31.9 to 34.3 MPa on the test date. The link spacing varied from half the cross section depth to the full cross section depth. In one of the specimens, a thinner plate was used to increase the slenderness of the flanges of the column (b / t) from 23.2 to 35.4, where b is the half-flange width and t is the flange thickness. The column dimensions of one column were less than the rest of the specimens to explore the size effect on the strength of the column. The failure mode in all the test specimens was local buckling of the steel flanges and crushing of the adjacent concrete core. Tremblay et al. (1998) observed that larger flange slenderness led to lower strength and faster strength degradation in the post-peak stage. Closer links also increased the ductility of the columns and improved the post-peak behavior of PEC columns.

To study the local buckling behavior of PEC columns under construction loadings and before attaining composite action, Fillion (1998) tested ten bare steel columns under concentric axial load. The columns were short enough to preclude global buckling. The changing parameters in this study were the flange slenderness (b/t), the link spacing, the link shape and the link cross-sectional area. The axial strength of the columns was predicted according to the North American Specification for the Design of Cold-Formed Steel Structural Members, CSA S136-94 (CSA 1994). According to this standard, the effective cross-sectional area was calculated by neglecting part of the flanges at their tip, to account for the local buckling effect. The average ratio of test to predicted peak load was 1.22 with a coefficient of variation close to 0.15, which indicated that design formulas were conservative in predicting the axial strength of these columns.

Chicoine et al. (2002a) tested five more stub PEC columns to further investigate the effect of extra longitudinal and transverse reinforcement, the overall cross section size, link spacing (s/b) and column flange slenderness (b/t), where s is the longitudinal link spacing, b is the half-flange width and t is the flange thickness. The cross sections of these columns were 600 mm \times 600 mm and the concrete strength was 34 MPa. The failure mode was similar to that of the previous six column specimens, tested by Tremblay et al. (1998). Those columns with link spacings equal to depth of the cross section, experienced local buckling of the flanges at around 75% of the peak load, while those with link spacings equal to one-half the depth of the cross section did not experience local buckling until after the peak load was reached and showed better post-peak behavior. The additional reinforcement was observed to improve the post-peak behavior and ductility of PEC columns. The effect of the transverse stresses in the flanges due to the concrete confinement was studied and it was observed it had a negligible effect on the axial capacity of PEC columns. It was recommended that the link spacing be limited to one-half the depth of the cross section and the slenderness of the flanges (b/t) be limited to 30. The use of extra reinforcement was determined to be unnecessary unless higher ductility and better post-peak behavior were required.

In order to have a better understanding of the long term behavior of PEC columns (as a member that incorporates concrete) and the effect of the construction loading sequence, seven stub PEC columns were tested by Chicoine et al. (2003). The cross section of these columns was either 300 mm × 300 mm or 450 mm × 450 mm and the concrete compressive strength was 30 to 36.8 MPa. First, the bare steel sections were loaded to reach 100 MPa in compression and then the concrete was cast and cured for two weeks. Four of the specimens were loaded under expected long term service load for 136 days, after the two week curing period. All the test specimens were loaded to failure, 150 days after the concrete was cast. The results indicated that the shrinkage of concrete introduced a compressive stress of 7 MPa in the steel. The creep strains were found to follow the same models as other concrete sections. The failure mode of the PEC columns under long term loading was similar to that of the short term loading tests. The axial capacity of the columns was not affected by the stress conditions before loading the specimens to failure.

A comprehensive experimental study was done by Bouchereau and Toupin (2003) on PEC columns under combined axial load and bending moment. A total of 22 stub PEC columns (or beam-columns) and two PEC beams were tested. The cross section of all the specimens was 450 mm × 450 mm, with a link spacing of 300 mm in the central part of the specimens. The nominal yield strength of all the steel plates was 350 MPa and the concrete had a compressive strength of around 34 MPa. The steel flange slenderness (b/t) was 23.6 in all the specimens. Almost half of the specimens had additional longitudinal and transverse reinforcement. Cyclic loading, with both large and small amplitudes, was applied to 11 specimens, while monotonic loading was applied to the rest of the specimens. The axial load was applied to the center of the column specimens or with an eccentricity to introduce bending moment in the column. The columns with eccentric axial load experienced a constant bending moment around one of their principal axes. The type of load application, i.e., monotonic versus cyclic, changed neither the peak loads nor the post-peak behavior of the columns, although all of the specimens

under cyclic load failed in a ductile manner. The results of the specimens with additional reinforcement indicated higher ductility with a slight increase in peak load (around 8%). Those specimens under monotonic eccentric load with respect to the weak axis and with additional reinforcement had significantly better behavior than those without additional reinforcement.

Following their experimental study, Bouchereau and Toupin (2003) constructed interaction diagrams by assuming a linear strain distribution in the cross section and using the typical methods adopted for reinforced concrete columns. Although the effect of the flange local buckling, concrete confinement and residual stresses in the steel section were neglected, there was good agreement between predicted and experimental results, especially when the bending moment was around the strong axis. In some cases where the bending moment was around the weak axis and there was no longitudinal reinforcement, the interaction diagrams overestimated the capacity of the columns and the difference was attributed to the accidental imperfections and improper installation in those specimens.

Prickett and Driver (2006) tested 11 stub PEC columns to further investigate the effect of link spacing (s/b) and load eccentricity and also challenge the requirement of the CSA S16-01 (CSA 2001) that limited the concrete compressive strength to 40 MPa. They used three types of concrete in their research: normal strength concrete (29.2 MPa), high strength concrete (62.6 MPa) and high strength steel-fiber reinforced concrete (51.1 MPa). The nominal yield stress of all steel plates was 350 MPa. The cross section of all the specimens was 400 mm \times 400 mm and all specimens were 2000 mm long. The flange slenderness (b/t) was 25 in all specimens and the local imperfections of the flanges between the links were inward in most cases. Seven specimens, consisting of two specimens with normal strength concrete, three specimens with high strength concrete and two specimens with high strength concrete with steel fibers, were tested

under concentric axial load. The remaining four specimens, which were made of high strength concrete, were subjected to eccentric axial load.

In the specimens under concentric load, the failure mode was concrete crushing and flange buckling. The failure of the specimens with high strength concrete was less ductile, although addition of steel fibers helped increase the ductility of the failure. The local buckling of the flange did not happen before the peak load in any specimen except the one with outward imperfections of the flange between links. It was observed that decreasing the link spacing increased the ductility of the failure. The stress in the links was the highest in the specimens with high strength concrete with steel fibers, as they sustained their peak load over a larger strain range. It was concluded that the degree of confinement of concrete in the steel section was low and it did not affect the axial load capacity of the columns. The average test to predicted capacity ratio was high, which indicated the formula in the CSA S16-01 (CSA 2001) was conservative and thus some modifications in the formula were proposed by Prickett and Driver (2006).

The failure mode in the specimens under eccentric load was similar to that of the specimens under pure axial load. The ductility of failure was different depending on the axis of bending, as the specimens with bending about the strong axis had a more gradual hinge formation and ductile failure compared to the ones with bending about the weak axis. The reason was that in the former, the extreme compressive fiber in the sections was steel and the concrete was better confined. Except in one case, local buckling of the flange happened at the peak load. The stress in the links was found to be relatively small (less than half the yield stress). The longitudinal strain distribution in the cross section was found to be almost linear, according to strain gauge readings. Prickett and Driver (2006) constructed axial load versus bending moment (P-M) interaction diagrams by considering the effect of the local buckling of flanges of the columns (i.e., by calculating the effective area of the flange under compression) and in all the cases, the predicted values were conservative.

2.2.2 Numerical studies on PEC columns

The first reported numerical study on partially encased composite columns with built-up steel sections was carried out by Maranda (1999). The finite element model included a quarter of the cross section between two links and in the modeling, the imperfection of the flanges, residual stresses in the steel section and contact elements between steel and concrete were addressed. The average numerical peak load obtained from this model was more than the experimental study peak loads, as reported by Tremblay et al. (1998). In some cases the peak load was not reached as the stiffness at the last converged point was observed to be positive.

Chicoine et al. (2002b) did a finite element analysis using a commercial finite element program, ABAQUS/Standard (HKS 2000). The created models were examined and calibrated using the results of the previous experimental studies on short PEC columns under axial load (Tremblay et al. 1998; Chicoine et al. 2002a). The finite element program included a quarter of the cross section between two links. The interaction between steel and concrete was modeled using springs with high compressive stiffness and very small tensile stiffness. The imperfection of the flanges was included in the model by giving an outward out-of-straightness to the tip of the flanges between links. The residual stress was considered as an initial condition in the steel plates. Steel material properties were defined in the program as a bilinear stress-strain curve based on the results of the tension coupon tests. The cracking model in ABAQUS/Standard (HKS 2000) was implemented to resemble concrete behavior in the models. The mechanical properties of concrete were defined by using an effective compressive strength and effective elastic modulus, as shown below:

$$f'_{ce} = 0.92\psi f'_c \quad (2.1)$$

$$E_{ce} = \sqrt{0.92\psi} E_c \quad (2.2)$$

$$\Psi = 0.85 \left(0.96 + \frac{22}{b} \right) \quad (0.85 \leq \Psi \leq 0.97) \quad (2.3)$$

where b is half-flange width.

The effective compressive strength, f_{ce} , and elastic modulus, E_{ce} , were calculated considering a reduction factor of 0.92 to take into account the lower quality of the structural concrete in the specimens compared to the concrete in the test cylinders, as well as another reduction parameter, Ψ , to take into account the size effect.

The developed numerical model by Chicoine et al. (2002b) was able to reach the peak point and pass it but was unable to trace the post-peak behavior of PEC columns. The concrete model was not able to reproduce the rapid volumetric expansion of concrete; thus the imperfection of the flanges had to be outward, unlike the real situation, to help the model enter the geometry nonlinearity and include the local buckling of flanges. The results showed that the degree of confinement of concrete was small and so Chicoine et al. (2002b) suggested neglecting the effect of confinement of concrete in design. It was observed that the presence of the residual stresses reduced the flange capacity by an average of 5% and the initial imperfection of flanges caused a 3% reduction in the flange capacity.

Begum et al. (2007) developed a more sophisticated model of the whole PEC column, contrary to the previous numerical studies which focused on a small portion of column, in order to get better results from their numerical study with regard to the effect of the initial imperfections, post-peak behavior and the behavior of PEC columns under combinations of axial load and bending moment. The modeling was done by using a commercial finite element program, ABAQUS/Explicit (HKS 2003). A damage plasticity model was used to simulate the concrete behavior. The advantage of the damage plasticity model was that it was capable to predict the concrete behavior in both compression and tension under low confining pressure. The dynamic explicit method was selected for analysis as it was

capable of determining the solution without iteration, which in the case of PEC columns was critical as the model was highly nonlinear, especially around the peak point and at the post-peak stage.

The steel material properties for plates and links were defined in the model using a tri-linear curve for the true stress-true strain relationship. Begum et al. (2007) modeled the imperfections of the flanges as in the real PEC column, i.e., inward imperfections, and were able to get the same failure mode as observed in the previous experimental studies (Tremblay et al. 1998; Chicoine et al. 2002a). The residual stresses were introduced in both flanges and the web as initial conditions and their distributions were assumed to be the same along the columns.

The results of the numerical study were in very good agreement with the experimental results. The experimental-to-numerical ratios for the peak load and longitudinal strain at peak point in the whole-column models were 1.00 and 1.01, respectively. The effect of the flange imperfections was observed to be negligible on the axial strength of columns, as they were inward. The effect of the link spacing was also investigated and it was seen that smaller link spacings caused more gradual failure. The effect of residual stresses on the behavior of columns was also determined to be negligible.

Tremblay et al. (2003) conducted a seismic dynamic study on two typical high-rise buildings, 16 and 24 stories, with concentrically braced steel frames and PEC columns to evaluate the flexural demand on both the gravity columns and the bracing bent columns. The concrete strength was either 30 or 60 MPa. It was observed that due to the higher mode effects, the columns in the top portion of the bracing bent were subjected to significantly higher demand and consideration of the flexural demand is essential at the design stage to avoid premature failure under code-level earthquakes. The maximum compressive and tensile stresses in the concrete were higher in columns with lower

concrete strength, as these columns were bigger in cross sectional size and thus carried greater values of story shear.

2.2.3 Prediction of the strength of the PEC columns

Following their experimental study on stub PEC columns, Tremblay et al. (1998) proposed the following equation to predict the overall PEC column strength under concentric axial strength:

$$C_r = A_{se}F_y + 0.85A_c f'_c + A_r F_{yr} \quad (2.4)$$

where A_{se} is the effective area of the built-up steel section, F_y is the nominal yield stress of steel plate, A_c is the cross sectional area of the concrete, f'_c is the concrete cylinder strength, and A_r and F_{yr} are, respectively, the cross-sectional area and nominal yield stress of the longitudinal rebars. The factor of 0.85 is used to relate the concrete cylinder strength to in-situ concrete strength.

Tremblay et al. (1998) proposed the following equation for the calculation of effective area of the built-up steel section:

$$A_{se} = (d - 2t + 4b_e)t \quad (2.5)$$

where d is the depth of the cross section, t is the plate thickness and b_e is the effective half-flange width. The effective half-flange width, b_e , was proposed to be calculated as follows:

$$b_e = \alpha \frac{1}{\lambda_p} b \leq 1.0 \quad (2.6)$$

$$\lambda_p = \frac{b}{t} \sqrt{\frac{12(1-u^2)F_y}{\pi^2 E k}} \quad (2.7)$$

$$k = \frac{4}{(s/b)^2} + \frac{15}{\pi^4} (s/b)^2 + \frac{20}{3\pi^2} (2 - 3u) \quad (2.8)$$

where α is an empirical factor to account for flange imperfections and residual stresses, λ_p is the flange slenderness, b is the half-flange width, u and F_y and E are, respectively, the Poisson's ratio, yield stress and Young's modulus of the steel plates, k is the plate buckling coefficient and s is the link spacing. Tremblay et al. (1998) proposed parameter α to be equal to 0.6 for the best fit of predicted strength to experimental results.

Tremblay et al. (2000a) observed that Equation (2.6) was non-conservative for larger cross sections so the following equation was proposed to calculate the effective half-flange width, b_e :

$$b_e = \frac{b}{(1 + \lambda_p^{2n})^{(1/n)}} \leq b \quad (2.9)$$

Parameter n in Equation (2.9) was proposed to be equal to 1.0 for a better fit, compared to the Equation (2.6), to experimental results for columns under short term axial loads.

Tremblay et al. (2000b) reduced the cross-sectional axial strength, C_r calculated from Equation (2.4), to account for the global buckling behavior of long columns. The double exponential format in the Canadian Steel Design Standard, CSA S16-09 (CSA 2009), was used and thus the proposed equation was:

$$C_u = C_r (1 + \lambda^{2.68})^{(-1/1.34)} \quad (2.10)$$

where λ is the global slenderness of the column, calculated as follows:

$$\lambda = \sqrt{\frac{C_r}{C_{ec}}} \quad (2.11)$$

$$C_{ec} = \frac{\pi^2 E I_e}{(KL)^2} \quad (2.12)$$

$$E I_e = E I_s + \frac{0.6 E_c I_c}{1 + D/T} \quad (2.13)$$

where C_{ec} is the Euler buckling load, $E I_e$ is the effective stiffness of the PEC column, KL is the effective column length, E and E_c are, respectively, the Young's modulus of steel and concrete, I_s and I_c are the moment of inertia of steel portion and concrete portion of the column, and D / T is the ratio of the dead load to total axial load.

Chicoine et al. (2001) did some finite element analysis on the elastic buckling of the unsupported steel flange panels and proposed the following equation to calculate the plate buckling coefficient, k :

$$k = \frac{0.9}{\left(\frac{s}{b_f}\right)^2} + 0.2 \left(\frac{s}{b_f}\right)^2 + 0.75 \quad (0.5 \leq \frac{s}{b_f} \leq 1) \quad (2.14)$$

where b_f is the total flange width.

Chicoine et al. (2002b) proposed replacing the coefficient 0.85 in Equation (2.4) with 0.92Ψ , as defined in Equation (2.1), to account for the concrete quality difference between test cylinder concrete and in-situ concrete, as well as the cross sectional size effect. Chicoine et al. (2002b) examined $n = 2.0$ in Equation (2.9) and got the best fit to the experimental results of the columns under long term axial loads. By considering $n = 1.5$, it was observed that the mean test-to-predicted ratio was 1.03. The researchers proposed $n = 1.5$ for design, as the possible imperfections in the columns could be larger than those measured in the tests.

Canadian Steel Design Standard CSA S16-01 (CSA 2001) adopted the proposed method by Chicoine et al. (2002b) to calculate the factored compressive resistance of the PEC

columns, C_{rc} , except that the concrete strength modifier factor, 0.92Ψ , was replaced with the conservative constant value of 0.8. The adopted equation in CSA S16-01(CSA 2001) was therefore as follows:

$$C_{rc} = (\phi A_{se} F_y + 0.8 \phi_c A_c f'_c + \phi_r A_r F_{yr}) (1 + \lambda^{2.68})^{(-1/1.34)} \quad (2.15)$$

In 2009, the Canadian Steel Design Standard, CSA S16-09 (CSA 2009), made some modifications to Equation (2.15) to better fit the predicted values to test results. The new design equation is as follows:

$$C_{rc} = (\phi A_{se} F_y + 0.95 \alpha_1 \phi_c A_c f'_c + \phi_r A_r F_{yr}) (1 + \lambda^{2.68})^{(-1/1.34)} \quad (2.16)$$

$$\alpha_1 = 0.85 - 0.0015 f'_c \geq 0.67 \quad (2.17)$$

Parameter α_1 is added to account for the effect of concrete strength on the axial capacity of PEC columns as the maximum permitted concrete strength limit is also increased in CSA S16-09 (CSA 2009) from 40 MPa to 70 MPa, based on the test results of Prickett and Driver (2006).

CSA S16-09 (CSA 2009) includes an equation to calculate factored bending resistance of PEC columns, as follows:

$$M_{rc} = C_r e + C'_r e' \quad (2.18)$$

$$T_r = \phi A_{st} F_y = C_r + C'_r \quad (2.19)$$

$$C'_r = 1.18 \alpha_1 \phi_c a (b - t) f'_c \quad \text{for strong axis bending} \quad (2.20)$$

$$C'_r = 1.18 \alpha_1 \phi_c a (b - 2t) f'_c \quad \text{for weak axis bending} \quad (2.21)$$

where T_r is the factored tensile resistance of the steel in tension part of the section and C_r and C_r' are, respectively, the factored compressive resistance of steel and concrete in the compression part of the section. e is the lever arm between C_r and T_r and e' is the lever arm between C_r' and T_r . a is the depth of the compression part and b is the dimension of the PEC column parallel to the bending axis.

For cases that both axial force and bending moments are applied to PEC columns, CSA S16-09 (CSA 2009) provides the following interaction equation for design:

$$\frac{C_f}{C_{rc}} + \frac{M_{fx}}{M_{rcx}} + \frac{M_{fy}}{M_{rcy}} \leq 1 \quad (2.22)$$

2.3 Reduced Beam Section (RBS) connections

Moore et al. (1999) summarized the studies on the design of the Reduced Beam Section (RBS) moment frame connections. One of the lessons learned from the Northridge earthquake was that the frame connections should be designed considering both the load and the deformation. In most of the post-Northridge connection designs, the plastic hinge is forced to form away from the column face. This requires the beam to be either strengthened at the ends, which tends to be costly, or weakened far enough from the column face.

The weakening is usually done by cutting part of the flange, typically both flanges, close to the frame connection, as shown in Figure 2.4a. Various shapes of cuts are possible, including constant cuts, tapered cut and radius cut. The shape, size and location of the cut affect the connection demands and performance. Various test programs have been conducted on straight cut, taper cut and radius cut to investigate the behavior of different types of RBS connections. Out of the different cut shapes, radius cut causes the least stress concentration, which reduces the chances of a fracture occurring within the

reduced sections (Engelhardt et al. 1996). The test results also indicated that inelastic deformation is distributed over the length of the reduced section.

By reducing the demand on the weld that connects the beam flange to the column and the surrounding base metal in connections, the possibility of fracture reduces. Although the RBS cuts reduce the stiffness of the frame, it has been shown that the reduction is very small. A study by Grubbs (1997) over a wide range of frame configurations, showed only a 5 to 7 percent reduction in the frame stiffness for a 50 percent reduction in the flange width.

The overall goal in sizing the RBS cuts is to limit the moment at the face of the column to 85 to 100 percent of the beam plastic moment. Figure 2.4b shows the typical geometry of the radius cut RBS. Dimension a, which is the distance from the face of the column to the starting point of the RBS cut, and dimension b, which is the length of the cut, should be short enough to minimize the moment increase between the plastic hinge and the column face. However, dimension a should be large enough to let the stress distribution in the flange become uniform by the face of the column. Dimension b should be large enough to avoid excessive plastic strains due to stress concentration. The following equations are suggested (Moore et al. 1999) to determine these dimensions:

$$a \cong (0.5 \text{ to } 0.75)b_f \quad (2.23)$$

$$b \cong (0.65 \text{ to } 0.85)d \quad (2.24)$$

where b_f is the beam flange width and d is the beam depth.

Dimension c, which is the RBS cut depth, should be determined so that the moment at the face of column remains between 85 to 100 percent of the beam plastic moment. It is suggested to limit the flange cut depth to 50 percent of the flange width.

As the RBS cut is normally made by thermal cutting, the cut should be made to avoid nicks, gouges and other discontinuities. The surfaces should be ground smooth to remove any notches in order to avoid fracture or low cycle fatigue in the cut portion. All corners should be rounded to minimize notch effects and, in addition, cut edges have to be ground to a surface roughness of less than 500 micro-inches to meet the requirements of AWS C4.1-77 class 4 (1977).

2.4 Steel plate shear walls

The steel plate shear wall consists of a vertical steel infill plate connected to a surrounding frame of beams and columns to brace it and transfer the lateral loads, such as forces introduced by wind and earthquake, to the foundation. In a qualitative manner, steel plate shear walls are similar to vertical plate girders. For seismic retrofit of some structures, using modular construction methods is attractive as they facilitate relocation of the infill plate. For these cases, steel plate shear wall is an attractive option as it is easily and fast executable (Berman and Bruneau 2005). Some other advantages like less use of steel and more space for architectural purposes can be gained by using steel plate shear walls (Sabouri-Ghomi 2001).

The analogy that the vertical boundary elements of a steel plate shear wall are similar to the flanges of a plate girder, the horizontal boundary elements to stiffeners, and the infill plate to the web of a plate girder, is useful in developing a general understanding of steel plate shear wall behavior. The main difference between a steel plate shear wall and plate girder is the stiffness of the boundary elements. Where plate girder flanges are typically plates with little out-of-plane flexural stiffness, the vertical boundary members of a steel plate shear wall are typically wide flange shapes that have a substantial flexural stiffness, which impacts the orientation of the angle of development of the tension field action, and makes possible the use of very slender webs (Berman and Bruneau 2004). By increasing

the number of stories, the flexural action of the frame increases and the roles of beams and columns become increasingly important.

In design of lateral load resisting systems in general, parameters like over-strength, ductility and energy absorption and dissipation capacity are important. Various analytical and experimental studies on steel plate shear walls, subjected to cyclic inelastic quasi-static and dynamic loading, have demonstrated their ability to behave in a ductile manner and dissipate significant amounts of energy compared to frames. Figure 2.5 shows the typical hysteretic loops for a moment frame and a steel plate shear wall (Elgaaly et al. 1993). The initial stiffness of a steel plate shear wall is significantly higher than that of a typical moment frame.

As the infill plate is considered to be the sacrificial element during an earthquake, the surrounding beams and columns are designed to remain essentially elastic, while the infill plate is fully yielded. Plastic hinge formation at the ends of beams and at the base of the columns is expected, as it is needed to develop the plastic collapse mechanism of the system and fully utilize the infill plate. Plastic hinge formation in the middle of surrounding members should be prevented as it prohibits the infill plate from yielding completely. Excessive flexural deformation of boundary members will also lead to non-uniform yielding of the infill plate.

2.4.1 Analytical studies on the column flexibility parameter

Wagner (1931) did an analytical study on flat sheet metal girders with very thin metal webs and developed an equation to calculate the required moment of inertia of flanges to develop a fairly uniform tension field.

In Wagner's study, the following assumptions were made to simplify the derivation of an analytical equation:

- The compressive stresses in transverse web stiffeners are equal;

- The transverse web stiffeners are flexibly attached to the flanges without lateral bending stiffness, i.e., pin connection;
- The dimensions of both flanges are such that the normal strains are constant in flanges (i.e. negligible strain gradient in flanges);
- The transverse stiffener spacing is not much larger than the height of the plate girder
- The angle of inclination of the tension field is constant (α);
- Each tension diagonal (strip) that starts from a junction point of the flange and stiffener, ends at another junction point of flange and stiffener.

The derived differential equation is as follows (in order to make the equations easier to follow, the notations have been changed to match those used in the Canadian steel design standard, CSA S16-09 (CSA 2009), for steel plate shear walls):

$$\frac{d^4(\eta_L - \eta_R)}{dZ^4} = \left(\frac{1}{I_L} + \frac{1}{I_R}\right)w \sin^2 \alpha \varepsilon_{\max} - \left(\frac{1}{I_L} + \frac{1}{I_R}\right)\frac{w \sin^4 \alpha}{L}(\eta_L - \eta_R) \quad (2.25)$$

where η_L and η_R are, respectively, the flexural deflections of the left and right columns within the story height (i.e., measured from a straight-line axis connecting the joints above and below) due to the tension field; Z is the vertical axis; I_L and I_R are the moments of inertia of the left and right columns; w is the infill plate thickness; L is the width of the wall between column centerlines; α is the angle of inclination of tension field diagonals (strips) from vertical and ε_{\max} is the maximum strain in the tension diagonals in the non-uniform tension field due to the inward column deflections.

By assuming the following conditions for both columns:

$$\eta=0 \text{ at } Z=0 \text{ and } Z=h \quad (2.26)$$

$$\frac{d\eta}{dZ} = 0 \text{ at } Z=0 \text{ and } Z=h \quad (2.27)$$

the maximum value for the solution of the differential Equation (2.25) was derived as:

$$(\eta_L - \eta_R)_{\max} = \frac{\varepsilon_{\max} L}{\sin^2(\alpha)} \left(1 - \frac{\sin(\frac{\omega_h}{2}) \cosh(\frac{\omega_h}{2}) + \cos(\frac{\omega_h}{2}) \sinh(\frac{\omega_h}{2})}{\sin(\frac{\omega_h}{2}) \cos(\frac{\omega_h}{2}) + \sinh(\frac{\omega_h}{2}) \cosh(\frac{\omega_h}{2})} \right) \quad (2.28)$$

where

$$\omega_h = h \sin(\alpha) \sqrt{\left(\frac{1}{I_L} + \frac{1}{I_R} \right) \frac{w}{4L}} \quad (2.29)$$

If the columns had infinite flexural stiffness, the infill plate would be subjected to a uniform tension field maximum principal stress ($\sigma_{t \text{ mean}}$), which could be calculated as:

$$\sigma_{t \text{ mean}} = \frac{2V}{Lw(\sin 2\alpha)} \quad (2.30)$$

where V is the shear force in the story.

Because of the inward flexural deformation of the columns, the tension field is not uniform and in some parts, stresses (i.e., maximum principal stresses) decrease due to the strain release, while in other parts stresses have to increase to fulfill equilibrium. In other words, the average stress should still be equal to the stress in the uniform tension field, i.e:

$$\frac{1}{h} \int_0^h \sigma_t \, dZ = \frac{2V}{Lw(\sin 2\alpha)} \quad (2.31)$$

The increase in tension field stress can be calculated as:

$$\frac{\sigma_{t \text{ mean}}}{\sigma_{t \text{ max}}} = \frac{2}{\omega_h} \left(\frac{\cosh(\omega_h) - \cos(\omega_h)}{\sinh(\omega_h) + \sin(\omega_h)} \right) \quad (2.32)$$

Wagner (1931) proposed the following approximate equations to calculate the maximum stress in tension field:

$$0 \leq \omega_h \leq 2 \Rightarrow \frac{\sigma_{t \text{ mean}}}{\sigma_{t \text{ max}}} = 1 \quad (2.33)$$

$$2 \leq \omega_h \leq \infty \Rightarrow \frac{\sigma_{t \text{ mean}}}{\sigma_{t \text{ max}}} = \frac{2}{\omega_h} \quad (2.34)$$

Figure 2.6 shows both the exact and approximate curves to find the maximum stress in a non-uniform tension field.

Kuhn et al. (1952) expressed the maximum stress in a non-uniform tension field, $\sigma_{t \text{ max}}$, by the following equation and by introducing parameter C_2 , as defined below:

$$\sigma_{t \text{ max}} = (1 + C_2) \sigma_{t \text{ mean}} = (1 + C_2) \frac{2V}{Lw(\sin 2\alpha)} \quad (2.35)$$

The parameter C_2 is a function of ω_h and is plotted versus ω_h in Figure 2.7.

Kuhn et al. (1952) made some more assumptions on the equation of ω_h to further simplify it. One of the assumptions was that the angle of inclination, α , is assumed slightly less than 45 degrees and thus $\sin \alpha = 0.7$. Also, the sum of the reciprocals could be replaced by four times the reciprocal of the sum. The simplified equation for calculation of the parameter ω_h was proposed as follows:

$$\omega_h = 0.7h \sqrt[4]{\frac{w}{L(I_L + I_R)}} \quad (2.36)$$

The Canadian steel design standard, CSA S16-09 (CSA 2009), adopted Equation (2.36) and further simplified it by assuming that both columns of the steel plate shear wall have

almost the same moment of inertia. The equation to calculate parameter ω_h , which is also known as the column flexibility parameter in the standard, is as shown here:

$$\omega_h = 0.7h^4 \sqrt{\frac{w}{2LI_c}} \quad (2.37)$$

To put an upper limit on ω_h , it is assumed that the columns should be rigid enough so that the maximum stress in tension field would not be 20% more than the average stress across panel height. In other words, parameter C_2 should not exceed 0.2. By revisiting Figure 2.7, parameter ω_h should be less than 2.5 in order to keep C_2 less than 0.2 (Montgomery and Medhekar 2001):

$$\omega_h = 0.7h^4 \sqrt{\frac{w}{2LI_c}} \leq 2.5 \quad (2.38)$$

This requirement can be accomplished by columns with moments of inertia greater than:

$$I_c \geq \frac{1}{2} \left(\frac{0.7}{2.5} \right)^4 \frac{wh^4}{L} = 0.00307 \left(\frac{wh^4}{L} \right) \quad (2.39)$$

2.4.2 Experimental studies on steel plate shear walls

Most of the experimental studies on steel plate shear walls include testing of the specimens under cyclic loading. The control parameters and test programs are commonly selected according to the Guideline ATC 24 (ATC 1992) published by Applied Technology Council.

The most important control parameters in ATC 24 (ATC 1992) are “deformation control parameter”, δ , “force control parameter”, Q , and the corresponding yield values, δ_y and Q_y . The deformation control parameter is the most relevant deformation quantity to the loading history in the test, normally the story drift. The force control parameter is the most relevant force to the selected deformation control parameter, such as story shear. The

yield deformation or force should be associated with significant yielding in critical regions of the specimen, which is reflected by a clear nonlinearity in the force–deformation curve. ATC 24 (ATC 1992) proposes the following method to define $\bar{\delta}_y$ and elastic stiffness, K_e , also shown in Figure 2.8. First the yield force, Q_y , should be defined using either a monotonic test or analytically. Then, the deformation at $0.75Q_y$, $\bar{\delta}^*$, is defined and $\bar{\delta}_y$ and K_e can be found as follows:

$$\bar{\delta}_y = 1.33\bar{\delta}^* \quad (2.40)$$

$$K_e = \frac{Q_y}{\bar{\delta}_y} \quad (2.41)$$

Based on the instructions of ATC 24 (ATC 1992), at least six elastic cycles should be undergone before reaching $\bar{\delta}_y$. The elastic cycles should be performed with force control. It is recommended that three cycles be carried out with a force amplitude of $0.75Q_y$. At least three cycles should be performed with a maximum deformation of $\bar{\delta}_y$. It is also recommended that three cycles be performed at maximum deformations of $2\bar{\delta}_y$ and $3\bar{\delta}_y$. From a maximum deformation of $4\bar{\delta}_y$, the number of cycles should be at least two for each deformation until failure of the specimen.

Driver et al. (1997) tested a half-scale four-story steel plate shear wall to evaluate overall in-plane behavior of the specimen under cyclic loading. The specimen consisted of a rigid frame with the infill plate welded to the surrounding frame members. The test specimen is shown in Figure 2.9. A constant gravity load was applied on top of each column during the test. Equal lateral loads were applied to the floor levels of the specimen. The control parameters were the deformation and shear force in the first story. A total of 30 cycles were performed, out of which 20 cycles were in the inelastic range. The initial stiffness of the specimen was relatively high and the specimen exhibited good ductility and energy absorption capacity. The deformation of the bottom panel in the last cycle was nine times

the yield deformation. In the post-peak stage, the strength of the specimen decreased gradually. Driver et al. (1997) did a study relating the observed behavior to the force modification factor, R , in the National Building Code of Canada (NBCC 1995). In developing this factor, they discussed how ductility, energy absorption and dissipation capacity, redundancy and previous performance in major and moderate earthquakes should be considered. The following equation was used by Driver et al. (1997) to calculate the force modification factor:

$$R = \frac{\bar{\delta}_{\max}}{\bar{\delta}_y} \quad (2.42)$$

They considered different story deformations as $\bar{\delta}_{\max}$ to calculate R . Figure 2.10 shows the envelope of the hysteretic curves of the first story. By assuming that the response beyond the point where the descending curve intersects the approximate bilinear curve, point A, cannot be utilized, R was calculated equal to 6. It was observed that the amount of dissipated energy in the first story was increasing up to story deformation of $8\bar{\delta}_y$. The corresponding R factor, if some strength degradation is acceptable, point B, was calculated equal to 8.

Astaneh-Asl and Zhao (2002) tested two half-scale steel plate shear wall systems to study the behavior of large steel tubes filled with high strength concrete as the columns in the system. The role of these columns was to carry a large portion of gravity loads and some part of the story shears. Figure 2.11 shows the test specimens. One of the specimens had two stories and the other one had three stories. The infill plates had bolted splice plates at mid-height of stories. The infill plate thickness was 9.5 mm and all the fasteners were 5/8 inch diameter A490 bolts designed for slip-critical behavior. The test specimen showed high ductility and good energy absorption. Up to a story drift of about 0.6% of the story height, both specimens behaved almost elastically. The

performance of the bolted splices was good, although they were slipping in the last cycles of the tests.

Behbahanifard et al. (2003) conducted a cyclic test on a half-scale three-story steel plate shear wall, which was the top three stories of the specimen previously tested by Driver et al. (1997). Constant gravity loads were applied on top of the columns and equal lateral loads were applied to the floor levels of the specimen. A total of 24 cycles were performed, out of which 14 cycles were in the inelastic stage. The specimen exhibited high elastic stiffness, excellent ductility and energy absorption capacity, stable hysteretic loops and redundancy. The stiffness provided by the infill plate in the first story was around 5.5 times that of the frame. The specimen reached its maximum base shear at a ductility ratio of 7.

Qu et al. (2008) tested a full-scale two-story steel plate shear wall with RBS connections and composite floors. The details of the test specimen and RBS connections are shown in Figure 2.12. This test program had two phases. In the first phase, the specimen was subjected to three pseudo-dynamic loads, as described in Qu et al. (2008). After the first phase, the buckled infill plates were removed by flame cutting and replaced by new ones which were welded to the fish plates. The restrainers were also removed during the second phase of the test. In the second phase, first the specimen was subjected to pseudo-dynamic loads to investigate the behavior of the repaired specimen to another earthquake and finally, the specimen was subjected to cyclic loading to investigate the ultimate behavior of the intermediate beam and cyclic behavior and ultimate capacity of the steel plate shear wall. The imposed deformation to the specimen corresponded to the first mode. No fracture was observed in the RBS cut region; however, the bottom flange of the intermediate beam fractured at the face of the columns. Although a substantial length of the weld connecting the infill plate of the first story to the intermediate beam and column un-zipped adjacent to the fractured bottom flange of the intermediate beam, the specimen was still able to exhibit stable force–displacement behavior, which

demonstrated the redundancy of the steel plate shear wall system. The results showed that the repaired specimen behaved quite similarly to the original one. The hysteretic curves from the cyclic load were pinched due to the inelastic deformations that the specimen experienced in the pseudo-dynamic test. However, the load–displacement behavior of the specimen was stable and a large amount of energy was dissipated.

Following the observations in the above-mentioned experiment, Qu and Bruneau (2010) studied the behavior of the intermediate beam in the steel plate shear wall system. Four sources of axial force as well as three sources of shear force at the end of the intermediate beams were discussed. The sources of the axial force in the beams were defined as boundary moment frame sway, horizontal component of tension fields on columns, vertical component of tension fields and unequal horizontal components of tension fields on top and bottom of the beam. The sources of shear force at the end of the intermediate beams were introduced as the moment frame sway action, horizontal components and unequal vertical component of tension fields on the top and bottom of the intermediate beam. An equation was proposed to define the minimum plastic modulus of the beam to avoid formation of in-span plastic hinges.

Qu and Bruneau (2010) did a finite element study on the RBS connection and observed that the plastic hinge did not form at the center of the RBS cut, which has the minimum plastic modulus. The plastic hinge formed closer to the column face, as shown in Figure 2.13a. The following equations were proposed to identify the plastic modulus of the section where plastic hinge forms, Z_{RBS} , and its offset from the center of the RBS cut toward the column face, Δx .

$$Z_{RBS} = \frac{(1+\eta)}{2} Z \quad (2.43)$$

$$\Delta x = \sqrt{(2R\Delta y - \Delta y^2)} \quad (2.44)$$

$$\Delta y = \frac{(1-\eta)Z}{4t_f(d-t_f)} \quad (2.45)$$

$$R = \frac{4c^2 + b^2}{8c} \quad (2.46)$$

where η is the plastic modulus reduction ratio at the center of the RBS cut, Z is the plastic modulus of the full section of the beam, R is the radius of the RBS cut, t_f and d are, respectively, the flange thickness and section depth of the beam and b and c are, respectively, the length and depth of the RBS cut, as shown in Figure 2.13b.

2.5 Test of a steel plate shear wall with PEC columns

Deng and Driver (2007) did a numerical study on their future experimental program and described some details of the test specimen such as the frame connections and the load transfer system. The specimen was designed to examine the performance of the PEC columns under a combination of axial load and bending moment due to both frame action and the development of the tension field in the infill plate. The aspect ratios of the panels were 0.75 and 0.66 in the first and second stories, respectively. Class 1 sections were used as the floor beams in the specimen to avoid any local buckling. The infill plate was selected so that the relatively low target material strength (yield stress of less than 300 MPa) was achieved. All of the steels used in the PEC columns, including the built-up section, links and side plates, had a nominal yield strength of 350 MPa. The concrete in the column had a strength on the test day of around 55 MPa.

In order to gradually transfer the moments at the end of the beams to the columns, the column side plates were welded to the flanges of beams. A lateral load transition system was developed to transfer the lateral load to the wall through the beams, as shown in Figure 2.14. The system was developed to better resemble the load transfer route from the floor diaphragms to the wall in a real building and also to avoid local failure in the

columns that may occur if the loads are transferred directly to the thin-walled columns as was done in previous tests.

A finite element model was developed to examine the test specimen and to predict the behavior of the specimen before the actual test. Figure 2.15 shows the undeformed and deformed meshed model. The results showed the failure of the columns consisted of a combination of local buckling of the steel flanges and crushing of the adjacent concrete. The plots showing the total lateral reaction force, as well as the proportion of the lateral reaction force that was carried by the columns and infill panel individually, versus the top lateral displacement, are shown in Figure 2.16.

Deng et al. (2008) conducted a large scale test on a two-story steel plate shear wall with PEC columns to study the behavior of PEC columns under loading that was particular to these walls. The overall height and width of the specimen were 4.09 m and 2.69 m, respectively, with story heights of 1.9 m. The columns were 250 mm by 250 mm in cross section and the infill plate thickness was 3 mm. The test specimen, prior to casting concrete in columns, is shown in figure 2.17. Each column sustained 600 kN of axial force to resemble the service gravity load. Lateral loads were applied to the top flanges of the floor beams equally and according the method outlined in ATC-24 (ATC 1992). The selected deformation and force control parameters were the first story deformation and the shear force in the first story (i.e., base shear). The applied base shear in the first three cycles was 316 kN, in cycles 4 to 6 the base shear was 632 kN, and during cycles 7 to 9, a base shear of 948 kN was applied to the specimen. The yielding displacement was selected to be 7 mm. A total of 30 cycles were completed with a maximum first story deflection of 63 mm in the last cycle.

The hysteretic loops of base shear versus the story deflection of panel 1 (i.e., first story) are shown in Figure 2.18. The first crack in the column concrete was detected in the first seven cycles and several cracks were detected in cycles 8 and 9, due to the frame

action. The stiffness of the specimen decreased considerably in cycle 13 of the test (cycle to reach first story deflection of 14 mm) due to the development of several horizontal and vertical cracks in the columns. The first sign of local buckling of the outer flanges of columns was detected in cycle 19. Tearing of the outer flanges of the columns started in cycle 21 (cycle to reach first story deflection of 35 mm) and the flanges of the columns tore completely in cycle 26, where the specimen experienced the first story deformation of 49 mm. The maximum base shear of 1817 kN was attained in cycle 21 at a first story deformation of 35 mm. The test was terminated due to significant propagation of the column flange tears into the webs of the columns. Severe concrete crushing was detected in the post-peak stage of this test, which indicates the presence of excessive compressive stress in the concrete at the bases of the columns. A few links failed at the bases of columns in the plastic hinge locations, which worsened the situation in that region as the confinement of concrete as well as the local buckling capacity of column flanges decreased.

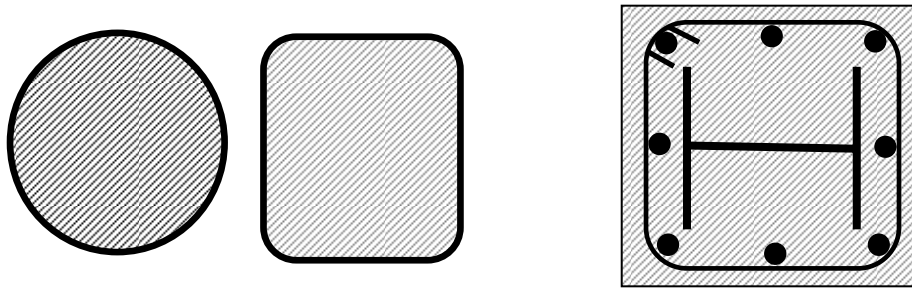


Figure 2.1: Concrete-filled tubes (left) and fully encased composite column (right)

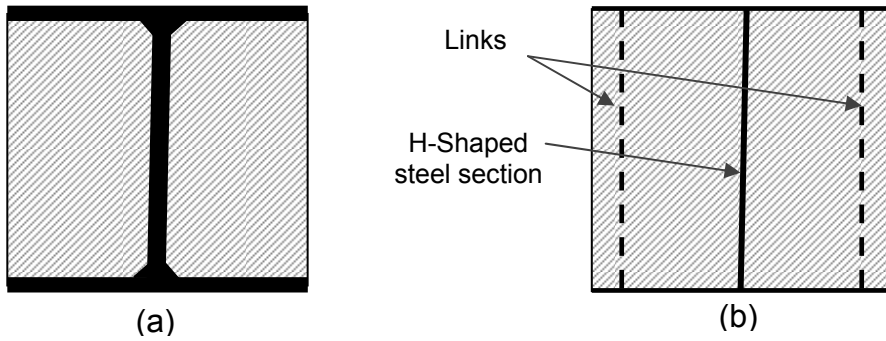


Figure 2.2: Partially encased composite columns with
 a) Standard steel section; b) Built-up steel section

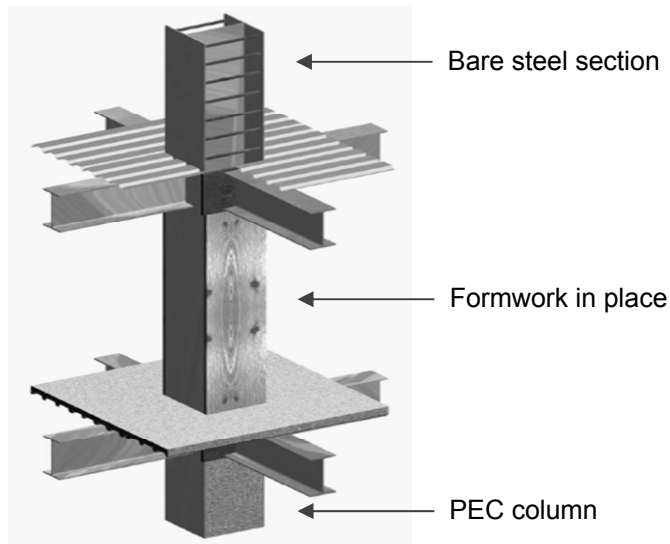


Figure 2.3: Sequence of construction of PEC column (Vincent and Tremblay 2001)

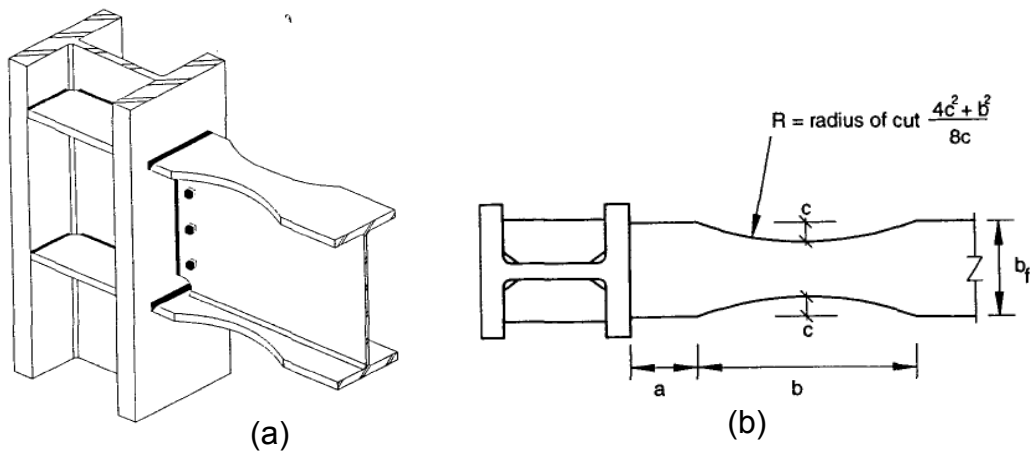


Figure 2.4: a) Typical radius RBS cut; b) Dimensions of radius RBS cut

(Moore et al. 1999)

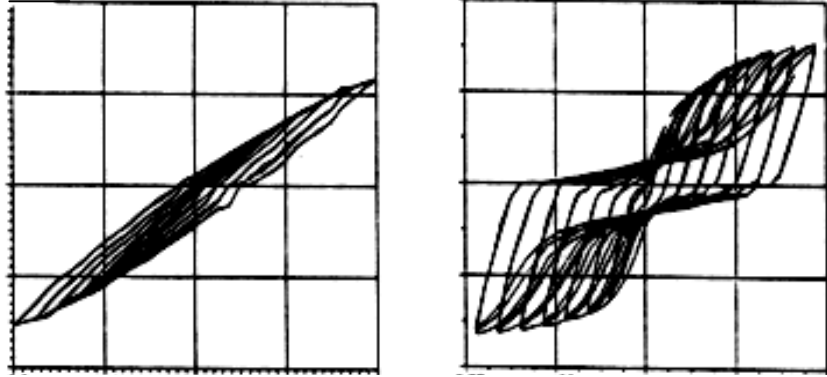


Figure 2.5: Hysteretic loops of a moment frame (left) and a steel plate shear wall (right)
(Elgaaly et al. 1993)

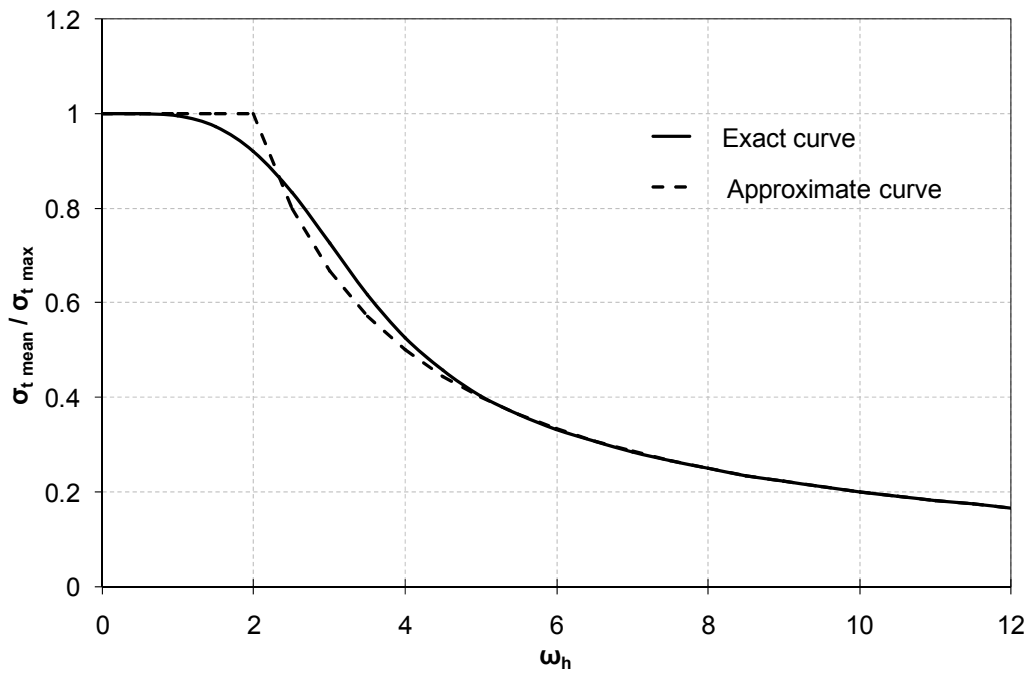


Figure 2.6: Exact and approximate curves to find the maximum stress in a non-uniform tension field (Wagner 1931)

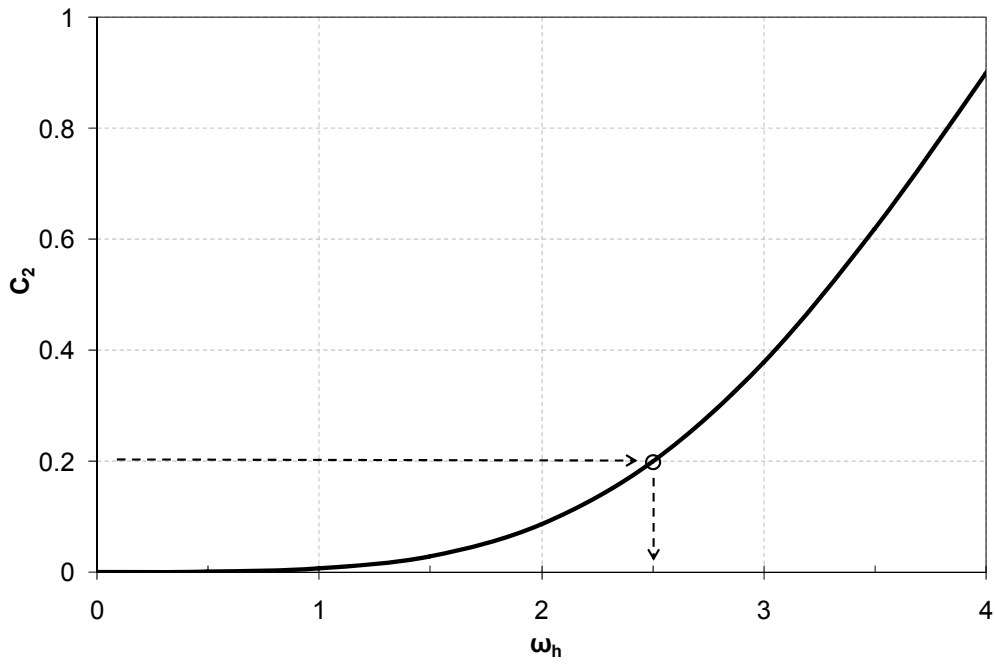


Figure 2.7: Parameter C_2 as a function of the parameter ω_h

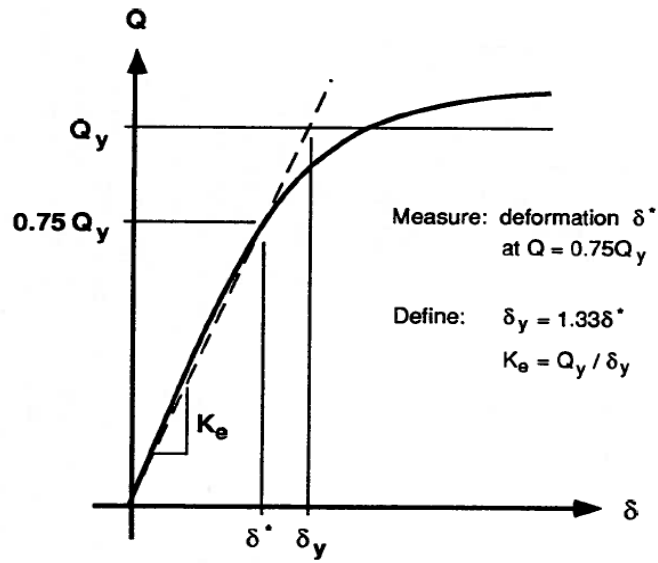


Figure 2.8: Method to define yield deformation and elastic stiffness (ATC 1992)

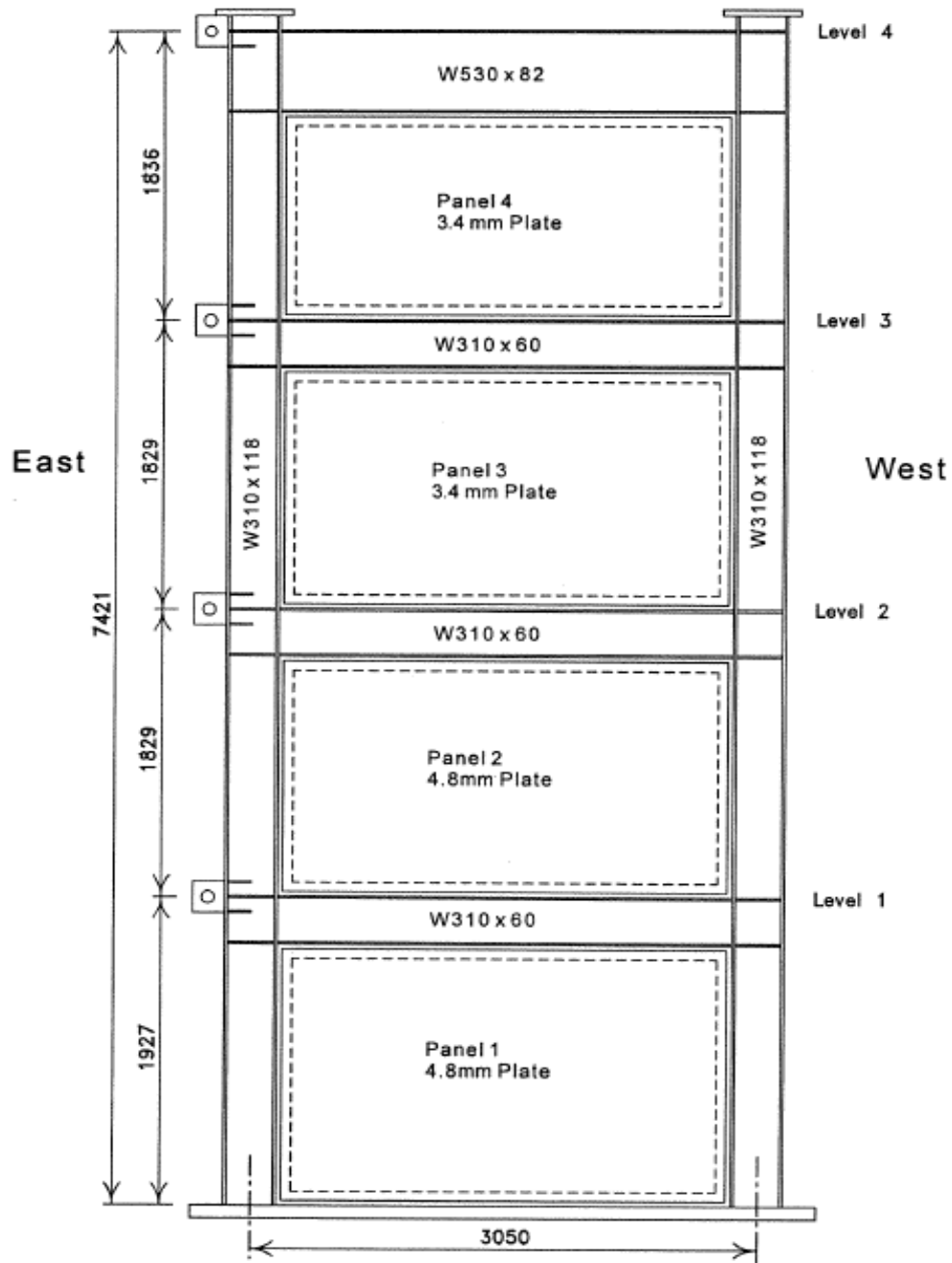


Figure 2.9: Four-story steel plate shear wall tested by Driver et al. (1997)

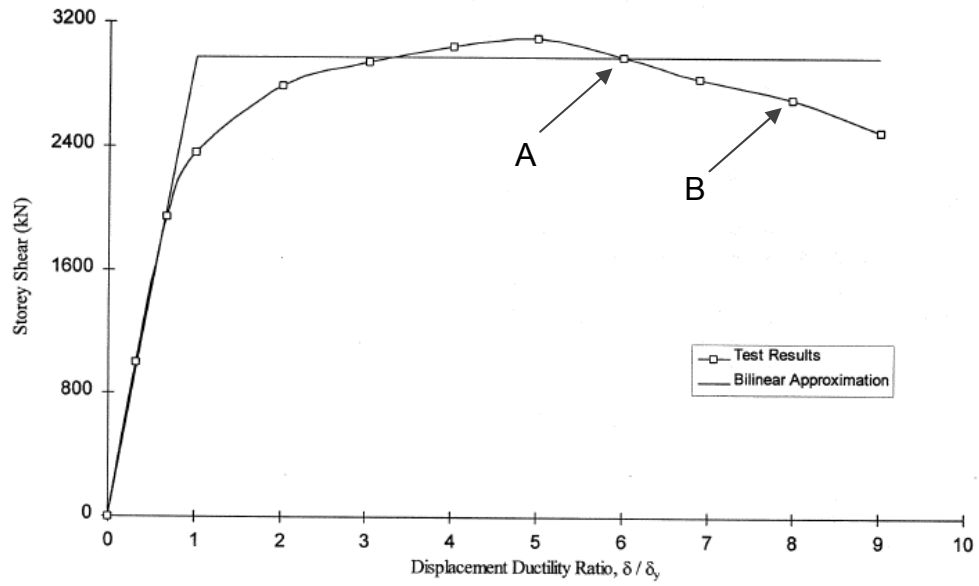


Figure 2.10: Envelope of hysteretic loops of the first story (Driver et al. 1997)

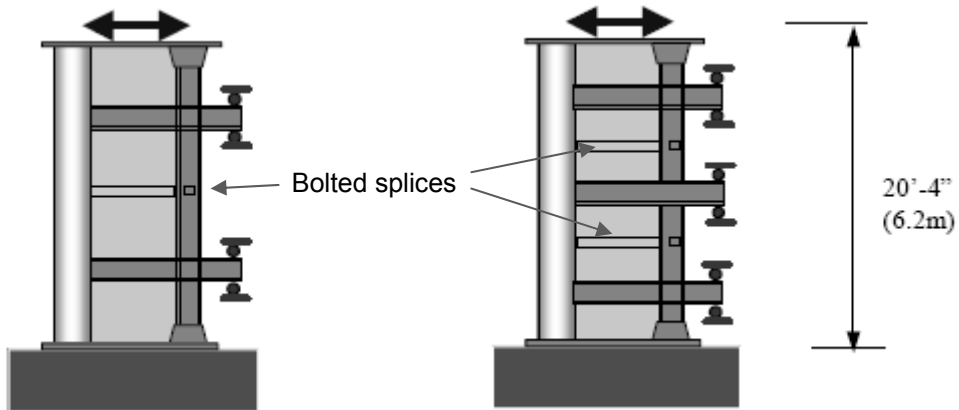


Figure 2.11: Steel plate shear walls tested by Astaneh-Asl and Zhao (2002)

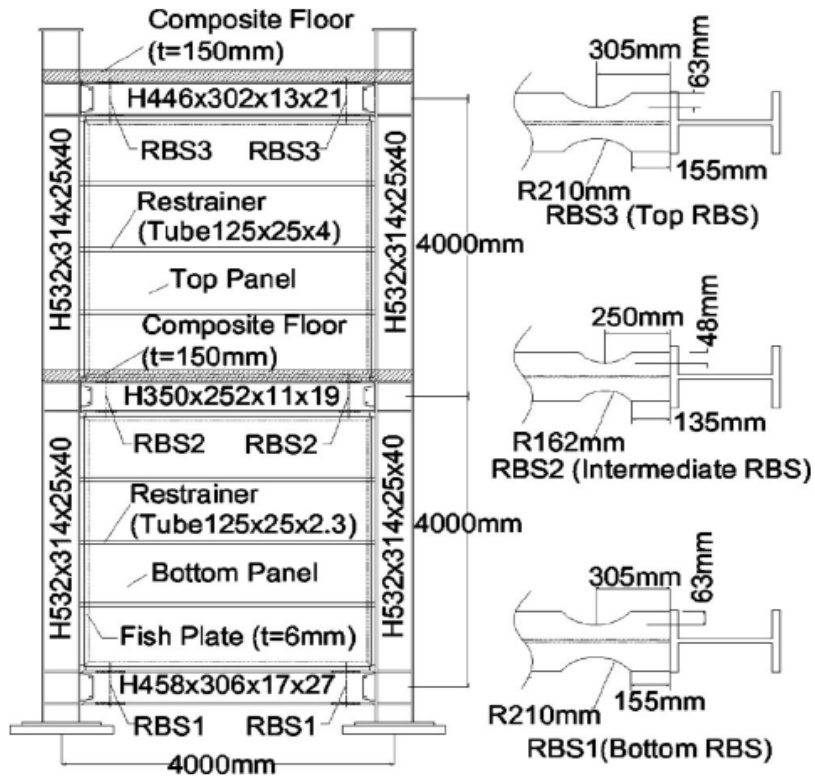


Figure 2.12: Specimen tested by Qu et al. (2008)

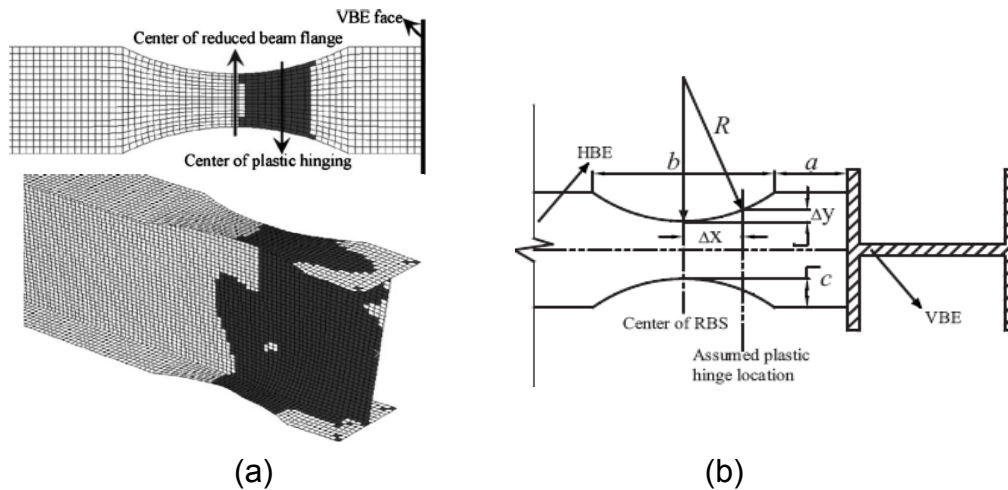


Figure 2.13: a) Offset of plastic hinge center toward column face; b) Dimensions of a typical radius RBS cut and offset of the plastic hinge (Qu and Bruneau 2010)

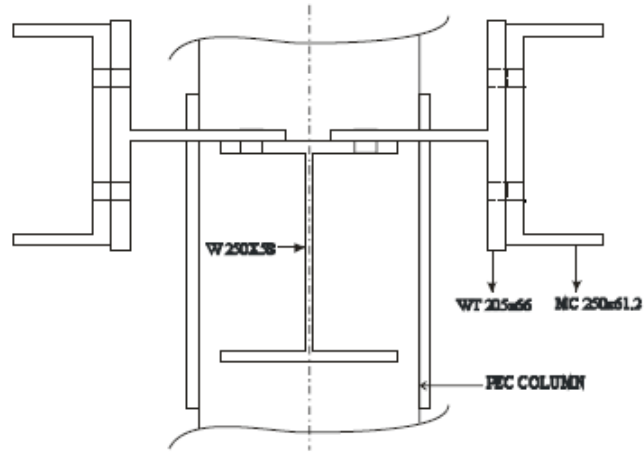


Figure 2.14: Lateral load transfer system designed by Deng and Driver (2007)

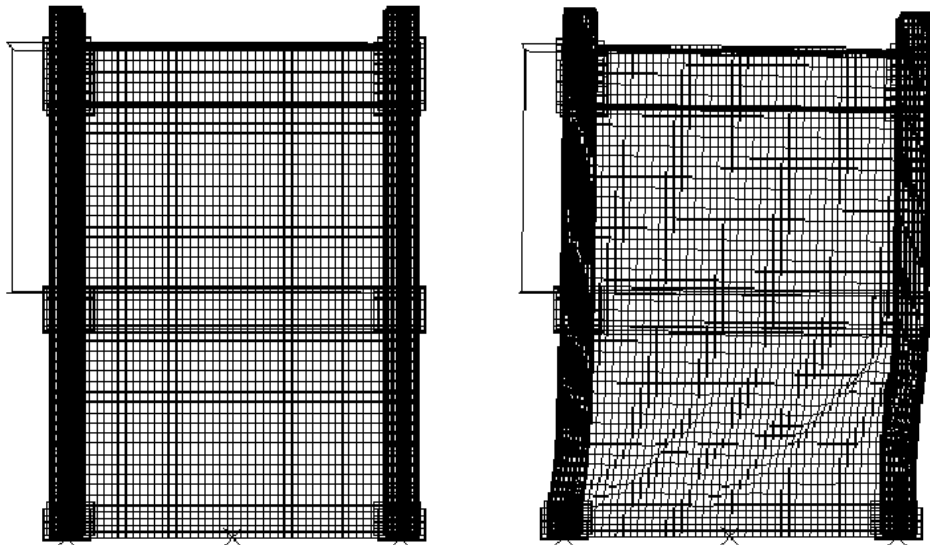


Figure 2.15: Undeformed (left) and deformed (right) meshed model in numerical study conducted by Deng and Driver (2007)

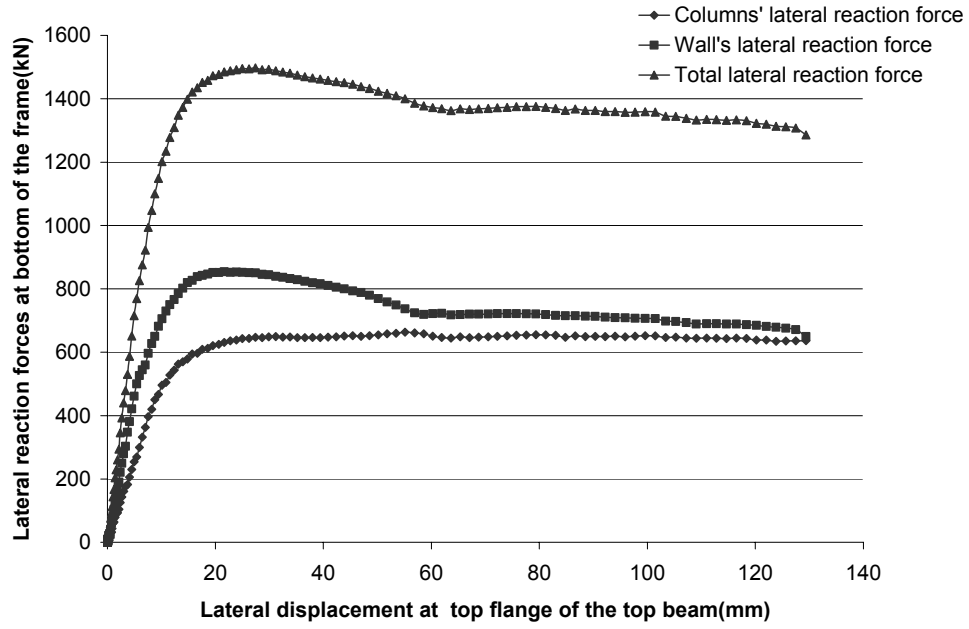


Figure 2.16: Lateral displacement versus lateral reaction (Deng and Driver 2007)



Figure 2.17: Test specimen before concrete was cast (Deng et al. 2008)

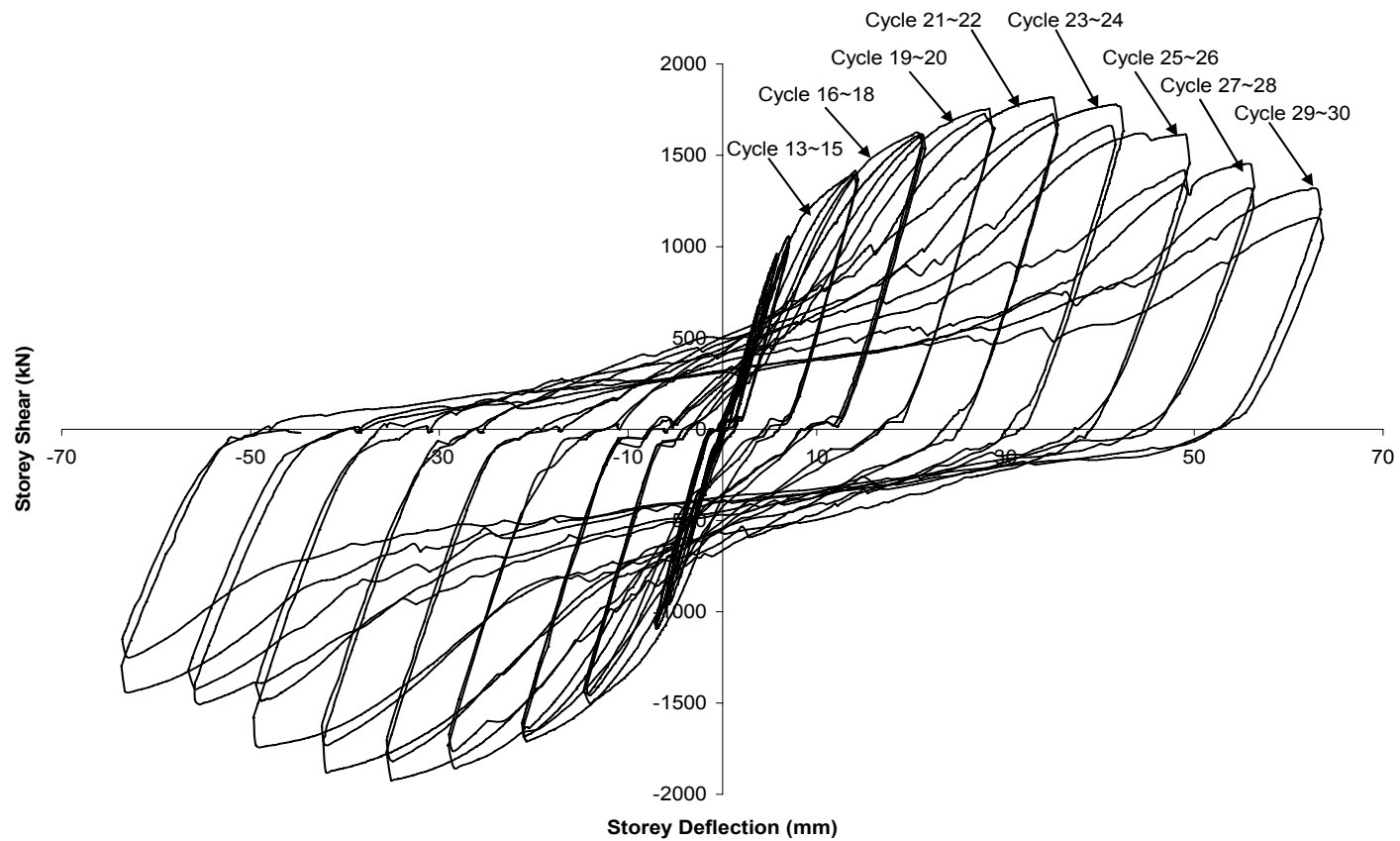


Figure 2.18: Hysteretic loops of story shear versus story deflection of first story (Deng et al. 2008)

3. FLEXURAL PARAMETERS FOR BOUNDARY FRAME MEMBERS IN STEEL PLATE SHEAR WALL SYSTEMS

3.1 Introduction

The assumptions made by Wagner (1931) in the derivation of Equation (2.29), as column flexibility parameter, reveal that it is not suitable for the columns near the top or the base of steel plate shear walls. This is because one end of each tension strip in these regions is anchored to the top beam or the foundation rather than to a column (shaded strip in Figure 3.1). The previous edition of the Canadian steel design standard CSA S16-01 (CSA 2001) addressed the need for a minimum stiffness of the top beam by requiring that its moment of inertia be high enough so that the variation of tensile stress across the panel width did not exceed 20%. This requirement would lead to an iterative solution, and in most common cases it could not be met. To resolve this issue, a new parameter is derived and its limits defined and verified.

First, a new flexibility parameter, ω_L , is developed for the top and bottom panels of steel plate shear walls, where some of the assumptions made for the typical story do not apply. The derivation of the parameter is based on the philosophy behind the parameter ω_n . The new parameter considers the interaction of the top or bottom beams with the adjacent panels.

An upper limit to the new flexibility parameter that produces column and beam stiffnesses that will achieve efficient overall performance of the wall is defined based on the results of numerical analyses, consisting of numerous finite element models. Also, a lower limit is determined to avoid negative stiffnesses for end beams.

The initial studies by Wagner (1931) and Kuhn et al. (1952) were on plate girders to determine the required flange stiffness for the development of a relatively uniform tension field in the web, with the assumption of pinned connections between the stiffeners and flanges. As these works form the basis of the steel plate shear wall flexibility parameters, all studies on both ω_h and ω_L have included the simplifying assumption that the connections between the beams and columns are pinned, thus allowing the angles at the corners of the panels to change. However, steel plate shear walls are more likely to be designed with moment-resisting member connections and the flexural deformation of the beams and columns resulting from connection rigidity causes a change in the pattern of the tension field in the panel. In this chapter, the effect of the connection rigidity on the behavior of the steel plate shear wall has been investigated by a numerical study.

3.2 End-panel flexibility parameter

The original equation for ω_h , Equation (2.29), consists of two terms, representing a measure of the released strain in the tension field. This release occurs due to the inward flexural deformations of the columns caused by the distributed load applied by the anchored tension strips themselves, as shown in Figure 3.2, where σ_t is the tensile stress in the tension field, q_c is its component perpendicular to the column, h is the column height in one story, and α is the angle of the inclination of the tension field from vertical.

The perpendicular distributed load along the column, q_c , can be calculated as follows:

$$q_c = \frac{(\sigma_t w (h \sin \alpha)) \sin \alpha}{h} = \sigma_t w \sin^2 \alpha \quad (3.1)$$

where w is the infill plate thickness.

Although the resulting flexural deflection of the anchoring column, δ_c , due to q_c , depends on the degree of rotational fixity at the top and bottom of column, it can be expressed as a proportionality, as follows:

$$\delta_c \propto q_c \frac{h^4}{I_c} \Rightarrow \delta_c \propto w \frac{h^4}{I_c} \sin^2 \alpha \quad (3.2)$$

where I_c is the moment of inertia of the column.

The shortening of a tension strip connected at its ends to the left and right anchoring columns, δ_{strip} , due to the deformations of those columns is:

$$\delta_{\text{strip}} = (\delta_{c_L} + \delta_{c_R}) \sin \alpha \quad (3.3)$$

where δ_{c_L} and δ_{c_R} are the inward deflection of the left and right columns, respectively.

The released strain in the strip because of the reduction in length is:

$$\epsilon_{\text{released}} = \frac{\delta_{\text{strip}}}{L_{\text{strip}}} \Rightarrow \epsilon_{\text{released}} \propto \left(\frac{h^4}{I_L} + \frac{h^4}{I_R} \right) \frac{w \sin^4 \alpha}{L} \quad (3.4)$$

where L_{strip} is the length of the tension strip and is equal to $L / \sin \alpha$, L is the span width and I_L and I_R are the moments of inertia of the left and right columns, respectively.

By comparing Equations (2.5) and (3.4), it can be concluded that they are related to each other as follows:

$$\omega_h = \sin \alpha \sqrt[4]{\left(\frac{h^4}{I_L} + \frac{h^4}{I_R} \right) \frac{w}{4L}} \Rightarrow \omega_h \propto \epsilon_{\text{released}} \quad (3.5)$$

In the top and bottom panels of steel plate shear walls, however, the tension field is not anchored to the columns at both ends, so the equation for ω_h is not directly applicable. Therefore, the new parameter ω_L must account for the effects of the inward flexural deformation of both the anchoring end-beam and the column, depicted in Figure 3.3. This parameter should represent the released strain in the strips and an analogous expression can be derived in the same way.

The applied perpendicular distributed load along the end beam by the anchored tension strips, q_b , can be calculated as:

$$q_b = \frac{\sigma_t w L \cos \alpha \cos \alpha}{L} = \sigma_t w \cos^2 \alpha \quad (3.6)$$

The flexural deflection of the beam, δ_b , due to the distributed load q_b is represented by the following proportionality, which is analogous to Equation (3.2) for the columns:

$$\delta_b \propto q_b \frac{L^4}{I_b} \Rightarrow \delta_b \propto w \frac{L^4}{I_b} \cos^2 \alpha \quad (3.7)$$

where I_b is the moment of inertia of the anchoring end beam.

The shortening of the strips due to a combination of the deflection of the anchoring beam and column at its ends can be calculated as follows:

$$\delta_{\text{strip}} = \delta_c \sin \alpha + \delta_b \cos \alpha \quad (3.8)$$

and the associated released strain in the strip can be calculated as:

$$\epsilon_{\text{released}} = \frac{\delta_{\text{strip}}}{L_{\text{strip}}} \Rightarrow \epsilon_{\text{released}} \propto \left(\frac{h^4}{I_c} + \frac{L^4}{I_b} \cot^3 \alpha \right) \frac{w \sin^4 \alpha}{L} \quad (3.9)$$

Similar to the treatment of ω_h , see Equation (3.5), the parameter ω_L can be formulated as:

$$\omega_L = \sin \alpha \sqrt[4]{\left(\frac{h^4}{I_c} + \frac{L^4}{I_b} \cot^3 \alpha \right) \frac{w}{4L}} \quad (3.10)$$

The value of α in conventional steel plate shear walls is generally close to, but slightly less than, 45° . Therefore, for simplicity, Equation (3.10) can be written as:

$$\omega_L = 0.7 \sqrt[4]{\left(\frac{h^4}{I_c} + \frac{L^4}{I_b}\right) \frac{w}{4L}} \quad (3.11)$$

Equation (3.11) is considered to represent the flexibility of the end panel boundary members sufficiently well that with appropriate limits set for design, it can ensure that a reasonably uniform tension field will form in the panel.

3.3 Limit analysis for the end-panel flexibility parameter

Numerous steel plate shear walls with various infill plate thicknesses and panel aspect ratios were modeled and analyzed using ABAQUS/CAE (HKS 2004) to determine a suitable upper limit for the parameter ω_L . A shear load that gives a mean tension field stress equal to the anticipated yield stress of the plate material in the panels was applied to all the panels. The analysis was done assuming linear material behavior and nonlinear geometric behavior.

The infill plates were meshed using four-node finite strain reduced integration (S4R) shell elements and all beams and columns were made up of two-node (B31) beam elements. An initial imperfection, equal to the thickness of the infill plate, was applied in the form of a small out-of-plane displacement at the center of each panel. The bending moment at both ends of all beams was released to ensure that the entire applied shear was carried by the infill plate.

In Figures 3.4, 3.5, and 3.6, the stress distributions (maximum principal stresses at the mid-surface of plate) across the panel diagonal are shown for several combinations of ω_h and ω_L with panel aspect ratios (L/h) of 0.5, 1.0 and 1.5, respectively. In all cases, the story height, h , is 4000 mm. For panels with $L=2000$ mm ($L/h = 0.5$), the tension field in first 1491 mm along the diagonal from the left is anchored to the end beam. For panels with $L=4000$ mm ($L/h = 1.0$) and $L=6000$ mm ($L/h = 1.5$), the tension fields in the first 2828 mm and 4327 mm from left, respectively, are anchored to end beam. Due to the

secondary bending moments introduced by the shear buckling of the infill plate, there is an unavoidable non-uniformity in the tension field stress (maximum principal stress) across the panel, and even an infinitely stiff beam would not result in a perfectly uniform stress pattern.

To define an appropriate upper limit for ω_L , the controlling parameter was taken as the percentage decrease in the average maximum principal (tensile) stress in the portion of the tension field anchored to the beam, as compared to the average tensile stress across the full tension field, and this parameter was named C_3 .

In Figure 3.7, parameter C_3 is plotted versus ω_L . Trend lines are also shown in the figure, grouped according to the value of ω_h in the end panels. With the same value of ω_L , panels with higher values of ω_h will have a more uniform tension field. This is because the parameters ω_h and ω_L are not independent, so for the same value of ω_L , a higher beam stiffness will result for a higher value of ω_h (i.e., lower column stiffness), and it is the beam stiffness that tends to be more influential in the end panels. It is apparent from Figure 3.7 that lowering ω_L below 1.0 produces negligible improvement in the stress uniformity across the tension field.

In Figure 3.8, the effect of the panel aspect ratio ($L/h = 0.5, 1.0, 1.33$ and 1.5) on the relationship between the parameter ω_L and the non-uniformity of the tension field stress is shown. With the same value of ω_L , as the panel aspect ratio (L/h) increases, the average stress in the tension field diagonals that are anchored to the end beam at one end increases (reducing C_3). The reason behind this is that most of these strips are anchored on the other end close to the beam-to-column connection or to the intermediate beam where the flexural deformation of the frame members is very small.

An upper limit of 2.5 for ω_L results in about a 10 to 40 percent decrease in tension field stress compared to the average panel stress for the cases analysed. Considering that the cross sections of columns in the top story are usually relatively small, and the column

flexibility parameter would be close to 2.5 in most cases, the average value for C_3 would be approximately -20 to -25 percent, which is considered acceptable at the top panel of the wall since it is not particularly influential to the overall system behavior. Thus, $\omega_L = 2.5$ is proposed to define the minimum stiffness of the boundary frame members in the top panel. Examples of hot-rolled wide-flange top-beam sections for which both parameters ω_h and ω_L are equal to 2.5 are tabulated in Table 3.1 for steel plate shear walls with different aspect ratios and an infill plate thickness of 4 mm. Table 3.1 indicates that reasonable sizes of top-beams result from this method.

In bottom panel, a more efficient tension field is needed as it carries the base shear and thus plays an important role in the overall behavior of the steel plate shear wall system. With a ω_L value less than 2.0, the decrease in tension field stress anchored to the end beam will be less than 20 percent in almost all cases and thus, an upper limit of 2.0 for ω_L in the bottom panel is appropriate.

It is important to check both ω_h and ω_L in the end panels and meet the requirements for both of them. By limiting ω_h to 2.5, as is the case in the Canadian steel design standard, CSA S16-09 (CSA 2009), the minimum required moment of inertia of the columns can be obtained by using Equation (2-39). By substituting the moment of inertia of the columns into Equation (3.11) and limiting ω_L to 2.5 or 2.0, the minimum required moment of inertia of the end beams will be obtained for the top and bottom panels, respectively. At the bottom panel of the wall, anchor beams would be much heavier due to the lower limit on ω_L and the possible presence of a thicker infill plate. As an economical solution at the bottom panel, the infill plate can alternatively be anchored directly to the foundation.

As mentioned before, the minimum permissible column stiffness is obtained by limiting ω_h . Since ω_L is a function of both the beam and the column stiffnesses, if the target value of ω_L is set too low, the beam would have to deflect in the opposite direction of the tension field force (i.e., it would require a negative stiffness) in order to obtain the desired

stress uniformity. To avoid obtaining a negative beam stiffness from Equation (3.11), a lower limit must also be set for ω_L . From Equation (3.11):

$$\omega_L^4 = (0.7)^4 \left(\frac{h^4}{I_c} \right) \frac{w}{4L} + (0.7)^4 \left(\frac{L^4}{I_b} \right) \frac{w}{4L} \quad (3.12)$$

Similarly, from Equation (2.37):

$$\omega_h^4 = (0.7)^4 \left(\frac{h^4}{I_c} \right) \frac{w}{2L} \Rightarrow \omega_L^4 - \frac{\omega_h^4}{2} = (0.7)^4 \left(\frac{L^4}{I_b} \right) \frac{w}{4L} \quad (3.13)$$

$$I_b \geq 0 \Rightarrow \omega_L^4 - \frac{\omega_h^4}{2} \geq 0 \quad (3.14)$$

$$\omega_L \geq 0.84 \omega_h \quad (3.15)$$

Therefore, the value of ω_L selected must be at least equal to 84% of the values of ω_h .

3.4 Effect of beam-to-column connection rigidity on flexural parameters

In order to determine the effect of the beam-to-column connection rigidity on the uniformity of stress in the tension field, a numerical investigation was conducted on steel plate shear walls with various panel aspect ratios and infill plate thicknesses. The research was conducted using the commercial general-purpose finite element analysis program, ABAQUS (2004). In order to reduce the time required for analysis, the infill plate was replaced with tension strips with an angle of inclination equal to 45 degrees, which approximates the angle of inclination of the tension field in the plate. The infill plate was divided into strips with equal width so that at least five strips were anchored to each surrounding member. The thickness of the strips was equal to that of the infill plate.

3.4.1 Effect of connection rigidity on column flexibility parameter (ω_h)

For this study, steel plate shear walls with a plate thickness equal to 3 mm and aspect ratios (L / h) of 0.5, 1.0 and 1.5 were chosen. All the walls had five stories, with a story height equal to 4000 mm. In all cases, the beam-to-column connection type was initially pinned, to verify the model with previous research, and then it was changed to fixed. The non-uniformity of the tension field (parameter C_2 , as defined in Chapter 2) was calculated in the middle story.

For the panel with width (L) and story height (h) equal to 4000 mm and infill plate thickness of 3 mm, the parameter C_2 is plotted with a solid line versus ω_h in Figure 3.9. For comparison and validating the finite element model, the results of the analytical study by Kuhn et al. (1952) are also plotted in Figure 3.9 using a dashed line. As can be seen in this figure, there is reasonable agreement between the results of the finite element study and those of the closed-form solution by Kuhn et al. (1952).

In Figures 3.10 to 3.12, the parameter C_2 (representing the non-uniformity of the tension field) in the middle story is plotted versus ω_h (i.e., columns with different moments of inertia) for different values of L / h . In each figure, the results for both rigid and pinned frame connections are shown.

Figures 3.10 to 3.12 show that the rigidity of the beam-to-column connections introduces greater non-uniformity in the tension field in the middle stories, regardless of the panel aspect ratio, and thus it increases the parameter C_2 . For an ideally uniform tension field, the deformed shape of the surrounding frame should be a parallelogram, and the surrounding frame members should remain straight. However, the rigidity of the beam-to-column connections causes the beams and columns to deform into an S-shape, resulting in a non-uniform tension field stress in the infill plate, which results in a higher value of C_2 . Figure 3.13 shows the deformed shape of panels in the middle stories with pinned and fixed connections.

In Table 3.2, the values of the parameter C_2 are tabulated for different aspect ratios and connection types. It can be seen that for the aspect ratio of 0.5, the non-uniformity of the tension field increases dramatically due to the rigidity of the connection. The upper limit of $\omega_h = 2.5$, specified in the current editions of both the Canadian and American design standards, was intended to keep the parameter C_2 less than 0.2 in panels of any aspect ratio. The parameter C_2 exceeds the targeted limit of 0.2 in panels with an aspect ratio equal to 1.0 as a result of invoking rigid connections, and in this case, the connection rigidity increases this parameter from 0.23 to 0.34 at the upper limit of ω_h . For this case, more stringent requirements may be justified as parameter C_2 exceeds the target value. For other aspect ratios, even with rigid beam-to-column connections, the parameter C_2 remains less than the targeted value of 0.2 when the parameter ω_h is less than 2.5.

3.4.2 Effect of connection rigidity on end-panel flexibility parameter (ω_L)

To study the effect of the beam-to-column connection rigidity on the uniformity of the tension field in end panels, five-story steel plate shear walls with aspect ratios (L / h) of 0.5, 1.0 and 1.5 and infill plate thicknesses of 3 and 6 mm are chosen. In Figures 3.14 to 3.17, parameter C_3 , which has been defined previously, is plotted against ω_L . For an aspect ratio of 1.0, two different infill plate thicknesses are studied to investigate the effect of the infill plate thickness. As many boundary member stiffness combinations were considered, there is significant scatter in the data when plotted in this way, so for convenience approximate linear trend lines are shown in these figures for generalized comparisons.

For smaller aspect ratios (L / h), the steel plate shear wall tends to deform in flexure rather than shear. When the wall deforms flexurally, there is little rotational demand at the beam-to-column connections.

As the aspect ratio increases, the deformation of the wall gradually becomes shear-dominant, which requires a considerable change in the angle between the beam and

column at the connections. As seen in Figure 3.14, when the aspect ratio of the panel is 0.5, rigidity of the beam-to-column connection causes a more uniform stress in the tension field of the end panel. Conversely, Figures 3.15 to 3.17 indicate that for larger panel aspect ratios, this is not necessarily so. The increasing need for frame connection rotation in panels with higher aspect ratios causes the rigid connections to improve the uniformity of the tension field in walls with smaller aspect ratios and for permissible values of ω_L (i.e, less than 2.0 for bottom panels and less than 2.5 for top panels) generally decrease the uniformity in walls with larger aspect ratios. As shown in Figures 3.15 to 3.17, in panels with larger aspect ratios only for higher values of ω_L does the connection rigidity help in reaching a more uniform tension field. Moreover, the presence of fixed connections reduces the dependence of the parameter C_3 on ω_L considerably for all panel aspect ratios.

In Table 3.3, the values of the parameter C_3 are tabulated for different panel aspect ratios and connection types for proposed maximum ω_L values of 2.0 and 2.5 (in the bottom and top panels, respectively). From this table, in the bottom panels the parameter C_3 for the aspect ratio of 1.5, where rigid connections appear to be most detrimental, is equal to -15 % and -23 % for panels with pinned and rigid frame connection, respectively. Considering that the target maximum value of C_3 for determining the proposed upper limit of ω_L was -20 %, this change can be considered acceptable. For the aspect ratio of 1.0, the values of C_3 are almost equal at the proposed limit for ω_L of 2.0 for the pinned and rigid connection cases.

In the top panel, parameter C_3 was between -10 to -40 percent for steel plate shear walls with pinned connections, depending on the column flexibility parameter values. In general, this criterion is also met for the steel plate shear walls with rigid frame connections. For the case of walls with pinned frame connections and small aspect ratios, more stringent requirements may be justified at the bottom panels.

3.5 Summary

In order to help engineers in the design of end (i.e., top and bottom) beams in steel plate shear wall systems, a new flexibility parameter for end panels (ω_L) was developed based on the philosophy behind the column flexibility parameter (ω_h). The uniformity of the tension field in end panels of the steel plate shear wall was the controlling parameter and was quantified as C_3 .

Based on the results of finite element analyses on steel plate shear walls with various characteristics, such as aspect ratio (L / h) and infill plate thicknesses, upper limits of 2.0 and 2.5 were proposed for ω_L for the bottom and top panels, respectively. The maximum target values of C_3 , for determining these limits, were -20 % for the bottom panel and -10 to -40 % for the top panel. In order to avoid obtaining negative moments of inertia for end beams, a lower limit of $0.84 \omega_h$ was defined for ω_L . The columns in end panels should meet both the ω_h and ω_L requirements.

As all the previous studies on parameters ω_h and ω_L assumed the beam-to-column connections to be pinned, a numerical study was conducted using the finite element method to investigate the effect of the rigidity of the frame connections on the uniformity of the tension field and to consider the necessity of changes in the limits of these two parameters. The infill plate was replaced with tension strips to reduce the time of analysis.

This study showed that the non-uniformity of the tension field (represented by parameter C_2) in middle panels increases by changing the frame connection type from pinned to fixed. For aspect ratios of 1.0, C_2 exceeded the target value of 0.2 for higher values of ω_h , while for the other aspect ratios (less and more than 1.0), they remained less than 0.2.

In bottom and top panels, for panels with an aspect ratio of 0.5, the rigidity of the frame connections reduced the non-uniformity of the tension field (represented by parameter

C_3). For higher aspect ratios, the connection rigidity helped in reaching a more uniform tension field only for higher values of ω_L . In almost all cases, C_3 remained less than the proposed upper limits when rigid frame connections were used. Also, it was shown that the connection rigidity reduces the dependence of C_3 on ω_L for all panel aspect ratios.

It should be emphasized that the requirements described in this chapter for the establishment of the beam and column stiffnesses are only to address the issue of tension field uniformity. Obviously the end beams and columns must also possess sufficient strength to resist the forces imposed by the tension field, as well as sufficient strength and stiffness to resist all other applied loads.

Table 3.1: Hot-rolled wide-flange sections for top beams ($\omega_h = \omega_L = 2.5$)

h (mm)	L (mm)	L / h	w (mm)	I_c (10^6 mm ⁴)	I_b (10^6 mm ⁴)	Top beam
4000	2000	0.5	4	1572	98	W360x39
4000	4000	1	4	786	787	W610x125
4000	6000	1.5	4	524	2655	W610x307

Table 3.2: The effect of the frame connection rigidity on the parameter C_2 for different values of ω_h and panel aspect ratios

ω_h	1.0	2.0	2.5	3.0	4.0
L/h= 0.5					
Pin connections	0.007	0.034	0.048	0.068	0.238
Rigid connections	0.175	0.180	0.205	0.221	0.307
% change	2333	434	326	226	29
L/h= 1.0					
Pin connections	0.007	0.100	0.227	0.387	0.998
Rigid connections	0.106	0.202	0.338	0.608	1.365
% change	1487	102	49	57	37
L/h= 1.5					
Pin connections	0.000	0.040	0.058	0.088	0.191
Rigid connections	0.073	0.089	0.113	0.160	0.348
% change	23243	125	94	81	82

Table 3.3: The effect of the frame connection rigidity on the parameter C_3 for proposed maximum values of ω_L and panel aspect ratios

ω_L	2.0	2.5
L/h= 0.5		
Pin connections	-33	-41
Rigid connections	-18	-22
% change	45	46
L/h= 1.0		
Pin connections	-23	-27
Rigid connections	-24	-24
% change	-4	11
L/h= 1.5		
Pin connections	-15	-19
Rigid connections	-23	-24
% change	-53	-26

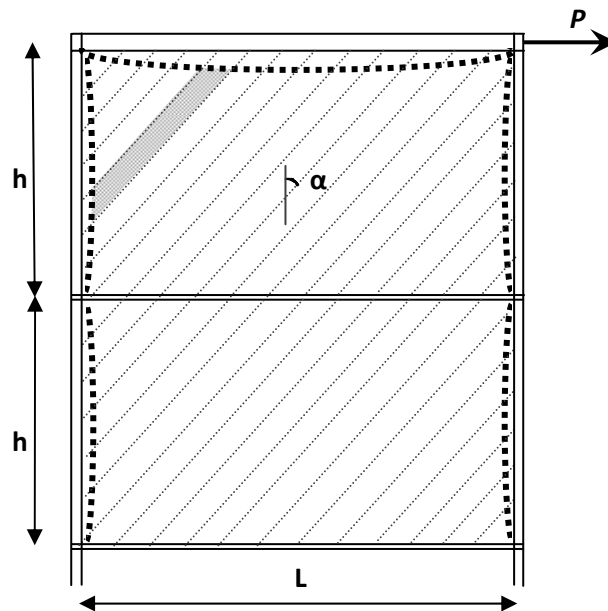


Figure 3.1: Tension strips anchored to surrounding frame members

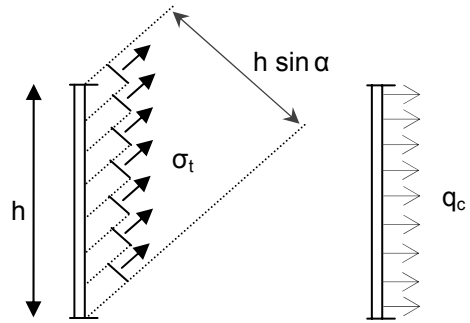


Figure 3.2: Distributed load along column applied by anchored tension strips

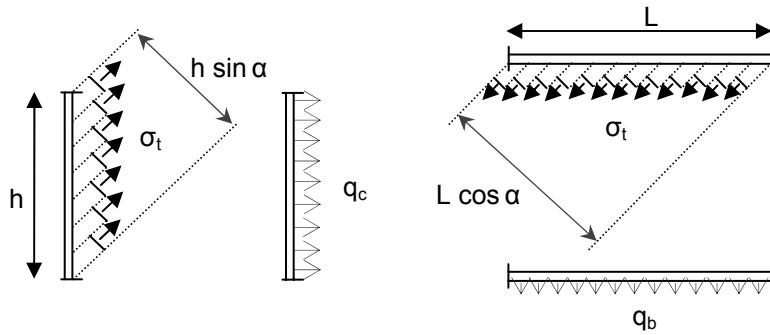


Figure 3.3: Distributed load along boundary members applied by anchored tension strips

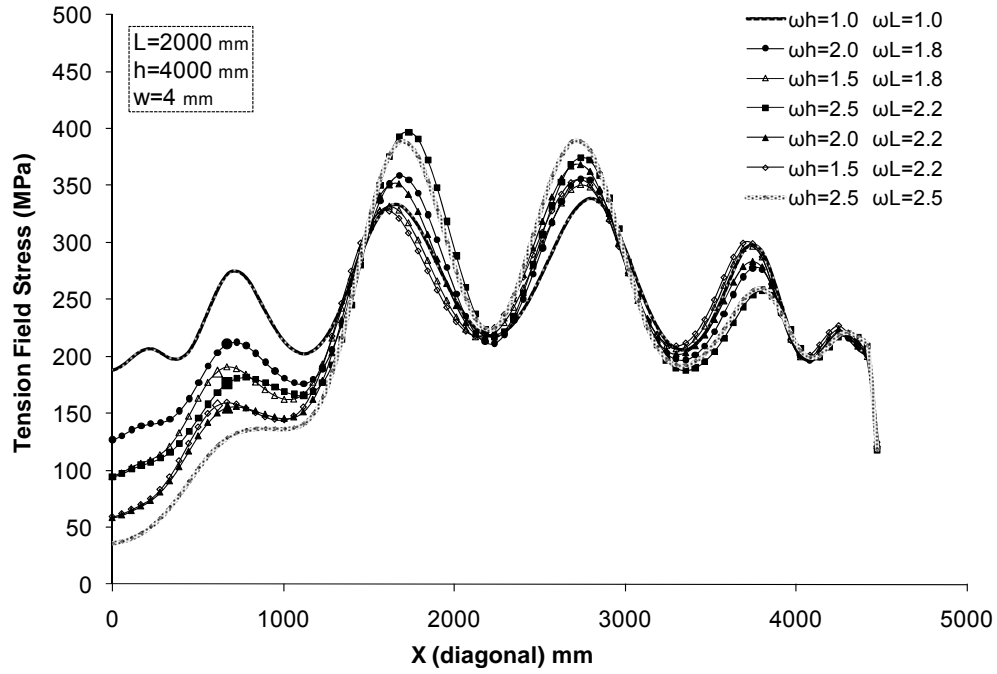


Figure 3.4: Stress distribution along the diagonal of the end panel with $L / h = 0.5$

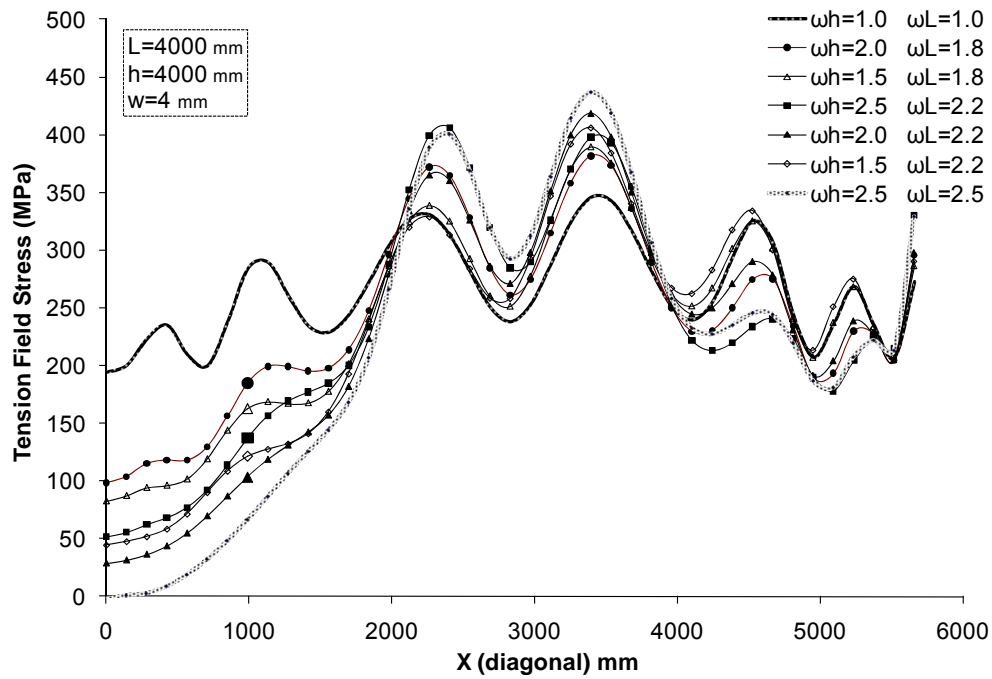


Figure 3.5: Stress distribution along the diagonal of the end panel with $L / h = 1.0$

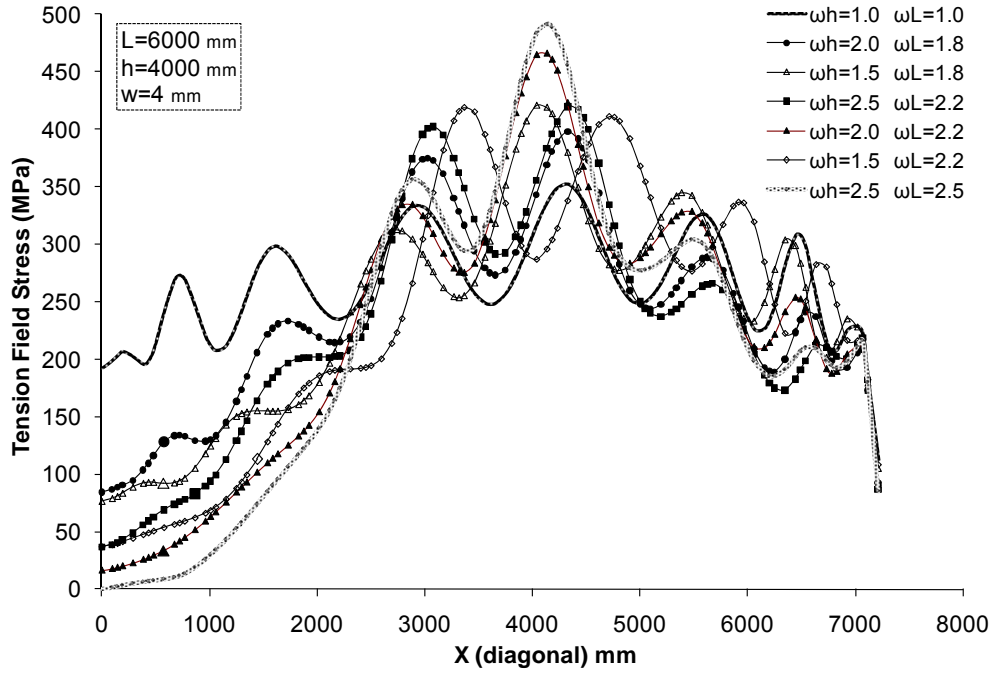


Figure 3.6: Stress distribution along the diagonal of the end panel with $L / h = 1.5$

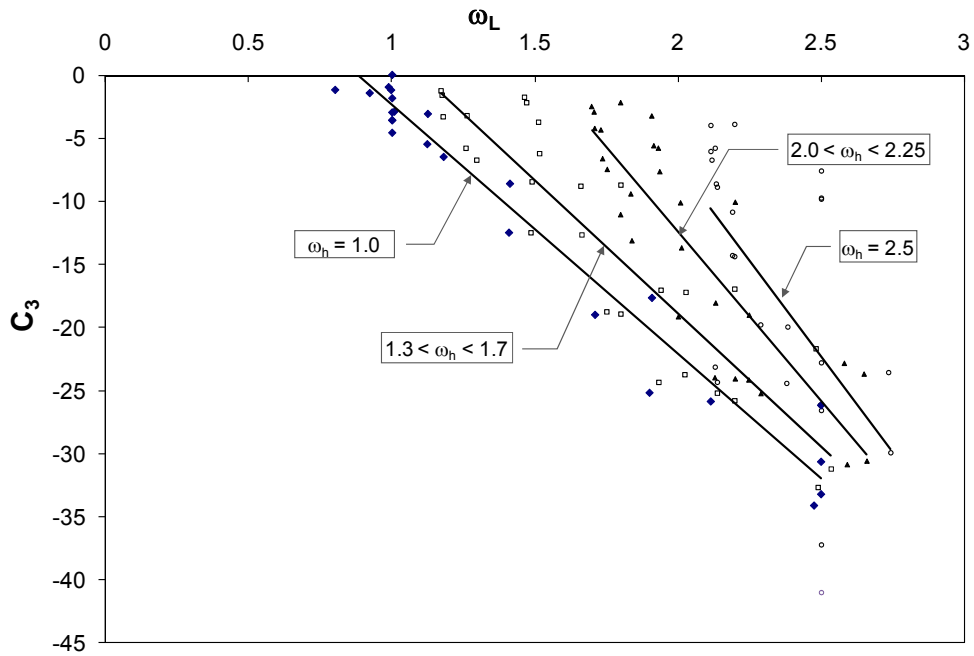


Figure 3.7: Non-uniformity of tension field stress as a function of ω_L and ω_h

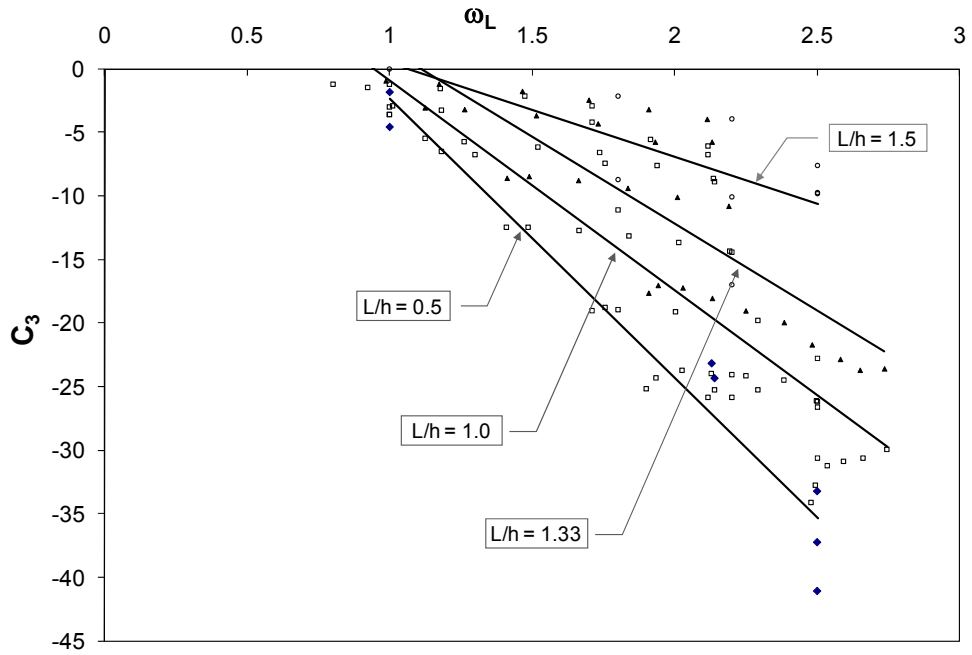


Figure 3.8: Non-uniformity of tension field stress as a function of ω_L and L/h

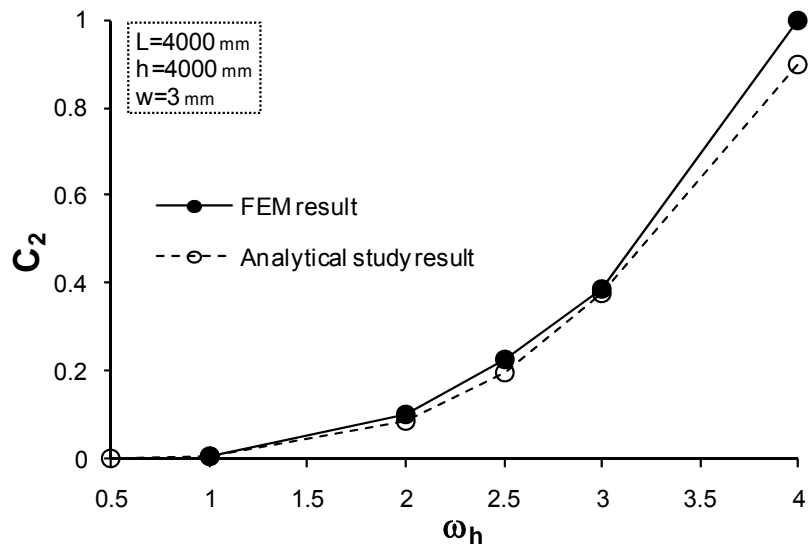


Figure 3.9: Comparison of the finite element analysis results and analytical study result

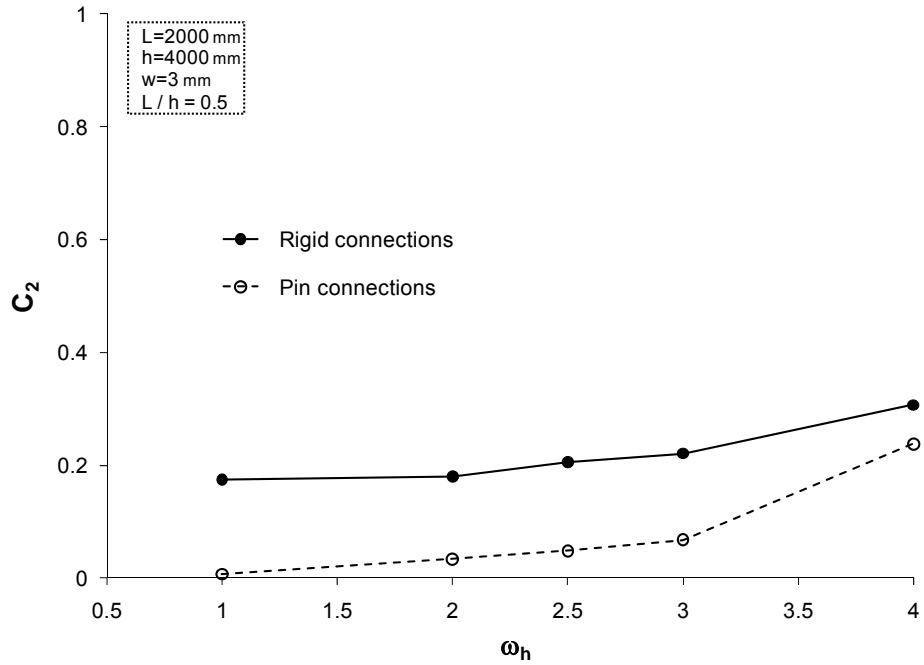


Figure 3.10: Parameter C_2 as a function of ω_h in panels with $L/h = 0.5$

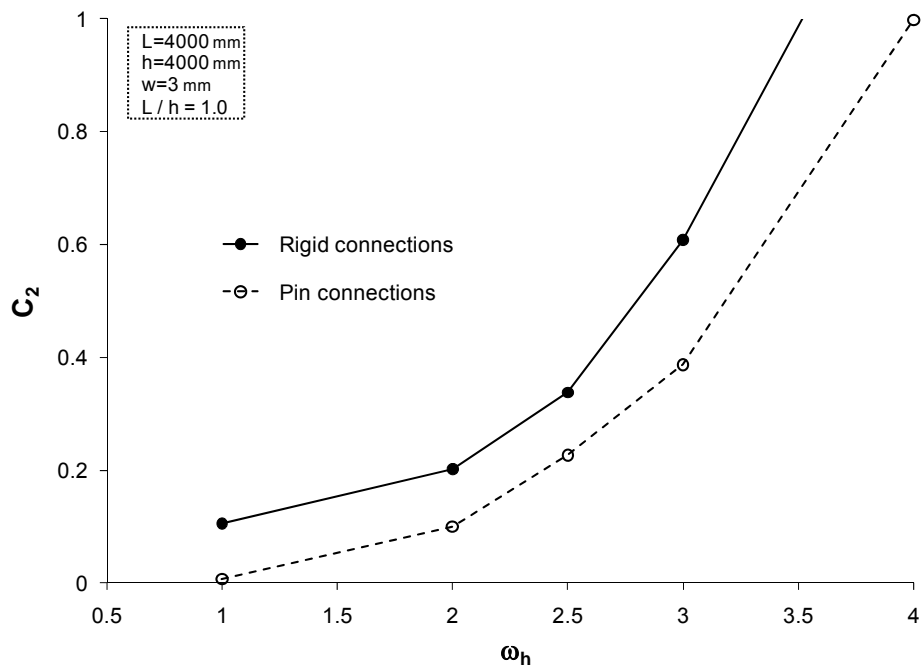


Figure 3.11: Parameter C_2 as a function of ω_h in panels with $L/h = 1.0$

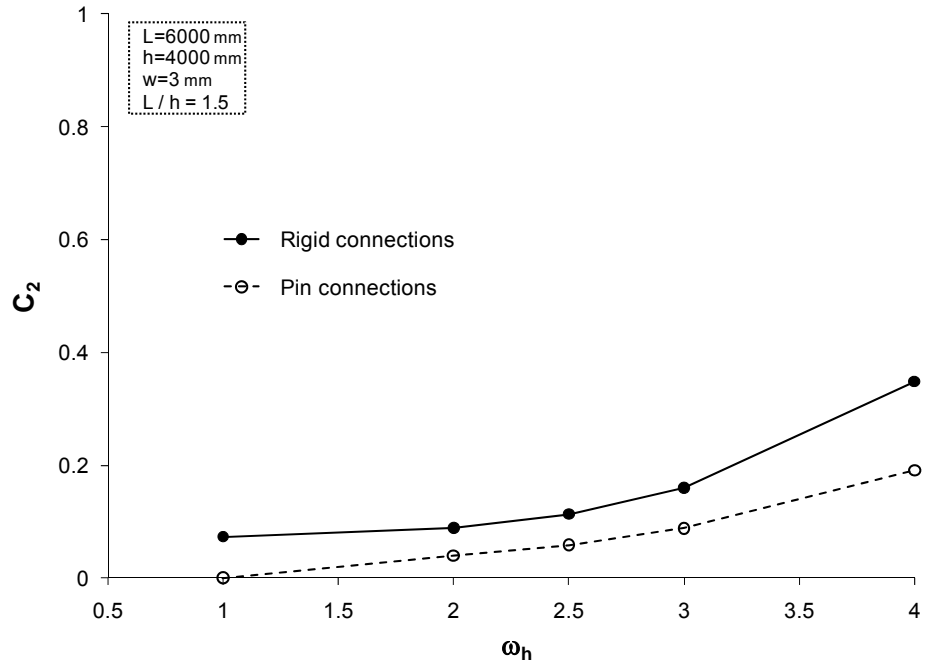


Figure 3.12: Parameter C_2 as a function of ω_h in panels with $L / h = 1.5$

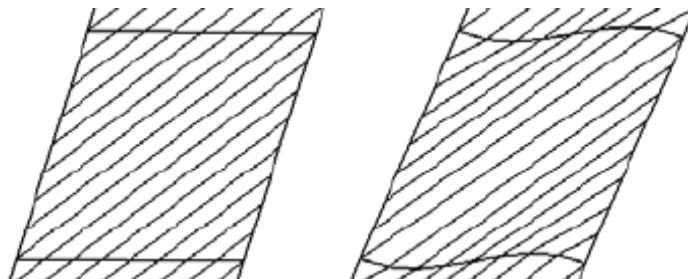


Figure 3.13: The deformed shape of panels in middle stories with pinned (left) or fixed (right) beam-to-column connections

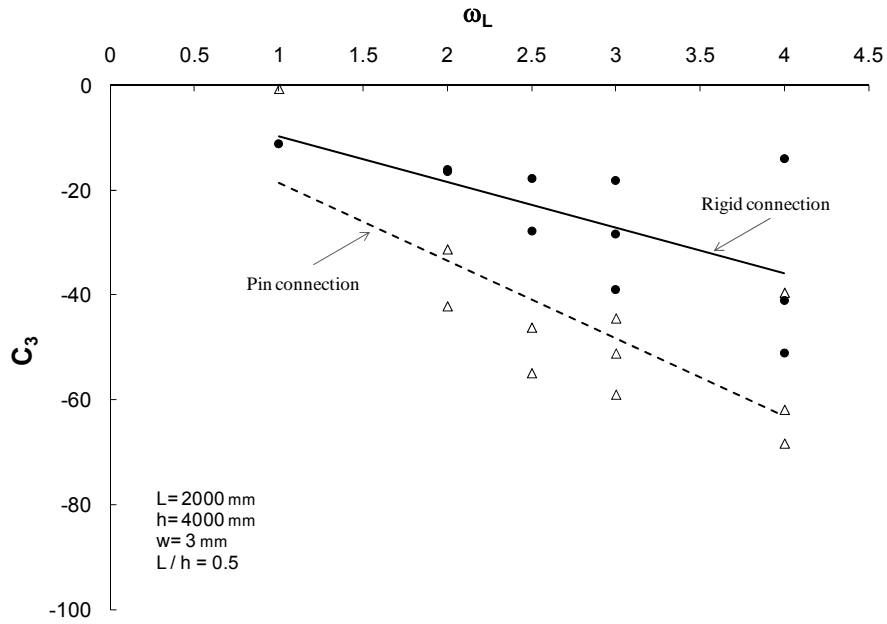


Figure 3.14: Effect of the frame connection rigidity on parameter C_3 for different values of ω_L in panels with $L / h = 0.5$ and infill plates with 3 mm thickness

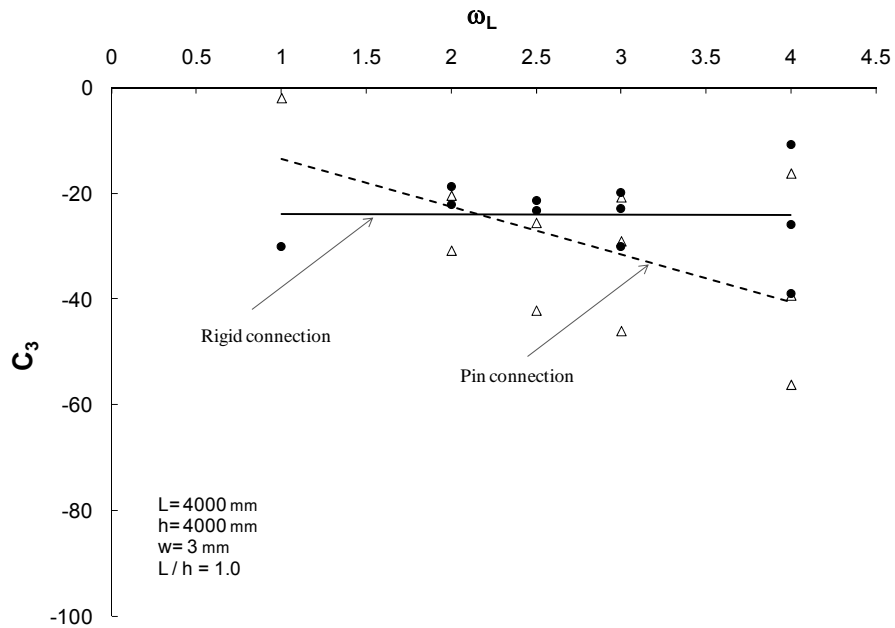


Figure 3.15: Effect of the frame connection rigidity on parameter C_3 for different values of ω_L in panels with $L / h = 1.0$ and infill plates with 3 mm thickness

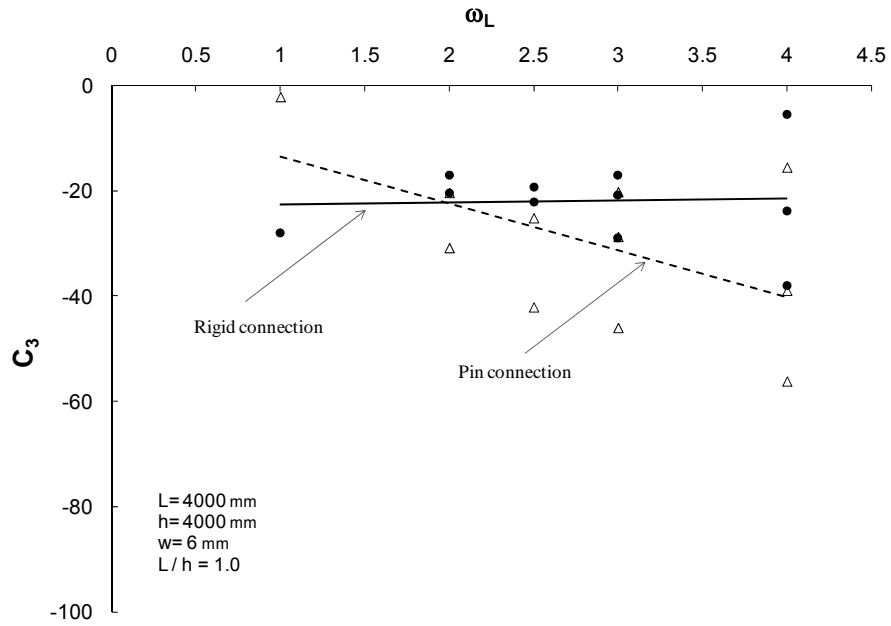


Figure 3.16: Effect of the frame connection rigidity on parameter C_3 for different values of ω_L in panels with $L/h = 1.0$ and infill plates with 6 mm thickness

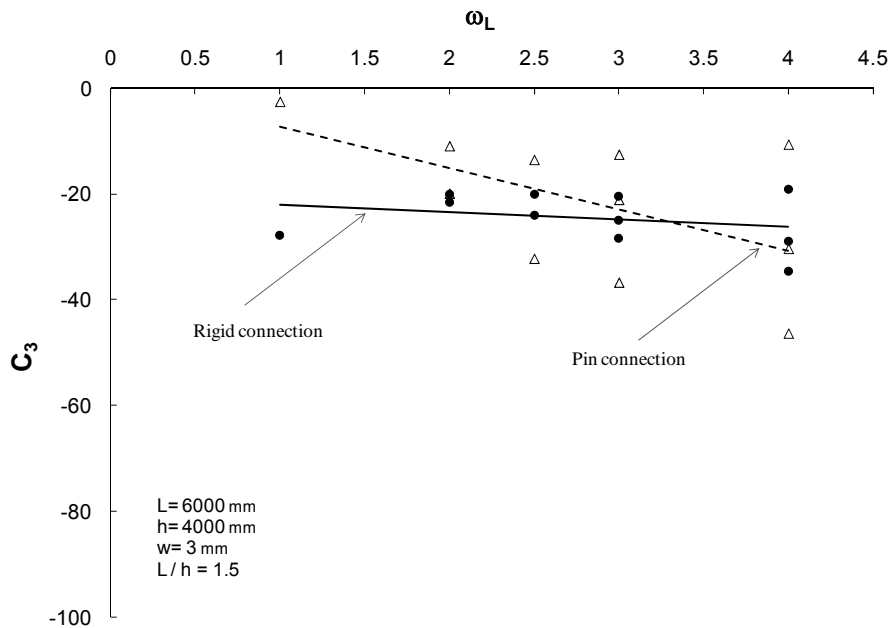


Figure 3.17: Effect of the frame connection rigidity on parameter C_3 for different values of ω_L in panels with $L/h = 1.5$ and infill plates with 3 mm thickness

4. TEST SPECIMENS, PROTOCOLS, PREPARATIONS AND MATERIAL PROPERTIES

4.1 Introduction

Advantages of composite columns that make them desirable for use as columns in steel plate shear wall systems include higher flexural stiffness and axial strength. One of the advantages of PEC columns over other types of composite columns in steel plate shear wall systems is that they provide steel surfaces (i.e., flange surfaces) for welding the infill plate to the columns. The infill plate is welded to the center of the flange, where the column web is welded to the other side of flange, thus it provides a direct transfer of force from the infill plate to the column.

Based on the observations from the benchmark test, conducted by Deng et al. (2008), two two-story steel plate shear walls with PEC column were designed to further study the performance of PEC columns in the system and to investigate the effect of the construction method and the frame connection type on the both overall and local behavior of the specimens. The intent of the first test specimen, referred to herein as the “modular” specimen, is to eliminate field welding by using a modular construction method and reduce the overall cost and time of construction. The second specimen, referred to as the “RBS” specimen, is intended to reduce the demand on the beam-to-column connection and to obtain a better seismic performance.

During both tests, a constant axial load was applied to the top of the columns of the test specimens and then a cyclic lateral load was applied to the first and second floor beams. The lateral load or displacement was gradually increased in each cycle, based on the testing protocols described in this chapter, until the specimen failed.

Preparation of the test specimens consisted of instrumentation, concrete placement and ancillary tests. In order to study the behavior of the specimens, as well as to monitor the specimen performances during both tests, close to 100 channels of data were monitored and recorded in each test. Some of the instruments were placed inside concrete, so they had to be installed before concrete was cast in the columns. The base of the north PEC column in the RBS test was monitored with two sets of a 3D camera system that measured full-field strains in the column to get a better understanding of the column performance and failure mode at the base.

Concrete was cast in the columns in two lifts. The slump of concrete had to be high to make sure it would fill all tight spaces in the columns. The concrete in the columns was intended to be the same as concrete that would be used in the floor slabs. During the concrete casting in both lifts, concrete cylinders were cast for material tests.

Several ancillary tests were done before the associated wall tests to determine the properties of the constituent materials in the test specimens. The ancillary tests consisted of concrete split cylinder tests, concrete compressive tests, tension coupon tests of the column, beam, and infill plate materials, as well as tension tests of the rebars and links used in the specimens.

In this chapter, after the introduction of the test specimens and descriptions of the design details, the test setup is explained and the gravity and lateral load protocols and mechanism of their application are discussed. Also, the preparation of the test specimens is discussed briefly. The results of the ancillary tests are shown at the end of the chapter.

4.2 Description of test specimens

4.2.1 Modular test specimen

The modular test was conducted to study the effect of a modular fabrication method on the behaviour of SPSW systems. The general target of the modular construction method

is to reduce the overall cost of the SPSW system for use in low to moderate seismic regions where maximum ductility is not required. In this method, the modules are bolted to each other, as shown in Figure 4.1. Modules are fabricated and inspected, and possibly pre-assembled to assure proper fit-up, in the shop and then shipped to the site for assembly. The modules may be fabricated in one or more story high assemblies to suit the fabrication, lifting, and assembly conditions of each individual project. The modular method of construction studied completely eliminates the need for field welding and, as a result, the cost of the shear wall system is expected to be reduced significantly.

The infill plate modules are connected to the PEC columns and beams through fish plates that have been welded to the columns and beams in the shop. To connect the infill plate modules to each other, double lap plate splices are used close to mid-height of the stories. The connection between floor beams and columns are shear connections. Since the floor beam flanges are not connected to the columns, the connection is able to accommodate somewhat larger rotations compared to rigid connections, which may reduce the chance of developing hinges in the columns close to the beam-to-column connections. The simple beam-to-column connections eliminate any significant contribution to the performance of the wall through frame action and, as a result, the modular system is likely to qualify for a somewhat lower seismic force modification factor for design than a shear wall with moment-resisting beam-to-column connections.

The modular specimen had an overall height of 4120 mm and an overall width of 2690 mm, excluding the base plate. Stories were 1900 mm high and the column centerline spacing was 2440 mm. The thickness of the infill panels was 3 mm. The PEC columns were 250 mm × 250 mm in cross-section and the thickness of flanges and web of both columns were 6.35 mm (0.25 in.). The size of PEC columns was designed so that their effective moment of inertia, obtained from Equation (2.13), would result in flexibility parameters less than the maximum permitted values in Canadian steel design standard, CSA S16-09 (CSA 2009). As large bending moments were expected at the bases of the

columns and under first floor beam-to-column connections, links were placed closer to postpone the buckling of the flanges. At the bases of the columns the link spacing was the least (i.e., 50 mm), as at this region the hinge would form and closer link spacing would increase the ductility of the hinge by providing confinement to the concrete and stabilize the steel flanges. Also, based on the observations in the benchmark test, in order to postpone the crushing of concrete within the plastic hinges at the bases of columns, 25M longitudinal rebars were placed to decrease the stress levels in the concrete and prohibit sudden crushing. Figure 4.2 shows the PEC column cross-section at the base of the column and at other elevations. In Figure 4.3, the modular test specimen elevation is shown.

The thickness of all fish plates, which were used to connect the modules to the base plate and PEC columns and beams, was 6.35 mm (i.e., the same thickness as the column flanges and web). All the modules were bolted to one side of the fish plates. The thickness of the splice plates used to connect the infill plates at the mid-height of stories, was 3 mm (i.e., the same thickness as the infill plate) and the splice plates were placed on both sides of the infill plate. All the fasteners were designed for bearing, although all of them were pre-tensioned one-third turn in accordance with the seismic provisions in the Canadian steel design standard, CSA S16-09 (CSA 2009). The spacing between the centerlines of the fasteners was 60 mm.

The connection between the floor beams and columns must transfer a significant compressive axial force. This force is mainly due to the tension field forces applied to the two columns by the infill plates. Also, the lateral load was applied to the top flange of the floor beams, which introduces an additional compressive axial force at one end of the floor beams. As a relatively thin fish plate (6.35 mm thick) was used to connect the floor beams to the columns, the first floor connection was not capable of transferring the compressive axial force without strengthening. There were two options: stiffening the fish plate or adding an additional connection element on the other side of the beam web. The

latter option (an additional fish plate bolted to the beam web) was chosen, as the height of the first floor beam was not enough to accommodate appropriate lateral stiffeners. Although the selected option would require field welding, a fully bolted option could also be employed. Figure 4.4 shows the additional fish plate in the connection between the first floor beam and column. The second floor connection did not need stiffening, as the beam was deep.

Side plates with a thickness of 12.7 mm were welded to the tips of the flanges of the columns in the frame connection regions. Generally, the column side plates have several functions. The side plates provide a steel surface and facilitate the connection of the floor beams in the perpendicular direction. As the tips of the column flanges are fixed by the side plates, the stiffness of the column flanges increases and they will deform less as a result of the tension forces that are applied by the flanges of the floor beams in the plane of the steel plate shear wall.

Further details of the modular test specimen can be found in the shop drawings provided in Appendix A.

4.2.2 RBS test specimen

The RBS test specimen was a two-story SPSW with a modified beam-to-column connection. In the benchmark test, tearing was observed in the flange of the intermediate beam and plastic hinges formed in the columns under the frame connections. In order to resolve these shortcomings, RBS connections with radius cuts were selected to be used in the beam-to-column connections at both ends of the intermediate beam. The use of RBS connections reduces the chance of the beam flange tearing and lowers the flexural demand on the columns. The cross-section of the second floor beam was not reduced, since based on the Canadian steel design standard, CSA S16-09 (CSA 2009), plastic hinges are permitted to form at the tops of columns instead of in the beams at the roof level. In the case of the RBS test specimen, even the deepest-cut RBS at the roof level

would not prevent a hinge from forming in the adjacent PEC columns because of the large depth of the beam.

The RBS test specimen had the same overall height (4120 mm) and width (2690 mm) as the modular test specimen. The story heights were 1900 mm and the columns had a center-to-center distance of 2440 mm. The PEC columns had a 250 mm x 250 mm cross-section. The flanges and web of the columns had a thickness of 6.35 mm and the infill plate thickness was 3.0 mm in both stories. Like the modular test specimen, PEC columns in the RBS test specimen were conforming to the requirements of the Canadian steel design standard, CSA S16-09 (CSA 2009) regarding the minimum moment of inertia. A W250x58 section was used as the first floor beam and the second floor beam was W460x67. Figure 4.5 depicts the RBS test specimen.

The RBS cuts were circular and the maximum suggested cut (i.e., one-quarter of the flange width on each side) was selected (Moore et al. 1999). The cut dimensions and location are as shown in Figure 4.6. Connection welding details are shown in Figure A.7. The flanges of the floor beams were beveled at 45 degrees for full penetration groove welds and backing bars were used and left in place. Fillet welds were used for all longitudinal welds. As the demand on the frame connections in steel plate shear walls is less than in conventional moment resisting frames, the performance of the frame connections was expected to be less sensitive to the welding procedures.

There were several notches in the RBS regions, with depths of up to 2 mm before the surface grinding operation. The cut portion was prepared according to the instructions provided by Moore et al. (1999). Figure 4.7 shows the surface condition of the cut, before and after grinding.

An extensive previous study by Grubbs (1997) on the effect of the RBS connections on the stiffness of moment frames, showed that for a 50 percent flange reduction, the lateral

stiffness was reduced by less than 7 percent; thus, the stiffness of the RBS specimen was expected to be less but close to that of the benchmark test.

The links were placed at a closer spacing at the locations where high bending moments and rotations were expected to occur during the test. This was to postpone the local buckling of the flanges of the columns and to increase the ductility of the hinges by providing better confinement for concrete. As the top beam was deep and its section was not reduced, the links were placed closer under the beam-to-column connection in the second floor, where plastic hinges might form.

Like the modular test specimen, 12.7 mm thick side plates were used in the columns at the floor levels in order to facilitate the connection of the floor beams in the perpendicular direction to the columns and to increase the stiffness of the flanges of the column in the frame connection. The presence of the side plates also reduces the demand on the transverse welds connecting the flanges of the beams to the adjacent column, as they are welded to the tips of the beam flanges close to the face of column, as shown in Figure A.7.

Further details of the RBS test specimen can be found in the shop drawings provided in Appendix A.

4.3 Test set-up

Figures 4.8 and 4.9, show the modular test and the RBS test set-ups, respectively. The test specimens were oriented in the North–South direction in the test set-up and the lateral loads in both stories were applied from the south side of the specimens. In the first half of each cycle, the specimens were pushed to the north and the resulting base shear (Q_1) and in-plane displacement (δ_1) were considered positive. In the second half of the cycles, the specimens were pulled to south, resulting in a negative base shear (Q_2) and in-plane displacement (δ_2).

Both test specimens were connected to the strong floor by twelve high-strength pre-tensioned anchor rods and sliding of the specimens was prevented by additional anchored plates installed on each end of the base plate. To ensure complete contact between the base plate of the specimens and the floor, the base plates were shimmed and voids were grouted.

The columns were braced near each floor level by articulated braces to prevent out-of-plane displacement. These lateral braces, known as Watt braces, do not resist in-plane displacements. Any out-of-plane movements of the columns were monitored during both tests to make sure that they remain small.

Gravity loads were applied to the tops of the columns equally through a cross-shaped distributing beam. Two sets of actuators were connected to the cross-beam through tension rods. Each of the four gravity load actuators was mounted on a gravity load simulator, which is used to keep the gravity loads vertical during the tests as the test specimens were expected to experience large in-plane displacements.

The rotation of the cross beam, as well as the forces in the tension rods, which were connecting the actuators to the cross beam, were monitored during gravity load application to make sure the gravity load was being applied equally to the two columns. The magnitude of the gravity load on both columns was measured by two load cells that were installed under the cross beam supports on top of the columns.

The lateral load was applied through two sets of actuators, which were supported by a reaction wall. To avoid local failure of the PEC column due to the loading mechanism itself, and to be as close as possible to the real situation of diaphragm loading and the lateral load transition route in real buildings, a lateral load transition system, which was initially designed by Deng and Driver (2007), was used at each floor to transfer lateral

loads from the actuators to the top flanges of the floor beams. Lateral loads were applied to each floor equally.

4.4 Loading regime

A constant gravity load of 600 kN was applied on top of each column to represent the service gravity loads during an earthquake. The gravity loads were close to 20 percent of the axial strength of the columns.

The lateral load regime was based on the method outlined in ATC-24 (ATC 1992). For the “force control” stage, the base shear (Q) was chosen as the controlling parameter and the first floor displacement was chosen as the controlling parameter in the “displacement control” stage, since the first floor was of primary interest. Figure 4.10 depicts the cyclic lateral load history that was applied to the test specimens. After estimating the Q_y and $\bar{\delta}_y$ values for each specimen based on the results of the benchmark test, nine “force control” cycles were applied to the specimens at $0.25 Q_y$, $0.5 Q_y$ and $0.75 Q_y$ levels. From $\bar{\delta} = \bar{\delta}_y$ to $\bar{\delta} = 3\bar{\delta}_y$, three cycles were applied at each displacement level and after that, two cycles were applied at each displacement level.

In the modular test, Q_y was estimated to be close but lower than that of the benchmark test as the frame connections were shear connections, and it was estimated to be around 1200 kN. The value for $\bar{\delta}_y$ was chosen as 8.5 mm. The targeted values for base shear and first floor displacement in different cycles are tabulated in Table 4.1.

In the RBS test, the value of Q_y was estimated to be close to that of the benchmark test, so it was expected to be close to 1400 kN. $\bar{\delta}_y$ was chosen equal to 10 mm for the RBS test specimen. In Table 4.2, the targeted values for base shear and first floor displacement in the RBS test are tabulated

4.5 Instrumentation and data collection

Figures 4.12 and 4.13 show the instrumentation layouts for the modular and RBS test specimens, respectively. To monitor the gravity load on top of the columns, two commercial flat load cells were used. The tension rods, which were used to connect the gravity load actuators to the cross-beam at the top of the specimens, were each instrumented by four strain gauges, forming a Wheatstone bridge circuit and acting like a load cell. Figure 4.11 shows the mechanism of gravity load application. The readings from these load cells were compared with the flat load cells at the top of the columns and used as a redundant measurement of the gravity loads. The load cell rods were closely monitored during gravity load application to make sure of a balanced load application to the cross-beam.

The two lateral loads were monitored using load cells installed between the lateral load actuators and the mechanism used to transfer load to the specimens at each floor level. These load cells had the capability of measuring both tension and compression.

In-plane and out-of-plane displacements of the specimens at each floor level were measured by cable transducers. As mentioned before, the base plates of the specimens were grouted and connected to the strong floor by twelve pre-tensioned rods and also locked to the reaction plates at each end. In order to make sure that the displacement of the base plates remained small throughout the test; the movement of the base plates was monitored by dial gauges. The readings from these gauges showed very small movements, which are considered negligible.

The rotations of the beam-to-column connections in the first and second floors of both specimens were measured by clinometers. In the modular test, at each floor level one clinometer was attached to the column side plate and another clinometer measured the rotation of the beam-end. In the RBS test, the first floor beam-to-column connection

rotation was measured by two clinometers, one measuring the rotation of the column side plate and the other measuring the beam rotation at the end of the RBS cut toward the center of the beam. At the second floor, as the connection was rigid and there was not any RBS cut in the beam, one clinometer was used, which was attached to the column side plate.

In the modular test, six linear variable displacement transformers (LVDTs) were used to have a redundant measurement of the strains in the north PEC columns. The LVDTs were connected to the flanges of the column in groups of two, in three levels. The gauge length of the LVDTs at the base of the column was 300 mm and at the other two levels, it was 200 mm.

In the modular test, 45 electrical resistance strain gauges were used, out of which 24 were in the form of eight strain gauge rosettes affixed to both sides of the infill plate in the first story at four levels. In the RBS test, more strain gauges were used as one of the RBS cuts was thoroughly monitored. The total number of strain gauges in this test was 96, out of which 30 were in the form of ten strain rosettes. Six strain gauge rosettes were affixed to both sides of the first story infill plate in three levels, and the rest (four strain gauge rosettes) were used to measure strains in the web of the beam in the RBS cut region. The strain in the longitudinal rebars, at the base of the PEC columns, was measured to have a better understanding of the strain distribution in the cross section of the PEC columns at the base in different stages of the tests. The gauge length of all the strain gauges in both tests was 5 mm, except those in the strain gauge rosette that had a gauge length of 2 mm.

A total of 93 channels of data were recorded in the modular test. In this test, all strain gauges and eight of the high-level channels (i.e., cable transducers, LVDTs and clinometers) were connected to one data acquisition system and the remaining eight high-level channels were connected to a separate system. The RBS test specimen was

monitored using 111 channels of data and all of them were connected to one data acquisition system.

Two 3D camera systems were used to monitor the base of the north column in the RBS test. The monitored areas were painted in white and then speckled by black paint to provide the contrast needed for full-field strain monitoring. Each set of cameras included two cameras, which took high resolution pictures of the same area at the same time from two different angles. Commercial software was used to post-process these images and by comparing the location of the speckle points to the reference pictures (the first pictures taken at the load-free stage), the software calculated the displacements, strains and rotations. In the RBS test, two sets of cameras were used to monitor two perpendicular sides (concrete and steel surfaces) of the north column at its base. Figure 4.14 shows one set of cameras that was used to monitor the concrete surface of the column at the base in the RBS test.

4.6 Concrete placement

All required concrete for the two specimens was commercially produced and delivered to the lab by ready-mix truck. The concrete casting, including its prior preparations, was a highly labour-intensive task. It included fabricating suitable clamps to hold the formwork in place and resist high concrete pressure, preparing the formwork and placing concrete in the columns of specimens in two stages, as well as casting concrete cylinders. To hold the formwork in place, eight clamps were used per specimen. Figure 4.15 shows one of the clamps. The formwork, which was made of $\frac{3}{4}$ in. plywood, had a 260 mm width, but the heights of the individual pieces were different depending on their locations. The formwork was epoxy-coated for protection against the concrete moisture. The concrete had to be placed in the columns by hand, due to the relatively small spacing of the links.

Casting of concrete in the columns was done in two stages due to the height of the columns, the pressure of the concrete on the formwork, the capacity of the clamps, and the required man-power to place, vibrate and install the formwork in a short period of time. Moreover, casting in two separate operations is representative of field conditions for casting two stories.

The first concrete casting was done on January 16th, 2009. In the first stage, concrete was cast in the columns of the first story of the specimens. The slump of the concrete was 120 mm to facilitate the concrete placement. To facilitate the vibration of the concrete, casting of the concrete in the first story of the columns was done in two lifts. Figure 4.16 shows the formwork before the concrete was cast. The height of the formwork in the first lift was 900 mm. The height of the formwork in the second lift was 540 mm and it filled the gap between the formwork in the previous lift and the side plate in the first floor beam-to-column connection. The concrete was then cast and vibrated from the top of the side plate. To prevent a cold joint in the column between the first and second lifts on the first day, the formwork was placed immediately after the completion of the first lift and the vibrator was plunged through the second lift and into the concrete from the first lift. Figure 4.17 shows the second lift of casting concrete in the columns of the specimens in first story.

The concrete was cast in the columns of the second story on January 22nd, 2009. The slump of concrete was 110 mm. The cold joint between the concrete in the two stories was located behind the side plate. Observations during both tests demonstrated that this cold joint had no effect on the performance of the specimens, as it was located in a relatively rigid region. Like the first story, concrete was cast in two lifts in the second story on the same day. The concrete for the second lift was cast in the column above the second floor side plate through a hole in the cap plate. A small gap of around 20 mm was intentionally left under the cap plate to accommodate the shrinkage of the concrete. The remaining top gap was filled with Masterflow 928 non-shrink grout, which is a hydraulic

cement-based mineral-aggregate grout with an extended working time, to better distribute the gravity load between the steel and concrete parts of the column. Figure 4.18 shows the grouting of the gap at the top of the columns.

In all stages of concrete casting, concrete cylinders (150 mm diameter) were cast in order to determine the material properties of the concrete at different ages and on the test dates.

4.7 Ancillary tests

Ancillary tests, to determine material properties of the steel and concrete, included tension tests of coupons taken from different steel parts of the specimens and concrete compressive and split cylinder tests. All tension coupon tests were conducted according to ASTM Standard A370-05 (ASTM 2005). Figure 4.19 depicts the dimensions of the tension coupons taken from plate materials. The modulus of elasticity of the concrete was obtained by using the described method in ASTM Standard C469-02 (ASTM 2002) and the concrete strength was obtained according to CSA Standard A23.2-04 (CSA 2004).

A total of 20 tension coupons were tested to determine the material properties of the steel parts of the modular specimen. All the infill plates in the modular specimen were cut from a single plate. The flanges and the webs of the columns of the modular specimen were also cut from one plate. A total of four tension coupons were taken from each plate. Two of these coupons were cut parallel to the rolling direction of these plates and the other two were cut in the transverse direction. Two tension coupons were taken from each flange and the web of each of the first and second floor beams. Two coupons were also taken from the longitudinal rebar and links. All the coupons were taken from extra material provided by the fabricator that was cut from the materials used in the specimens (see Figure 4.20).

A total of 24 tension coupons were taken from the steel parts of the RBS specimen. The infill plates in the first and second stories of the RBS specimen were taken from two different plates; therefore four extra tension coupons were necessary compared to the modular specimen.

All the tension coupon tests were conducted in an MTS 1000 universal testing machine at the I.F. Morrison Structural Engineering Laboratory at the University of Alberta. Load measurement was done by an internal load cell in the MTS 1000. The elongation of the coupon was measured by an extensometer with a gauge length of 50 mm. The loading rate was 1 mm/min up to strain-hardening, and 5 mm/min afterwards. Figure 4.21 shows one of the plate and rebar coupons during the tension tests.

The compressive strength of the concrete was determined at 7- and 28-days, as well as on the associated test date. The tensile strength of the concrete was determined on the test dates by conducting a cylinder split test. The material tests to determine the compressive and tensile strengths of concrete were conducted in the Concrete Material Laboratory at the University of Alberta. Figures 4.22 and 4.23, respectively, show concrete cylinders after a compressive strength test and split cylinder test.

In order to obtain the stress vs. strain material behavior of concrete, a few concrete cylinders were tested in the MTS 2600 universal testing machine at the I.F. Morrison Structural Engineering Laboratory at the University of Alberta on the associated test dates. Three LVDTs with gauge lengths of 200 mm were used to measure the shortening of the cylinders, while the compressive load was measured by an internal load cell in the MTS machine. Figure 4.24 shows one of the cylinders in the MTS 2600 during the test.

4.8 Material properties

The static yield stress of the infill plates in the modular test specimen was 256 MPa, which is very close to those of the infill plates in the RBS test (259 and 261 MPa). The

result of the tension coupon tests of the infill plates generally showed a very small yield plateau, which is due to the excessive rolling of these thin plates. All of the infill plate coupons had large ultimate strains in the neighbourhood of 18 percent. The column plates had a static yield stress of around 450 MPa in both specimens. The yield strain and strain-hardening were close to typical values for structural steel. As expected, the coupons that were cut parallel to the rolling direction showed a slightly higher yield stress. In Figures 4.25 and 4.26, sample stress–strain curves of the infill plates and column plates are depicted.

The flanges of the first floor beams in both specimens had a static yield stress of around 350 MPa, while the coupons taken from their webs showed a higher yield stress of close to 380 MPa, which is likely due to the smaller thickness of the web compared to the flanges, requiring more severe rolling. The flange thickness of the second floor beams in both specimens were less than the first floor beam flange thicknesses, which led to higher yield stress of around 360 MPa. The yield strain and strain-hardening values were close to typical values for structural steel.

The longitudinal rebars (25M) had lower than expected modulus of elasticity values. The static yield stress of the rebars was close to 450 MPa and their ultimate strain was close to seven percent, which is low. The links (10 mm round bars) had a static yield stress of 400 MPa with a long yield plateau. The results of the tension coupon tests related to the modular and RBS specimens are tabulated in Tables 4.3 and 4.4, respectively. Further information about the results of the tension coupon tests can be found in Appendix B.

The average density of concrete was 2465 kg/m³. The average compressive strength of concrete in the first story of the specimens was around 51 MPa which was reasonably close to the compressive strength of concrete in the first story of the benchmark test specimen (i.e., 55 MPa). Since observations during both tests showed that all concrete crushing occurred in the first story of the specimens, the overall performance of the

modular and RBS tests can be compared to the performance of the benchmark test. The average modulus of elasticity, compressive and tensile strengths of concrete in the first and second stories of the modular and RBS test specimens on the associated test dates are tabulated in Table 4.5. Further information is included in Appendix B.

Table 4.1: Targeted base shear and first floor displacement values in different cycles of the modular test

Cycle No.	Force control parameter Base shear (kN)	Displacement control parameter First Floor Displacement (mm)
Cycles 1-3	± 300	-
Cycles 4-6	± 600	-
Cycles 7-9	± 900	-
Cycles 10-12	-	$\delta_y = \pm 8.5$
Cycles 13-15	-	$2\delta_y = \pm 17.0$
Cycles 16-18	-	$3\delta_y = \pm 25.5$
Cycles 19-20	-	$4\delta_y = \pm 34.0$
Cycles 21-22	-	$5\delta_y = \pm 42.5$
Cycles 23-24	-	$6\delta_y = \pm 51.0$
Cycles 25-26	-	$7\delta_y = \pm 59.5$
Cycle 27	-	$8\delta_y = \pm 68.0$

Table 4.2: Targeted base shear and first floor displacement values in different cycles of the RBS test

Cycle No.	Force control parameter Base shear (kN)	Displacement control parameter First Floor Displacement (mm)
Cycles 1-3	± 350	-
Cycles 4-6	± 700	-
Cycles 7-9	± 1050	-
Cycles 10-12	-	$\delta_y = \pm 10$
Cycles 13-15	-	$2\delta_y = \pm 20$
Cycles 16-18	-	$3\delta_y = \pm 30$
Cycles 19-20	-	$4\delta_y = \pm 40$
Cycles 21-22	-	$5\delta_y = \pm 50$
Cycles 23-24	-	$6\delta_y = \pm 60$
Cycles 25-26	-	$7\delta_y = \pm 70$
Cycle 27	-	$8\delta_y = \pm 80$

Table 4.3: Tension test results of all the coupons, related to the modular test specimen

Coupon mark	Elastic modulus	Dynamic yield stress*	Static yield stress	Dynamic ultimate stress*	Yield strain	Hardening strain	Ultimate strain	Comments
	MPa	MPa	MPa	MPa	%	%	%	
infill plate								
PR1	201500	N/A	N/A	368	N/A	N/A	16.602	no plateau**
PR2	196600	258	249	365	0.127	0.164	16.638	**
PR3	195400	268	259	367	0.133	0.545	17.219	***
PR4	200200	269	261	368	0.130	0.590	17.034	***
mean	198400	265	256	367	0.130	0.433	16.873	
column plate								
MAP1	178400	435	428	515	0.240	1.416	15.631	**
MAP2	191000	434	418	507	0.219	1.612	16.120	**
mean	184700	434.5	423	511	0.229	1.514	15.876	
MAP3	192500	456	437	526	0.227	1.693	15.588	***
MAP4	189800	454	443	523	0.233	1.519	15.704	***
mean	191200	455	440	524.5	0.230	1.606	15.646	
first floor beam								
B1F1	208500	359	342	515	0.164	0.815	15.580	flange
B1F2	212500	355	352	517	0.166	0.627	16.035	flange
mean	210500	357	347	516	0.165	0.721	15.808	flange
B1W1	197600	394	376	515	0.190	1.960	16.171	web
B1W2	191300	398	392	516	0.205	2.039	16.214	web
mean	194500	396	384	516	0.198	2.000	16.193	web
second floor beam								
B2F1	213600	370	356	507	0.167	1.322	16.675	flange
B2F2	216200	369	366	507	0.169	1.281	16.623	flange
mean	214900	370	361	507	0.168	1.302	16.649	flange
B2W1	218900	382	377	513	0.172	1.431	16.255	web
B2W2	216200	385	379	521	0.175	1.361	15.590	web
mean	217600	384	378	517	0.174	1.396	15.923	web
25M rebar								
25M-RA1	169800	478	462	600	0.272	1.172	7.174	
25M-RA2	172400	484	470	598	0.273	1.049	6.274	
mean	171100	481	466	599	0.272	1.111	6.724	
10mm dia. Bar								
10M-RB1	190300	566	402	429	0.211	2.886	9.083	
10M-RB2	201300	402	397	457	0.197	3.193	11.658	
mean	195800	484	399.5	443	0.204	3.040	10.371	

Notes:

* Speed of the load application was 1.0 mm/min and 5.0 mm/min before and after strain hardening, respectively.

** Coupon marks, taken from plates, ending in 1 or 2 are perpendicular to the rolling direction.

*** Coupon marks, taken from plates, ending in 3 or 4 are parallel to the rolling direction.

Table 4.4: Tension test results of all the coupons, related to the RBS test specimen

Coupon mark	Elastic modulus	Dynamic yield stress*	Static yield stress	Dynamic ultimate stress*	Yield strain	Hardening strain	Ultimate strain	Comments
	MPa	MPa	MPa	MPa	%	%	%	
1st story infill plate								
SA1	209700	268	256	370	0.122	0.579	19.388	**
SA2	213800	270	258	369	0.121	0.490	17.373	**
SA3	200200	267	259	366	0.129	0.538	18.663	***
SA4	196700	268	263	366	0.134	0.450	18.641	***
mean	205100	268	259	368	0.126	0.514	18.516	
2nd story infill plate								
SB1	198500	273	257	372	0.129	0.472	18.346	**
SB2	192000	267	261	370	0.136	0.390	18.479	**
SB3	202900	268	264	366	0.130	0.524	18.098	***
SB4	190400	267	262	366	0.138	0.555	17.670	***
mean	196000	269	261	369	0.133	0.485	18.148	
column plate								
PAA1	197200	438	428	520	0.217	0.985	15.246	**
PAA2	194600	442	438	525	0.225	1.037	15.742	**
mean	195900	440	433	523	0.221	1.011	15.494	
PAA3	204000	454	447	518	0.219	0.713	13.617	***
PAA4	204300	452	449	516	0.220	0.717	13.665	***
mean	204200	453	448	517	0.219	0.715	13.641	
first floor beam								
MAF1	212100	366	357	522	0.168	0.888	16.025	flange
MAF2	208000	361	347	517	0.167	0.722	15.768	flange
mean	210050	364	352	520	0.168	0.805	15.897	flange
MAW1	192200	400	389	515	0.202	2.199	16.261	web
MAW2	189700	392	371	512	0.196	1.988	16.511	web
mean	191000	396	380	514	0.199	2.094	16.386	web
second floor beam								
MBF1	224300	368	354	502	0.158	1.286	N/A	flange
MBF2	203200	370	358	510	0.176	1.327	17.772	flange
mean	213800	369	356	506	0.167	1.307	17.772	flange
MBW1	212600	373	359	502	0.169	1.431	16.671	web
MBW2	215600	378	360	512	0.167	1.417	16.548	web
mean	214100	376	359.5	507	0.168	1.424	16.610	web
25M rebar								
25M-RC1	167700	464	452	580	0.270	1.639	6.881	
25M-RC2	195600	456	441	592	0.225	1.576	N/A	
mean	181700	460	446.5	586	0.247	1.608	6.881	
10 mm dia. Bar								
10M-RA1	192600	407	400	465	0.208	2.847	16.009	
10M-RA2	200000	420	410	460	0.205	2.709	N/A	
mean	196300	414	405	463	0.206	2.778	16.009	

Notes:

* Speed of the load application was 1.0 mm/min and 5.0 mm/min before and after strain hardening, respectively.

** Coupon marks, taken from plates, ending in 1 or 2 are perpendicular to the rolling direction.

*** Coupon marks, taken from plates, ending in 3 or 4 are parallel to the rolling direction.

Table 4.5: Concrete cylinder properties on associated test dates

	Casted on	Tested in	E (MPa)	f_c (MPa)	f_t (MPa)
Modular test					
First story	JAN.16 th , 2009	AUG. 2009	23800	51.9	3.3
Second story	JAN.22 nd , 2009	AUG. 2009	21200	44.2	3.1
RBS test					
First story	JAN.16 th , 2009	FEB. 2010	23300	49.2	3.3
Second story	JAN.22 nd , 2009	FEB. 2010	20800	43.7	3.0

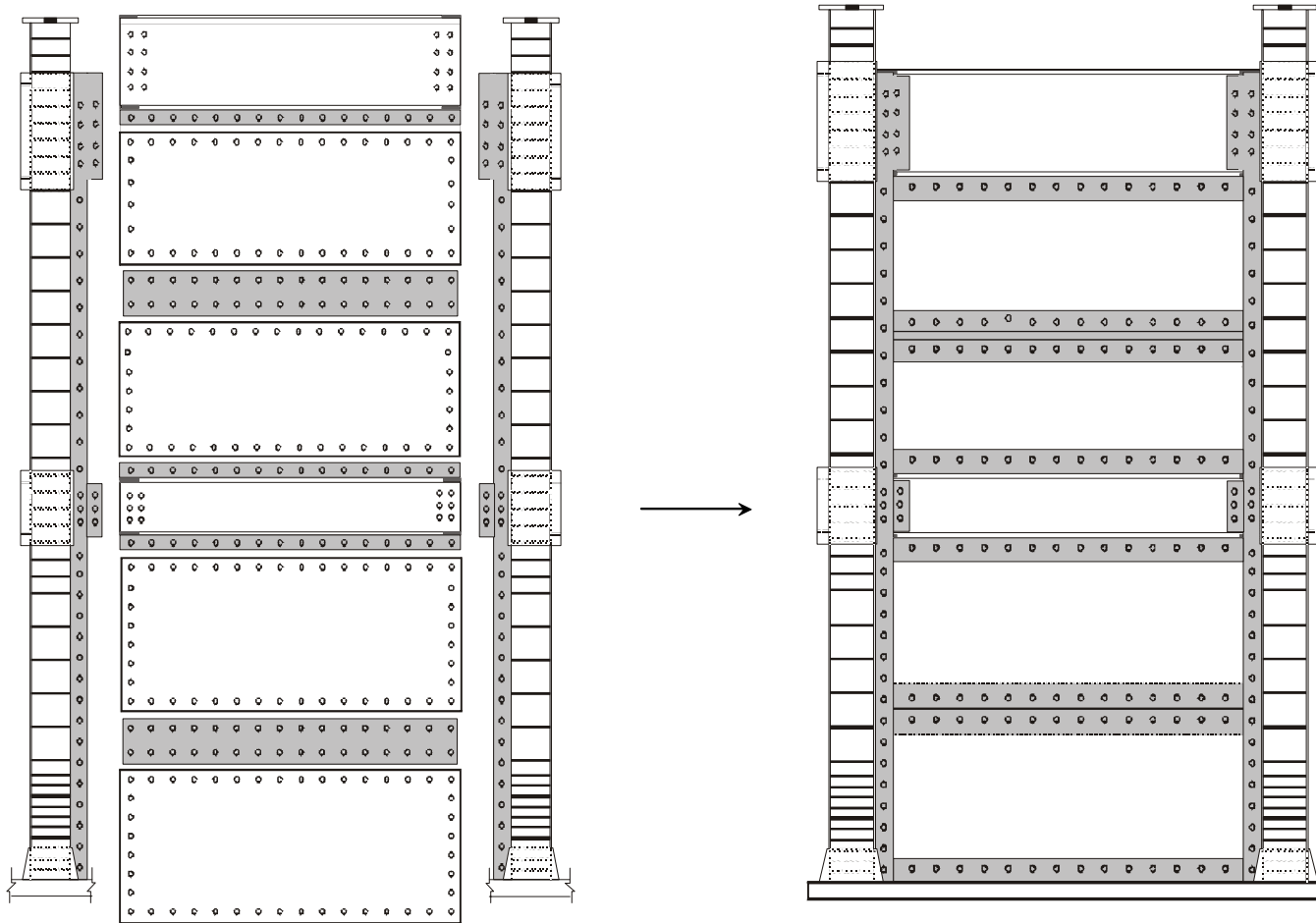


Figure 4.1: Exploded (left) and assembled (right) view of the modular test specimen

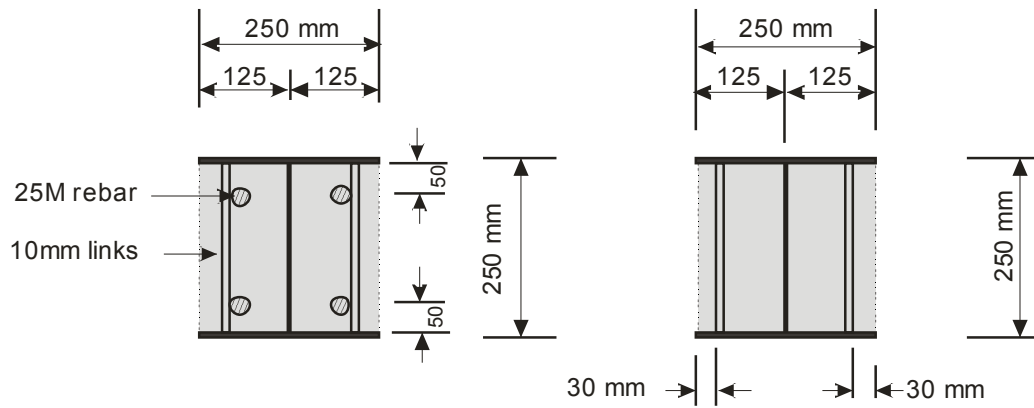


Figure 4.2: Cross-section of PEC columns with longitudinal rebar at the base (left) and without longitudinal rebar at other levels (right)

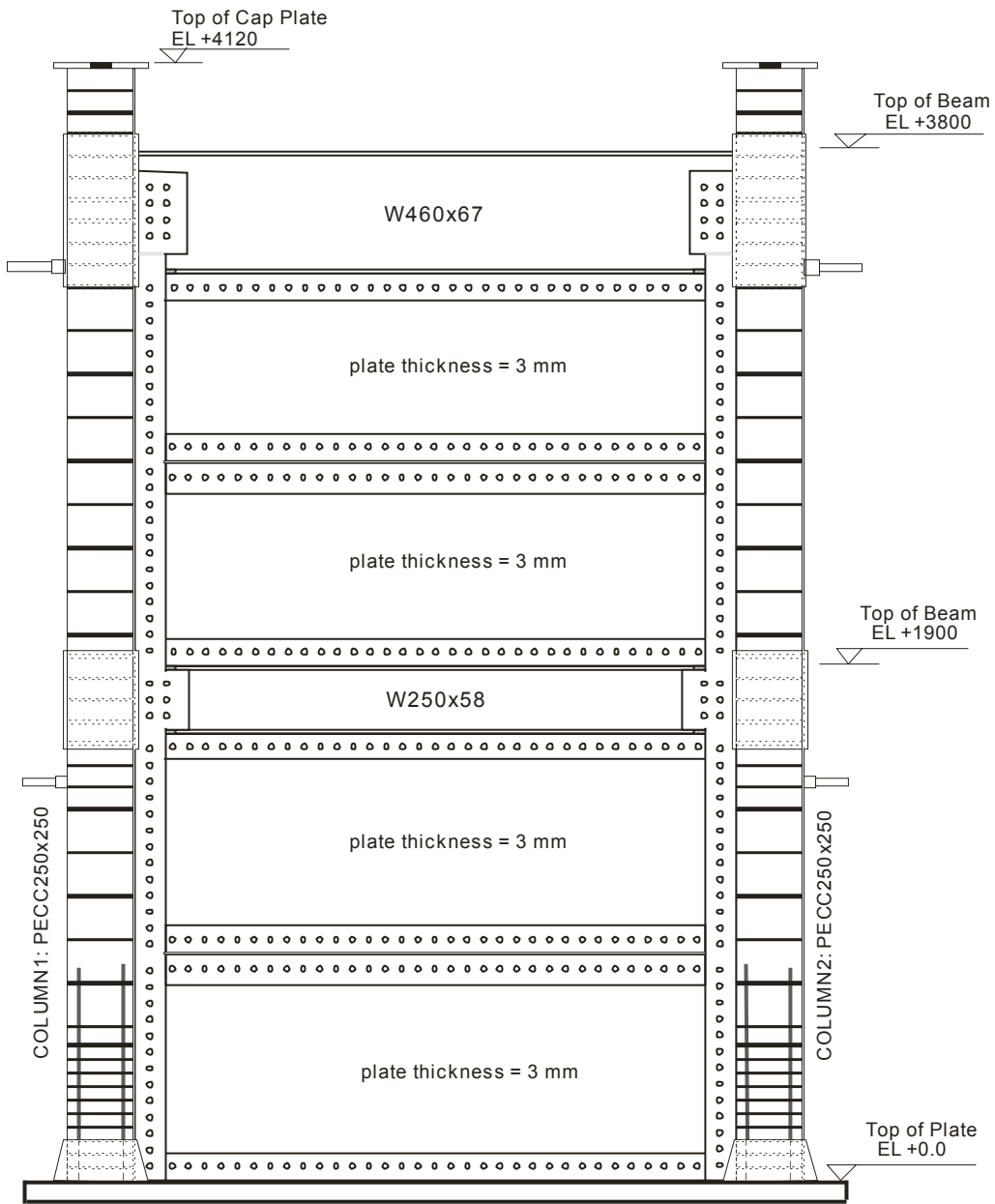


Figure 4.3: Modular steel plate shear wall test specimen



Figure 4.4: Additional fish plate in the first floor beam-to-column connection of the modular test specimen

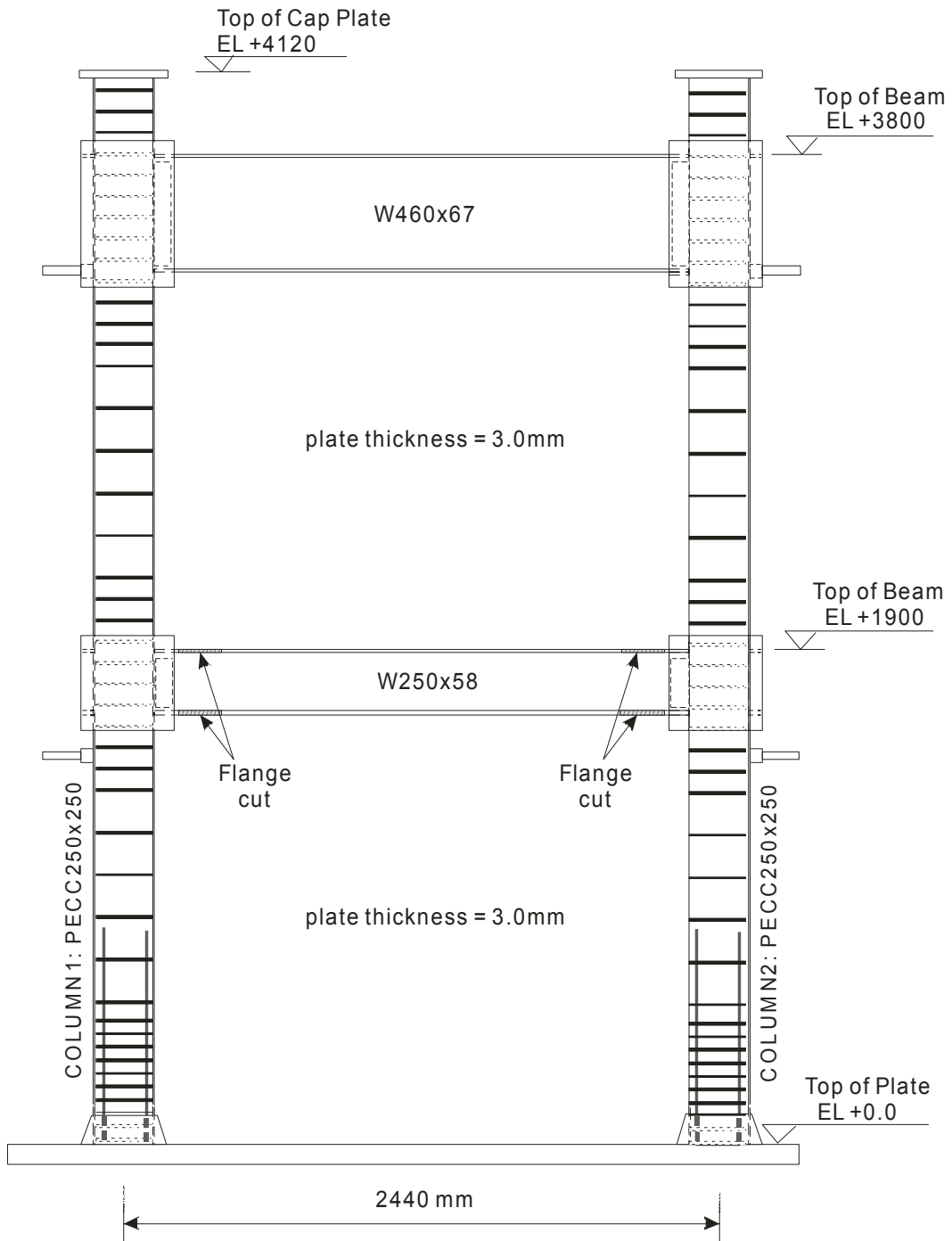


Figure 4.5: Steel plate shear wall test specimen with RBS connections in the first story

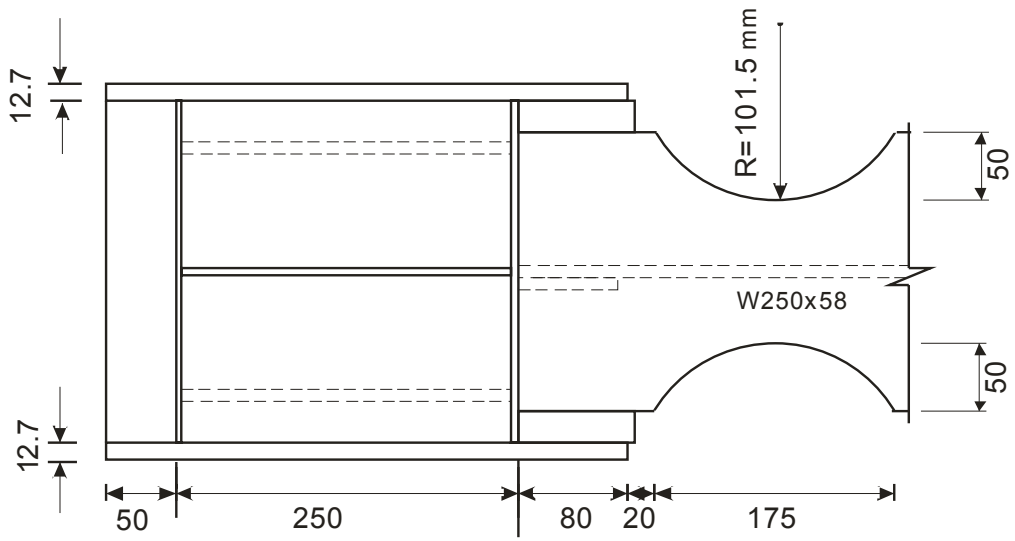


Figure 4.6: Detail of the first floor frame connection in the RBS specimen

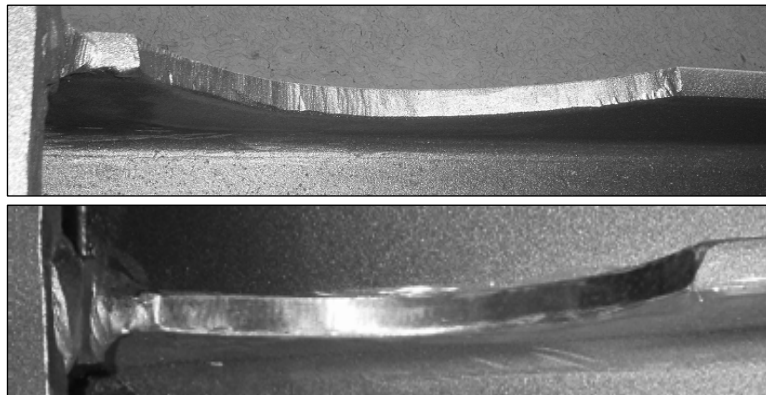


Figure 4.7: RBS cut surface condition; before grinding (top) and after grinding (bottom)

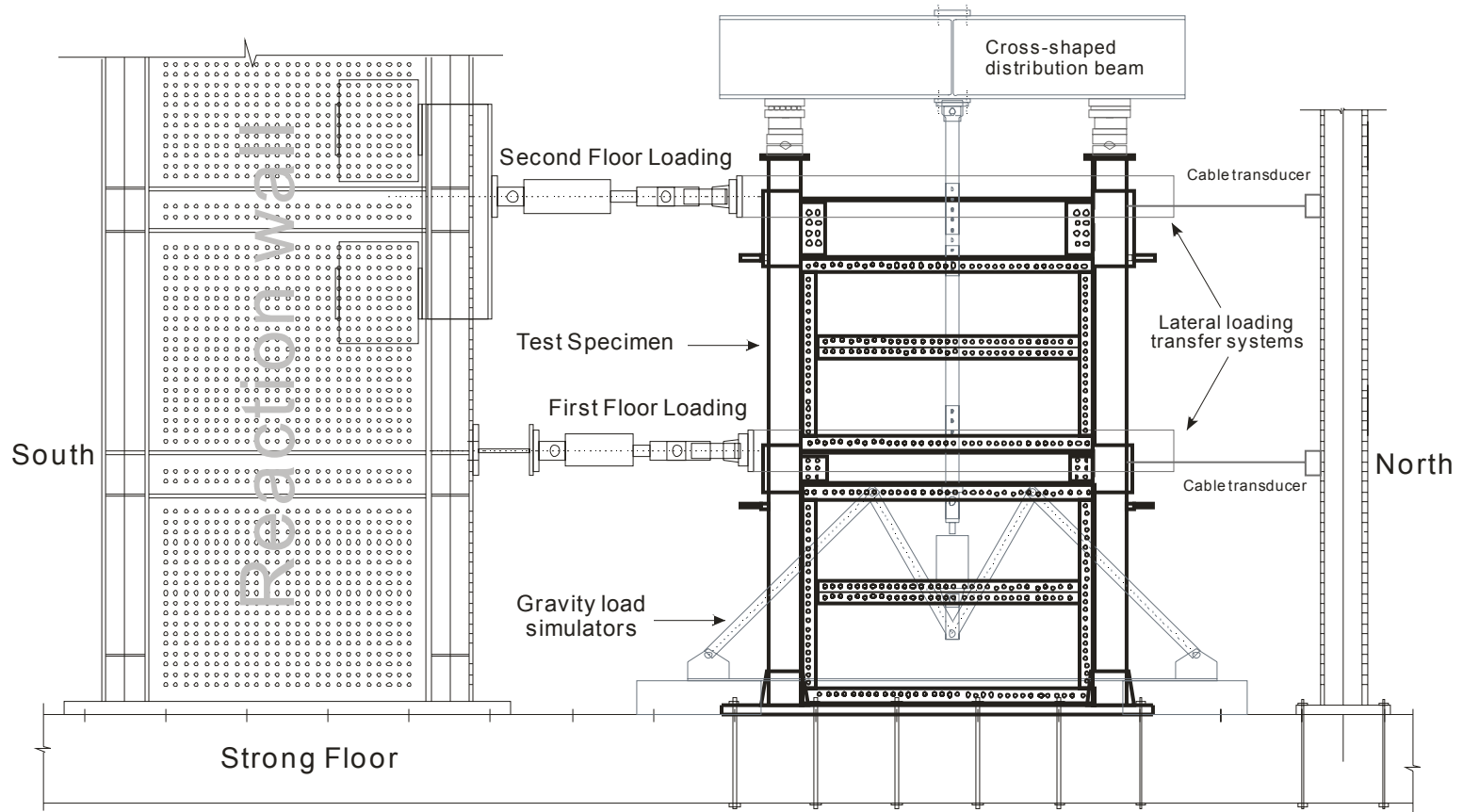


Figure 4.8: East elevation of the modular test set-up

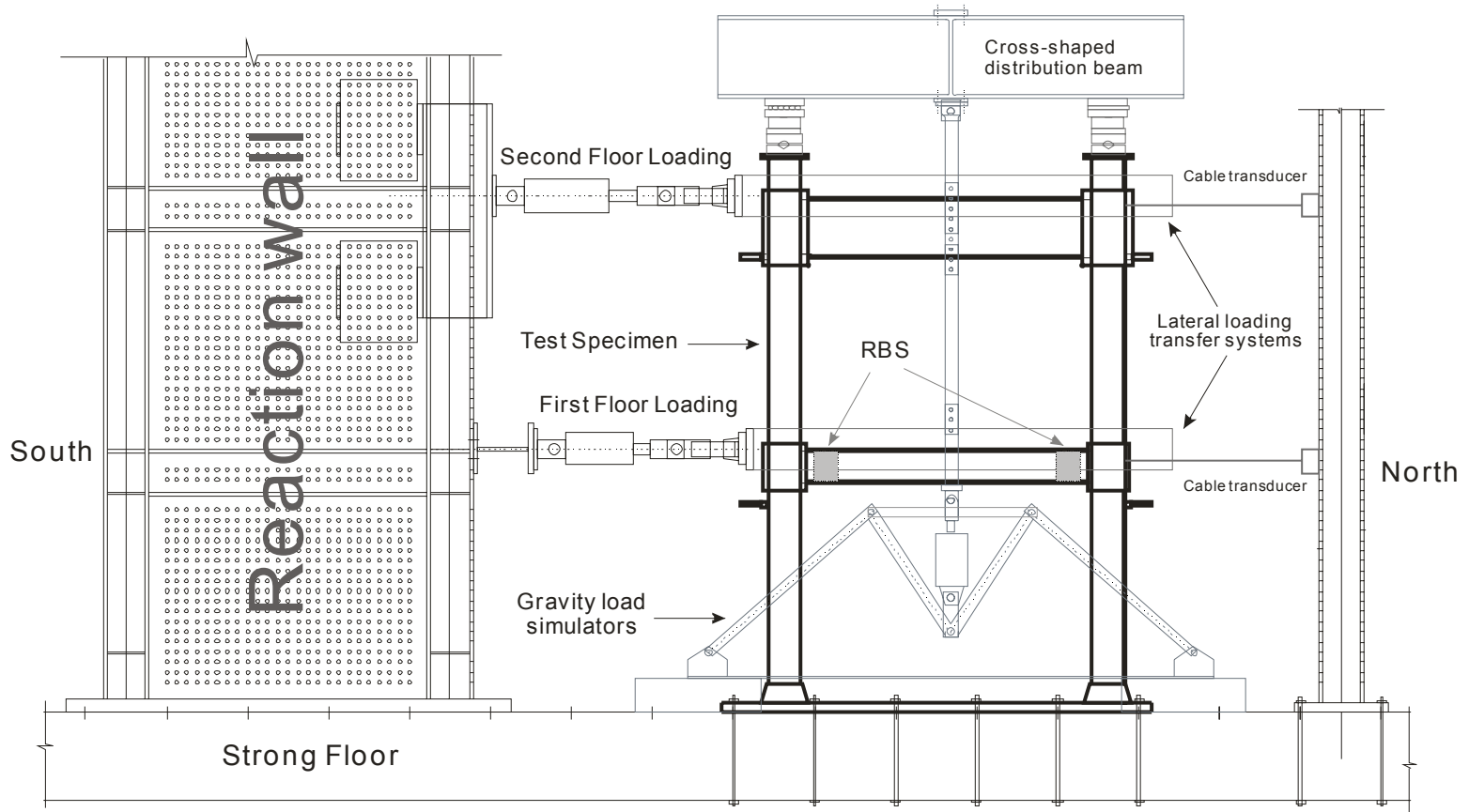


Figure 4.9: East elevation of the RBS test set-up

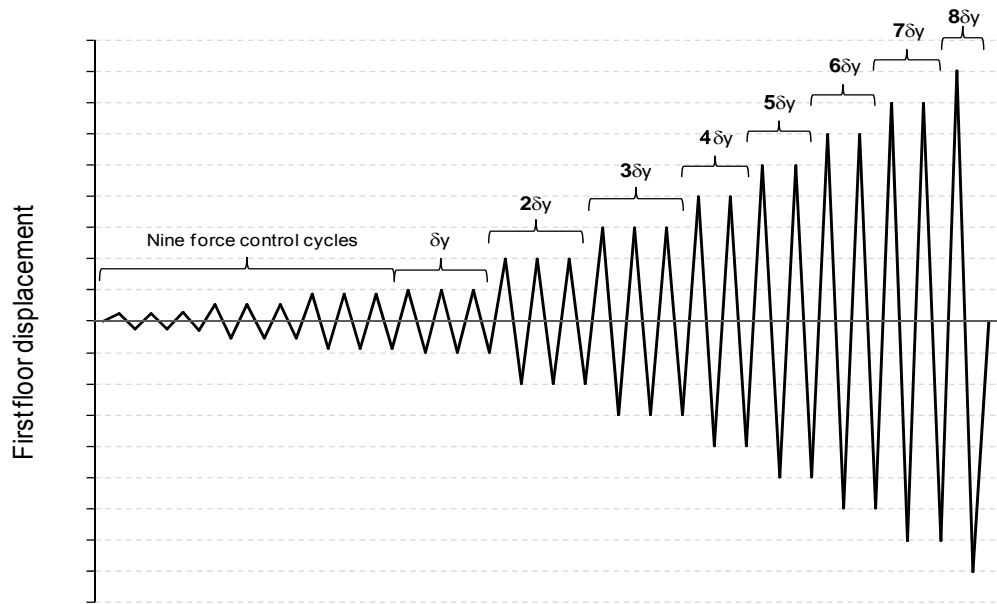


Figure 4.10: Applied cyclic lateral load history to the modular and RBS test specimens

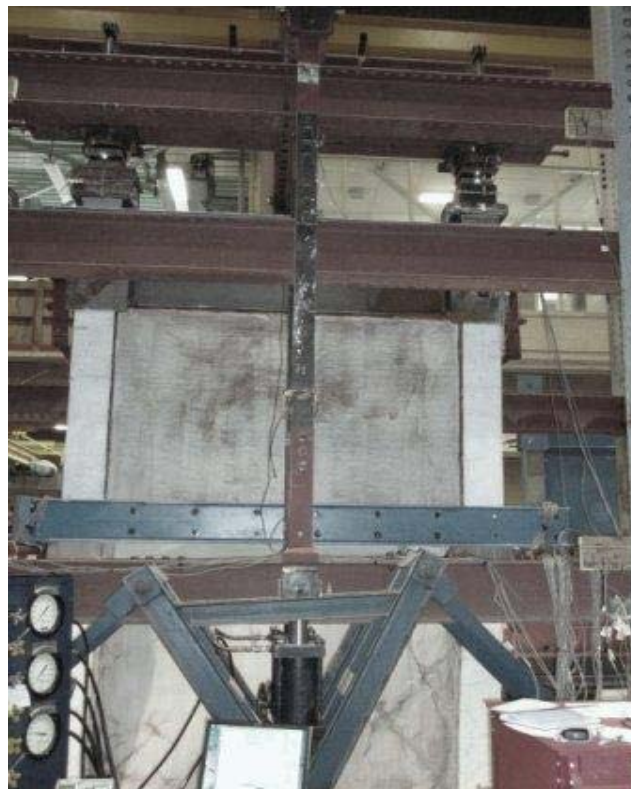
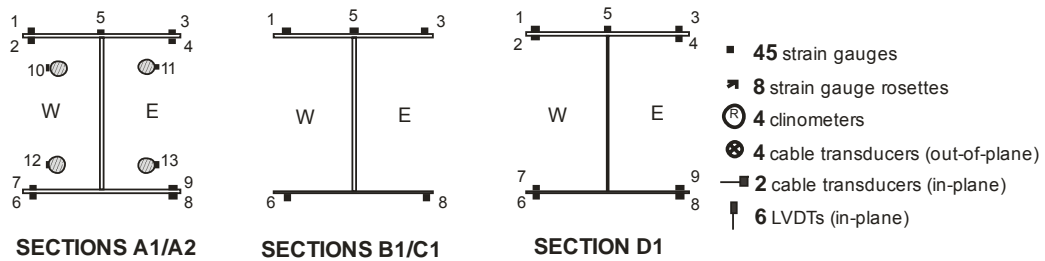
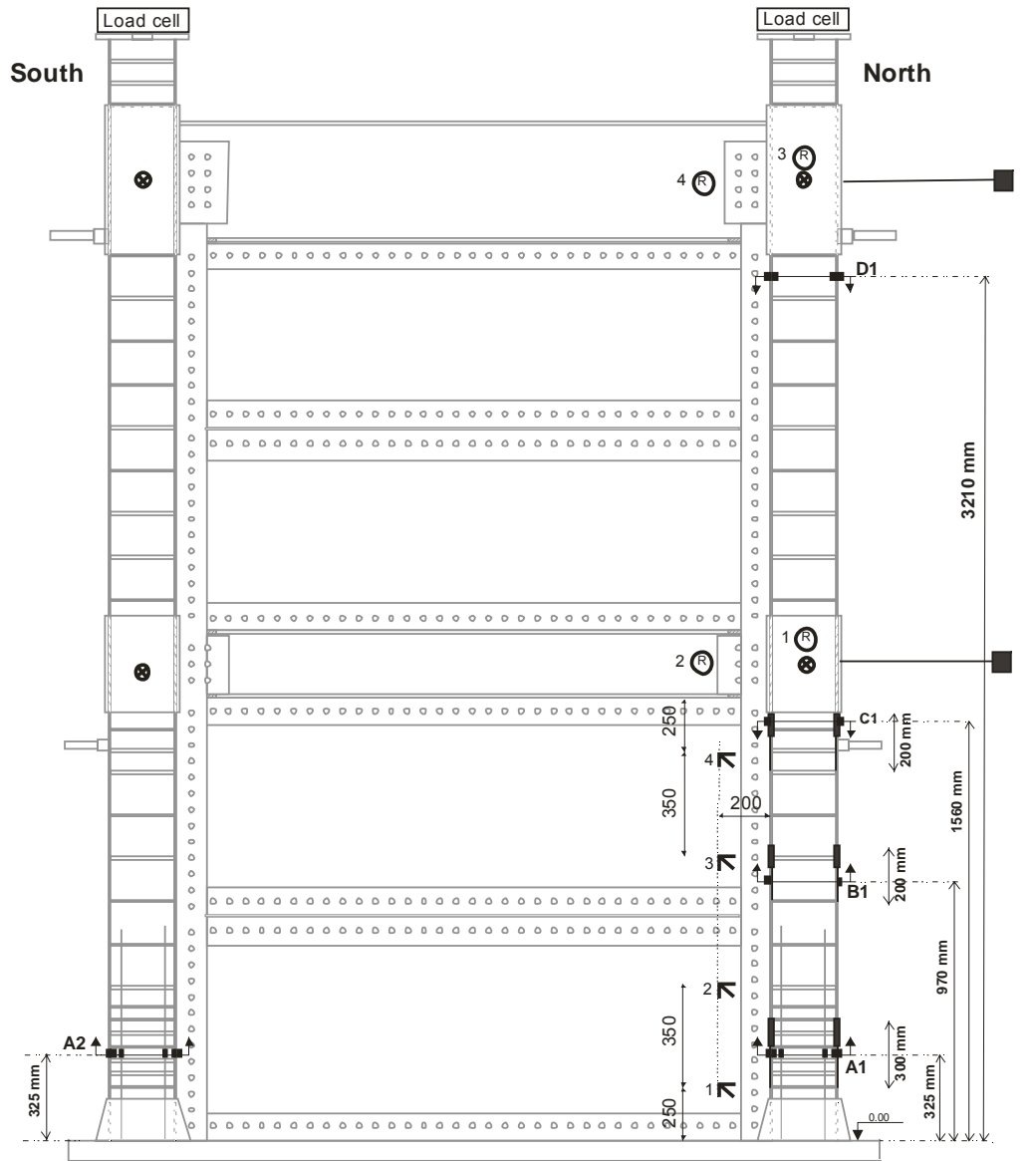
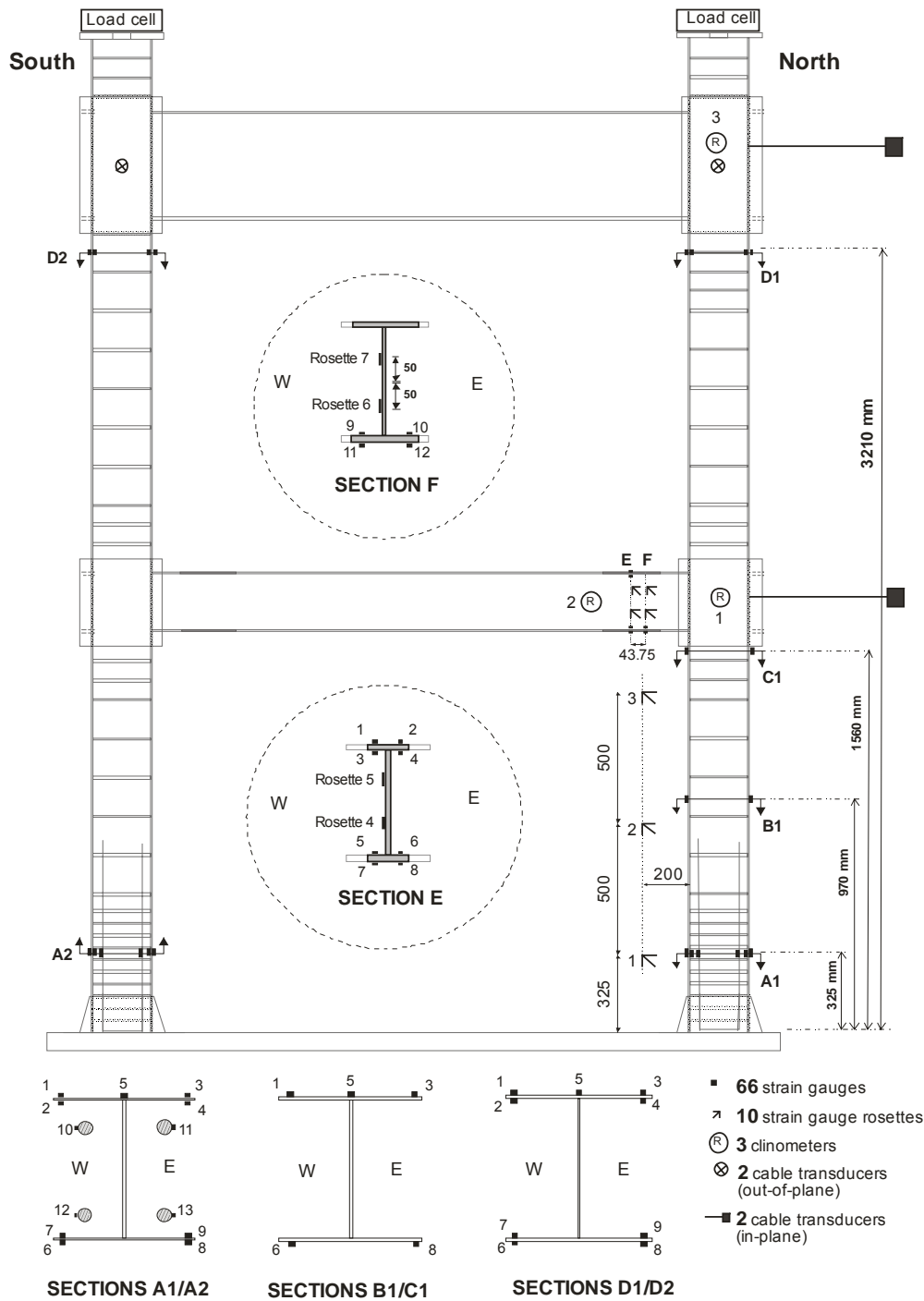


Figure 4.11: Gravity load application mechanism



Notes:
 - Strain gauges, which are close to the tip of the flanges of columns in sections A1, A2, B1, C1 and D1, are 15 mm away from the flange tips.

Figure 4.12: Instrumentation layout for the modular test specimen



Notes:

- Strain gauges, which are close to the tip of the flanges of columns in sections A1, A2, B1, C1, D1 and D2 are 15 mm away from the flange tips.
- Strain gauges, which are close to the tip of the flanges of the floor beam in sections E and F are 25 mm away from the flange tips.

Figure 4.13: Instrumentation layout for the RBS test specimen



Figure 4.14: One set of cameras, monitoring the concrete face of PEC column at base



Figure 4.15: Hand-made formwork clamps



Figure 4.16: Formwork before the first cast of concrete in columns



Figure 4.17: Second lift of the concrete cast in the PEC columns in the first story



Figure 4.18: Grouting of the remaining gap under the cap plate

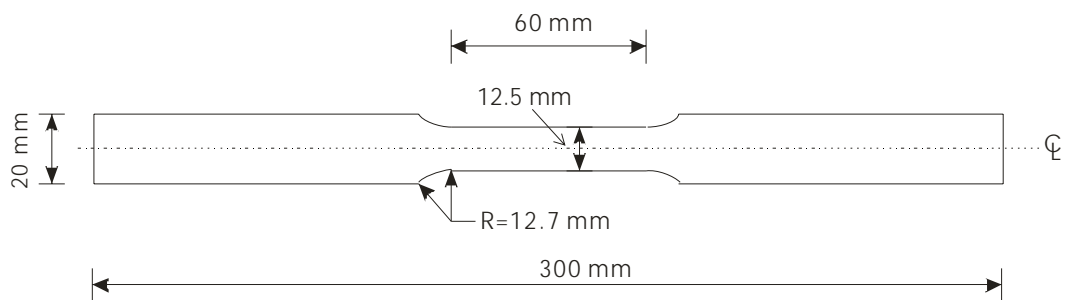


Figure 4.19: Dimensions of the tension coupons taken from plate material



Figure 4.20: Remaining material after the coupons were removed



Figure 4.21: Tension test of the coupons taken from the 25M rebar (left) and the column plate (right)



Figure 4.22: “Split and cone” type of failure of the concrete cylinder in compression test



Figure 4.23: The concrete split cylinder test to determine the tensile strength of concrete



Figure 4.24: Compression test to obtain the stress vs. strain material properties of the concrete cylinder

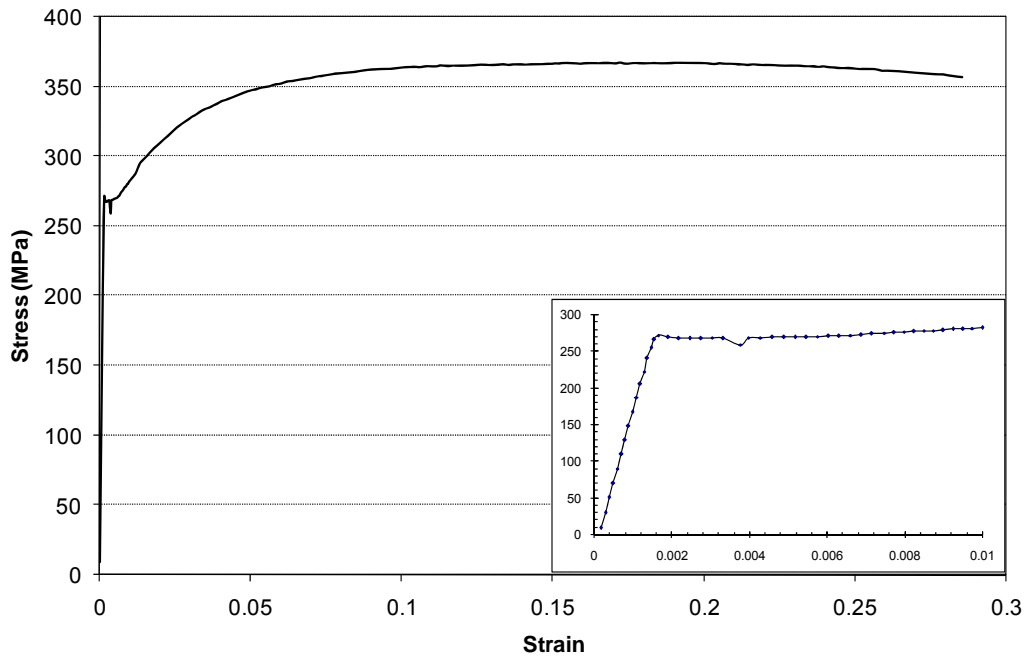


Figure 4.25: Typical stress vs. strain curve for the infill plates (coupon mark: PR1)

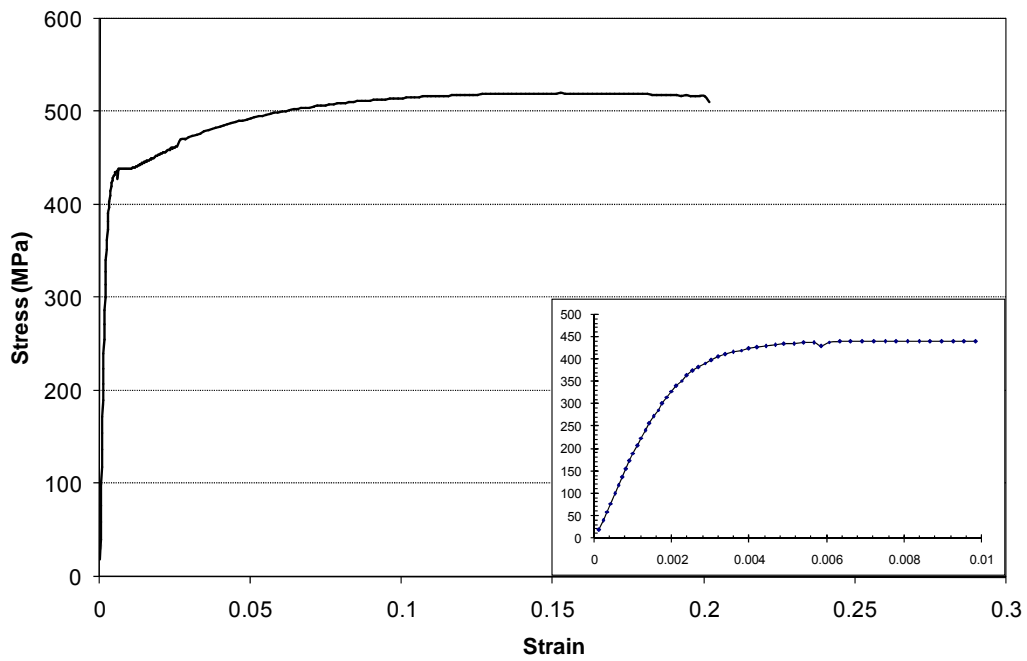


Figure 4.26: Typical stress vs. strain curve for the column plates (coupon mark: PAA1)

5. MODULAR STEEL PLATE SHEAR WALL TEST RESULTS

5.1 Introduction

In this chapter, the general behavior of the modular steel plate shear wall and the observations made during the test are discussed. The hysteretic loops of both stories are shown and the envelope of the hysteretic loops of the first story is discussed. The ductility of the specimen is evaluated at different load levels and the amount of the energy that was dissipated during the test is studied. Finally, strain data from critical zones are analyzed.

The maximum out-of-plane imperfection of the first story infill plate from the plane of the wall was 38 mm and was located close to the splice plate at the mid-height of the first story. The imperfection included one half-wave and, thus, was similar to the first mode of the plate buckling in shear, except that it was not diagonal. The flanges of the column had a maximum inward deformation of 2 mm between the links, which was due to the welding process.

The modular test took seven days to complete. A total of 27 cycles were performed and the specimen reached a peak load of $Q_{p1} = 1821$ kN when it was pushed to north (i.e., the first half of the cycle) and $Q_{p2} = -1891$ kN when it was pulled to south (i.e., the second half of the cycle). The specimen showed very good local and global performances during the test. There was no significant damage to the beam-to-column connections. All bolted connections performed well and no failure was detected in them. The columns at the base also performed well. The concrete crushing did not happen until the cycles with very high lateral displacement. The column flanges tore completely and extended into the web. No tearing or unzipping happened in any weld in the test specimen.

The specimen showed large ductility and good energy dissipation capacity. It also exhibited reliable post-peak behavior. All these observations demonstrate the ability of this system to resist extreme cyclic loading during earthquake.

5.2 General observations

5.2.1 Gravity load application

A constant 600 kN gravity load was applied at the top of each column throughout the test. The gravity load at the end of each cycle was controlled and, if necessary, adjusted. Because of the movement of the specimen, the gravity load was slightly less or more than 600 kN at the extreme displacements, depending on the direction of the lateral loading. The gravity load was removed at the end of each day of testing and reapplied at the beginning of the test on the next day.

During the gravity load application, no buckling was detected in the flanges of the columns. The infill plates had an initial out-of-plane displacement in both stories and so there was no buckling visible during the gravity load application. The concrete in the columns did not crack or crush which indicated essentially elastic behavior in this stage.

5.2.2 "Force control" cycles

Nine "force control" cycles were applied to the modular test specimen. In the first three cycles, in which the base shear reached $Q_p=300$ kN, the shape of the initial imperfection of the infill plate in the first story changed to the first mode of shear buckling (i.e., one diagonally oriented buckle wave). There was no detectable change in the shape of the initial imperfection of the infill plate in second story.

The first cracks in the concrete of the PEC columns were observed in the first story during cycles 4 to 6, in which the base shear reached $Q = 600$ kN. The location of the horizontal cracks indicated double-curvature deformation of column in the first story, as

they were located at the top and bottom of the column in the first story and adjacent to opposite flanges.

In cycles 7 to 9, in which the specimen experienced a base shear of $Q = 900$ kN, the infill plate of the first story buckled into two buckle waves (i.e., second mode of shear buckling) and in the second story, the infill plate buckled in the first mode (i.e., one buckle wave). The buckling of the infill plates was accompanied by several loud noises as the plate buckle waves popped through and reoriented during the load reversal. Similar noises were heard in all subsequent cycles. The cracks that initiated in cycles 4 to 6 propagated, and a few more cracks developed close and parallel to the previous cracks. The cracks were relatively horizontal adjacent to the steel flange and they became diagonal, with an approximate angle of inclination of 45 degrees, at the mid-depth of the column, which indicates the presence of high shear force in the columns at the base. Figure 5.1 shows the cracks in the concrete at the base of the north column in cycle 9. The beam-to-column connections at the first floor rotated very little, imposing a double curvature deformation to the columns in the first story. The cracks in the concrete also indicated the double curvature deformation of the columns. No rotation was detected in the frame connections in the second floor.

5.2.3 “Displacement control” cycles

In cycles 10 to 12, the yielding displacement ($\delta_y = 8.5$ mm) was reached in the first floor in both directions. The specimen experienced maximum base shears of $Q_1 = 1118$ kN (61% of Q_{p1}) when it was pushed to the north and $Q_2 = -1140$ kN (60% of Q_{p2}) when it was pulled to the south. In these cycles, the columns continued deforming in double curvature. Some new cracks in the concrete were seen on the tension side of the columns at the top and bottom of the columns in the first story. Yet, no significant rotation was detected in the beam-to-column connections. The infill plate of the first story buckled in three waves in both directions, while the infill plate of the second story buckled in two waves. When the specimen was close to the extreme displacements in cycles 10 to 12,

frequent slight noises were heard from the fasteners of the splice plate in the first story and in the perimeter of the infill plate due to the slippage of these connections. The whitewash on the infill plate of the first story started to flake off, which was an indication of the yielding of the infill plate. The second floor displacements were +14 mm and -13 mm in the first second halves of cycle 12, respectively.

In cycles 13 to 15, the imposed first floor displacement was twice the yielding displacement ($\delta = 2\delta_y = \pm 17$ mm). The maximum base shear in the first half of these cycles was $Q_1 = 1490$ kN (82% of Q_{p1}) and in second half it was $Q_2 = -1505$ kN (80% of Q_{p2}). In the first half of cycle 13, when the first floor displacement was $\delta_1 = 13.5$ mm and the base shear was $Q_1 = 1375$ kN (76% of Q_{p1}), the beam-to-column connections slipped with a very loud noise, mainly from the second floor connections. The infill plates adjacent to the compression side of the frame connections folded and clear signs of rotation were observed (see Figure 5.2). In the second half of cycle 13, at a displacement of $\delta_2 = -15.9$ mm and a base shear of $Q_2 = -1502$ kN (79% of Q_{p2}), another loud noise was heard due to the slippage of the frame connection in the opposite direction. At the end of the longitudinal column rebars, close to mid-height of the first story, several horizontal cracks (flexural-type) were observed. New diagonal cracks formed close to the bases of the columns in the expected locations of hinge formation. The infill plates buckled in five and three buckle waves in the first and second stories, respectively. Based on the observations in this cycle, it was concluded that significant yielding happened during this cycle. This issue is further discussed later in this chapter. In cycles 14 and 15, similar observations were reported except that instead of one loud noise, several slighter noises were heard, which indicated that the frame connections slipped several times instead of one big slippage. Several yield lines were visible on the infill plate of the first story. Figure 5.3 shows the infill plate of the first story in cycle 15. The second floor displacements were +29 mm and -23.7 mm in the first and second halves of cycle 15, respectively. These displacements are almost twice the readings in cycle 12.

The first signs of the local buckling of the column flanges were observed during cycle 16 ($\bar{\delta} = 3\bar{\delta}_y = \pm 25.5$ mm). In this cycle, the base shear in the first half of the cycle reached $Q_1 = 1694$ kN (93% of Q_{p1}) and in the second half, the base shear was $Q_2 = -1728$ kN (91% of Q_{p2}). In the second half of this cycle, the outer flange of the south column buckled locally in four locations. The buckling of the flange occurred in mid-height of the columns in the first story at the end of the longitudinal rebars, and the measured rise of the tip of the flange was 2 mm. Due to the discontinuity of the longitudinal rebars, there was a sudden change of stiffness in that location and the link spacing was also the biggest (160 mm). In cycles 16 to 18, the infill plates buckled with one more buckle wave compared to cycles 13 to 15. The outer flange of the north column buckled locally close to mid-height of the column. The tearing of the outer flanges of the columns at the base started in cycle 17. The tears started at the flange tips adjacent to the tops of the side plates at the base of columns. During cycle 18, the infill plate in the first story started to tear in the top north corner. The tear was due to low cycle fatigue as the infill plate experienced cyclic kinking in that region in load reversals during previous cycles. The diagonal cracks in the concrete became more pronounced close to the base of columns. Figure 5.4 shows the bottom half of the south column in the first story during cycle 17. The local buckling of the outer flange can also be seen in this figure. The second floor displacements in cycle 18 (+43.8 mm in the first half and -34.9 mm in the second half) were almost three times the readings in cycle 12.

Starting from cycle 19, the first cycle in which the first floor displacement reached $\bar{\delta} = 4\bar{\delta}_y = \pm 34$ mm, each displacement stage consisted of two cycles only. In cycle 19, the base shear reached $Q_1 = 1773$ kN (97% of Q_{p1}) in the first half and $Q_2 = -1828$ kN (97% of Q_{p2}) in the second half of the cycle. During this cycle, the flange tears in both columns propagated to a total (west plus east flange tears) length of approximately 45 mm. The infill plates buckled with more buckle waves and more crack propagation was observed at the base of columns. The outer flanges of columns buckled locally at the mid-height of the first story, with rises of around 3 mm. The maximum tear opening in the infill plate of

the first story (with the specimen under load) was 3 mm, with a length of 21 mm. In cycle 20, the outer flange of the north column buckled locally at the base, as shown in Figure 5.5, and the surface of the adjacent concrete crushed and spalled. The outer flanges of the columns buckled between the side plates at the base of the columns, where their flange tips were welded to the side plates, which indicated large compressive stresses in the flanges (see Figure 5.6). The combined length of the tears propagating from the two opposite flange tips in cycle 20 reached 77 mm in the south column and 65 mm in the north column (i.e., just under 30% of the total flange width). The fish plates in the first floor frame connections showed signs of lateral movement due to the compressive force in the beam. In cycle 20, the second floor displacements were +59 mm and -46.8 mm.

The test specimen reached its peak strength in cycle 21, in which the displacement of the first floor was $\delta = 5\delta_y = \pm 42.5$ mm. The base shears of $Q_1 = Q_{p1} = 1821$ kN in the first half and $Q_2 = Q_{p2} = -1891$ kN in the second half were attained in this cycle. The infill plates buckled in six buckle waves in both stories. The length of the tear in the infill plate increased to 50 mm, with a maximum opening of 8 mm. New diagonal cracks in the concrete developed and the concrete crushed on the compression side of the columns close to the bases. The total flange tear lengths in the south and north columns reached 135 mm (54% of the flange width) and 110 mm (44% of the flange width), respectively. The openings of the tears in the tips of the flanges of the south and north columns were 8 mm and 7 mm, respectively, when that flange was in tension.

In cycle 22, the same first floor displacement as cycle 21 was applied to the specimen. A new tear, with a length of 20 mm and an opening of 4 mm, was detected in the top south corner of the infill plate in the first story. The flange tears of the columns developed to 65% and 56% of the flange width of the south and north columns, respectively. The rise of the flange tip at the location of the local buckling was around 5 mm. In order to make sure that the base plate movement would remain negligible during the test, two dial

gauges were used. The readings from these dial gauges showed a movement of less than 0.5 mm from the extreme negative displacement in cycle 21 to the extreme positive displacement of cycle 22. The second floor experienced a displacement of +73 mm and -60.3 mm in this cycle.

In cycles 23 and 24, the test specimen experienced a first floor displacement of $\delta = 6\delta_y = \pm 51$ mm. Base shears of $Q_1 = 1778$ kN (98% of Q_{p1}) and $Q_2 = -1845$ kN (98% of Q_{p2}) were attained in the first and second halves of cycle 23. The total length of the tears in the flanges of columns reached 222 mm (89% of the flange width) and 190 mm (76% of the flange width) in south column and north column, respectively. Another tear started in the bottom north corner of the infill plate in the first story. The column flanges tore completely in cycle 24 and the opening of the tears was 10 mm. In Figure 5.7, which shows the outer flange of the south column at the base in cycle 24, the end of the tears in each associated cycle is marked. The concrete started to crush more and spall from the compression side of the columns at the base. The rise of the flange tips, in some locations where local buckling happened, reached 8 mm. A new tear was detected close to the center of the infill plate in the first story, with a length of 24 mm and an opening of 2 mm. The length of tears in the top north corner and top south corner of the infill plate of the first story increased to 134 mm and 60 mm, respectively. As a result of all these damage locations, the maximum attained base shears were reduced slightly from the peak value to $Q_1 = 1677$ kN (92% of Q_{p1}) and $Q_2 = -1675$ kN (89% of Q_{p2}) in the first and second halves of this cycle, with second floor displacements of +85.5 mm and -71.6 mm.

In cycles 25 and 26, in which the first floor displacement reached $\delta = 7\delta_y = \pm 59.5$ mm, the tears further developed in the webs of the columns. The opening of the tears in the flanges were 15 mm and 17 mm in the south and north columns, respectively. Several new tears were detected in the infill plate of the first story. Concrete started to crush and spall out of the columns close to the end of the longitudinal rebars. This observation indicates that the region where the rebars are terminated should have closer links to

postpone local buckling and the resultant crushing of concrete. In cycle 26, base shears of $Q_1 = 1580$ kN (87% of Q_{p1}) and $Q_2 = -1581$ kN (84% of Q_{p2}) were attained in the first and second halves of the cycle. The second floor displacements were +97.4 mm and -83.2 mm in cycle 26.

The test was completed with cycle 27, in which the first floor displacement reached $\delta = 8\delta_y = \pm 68$ mm. Base shears of $Q_1 = 1614$ kN (89% of Q_{p1}) and $Q_2 = -1595$ kN (84% of Q_{p2}) were attained in the first and second halves of this cycle. The second floor displacements were +109.2 mm and -94 mm in the last cycle. The test was terminated at this point as the columns of the first story were damaged both at mid-height and at the base, and the tears in the infill plate started to lengthen rapidly. Figure 5.8 shows the first story of the test specimen at the end of the test. The locations of the tears in the infill plate of the first story are depicted in Figure 5.9. Other than the first story infill plate and the bases of the columns, no tearing was observed. Of particular note, no tearing occurred in the infill plate connections or the fish plates at the beam-to-column connection locations. During the test, no cracking in concrete of columns in the second story was observed and the flanges of column did not show any sign of local buckling in the second story.

5.3 Hysteretic behavior

5.3.1 Hysteretic loops of the first and second stories

The controlling parameter during the displacement control stage of the test was the first story deflection (i.e., the displacement of the first floor beam). In Figure 5.10, the base shear versus the first story deflection is plotted. The base shear versus the second floor displacement (i.e., the displacement of the floor beam in the second story, which is the summation of the individual deflections of the first and second stories) plot is shown in Figure 5.11. To have a better understanding of the behavior of the second story of the specimen, the shear force in the second story is plotted versus the second story

deflection (i.e., the difference between the second floor beam displacement and the first floor beam displacement) in Figure 5.12.

All the hysteretic loops in Figures 5.10 to 5.12 show similar characteristics to those in previous tests on unstiffened steel plate shear walls. In the first few cycles, the specimen behaved elastically with a very high stiffness. As some parts of the specimen started to yield and concrete began to crack, the stiffness of the specimen started to decrease in some stages of the cycles. By increasing the lateral displacement, the curves started to show the well-known pinched shape.

In Figure 5.13, the base shear vs. first story deflection curves from cycles 17 ($\delta = 3\delta_y$) and 27 ($\delta = 8\delta_y$) are shown. The segment a-b has the smallest slope, which is mainly because the tension field developed in the previous cycle is released and because of the permanent plastic deformation of the infill plate, the frame must pass this segment (a-b) for the tension field to reorient in the other direction. During this part, the infill plate is not very effective and most of the stiffness is provided by the frame itself. The slope of the segment a-b in cycles 17 and 27 are obtained as 35 kN/mm and 8 kN/mm, respectively. During the segment b-c, the tension field redevelops and the stiffness increases accordingly. The stiffnesses in this segment of the curves are 75 kN/mm and 40 kN/mm in cycles 17 and 27, respectively. In segment c-d, as the load approaches the maximum load achieved in the cycle, some parts of specimen yield or crack, which gradually decrease the stiffness of the specimen. The segment d-a' represents the load removal and its slope is relatively close to, but less than, the initial stiffness of the specimen. The slope of this part of the curve is 165 kN/mm in cycle 17 and 130 kN/mm in cycle 27. Curve a'-b'-c'-d'-a represents reloading and unloading in the opposite direction and the same behavior repeats.

5.3.2 *Rotation of the frame connections*

Four clinometers were used on the north side of the specimen to monitor rotations at the frame connections in the first and second floors. Clinometer 1 was attached to the side plate of the column in the first floor and clinometer 2 was attached to the north end of the first floor beam. The readings of these two clinometers are plotted in Figure 5.14. Both clinometers were mounted on the east side of the specimen, so a positive reading represents a clockwise rotation and a negative reading represents a counter-clockwise rotation. As shown in Figure 5.14, the side plate rotated both ways during the test and the maximum total rotation in cycle 27 was more than 3 degrees. Conversely, the total rotation of the end of the floor beam was relatively small (less than -0.5 degrees in cycle 27) and always counter-clockwise, as the anchored tension field in the first story was always bigger than that of the second story causing the first floor beam to deflect downward regardless of the direction of the lateral load application. The resulting rotation in the beam-to-column connection in the first floor (i.e., relative rotation of the adjacent clinometers) is depicted in Figure 5.15. The maximum total rotation of the connection in the first floor was 3 degrees in cycle 27.

The readings of clinometers 3 and 4, which were respectively attached to the side plate of the column and the north end of the floor beam in the second floor, are plotted in Figure 5.16. Up to cycle 13, the column and the end of the beam had relatively the same rotation, but a sudden counter-clockwise rotation at the end of the beam happened in cycle 13 and because of the tension field in the second story, the floor beam deformed downward, resulting in the counter-clockwise rotation of the end of the beam. The maximum absolute rotation of the end of the beam was close to -3.0 degrees in cycle 27. The beam-to-column connection rotation in the second floor is shown in Figure 5.17, which shows a maximum rotation of 3.5 degrees in cycle 27. According to the strain readings from the strain gauge rosettes on the infill plate of the first story, the sudden rotations of the frame connections in cycle 13 caused a relatively uniform yielding pattern

to develop in the infill plate of the first story, and significant yielding in all critical areas happened right after this point.

5.4 Energy dissipation capacity, stiffness and ductility

During 15 cycles, out of the total of 27 cycles that were applied to the specimen, the specimen experienced significant yielding, which is greater than the number of inelastic cycles that would be expected to occur in a typical earthquake event. Almost all the energy dissipation happened in these cycles and the displacement ductility of the specimen was dependent on these cycles.

5.4.1 Energy dissipation capacity

The enclosed area of each hysteretic loop is a measure of the amount of dissipated energy through the associated cycle. The hysteretic loops resulting from the modular test were fairly wide, which indicates the ability of the system to absorb and dissipate a large amount of energy during an earthquake. The energy was mainly dissipated by yielding of the steel parts and crushing of the concrete. In order to assess the performance of the modular test specimen quantitatively, the amount of dissipated energy in each story during each cycle is shown in Figure 5.18. The majority of the energy was absorbed and dissipated in the first story, as the force and deflections were more than in the second story. Also, most of the damage happened in the first story. As can be seen in Figure 5.18, the amount of energy dissipated in the first story had sudden increases in cycles 7 and 10. These jumps are related to the beam-to-column connection rotations at the first floor level, as shown in Figure 5.15. The amount of energy dissipated in the second story was negligible up to cycle 13, where the second floor frame connection rotated. There was a sudden increase in the amount of energy dissipated in both the first and second stories in cycle 13 as the tension field developed in the second story and the tension field in the first story became more uniform. This observation endorses the notion that frame connection rotations affect the ability of the infill plates to develop tension

fields in all stories of a multi-story building. The amount of energy dissipated in the first cycle of each stage of displacement was larger compared to subsequent cycles of that stage, which was mainly because most of the damage (i.e., tearing of steel, cracking and crushing of concrete) happened in these cycles where the specimen experienced larger deformations for the first time. In Figure 5.19, the total amount of energy dissipated in the specimen is plotted vs. the first floor displacement. At point A, the slope of the curve shows a sudden increase due to the rotation of the frame connections, increasing the deformations and yielding in the system. The second sudden change of slope happened at point B, where more than 50 percent of the column outer flange tore and caused a reduction in the slope of the curve. At point C, the outer flange of the columns tore completely and the longitudinal rebars at the bases of the columns carried all the tensile force in the columns. As shown in this figure, no decrease in the energy dissipation capacity of the specimen was observed despite all the tears, cracks and crushes. This demonstrates that the system was highly redundant and capable of changing the load transfer routes.

5.4.2 Stiffness and ductility

Besides the large energy dissipation capacity, large initial stiffness and displacement ductility are two important characteristics of any efficient lateral load resisting system. High initial stiffness is very important to minimize story drifts under service loads and wind load, which occurs more frequently compared to earthquake loading. A high displacement ductility enables the system to undergo large nonlinear deformations without significant strength degradation, which leads to more energy absorption in the lateral load resisting system.

In order to further study the performance of the first story during the modular test and define its stiffness and ductility, the envelope of the corresponding hysteretic loops with positive deformations and base shear values is shown in Figure 5.20. The initial stiffness of the first story of the specimen during the elastic cycles (i.e., up to a base shear of

900 kN) was 180 kN/mm. During cycle 13, significant yielding was observed in the critical regions of the specimen, designated as protected zones in the Canadian steel design standard (CSA 2009), when the base shear reached $Q = 1400$ kN. The strain gauges affixed to the outer flanges of the columns at the base (i.e., sections A1 and A2, as shown in Figure 4.12) showed complete yielding of the flanges and the data from strain gauge rosettes on the infill plate of the first story showed yielding at all four levels, which indicates uniform yielding of the whole infill plate of the first story. The value of the yielding displacement (i.e., first story deformation) was calculated according to the method outlined in ATC-24 (ATC 1992) and it was defined as 10 mm.

To define the displacement ductility, R , of the modular specimen, Equation (2.42) was used at the peak base shear and in the post-peak phase. The first story deformation at the peak base shear ($Q_{p1} = 1821$ kN) was 42.5 mm, which leads to a displacement ductility of $R = 4.25$. The displacement ductility at 90 percent of the peak base shear in the post-peak phase ($Q_{0.9p1} = 1639$ kN), where the first story deformation was 65 mm, is $R = 6.5$. As the dissipated energy capacity did not decrease in the last cycle, the displacement ductility could be more than 6.5.

5.5 Strain gauge data

A total of five column cross-sections were monitored using strain gauges to study the behavior of the columns. Out of these sections, one was on south column (A2) and the main purpose was to confirm the readings from section A1 on the north column, which was located at the same level. The strain readings at section A2 were very close to those at section A1; thus, in this part just the behavior of the north column is discussed.

At the beginning of the test, a gravity load of 600 kN was applied at the tops of the columns. The strain readings at section A1 (the section located at 325 mm above the base plate) showed that the average strain in the H-shaped steel part was $-217 \mu\epsilon$. The average strain in the longitudinal rebars was $-224 \mu\epsilon$. These results indicate that the

axial load was uniformly distributed in that section. The cross-sectional area of the H-shaped steel part was 4682 mm^2 and the modulus of elasticity of the column plates parallel to the rolling direction, as shown in Table 4.3, was 191,200 MPa; thus, the resulting axial force in the H-shaped steel part, due to the applied gravity load, was approximately 195 kN. This indicates that close to 33 percent of the gravity load was carried by this part of the section. The four longitudinal rebars carried almost 75 kN in total. As mentioned in Table 4.5, the modulus of elasticity of the concrete in the first story was 23,800 MPa. As the area of the concrete in section A1 was $55,818 \text{ mm}^2$ and by assuming complete bond between the concrete and the longitudinal rebars, the axial load in the concrete part of the section was almost 300 kN. The concrete in the column was partially confined, which means that the actual axial load in the concrete part would be slightly higher than the calculated value.

The average strain in the steel part of section D1 (located at the top of the north column, under the side plate at the second floor) was $-380 \mu\epsilon$. The resulting axial force in the steel part of the section was therefore approximately 340 kN. The reason that the strains in the steel part were higher at section D1 compared to section A1 is that no rebars were present at the top of the column and the gravity load was transferred through a steel cap plate welded to the steel part. The transfer of force to the contiguous concrete may have been somewhat less efficient, depending on the effectiveness of the grouting operation.

The curvature of the north column at sections A1, B1, C1 and D1 for the maximum positive base shears during cycles 1 to 13 was calculated using the strain readings in these sections and are plotted in Figure 5.21. As a significant connection rotation happened during cycle 13, the curvature of the north column was also calculated just before and just after this rotation, and cycle numbers of 13a and 13b, respectively, are assigned to them. Up to cycle 13, the curvature of the column in sections A1 and C1 was approximately equal but opposite, which proves that the column deformed in double curvature resulting in concrete cracks adjacent to opposite flanges at the top and bottom

of the column in the first story of the specimen. The curvature at section B1, located 970 mm above the base plate, had values intermediate to those at sections A1 and C1 throughout these cycles, as expected. As the frame connections rotated substantially during cycle 13, the curvature of the column decreased significantly at section C1 and slightly at section A1 from cycle 13a to 13b. The connection rotation did not affect the curvature at section B1 significantly. The curvature at section D1 remained small for the first 13 cycles of the test, as seen in Figure 5.21.

The location of the neutral axis at section A1 was calculated to determine the cycles in which the concrete part of the section was in tension for the first time. When the base shear reached -276 kN in cycle 1, the neutral axis entered into the concrete part of the section from the north. During cycle 4, the concrete adjacent to the north flange reached its tensile strength and started to crack at a base shear of approximately -370 kN. The neutral axis entered into the concrete part of section A1 from the south during cycle 16, when the base shear reached $+1528$ kN, and the concrete reached its tensile strength in the same cycle (i.e., cycle 16) when the base shear was close to $+1620$ kN.

To study the local buckling behavior of the flanges of the column, sections A1 and D1 were considered. The strain readings from the strain gauges close to the tip of the outer flange on the west side were plotted to define the cycle in which the local buckling started. The strain gauge number for the one on the outside of the flange is "01", and "02" is the inside one, as can be seen in Figure 4.12. In order to simplify the diagram and neglect the local strain fluctuations due to the cyclic nature of the loading regime, sixth-order polynomial trend lines of the curves are plotted. Figure 5.22 shows the strain readings at section A1, where the flange of the column showed no sign of local buckling up to cycle 13. From cycles 13 to 21, the strain readings from the two faces of flange started to diverge, which indicates the initiation of local buckling. The difference increased gradually as the applied lateral load increased. After cycle 21, where the specimen reached its maximum strength, the difference between the strain readings from

the two sides of the flange started to increase dramatically. Figure 5.23 shows the strain readings at sections D1. Like the treatment in Figure 5.22, sixth-order polynomial trend lines of the curves were used in Figure 5.23. At this section, the difference between the strain readings did not change during the test, which confirms that no local buckling occurred at this section during the test.

A total of eight strain gauge rosettes were used to monitor the strains in the infill plate of the first story at four elevations (as shown in Figure 4.12). Rosettes on both sides of the infill plate permit the state of strain to be determined at the mid-surface of the plate. The infill plate did not yield in the first three cycles. During cycle 4, the infill plate yielded at location 1, which was located 250 mm above the base plate. In cycle 7, in which the base shear was $Q = 900$ kN, the infill plate was still elastic at locations 2 to 4. The angle of inclination of the tension field from vertical was 45 degrees at locations 2 and 3, while it was 33 degrees at location 4. Location 4 was close to the frame connection and because of the very limited rotation of the frame connection at this point in the test, the infill plate was affected by the gravity load in the column. The maximum principal strain at location 4 was $580 \mu\epsilon$. The infill plate yielded at locations 2 and 3 during cycle 10, in which $\delta = \delta_y = 8.5$ mm, but at location 4 the infill plate remained elastic (with a maximum principal strain of $630 \mu\epsilon$) and the angle of inclination of the tension field did not change compared to cycle 7. In cycle 13, during which the frame connections started to rotate substantially, the infill plate of the first story yielded completely and the maximum principal strain in location 4 was over $2600 \mu\epsilon$, which shows a significant increase in the principal strains in location 4. In cycle 21, in which the specimen reached its maximum strength, the maximum principal strain in the infill plate of the first story reached $16,000 \mu\epsilon$ at location 1.



Figure 5.1: Cracks in concrete of the north PEC column in cycle 9



Figure 5.2: First story infill plate fold due to rotation of the frame connection



Figure 5.3: Yield lines in the infill plate of the first story during cycle 15



Figure 5.4: Base of the south column during cycle 17



Figure 5.5: Local buckling of the outer flange just above the side plate at the base of the north column during cycle 20



Figure 5.6: Buckling of the flange between side plates at the base of south column in cycle 20



Figure 5.7: Outer flange of the south column at the base in cycle 24



Figure 5.8: First story of the specimen at the end of the test

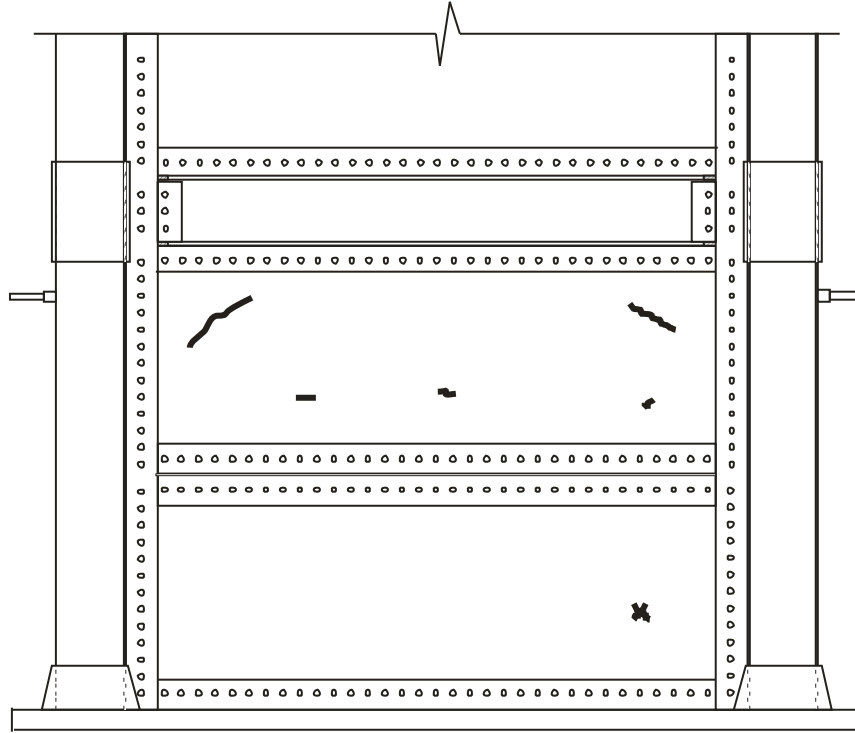


Figure 5.9: Location of first story infill plate tears at the end of the test (East view)

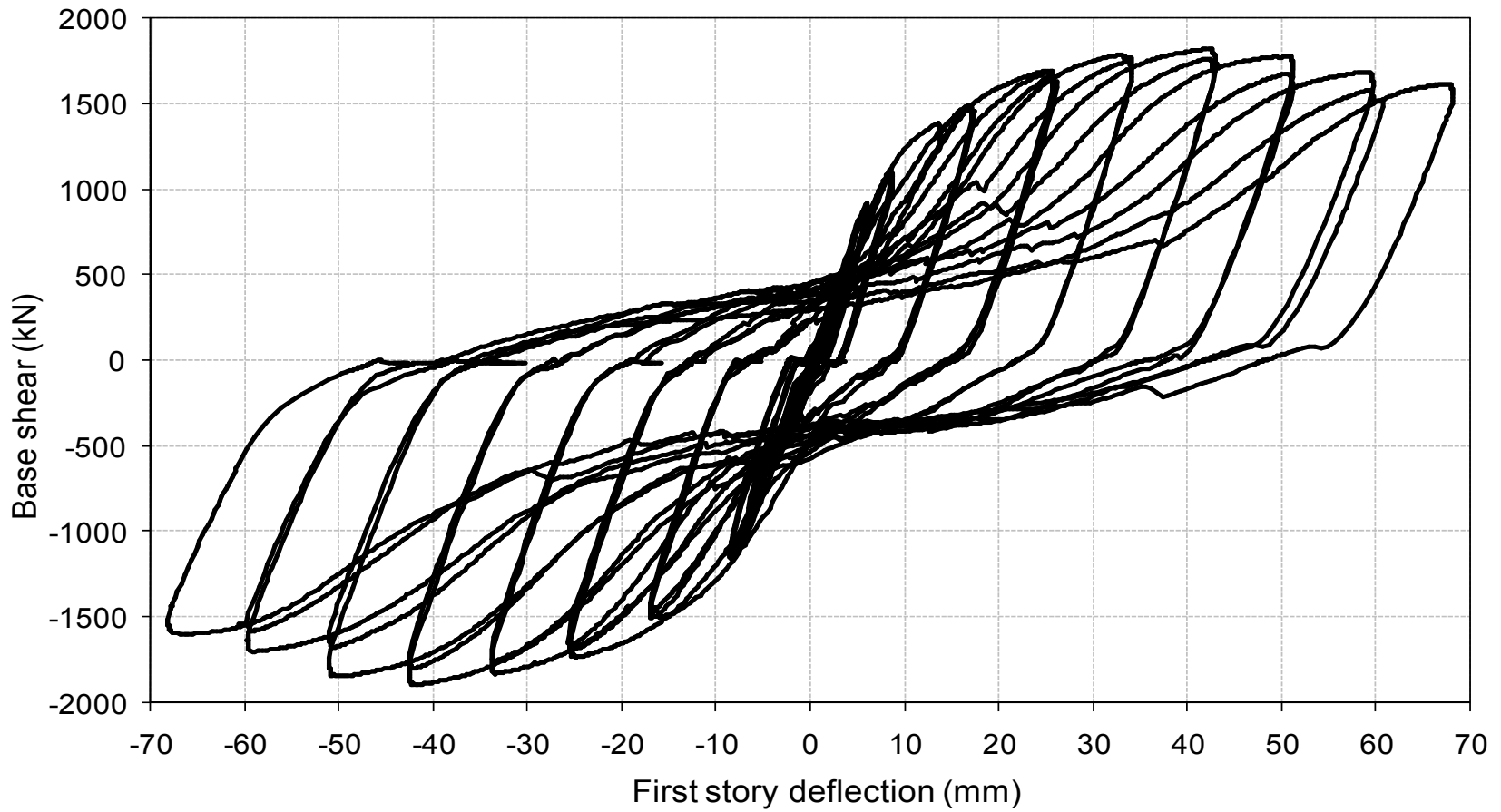


Figure 5.10: Base shear versus first story deflection in the modular test

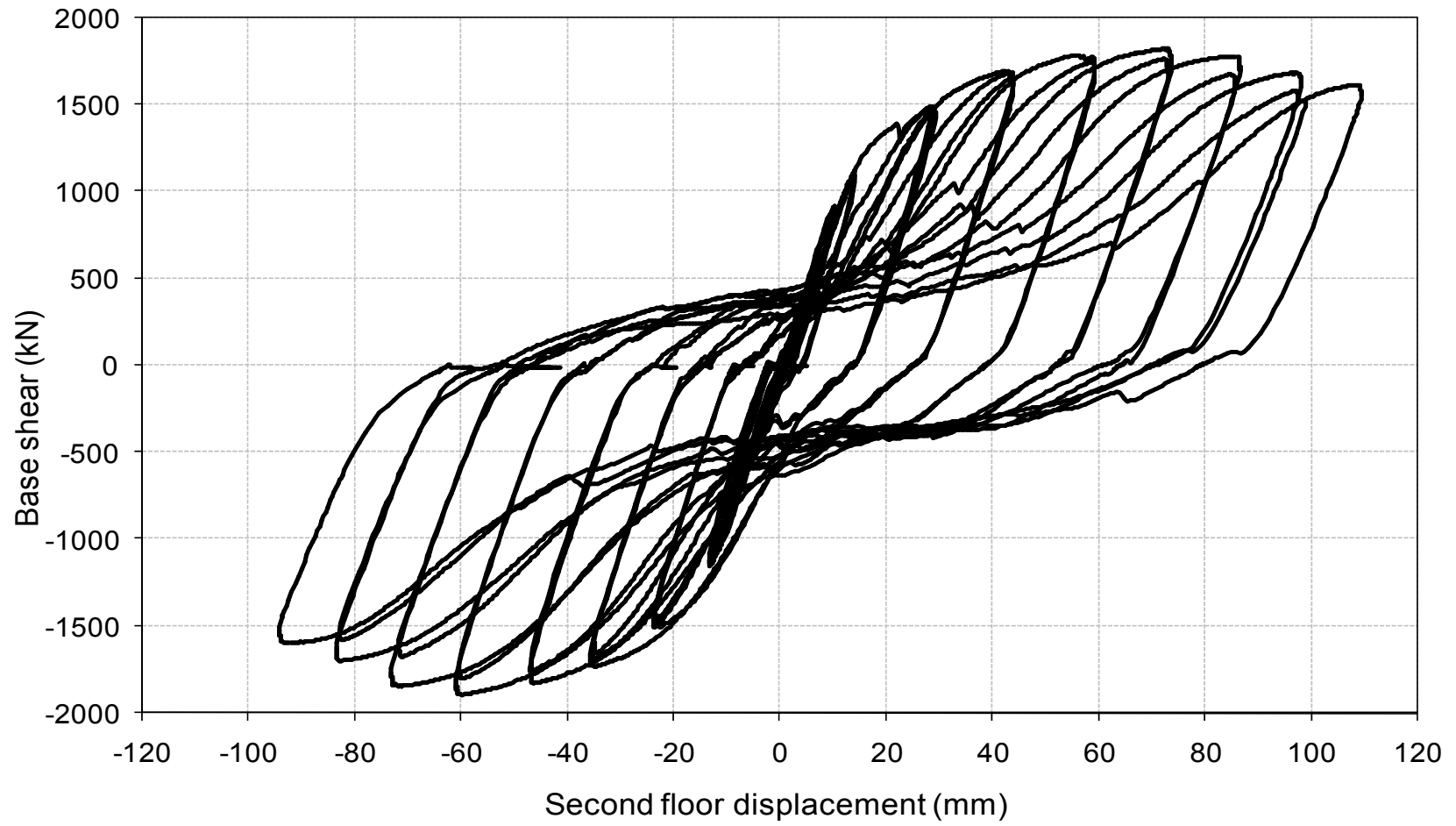


Figure 5.11: Base shear versus second floor displacement in the modular test

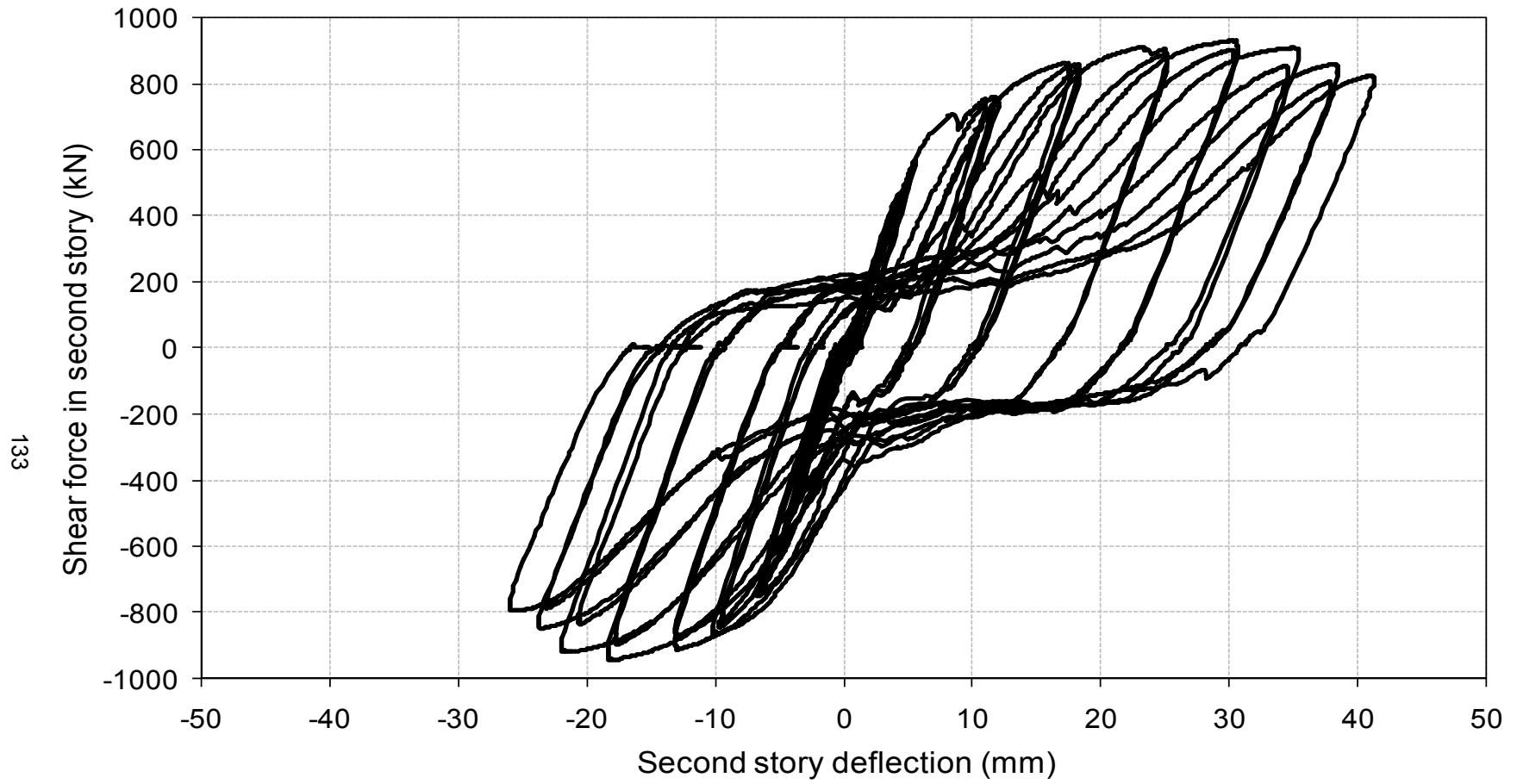


Figure 5.12: Shear force in the second story versus second story deflection in the modular test

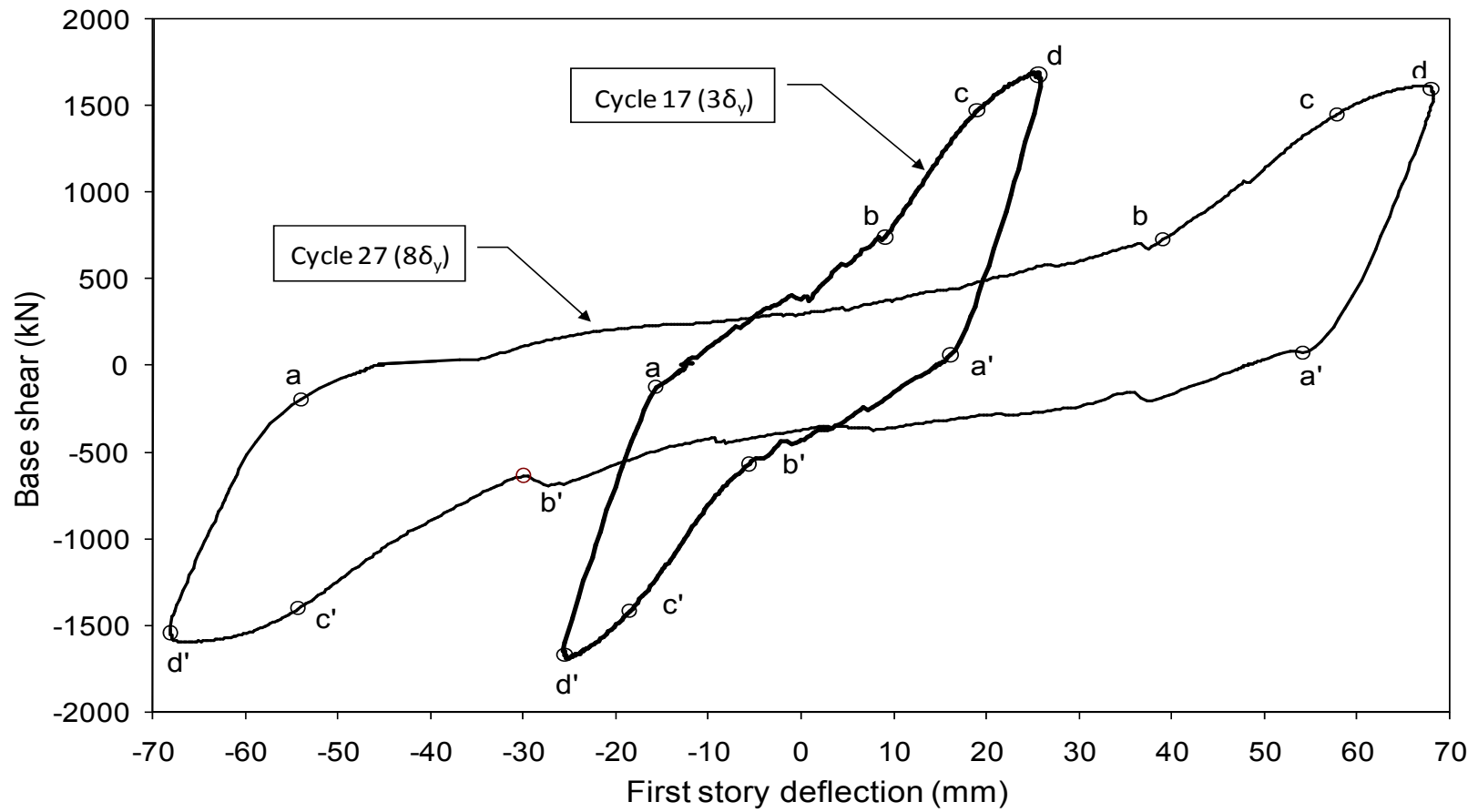


Figure 5.13: Hysteretic loops of cycles 17 and 27

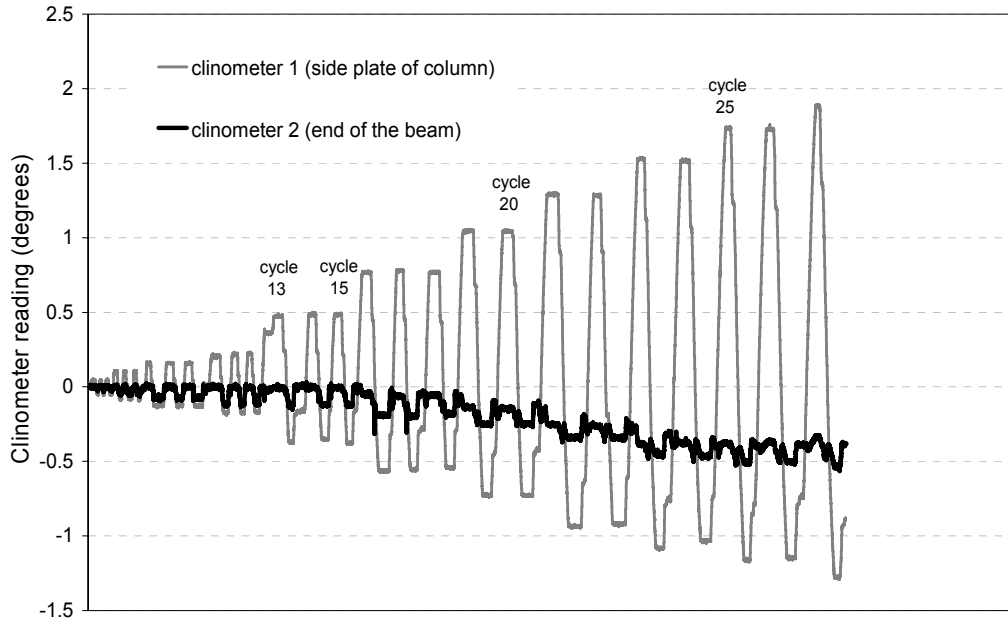


Figure 5.14: Rotation history of the side plate of column and end of the beam in the first floor of the modular test specimen

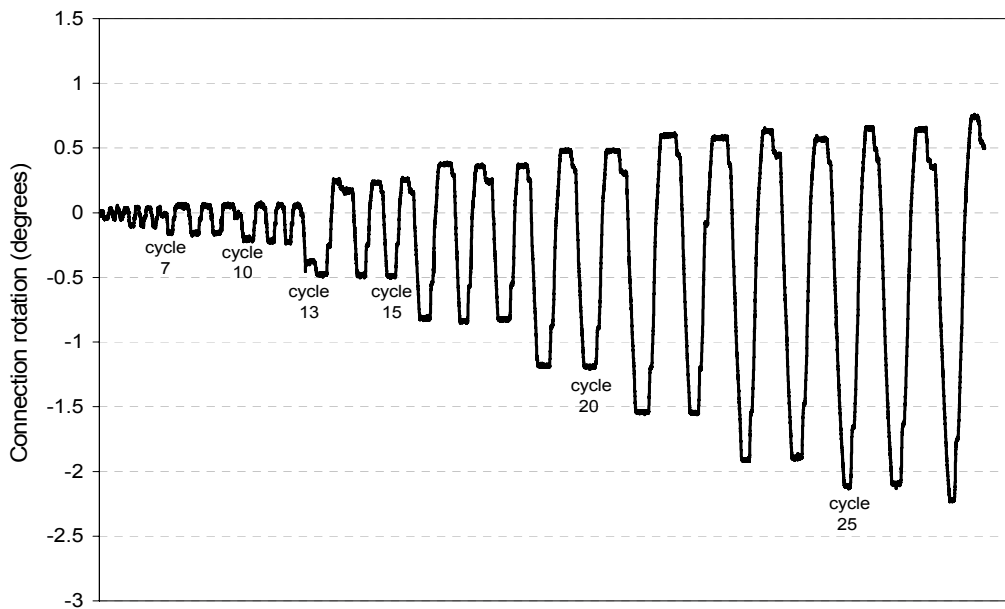


Figure 5.15: Rotation history of the frame connection in the first floor during the modular test

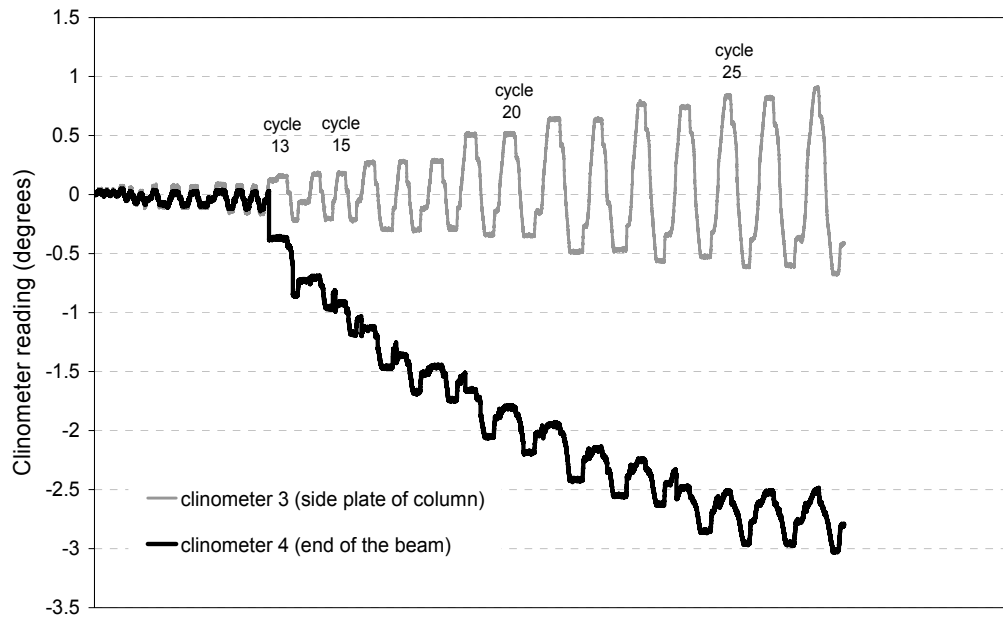


Figure 5.16: Rotation history of the side plate of column and end of the beam in the second floor of the modular test specimen

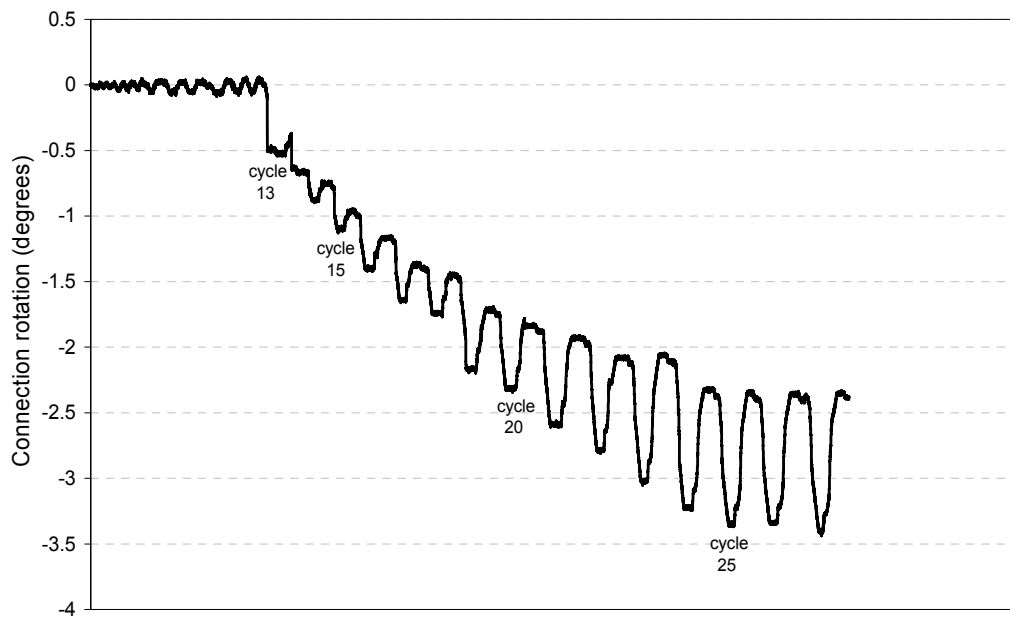


Figure 5.17: Rotation history of the frame connection in the second floor during the modular test

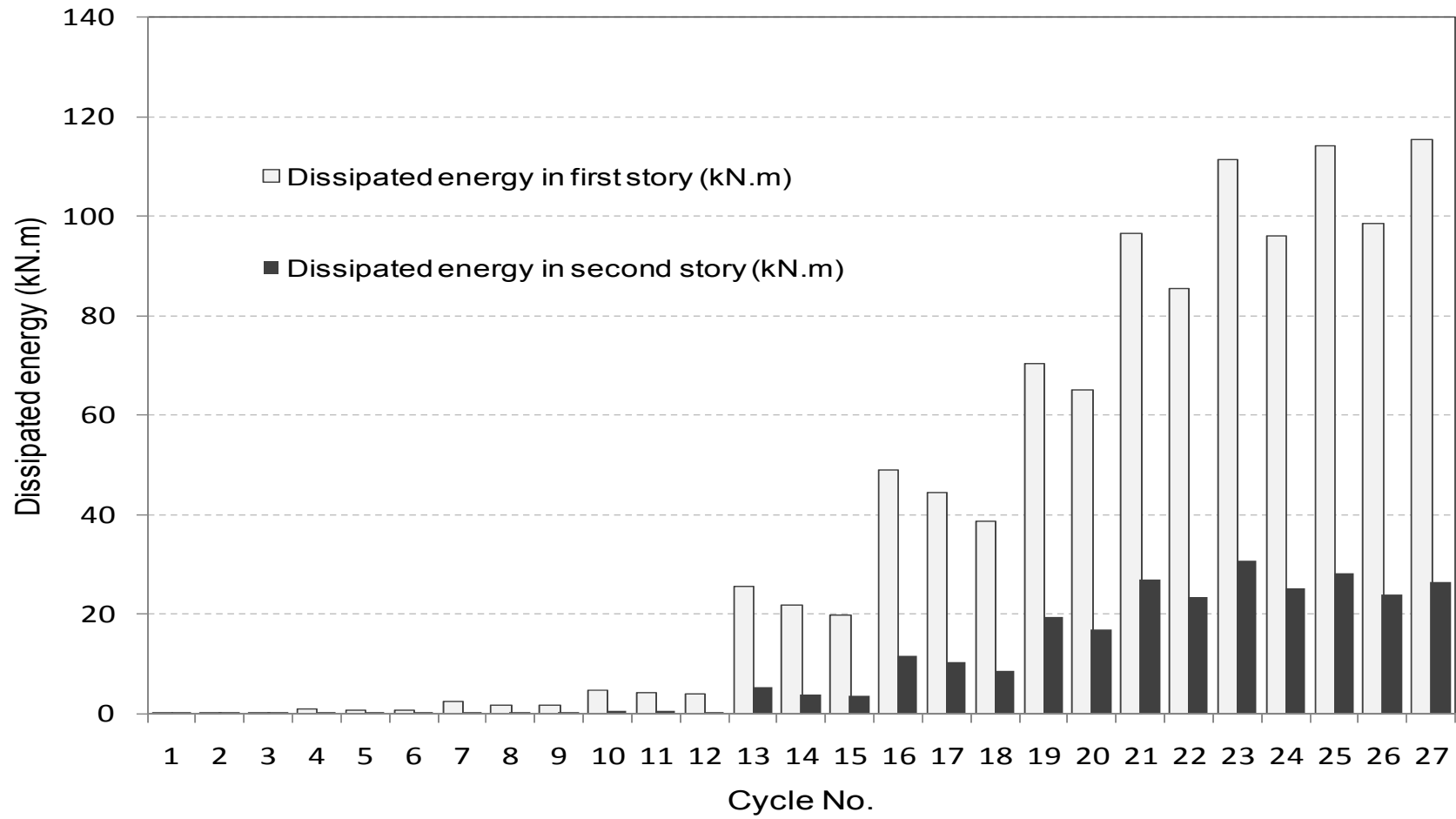


Figure 5.18: Dissipated energy in the first and second stories of the modular specimen in each cycle

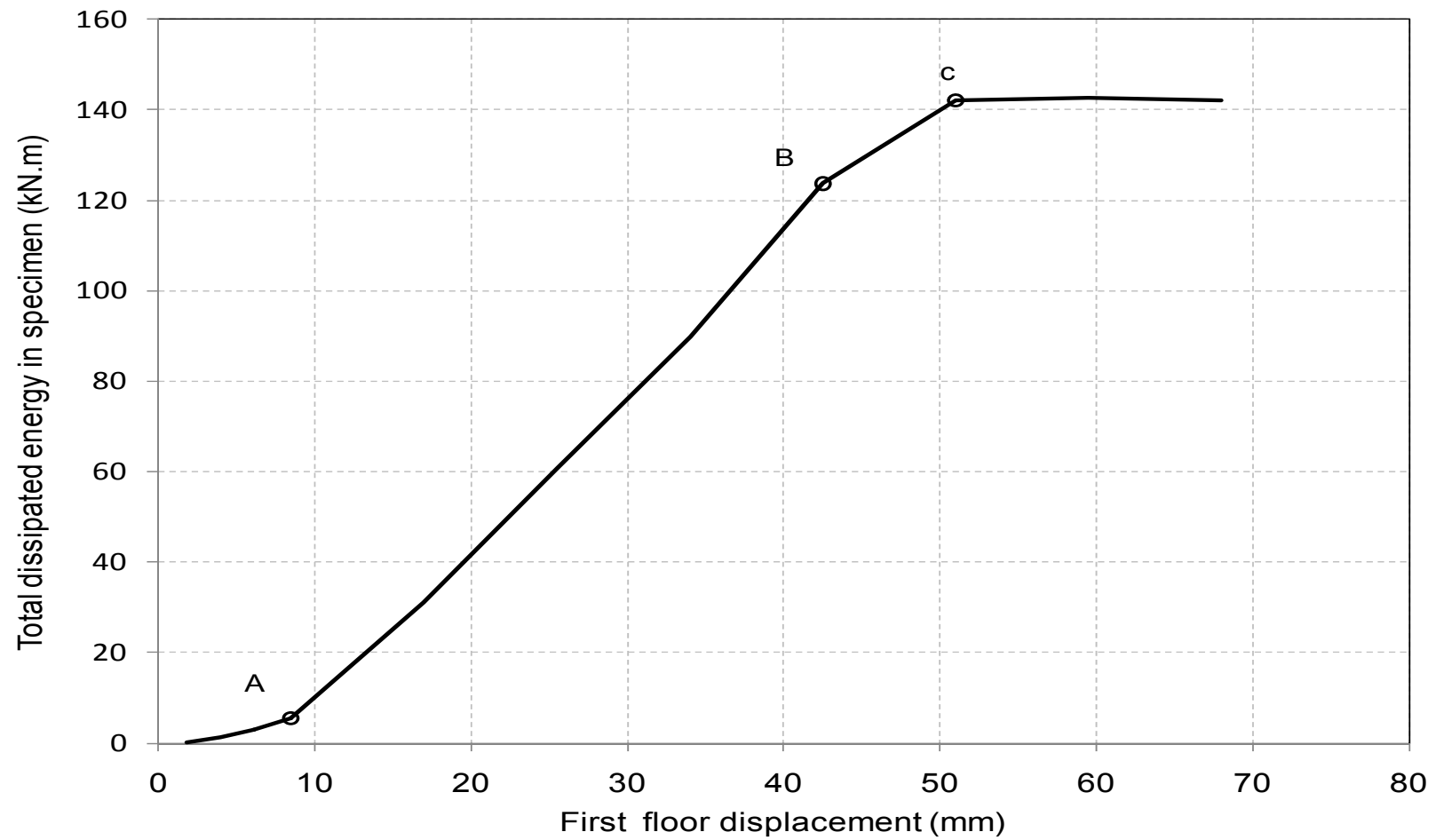


Figure 5.19: Total dissipated energy in the modular specimen versus first floor displacement

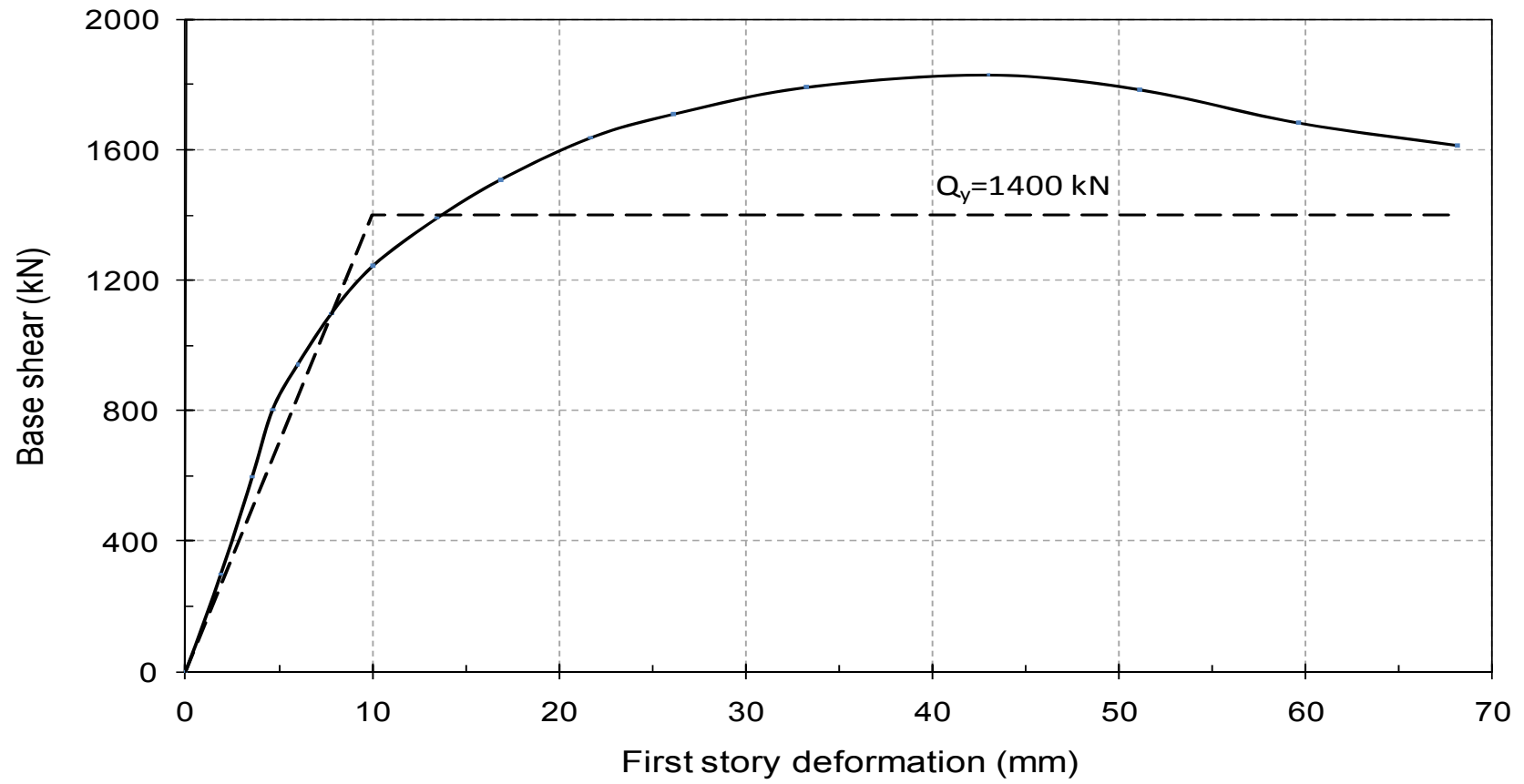


Figure 5.20: Envelope of the hysteretic loops of base shear versus first story deformation in the modular test

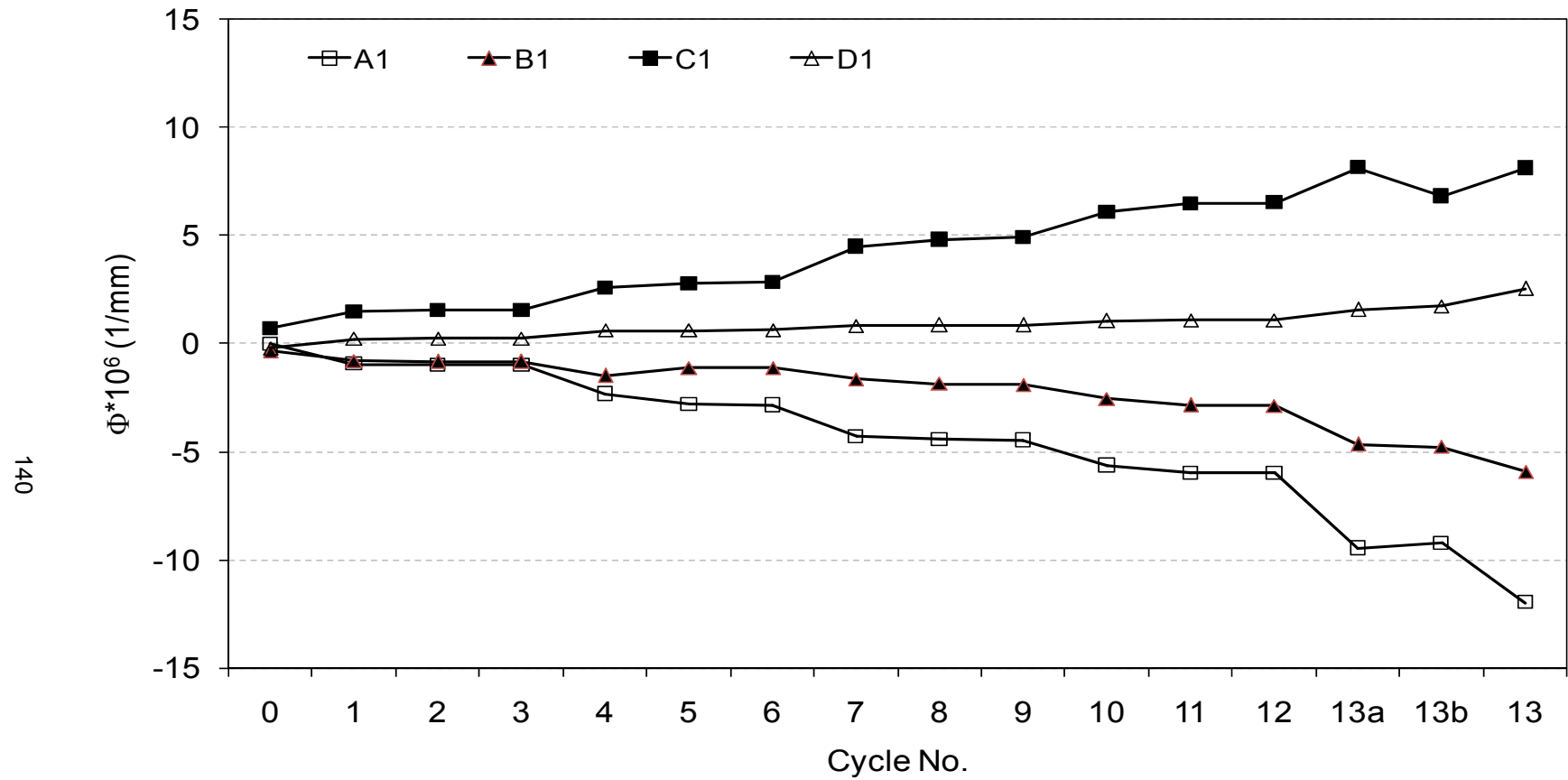


Figure 5.21: Curvature of the north column at four sections in cycles 1 to 13

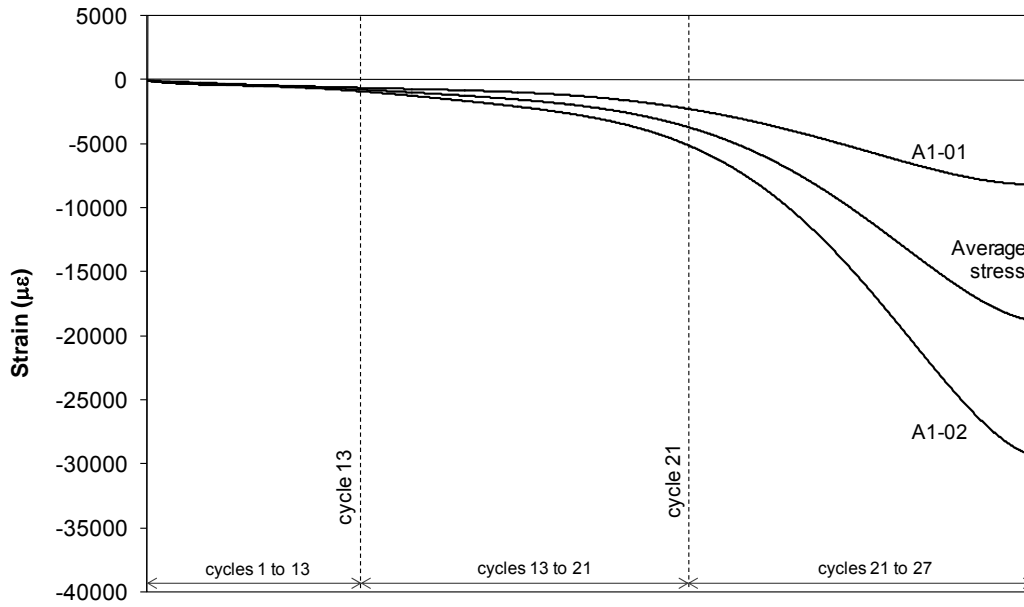


Figure 5.22: Strain readings on both sides of the outer flange at section A1

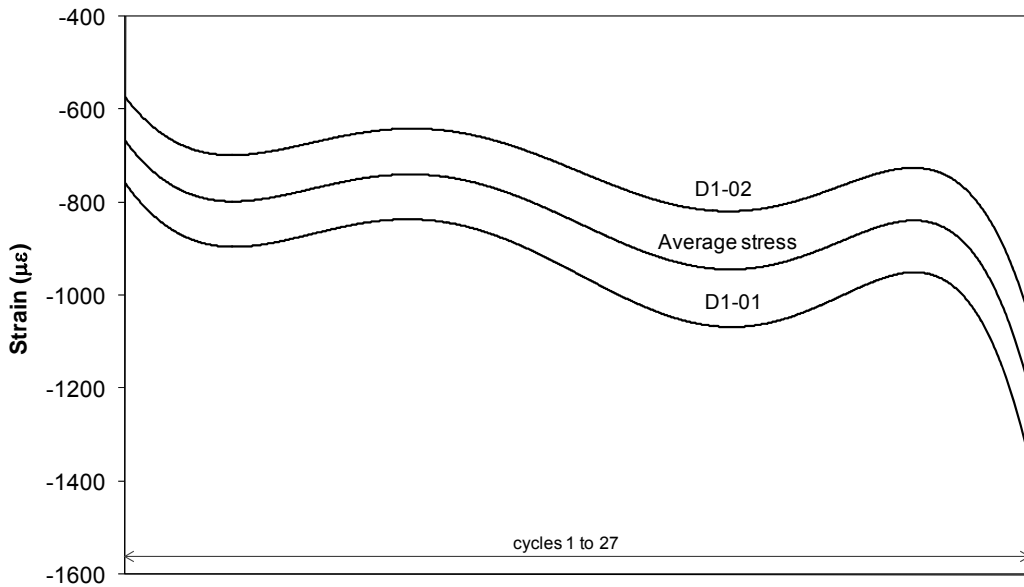


Figure 5.23: Strain readings on both sides of the outer flange at section D1

6. TEST RESULTS OF STEEL PLATE SHEAR WALL WITH RBS CONNECTIONS

6.1 Introduction

In order to investigate the behavior of steel plate shear walls with “Reduced Beam Section” (RBS) connections and to have a better understanding of the effect of this type of connections on the seismic performance of the wall systems with PEC columns, a specimen, called the RBS specimen hereafter, was tested at the University of Alberta. Modified detailing was used in the PEC columns and the connections were modified to overcome some observed shortcomings in the benchmark test, such as excessive stress in the welded flange connections and soft story formation. The outcome of the test and the observations are discussed in this chapter. The hysteretic loops of both stories are shown and the envelope of the hysteretic loops of the first story is extensively studied. Some key characteristics of the test specimen, as an earthquake load resisting system, like initial stiffness, displacement ductility and energy dissipation capacity, are discussed. The strain data obtained from critical regions of the specimen are also studied. In this test, a 3D camera system was used to monitor the base of the north column. The last part of this chapter is devoted to showing some outcomes of the 3D camera system measurements.

The maximum out-of-plane imperfection in the infill plate of the first story, from the plane of the wall, was 15 mm. The imperfection of the infill plate in the first story included two half-waves, and thus it was similar to the second mode of the plate buckling in shear, except that the waves were not diagonal. The infill plate of the second story was almost flat. The tip of the flanges of the columns had a maximum initial inward deformation of less than 2 mm between the links, which was due to the welding process.

The RBS test took five days to complete. As with the modular wall, a total of 27 cycles were applied to the specimen. The peak attained base shears were $Q_{p1} = 1890$ kN when it was pushed to the north (i.e., the first half of the cycle) and $Q_{p2} = -1896$ kN when it was pulled to the south (i.e., the second half of the cycle).

6.2 General observations

6.2.1 Gravity load application

In order to resemble the gravity load during the earthquake, a 600 kN load was applied at the tops of the columns at the beginning of the test. The gravity load did not cause any local buckling in the column, as expected, and the concrete did not crack, which was indicative of relatively concentric load application. The shape of the infill plate imperfection did not change.

The gravity load was continuously controlled and adjusted, if necessary, at the end of the cycles. Because of the deflection of the specimen, especially in cycles with high imposed lateral deformations, the gravity load was not 600 kN at all times and at the extreme deformations, it was more or less than 600 kN, depending on the direction of the deformations. The gravity load was removed at the end of each day of the test and reapplied at the beginning of the test on the next day.

6.2.2 "Force control" cycles

Nine force control cycles were conducted in the RBS test. During the first three cycles, the specimen reached a maximum base shear of 350 kN. The displacements of the first and second floors were 2.6 mm and 4.6 mm, respectively. The infill plate in the first story snapped to one diagonal buckle wave and in the second story, no sign of shear buckling was observed in the infill plate. The concrete in the columns did not crack and the specimen remained elastic.

The target base shear for cycles 4 to 6 was 700 kN and the floor displacements were 5.3 mm and 9.2 mm in the first and second floors, respectively. The concrete cracked close to the base of the columns, as shown in Figure 6.1. The cracks started horizontally adjacent to the column flanges and became diagonal at the center of the section, indicating a high shear force at the bases of the columns. There was no sign of local buckling in the flanges of the columns and no yielding was detected in the infill plates.

During cycles 7 to 9, the specimen reached a base shear of 1050 kN (i.e., 55 % of the maximum base shear). The floor displacements were 8.5 mm and 14.1 mm in the first and second floors, respectively. The infill plate in the first story buckled in two buckle waves in the first story and one buckle wave in the second story. Figure 6.2 shows the infill plate buckling during cycle 9. Like other experimental tests on steel plate shear walls with infill plates, several loud noises were heard during the load reversal due to the reorientation and popping through of the buckle waves. These noises were heard in all subsequent cycles. Some horizontal cracks developed at the tops of the columns in the first story, close to the column side plates, which indicated that the columns were deforming in double curvature. This was mainly due to the limited frame connection rotation in the first floor. There were some diagonal crack propagations close to the bases of the columns, as shown in Figure 6.3. The cut region of the RBS connection did not show any sign of yielding and no local buckling was detected in the flanges of the PEC columns.

6.2.3 “Displacement control” cycles

During cycles 10 to 12, the RBS test specimen experienced the yield displacement. It was expected that the RBS specimen would behave similarly to the modular test in the early cycles, where the frame connection rotations were small. Thus, the yield displacement was estimated to be 10 mm. The attained maximum base shears in the first and second halves of cycle 10 were +1174 kN and –1183 kN, respectively. These base shears are approximately 62 % of the specimen’s peak base shear. The cracks

propagated diagonally close to the bases of the columns and new cracks developed parallel to the existing cracks. The configuration of the cracks in the concrete indicated the the deformation of the columns was in double curvature. Whitewash started to fall from some parts of the infill plate of the first story, which was an indication of infill plate yielding. Three buckle waves were observed in the infill plate of the first story. The infill plate buckled in two waves in the second story. The second floor displacements were +15.9 mm and -16.4 mm in the first and second halves of cycle 12, respectively.

In cycles 13 to 15, the first floor displacement was double the yield displacement ($\delta = 2\delta_y = \pm 20$ mm). The maximum base shear in the first half of cycle 13 was $Q_1 = 1606$ kN (85 % of Q_{p1}) and the maximum base shear in the second half of this cycle was $Q_2 = -1649$ kN (87 % of Q_{p2}). The infill plates buckled in five and three buckle waves in the first and second stories, respectively. The whitewash on the outer flanges of the columns at the base started to fall, which was an indication of the yielding in that region. New diagonal concrete cracks were detected close to the bases of the columns in the expected locations of plastic hinge formation. The first signs of the yielding of the bottom flanges and the web of the first floor beam in the RBS cut region were detected in cycle 13. As the bases of the columns, the RBS cut regions, and the infill plate of the first story were considered the critical regions of the test specimen, designated as protected zones in the Canadian steel design standard (CSA 2009), and since yielding happened in all these regions during cycle 13, it was concluded that significant yielding happened during this cycle. This issue will be further investigated later by studying the strain gauge data. The general observations during cycles 14 and 15 were the crack propagations in the concrete close to the bases of the columns and new yield line formations in the infill plate of the first story. The second floor displacements were +29.8 mm and -29.7 mm in the first and second halves of cycle 15.

During cycles 16 to 18, the maximum first floor displacement was three times the yield displacement ($\delta = 3\delta_y = \pm 30$ mm). The base shear in the first half of cycle 16 reached a

maximum of $Q_1 = 1818$ kN (96 % of Q_{p1}) and in the second half, the maximum base shear was $Q_2 = -1853$ kN (98 % of Q_{p2}). The numbers of buckle waves in the infill plates of the first and second stories were five and three, respectively. The main observation in cycle 16 was the propagation of diagonal cracks in the concrete close to the base of the columns. The concrete started to crush locally at the base just above the side plates in the compression region. The outer flanges of the columns started to tear in cycle 17. The tears started from the top surface of the side plates at the bases of columns, with a length less than 10 mm. The outer flanges of the columns buckled at the mid-height of the first story, where the longitudinal rebars were terminated, which indicated the necessity of having closer links in that region. The tears in the column flanges grew in cycle 18 and the total length of tears in east and west side of the north and south columns were 58 mm and 32 mm, respectively. The outer flanges of the columns buckled in two more locations at the mid-height of the column in the first story, with a rise of the flange tips of around 2 mm. The outer flange of the columns also buckled at the base of columns both between and above the side plates in this cycle. The infill plate started to tear from the welding access hole in the top south corner of the infill plate of the first story. The second floor displacements in cycle 18 were +43.4 mm in the first half and -42.2 mm in the second half of cycle 18.

In cycles 19 and 20, the maximum first floor displacement was $\delta = 4\delta_y = \pm 40$ mm. The maximum base shears were attained in cycle 19. The base shear reached $Q_1 = Q_{p1} = 1890$ kN in the first half and $Q_2 = Q_{p2} = -1896$ kN in the second half of cycle 19. The infill plates buckled in seven buckle waves in the first story and four buckle waves in the second story. During this cycle, the total outer flange tear lengths were 130 mm and 70 mm in the north and south columns, respectively. The diagonal cracks in the concrete propagated more at the hinge locations close to the bases of columns. The concrete crushed in the compression region of the hinge location and the resulting vertical cracks formed in those regions. Figure 6.4 shows the bottom part of the east face of the north column in cycle 19. The performance of the north column at the base will be

further studied later in this chapter. In cycle 20, the total length of the tears in the outer flanges of the columns at the base reached 125 mm in the south column and 152 mm in north column (i.e., more than 50% of the total flange width). More extensive crushing of the concrete in compression happened during cycle 20. The second floor displacements were +56.4 mm and -54.3 mm in this cycle.

During cycles 21 and 22, the maximum displacement of the first floor was $\delta = 5\delta_y = \pm 50$ mm. The attained base shears reduced to $Q_1 = 0.98 Q_{p1} = 1861$ kN in the first half and $Q_2 = 0.99 Q_{p2} = -1877$ kN in the second half of cycle 21. The infill plates buckled with the same number of waves as in cycles 19 and 20. The total outer flange tear lengths in the south and north columns were 190 mm (76 % of the flange width) and 210 mm (84 % of the flange width), respectively. The openings of the tears at the tips of the flanges of the south and north columns were 12 mm and 15 mm, respectively, when the flange was in tension. The rise of the tip of the flanges in some local buckling locations in mid-height of the columns in the first story reached 3 mm. The infill plate of the first story started to tear diagonally close to the north bottom corner in cycle 21. In cycle 22, the outer flanges of columns at the bases tore completely. The maximum base shears decreased to 92 percent of those of cycle 21, with the same floor displacements. A new diagonal crack was detected in the top portion of the north column, as depicted in Figure 6.5. The crack was indicating the presence of a high shear force in the columns and it was located in the region with the largest link spacing, which has less shear capacity. There were some diagonal crack propagations in the hinge locations close to the bases of the columns. The inner flanges of the columns buckled under the side plate of the first floor and the adjacent concrete crushed locally and spalled out, as shown in Figure 6.6. The maximum second floor displacements were +68.6 mm and -65.9 mm in this cycle.

In cycles 23 and 24, the test specimen experienced a maximum first floor displacement of $\delta = 6\delta_y = \pm 60$ mm. Base shears of $Q_1 = 1728$ kN (91 % of Q_{p1}) and $Q_2 = -1762$ kN (93 %

of Q_{p2}) were attained in the first and second halves of cycle 23. The infill plate in the first story buckled in nine waves and in the second story, the infill plate buckled in four waves. The buckled infill plate of the first story is shown in Figure 6.7. The openings of the tears in the outer flanges of the columns were 15 mm and 18 mm in the south and north columns, respectively. Part of the steel web of the columns tore and the length of the web tears were estimated to be approximately 30 mm. The rise of the tip of the outer flanges in the local buckling locations at the mid-height of the first story increased to 4 mm. Another diagonal tear in the infill plate was detected in the south top corner of the infill plate in the first story. The major event in cycle 24 was the sudden tearing of the infill plate in the vertical direction, with a loud noise, adjacent to the connecting weld to the south column. The length of the vertical tear was approximately 280 mm in the first half of the cycle and 380 mm in the second half, and it was located at the mid-height of the first story. Despite the partial separation of the infill plate from the column, the base shear capacity was not greatly affected, which can be attributed to the redundancy of the system. The lengths of the diagonal tears in the infill plate of the first story, close to the north bottom corner and south top corner, were both approximately 15 mm. No increase in tear length in the steel web of the columns was observed. As a result of all these damage types, the maximum attained base shears were reduced to $Q_1 = 1599$ kN (85 % of Q_{p1}) and $Q_2 = -1620$ kN (85 % of Q_{p2}) in the first and second halves of cycle 24. The base shears were eight percent less than those of the cycle 23. The maximum second floor displacements were +80.1 mm and -77.3 mm.

In cycle 25, in which the first floor displacement reached $\delta = 7\delta_y = \pm 70$ mm, base shears of $Q_1 = 1613$ kN (85 % of Q_{p1}) and $Q_2 = -1584$ kN (84 % of Q_{p2}) were attained in the first and second halves of the cycle. The length of the vertical tear in the infill plate, adjacent to south column, reached 800 mm, which caused a reduction in the number of buckle waves from nine to five in the first story. The buckle waves were concentrated in half of the infill plate, which was anchored to north column, as shown in Figure 6.8. A new diagonal tear was detected in the north top corner of the infill plate in the first story. The

major event in the columns was the buckling of the inner flange of the south column, with a rise of 12 mm, about 400 mm below the side plate of the first floor, as shown in Figure 6.9. This event was an indication of the extra demand on the column due to the vertical tear of the infill plate adjacent to this column. The outer flanges of the north column buckled under the side plate of the first floor, as shown in Figure 6.10, which indicated the formation of a hinge under the side plate of column at the first floor. During cycle 26, the vertical tear in the infill plate reached the base plate and practically, the infill plate was no longer connected to the south column in the first story. The base shear decreased substantially in cycle 26 and it reached $Q_1 = 1418 \text{ kN}$ (75 % of Q_{p1}) in the first half and $Q_2 = -1433 \text{ kN}$ (76 % of Q_{p2}) in the second half of the cycle. The infill plate in the first story started to tear diagonally from the top corners in north and south, where the weld access holes were located. The openings of the tears of the outer flanges of the columns at the base did not increase, which was an indication that the tear did not propagate further in the web of the columns. Plastic hinges were obvious at the tops of the columns in the first story, as shown in Figure 6.11. The second floor displacements were +91.2 mm and -87.4 mm in cycle 26.

During cycle 27, which was the last cycle of the test, the maximum first floor displacement was $\delta = 8\delta_y = \pm 80 \text{ mm}$. Base shears of $Q_1 = 1334 \text{ kN}$ (71 % of Q_{p1}) and $Q_2 = -1410 \text{ kN}$ (74 % of Q_{p2}) were attained in the first and second halves of this cycle. The second floor displacements were +101.9 mm and -98.9 mm in this cycle. The test was terminated at this point as the base shear decreased to 75 percent of the peak base shear and there was serious damage in the columns and the infill plate of the first story. Figure 6.12 shows the condition of the base of the north column at the end of the test. In Figure 6.13, the south column in the first story is shown at the end of the test. The yield lines and the vertical tear of the infill plate can be seen in this figure. The locations of the tears in the infill plate of the first story are depicted in Figure 6.14.

6.3 Hysteretic behavior

6.3.1 Hysteretic loops of the first and second stories

Figure 6.15 depicts the base shear versus the first story deflection (which is equal to first floor displacement) of the RBS test specimen. The base shear versus the second floor displacement (i.e., the summation of the individual first and second stories deflections) diagram is shown in Figure 6.16. To have a better understanding of the behavior of the second story of the specimen, the shear force in the second story is plotted versus the second story deflection (i.e., the difference between the second floor and first floor displacements) in Figure 6.17. During the first few cycles the specimen remained elastic with a very high stiffness. As the infill plate in the first story had to snap from its initial imperfection shape with two half waves to one buckle wave, there was a horizontal part (i.e., deformation without increase in the base shear) in the hysteretic loops of the first three cycles. The effect of the shape of the initial imperfection disappeared as the infill plate started to yield. As the test progressed, the steel parts of the specimen started to yield and the concrete began to crack, which reduced the stiffness of the specimen in some stages of the cycles. As the floor displacements increased, the hysteretic curves became more pinched around the zero displacement where the buckle waves reoriented in the other direction. In Figure 6.18, the base shear vs. first story deflection curves resulting from cycles 17 ($\delta = 3\delta_y = 30$ mm) and 27 ($\delta = 8\delta_y = 80$ mm) are shown. The slope of the curve in segment a-b, which is the pinched part of the curve, is the smallest among the various parts of each curve which is mainly due to the reorientation of the tension field. During this part, the infill plate is not very effective and most of the stiffness is provided by the frame itself. The slope of the segment a-b in cycles 17 and 27 are obtained as 30 kN/mm and 7 kN/mm, respectively. The slope of the segment b-c, during which the tension field redevelops and causes the stiffness to increase, was 70 kN/mm and 23 kN/mm in cycles 17 and 27, respectively. Most of the damage, including the tearing and yielding of steel as well as cracking of the concrete, happened during

segment c-d, as the base shear approached its maximum value in these cycles. The damage in this part caused a gradual decrease in the stiffness of the specimen. The lateral load was removed during segment d-a'. The slope of this part of the curve was obtained 163 kN/mm in cycle 17 and is 105 kN/mm in cycle 27. Curve a'-b'-c'-d'-a represents reloading and unloading in the opposite direction and the same behavior repeats.

6.3.2 *Rotation of the frame connections*

In order to monitor the rotation of the connections, three clinometers were used at the north side of the specimen. Clinometer 1 was attached to the side plate of the column in the first floor and clinometer 2 was attached to the web of the first floor beam at the end of the RBS cut region farthest from the column, as shown in Figure 4.13. The readings of these two clinometers are plotted in Figure 6.19. Unlike the modular specimen, these clinometers were mounted on the west side of the specimen so a positive reading represents a counter-clockwise rotation when looking from the east, and vice versa. Both the side plate and the end of the beam rotated both ways during the test and the maximum rotation ranges in cycle 27 were approximately 1.75 and 1.0 degrees, respectively. Due to the bigger anchored forces from the tension field in the first story compared to the second story, the end of the floor beam tended to rotate more in the positive (i.e., counter-clockwise) direction. The rotation history of the frame connection in the first floor is depicted in Figure 6.20. This figure shows the relative rotations of the two adjacent clinometers, with the majority of these deformations taking place within the RBS region. The maximum rotation of the connection in the first floor was approximately 0.9 degrees. A closer look at Figure 6.20 reveals that the RBS connection started to rotate, due to plasticity, in cycle 13, during which the connection rotation was almost twice that of cycle 12. The maximum rotation in the first floor frame connection happened in cycle 23. Due to the formation of the plastic hinges in the tops of the first story columns under the side plates, the beam-to-column connection rotation decreased from cycle 25.

The reading of clinometer 3, which was attached to the east side plate of the column at the second floor, is plotted in Figure 6.21. As the clinometer 3 was mounted on the east side, a positive reading means clockwise rotation, when looking from east. Figure 6.21 shows that clinometer 3 rotated both ways in all cycles with a relatively similar amount. The maximum rotation range was approximately 0.9 degrees in cycle 27.

6.4 Energy dissipation capacity, stiffness and ductility

Out of the 27 cycles applied, the RBS specimen experienced significant yielding during 15 cycles, i.e., cycles 13 to 27. Almost all the energy was dissipated during these cycles and the displacement ductility of the specimen was dependent on these cycles.

6.4.1 Energy dissipation capacity

The hysteretic loops resulting from this test were fairly wide with a relatively large area. As the enclosed area by each hysteretic loop is a measure of the amount of the dissipated energy through the associated cycle, the system was able to absorb and dissipate a large amount of energy during the test. The main sources of the energy dissipation were yielding of the steel parts and crushing of the concrete parts. In Figure 6.22, the amount of dissipated energy in the first and second stories of the RBS test specimen during each cycle is shown. Due to the presence of a larger force and deflections in the first story compared to the second story, most of the damage happened in the first story and, as a result, the majority of the energy was absorbed and dissipated in the first story. As can be seen in Figure 6.22, the amount of energy dissipated in the first story had two sudden increases in cycles 7 and 13. During cycle 7, the first yielding happened in some parts of the infill plate in the first story and in cycle 13, some parts of the RBS cut regions yielded and a partial plastic hinge formed there, resulting in yielding of all parts of the infill plate in the first story. The amount of the dissipated energy in the second story was negligible up to cycle 13, where the frame connections of the first floor started to rotate and, as a result, parts of the infill plate in the second story yielded.

Similar to other steel plate shear wall test results, most of the damage (i.e., tearing of steel, cracking and crushing of concrete) happened in the first cycle of each stage of displacement and, as a result, the amount of the dissipated energy in the first cycle of each stage was larger compared to subsequent cycles of that stage. In Figure 6.23, the total amount of energy dissipated in the specimen is plotted vs. the first floor displacement. At point A, which represents the cycle during which the specimen reached its yielding displacement, the slope of the curve has a sudden increase due to the significant yielding in the infill plates and the frame connections in the first story. The slope decrease at point B is mainly due to the tearing of the outer flanges of the columns at the bases, whereas at point C it is due to the vertical tear in the infill plate of the first story, which completely detached the infill plate from the south column. As shown in Figure 6.23, not only was there no decrease in the energy dissipation capacity of the specimen despite all the damage after point C, but also the specimen dissipated slightly more energy in the last cycle (i.e., cycle 27 with $\delta = \pm 80$ mm) compared to cycle 25. This demonstrates that the system is highly redundant and capable of changing the load transfer routes, which helped the system to fulfill its function.

6.4.2 Stiffness and ductility

In this part of the chapter, two important characteristics of an efficient earthquake load resisting system, i.e., high initial stiffness and displacement ductility (R), are determined for the RBS test specimen. The high initial stiffness is important for service loads and the displacement ductility is important since during an earthquake, the lateral load resisting system should be capable to undergo relatively large deformation without significant loss of strength.

In order to study the performance of the infill plate of the first story and define its stiffness and ductility, the envelope of the corresponding hysteretic loops with positive deformations and base shear values is shown in Figure 6.24. The lateral stiffness of the first story of the RBS specimen during the elastic cycles was 140 kN/mm. During

cycle 13, significant yielding was observed in the critical regions of the RBS test specimen. The strain gauges affixed to the outer flanges of columns at the base showed complete yielding of the flanges and the data from strain gauge rosettes on the infill plate of the first story showed yielding at all three levels, which indicates uniform yielding of the whole infill plate of the first story. Also, the strain readings from the RBS cut region indicated that the bottom flange and part of the web of the beam in the first floor yielded. According to Figure 6.23, the yielding deformation of the specimen was estimated as $\delta = 10$ mm and, based on the strain readings, the yielding base shear was concluded to be $Q_y = 1400$ kN.

To define the displacement ductility, R , of the RBS specimen, Equation (2.42) was used at the peak base shear and in the post-peak phase. The story deformation at the peak base shear ($Q_{p1} = 1890$ kN) was 40 mm which led to a displacement ductility of $R = 4$, and the displacement ductility at 90 percent of the peak base shear in post-peak phase ($Q_{0.9p1} = 1701$ kN), where the first story deformation was 62 mm, was $R = 6.2$. These values are similar to those obtained for the modular test specimen described in Chapter 5. The first story deformation of the specimen when its maximum base shear decreased to $Q_y = 0.74 Q_{p1} = 1400$ kN was approximately 77 mm, which leads to a displacement ductility of $R = 7.7$, although at this stage the shear wall capacity is deteriorating rapidly.

6.5 Strain gauge output data

6.5.1 Strain data obtained from columns

A total of six sections in the columns were monitored using strain gauges to further study the behavior of the columns. Four sections, named A1, B1, C1 and D1 (see Figure 4.13), were located in the north column. Two sections (A2 and D2) were in the south column and their main purpose was to confirm the readings from the sections A1 and D1 in the north column, which were located at the same level. The strain readings in sections A2

and D2 were very close to those of sections A1 and D1; thus, only the behavior of the north column will be discussed.

At the beginning of the test, a gravity load of approximately 600 kN was applied at the tops of the columns. The resulting strain readings in section A1, which was located at 325 mm from the base plate, showed that the average strain in the H-shaped steel part was $-275 \mu\epsilon$ and the average strain in the longitudinal rebars was $-320 \mu\epsilon$. This indicated that the axial load was distributed fairly uniformly in that section. By assuming a complete bond between the concrete and the longitudinal rebars, it was seen that 33 percent of the total applied axial force was carried by the H-shaped section.

The strain reading in the steel part of section D1 (located at top of the north column, under the column side plate at the second floor) was $-370 \mu\epsilon$. The strain readings in the H-shape part of the section D1 were larger than those of the section A1. The proximity of the section D1 to the load application point was one reason for this difference. Also, there were no longitudinal rebars in section D1, which increased the demand on the H-shaped steel part of this section compared to section A1.

The curvatures of the north column at sections A1, B1, C1 and D1 at the maximum positive base shears during cycles 1 to 16 were calculated using the strain readings in these sections and are plotted in Figure 6.25. The curvature of the north column at sections A1 and C1 (i.e., bottom and top of the column in the first story) are similar but in opposite directions, which indicates that the column in the first story deformed in double curvature. In cycle 13, the curvatures increased significantly due to the yielding of some parts of the specimen. The curvature of section A1 was less than that of section C1 up to cycle 16. In cycle 16, the plastic hinge in the RBS cut region formed completely, which caused the curvature of C1 to be less than the curvature of section A1.

Using the strain readings in section A1, the location of the neutral axis was calculated to determine the cycles in which the concrete part of the section was in tension for the first

time. The neutral axis entered the concrete part of section A1 from the north in cycle 1⁻. During cycle 4⁻, the concrete adjacent to the north flange reached its tensile strength and started to crack. The neutral axis entered into the concrete part of section A1 from the south during cycle 13⁺, although no visible crack was detected until cycle 16. It was during cycle 16 that the first cracks were observed in the concrete part of the section A1 adjacent to the inner flange of the column, as shown in Figure 6.26. The study of the strain readings in section D1 showed that the neutral axis entered the section in cycle 14, but the concrete strains were not large enough throughout the test (under 600 $\mu\epsilon$) to cause visible concrete cracks.

6.5.2 Strain data obtained from the infill plate of the first story

A total of six strain gauge rosettes were used to monitor the infill plate of the first story. As the infill plate was relatively thin and a small lateral deformation could cause large flexural stresses, the rosettes were affixed to both sides of the plate in three locations (as shown in Figure 4.13) and the average reading was used as the strain in the infill plate in the vertical, horizontal and diagonal directions. The infill plate did not yield in the first six cycles. During cycle 7, the infill plate yielded in locations 1 and 2. The maximum principal strain in location 1 increased from 940 $\mu\epsilon$ in cycle 6 to 3080 $\mu\epsilon$ in cycle 7⁻ and in location 2, the maximum principal strain increased from 1280 $\mu\epsilon$ in cycle 6 to 2710 $\mu\epsilon$ in cycle 7. In location 3, the maximum principal strain in cycle 6 was 960 $\mu\epsilon$ and it increased to 1440 $\mu\epsilon$ in cycle 7. The strains did not increase significantly until cycle 13, during which the maximum principal strains were twice the values in cycle 12 in locations 1 and 2. In location 3, the maximum principal strain was almost three times the value in cycle 12, which was mainly due to the rotation in RBS cut regions. The maximum principal strain reached almost 20,000 $\mu\epsilon$ in all three locations throughout the test.

6.5.3 Strain data obtained from RBS cut region

Two sections within the RBS cut region in the north end of the first floor beam were instrumented to study the performance of the RBS connection, as shown in Figure 4.13.

Section E was located in the center of the cut. Eight strain gauges were used to monitor longitudinal strains in the top and bottom flanges. The strain gauges were attached to both sides of the flanges to capture any possible local buckling of the flanges. Strain gauge rosettes 4 and 5 were used to monitor the bottom half and top halves of the web, respectively. Section F was located at the quarter point of cut closer to the north column. At this section, the bottom flange was monitored by four strain gauges and the web was monitored by strain gauge rosettes 6 and 7 in the bottom and top halves of the web, respectively.

The first yielding in the RBS cut region happened during cycle 13 at both sections E and F. As there was a significant compressive force in the floor beam, the bottom flanges of the beam in both sections, as well as the lower half of the web, yielded in the first half of this cycle. In the second half of the cycle, the material behaved elastically. The strain readings were bigger at section F compared to section E. The same observation was made by Qu and Bruneau (2010) in a large scale test on a steel plate shear wall with RBS connections. During cycle 16, both flanges and most of the web in both sections E and F yielded and a fully developed plastic hinge developed.

6.6 3D camera system output

The north face of the north column at the base was monitored by one set of cameras to study the behavior of the flange and its tearing. In Figure 6.27, the out-of-flatness deformation of the outer flange of the north column is shown in cycle 18⁺. As can be seen in this figure, the flange buckled above the side plate as well as between the side plates at the base. The maximum strain at the crest of the buckling waves in the same cycle, as shown in Figure 6.28, was around four percent, which is higher than the strain-hardening strain. The path of the tear in the flanges of the column at the base, which started in cycle 17, was through the crest of the buckling wave, between the side plates. This

observation confirms that the reason for the tearing in this area was fatigue of the steel due to several cycles of folding and unfolding there.

To study the behavior of the concrete in the columns at the expected hinge location close to the base, the west side of the north column was monitored by another set of cameras. Figure 6.29 shows the principal strain distribution in cycle 4⁻, showing the appearance of the first cracks. The pattern of the cracks from the 3D camera system is similar to the pattern of cracks shown in Figure 6.1. The concrete started to crack adjacent to the inner flange during cycle 13⁺, as can be seen in the maximum principal strain distribution in Figure 6.30. The crushing of the concrete in compression close to the base of the column can be seen in Figures 6.31 to 6.33, in which the maximum principal strain distribution in the concrete is shown in cycles 19⁺, 21⁺ and 23⁺, respectively.



Figure 6.1: East face of north column in cycle 4

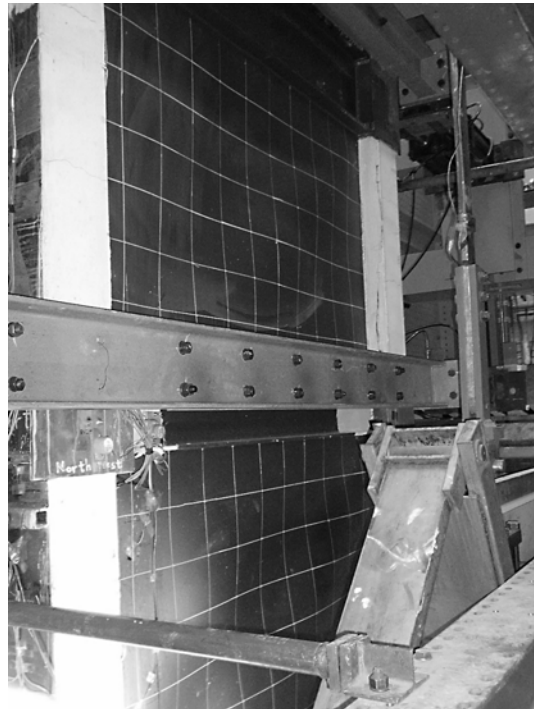


Figure 6.2: Buckling of the infill plates in cycle 9



Figure 6.3: Cracks in concrete on the east face of north column in cycle 9



Figure 6.4: Bottom part of east face of the north column in cycle 19



Figure 6.5: Diagonal crack close to top of the north column on west side in the first story during cycle 22

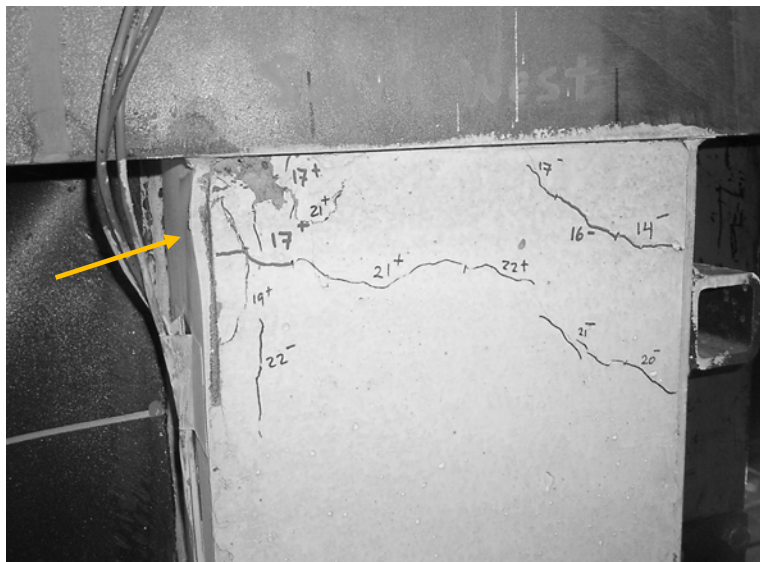


Figure 6.6: Buckling of inner flange and local crushing of the adjacent concrete under the side plate of first floor in cycle 22



Figure 6.7: Buckled infill plate of the first story in cycle 23



Figure 6.8: Effect of the vertical tear in the infill plate, adjacent to south column, on the buckled shape of the infill plate of the first story during cycle 25 (from north).

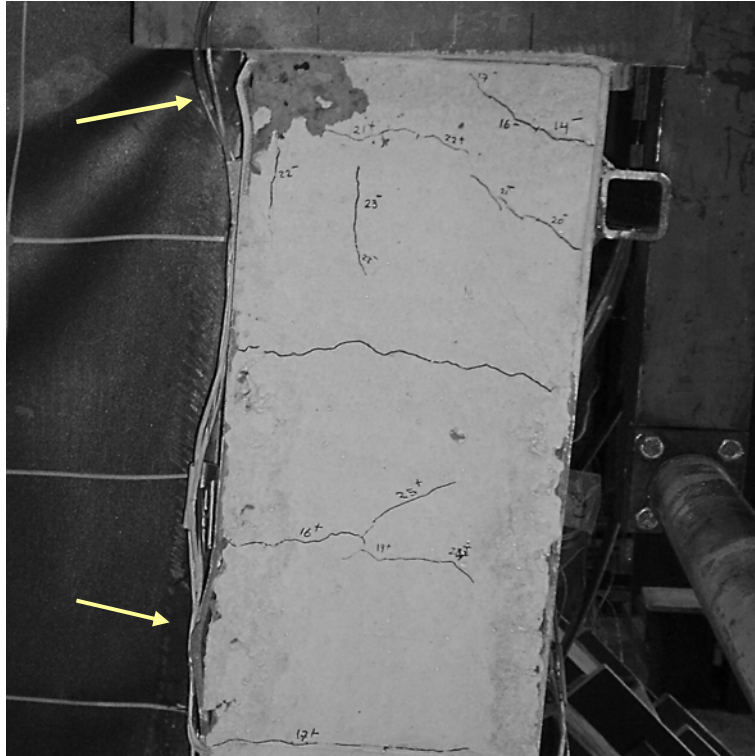


Figure 6.9: Buckling of the inner flange of the south column in cycle 25⁻ (west face)

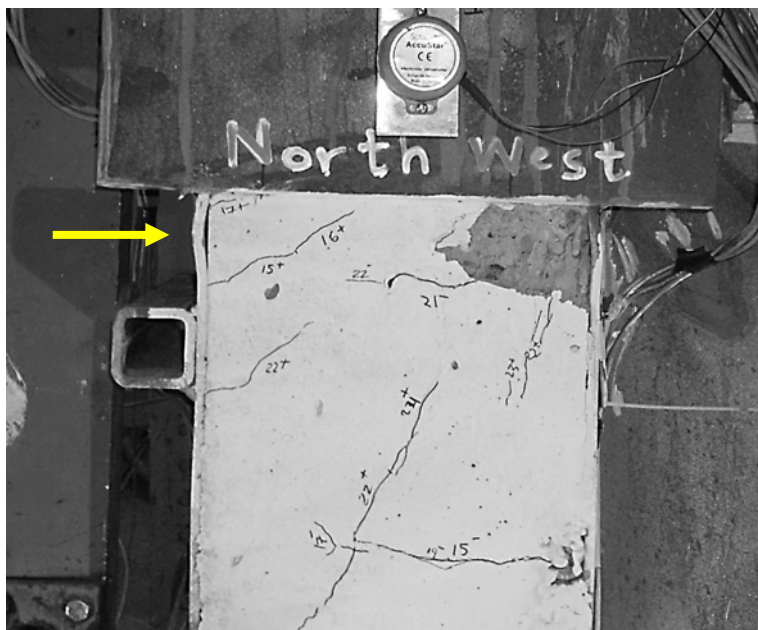


Figure 6.10: Buckling of the outer flange of the north column in cycle 25⁻ (west face)

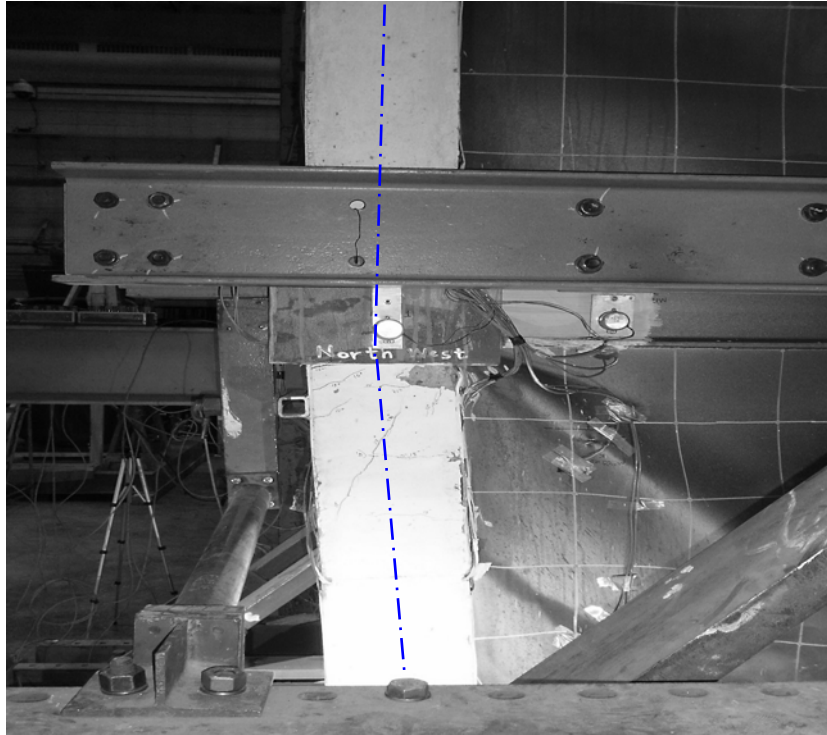


Figure 6.11: Plastic hinge at top of the north column in cycle 26



Figure 6.12: Base of the north column and adjacent infill plate at the end of the test



Figure 6.13: Base of the south column and adjacent infill plate, separated from the column, at the end of the test

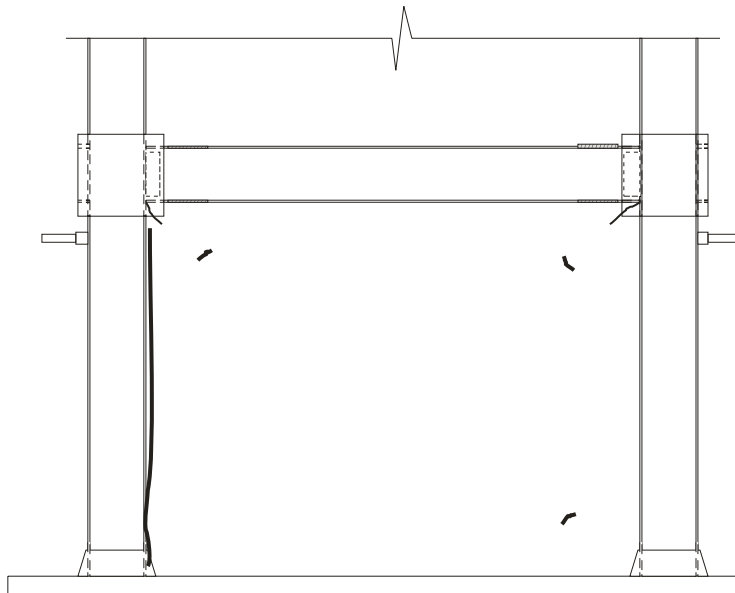


Figure 6.14: Tears in the infill plate of first story at the end of the RBS test

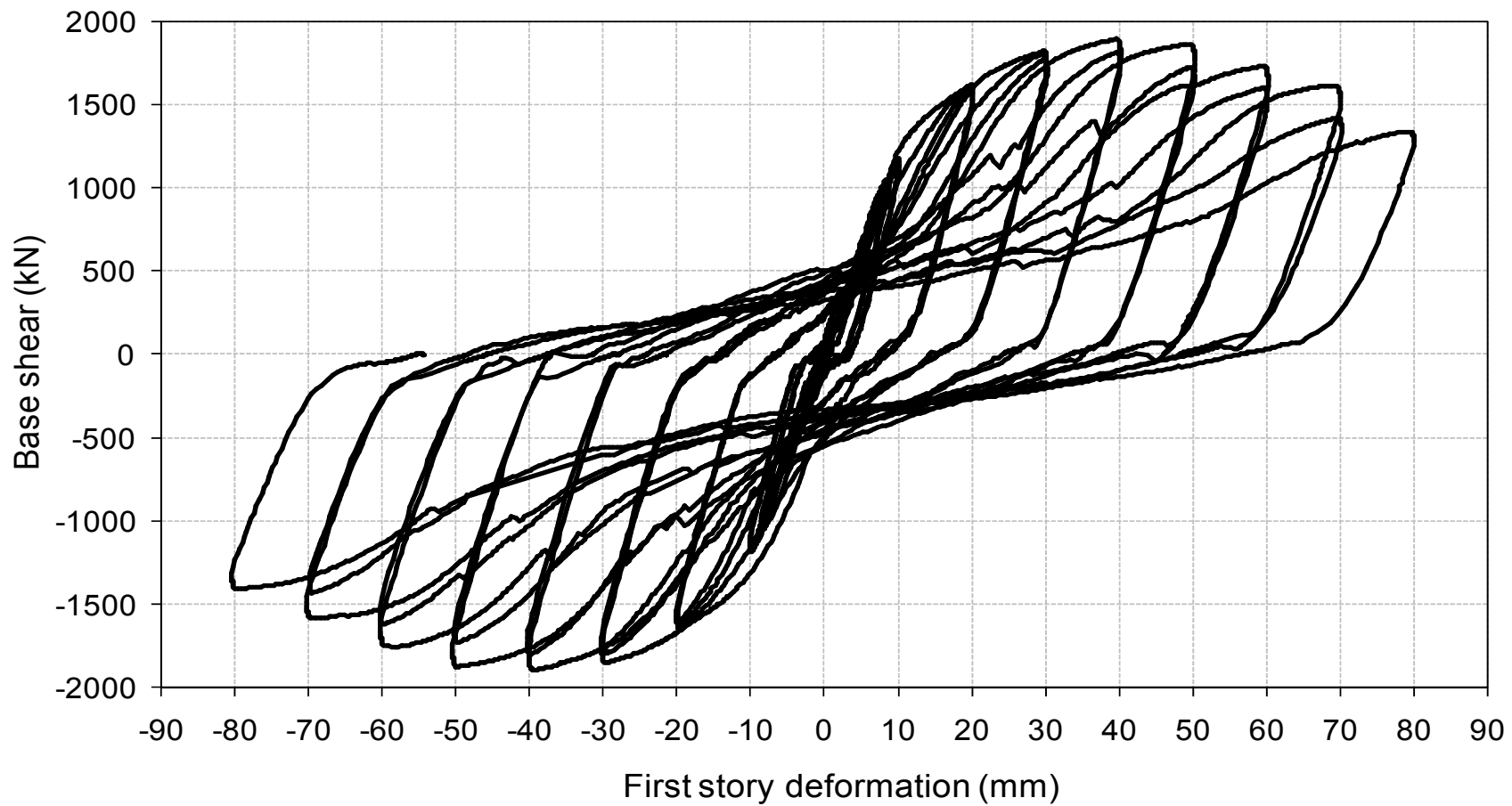


Figure 6.15: Base shear versus first story deflection in the RBS test

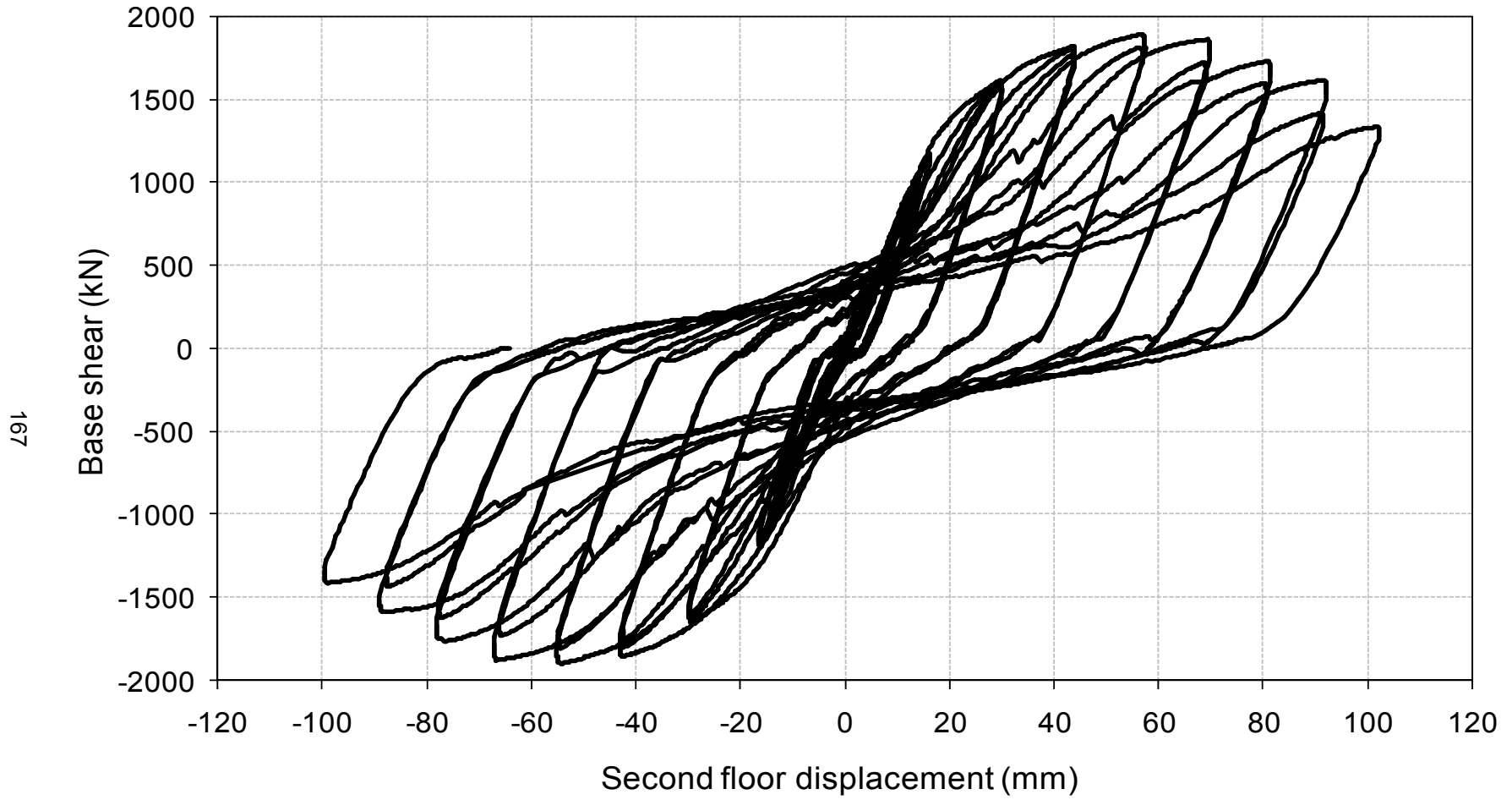


Figure 6.16: Base shear versus second floor displacement in the RBS test

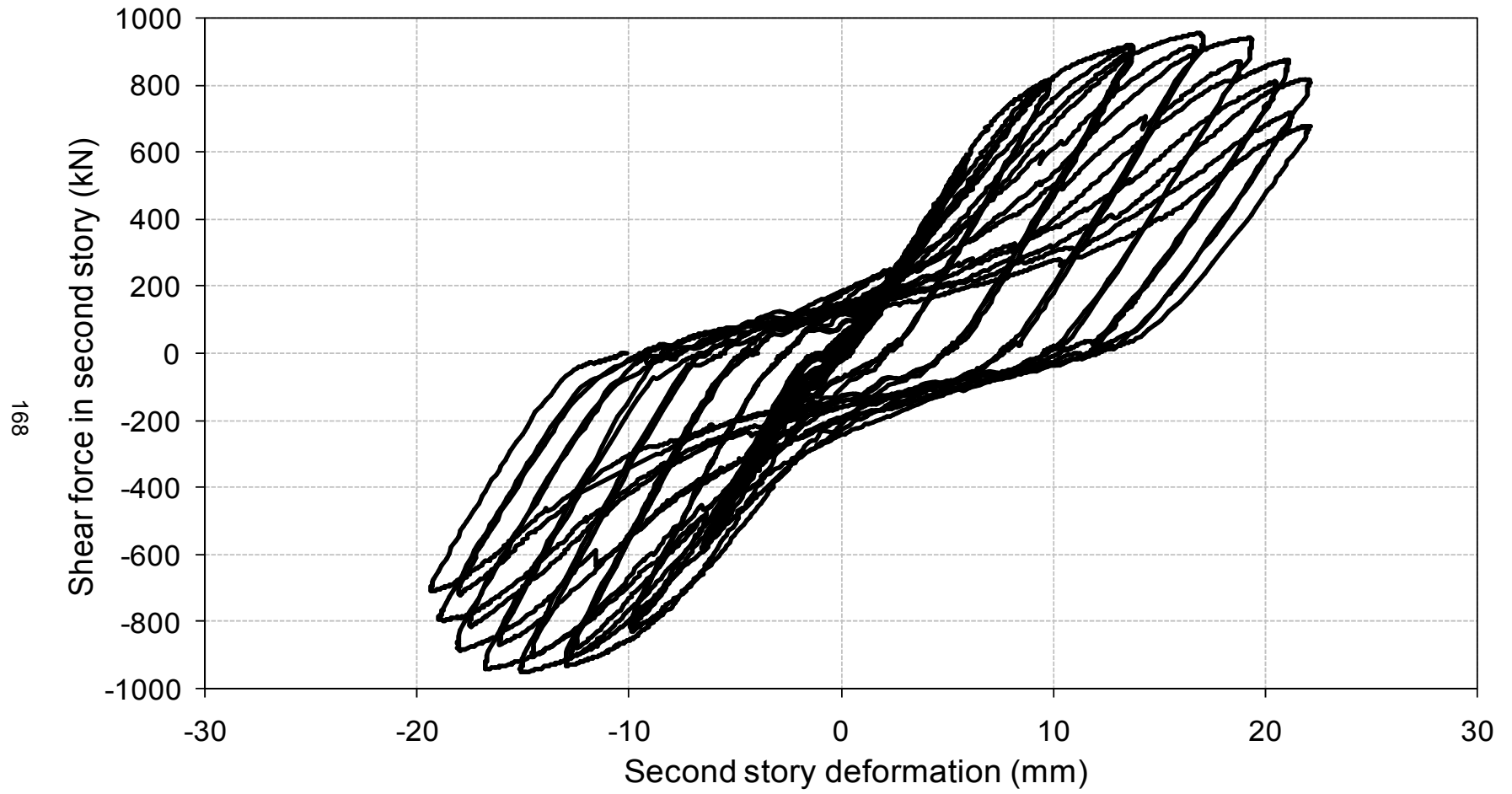


Figure 6.17: Shear force in the second story versus second story deflection in the RBS test

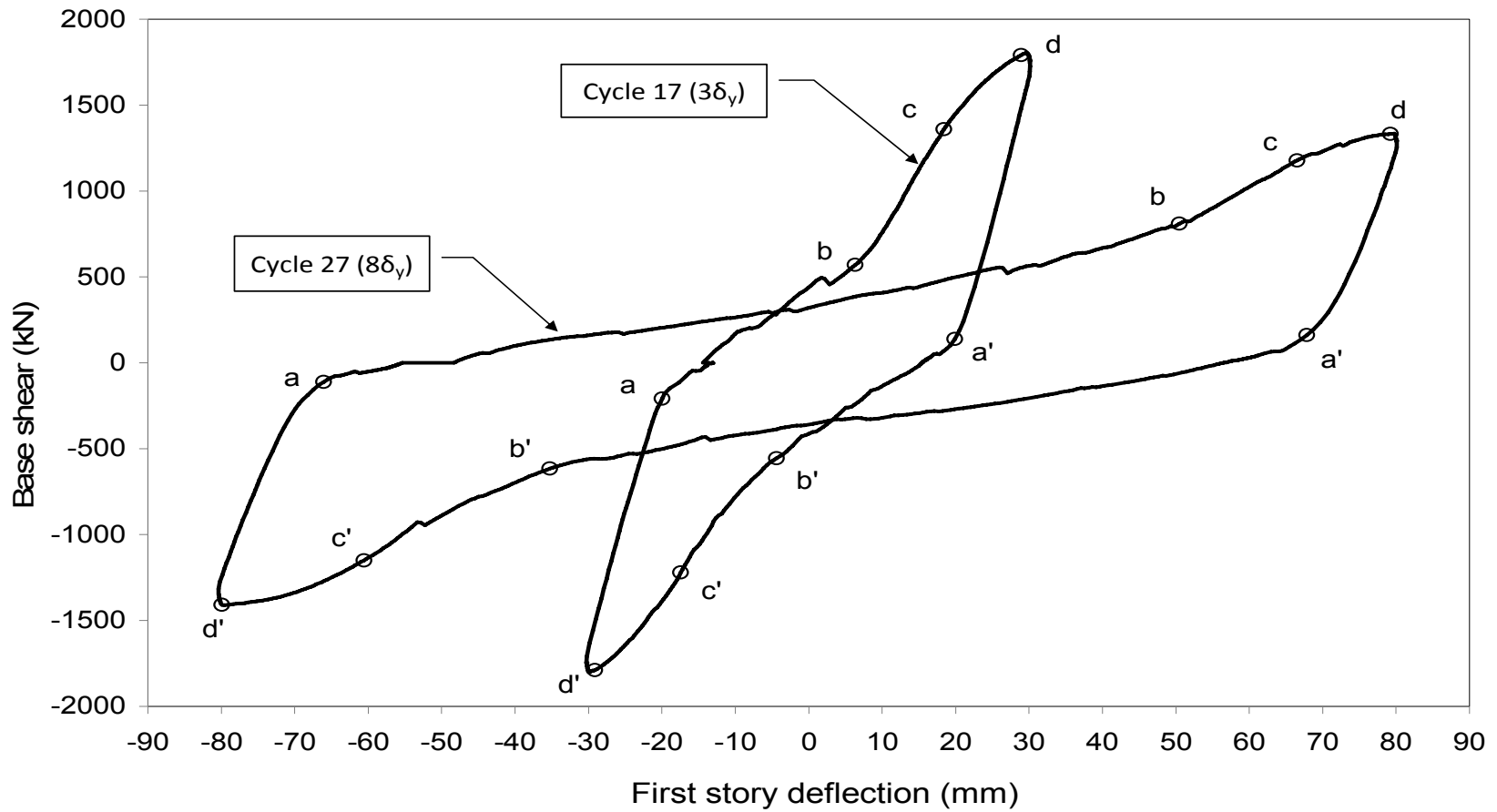


Figure 6.18: Hysteretic loops of cycles 17 and 27 of the RBS test

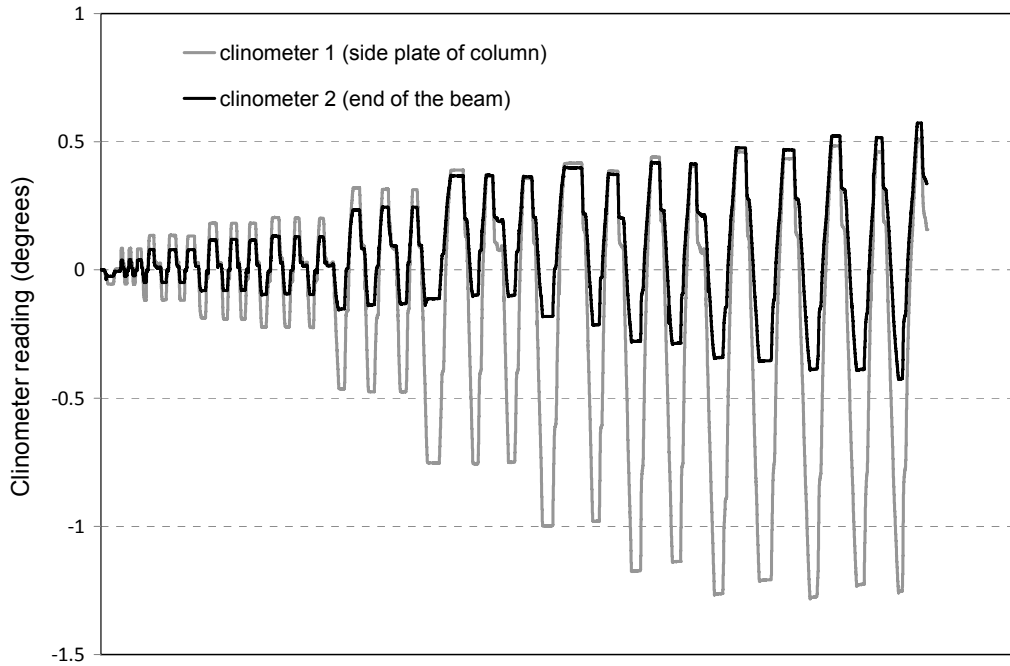


Figure 6.19: Rotation history of the side plate of column and end of the beam in the first floor of the RBS test specimen

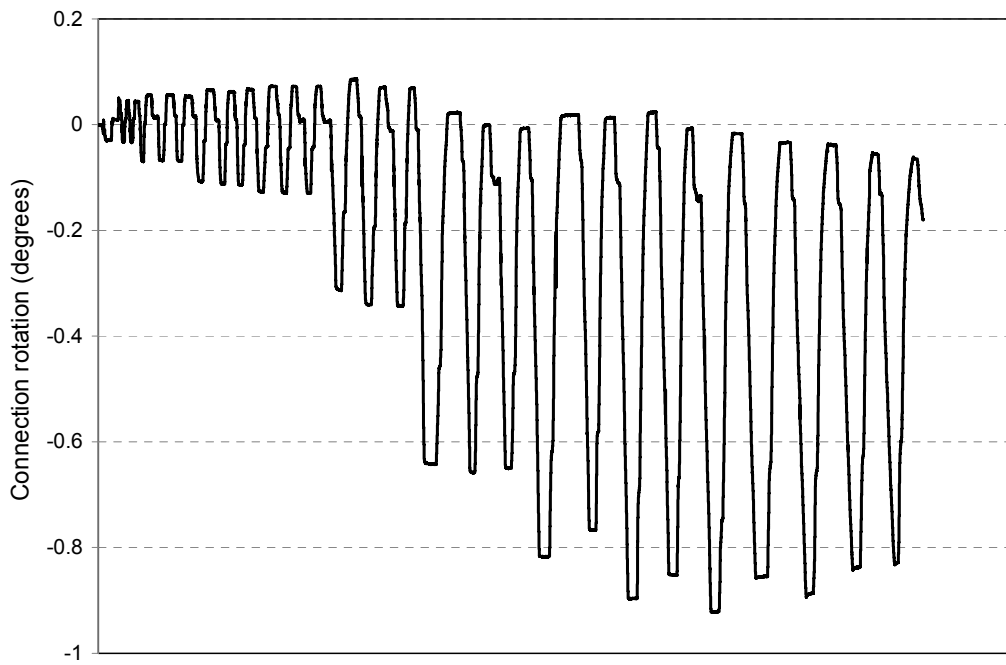


Figure 6.20: Rotation history of the frame connection in the first floor during the RBS test

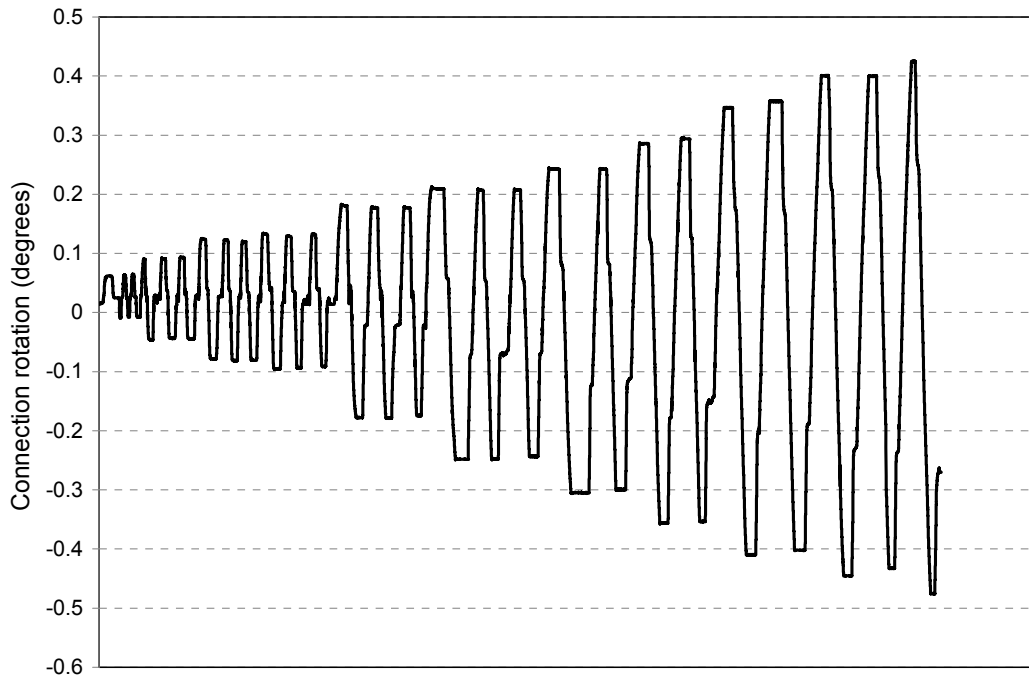


Figure 6.21: Rotation history of the side plate of column in the second floor of the RBS test specimen

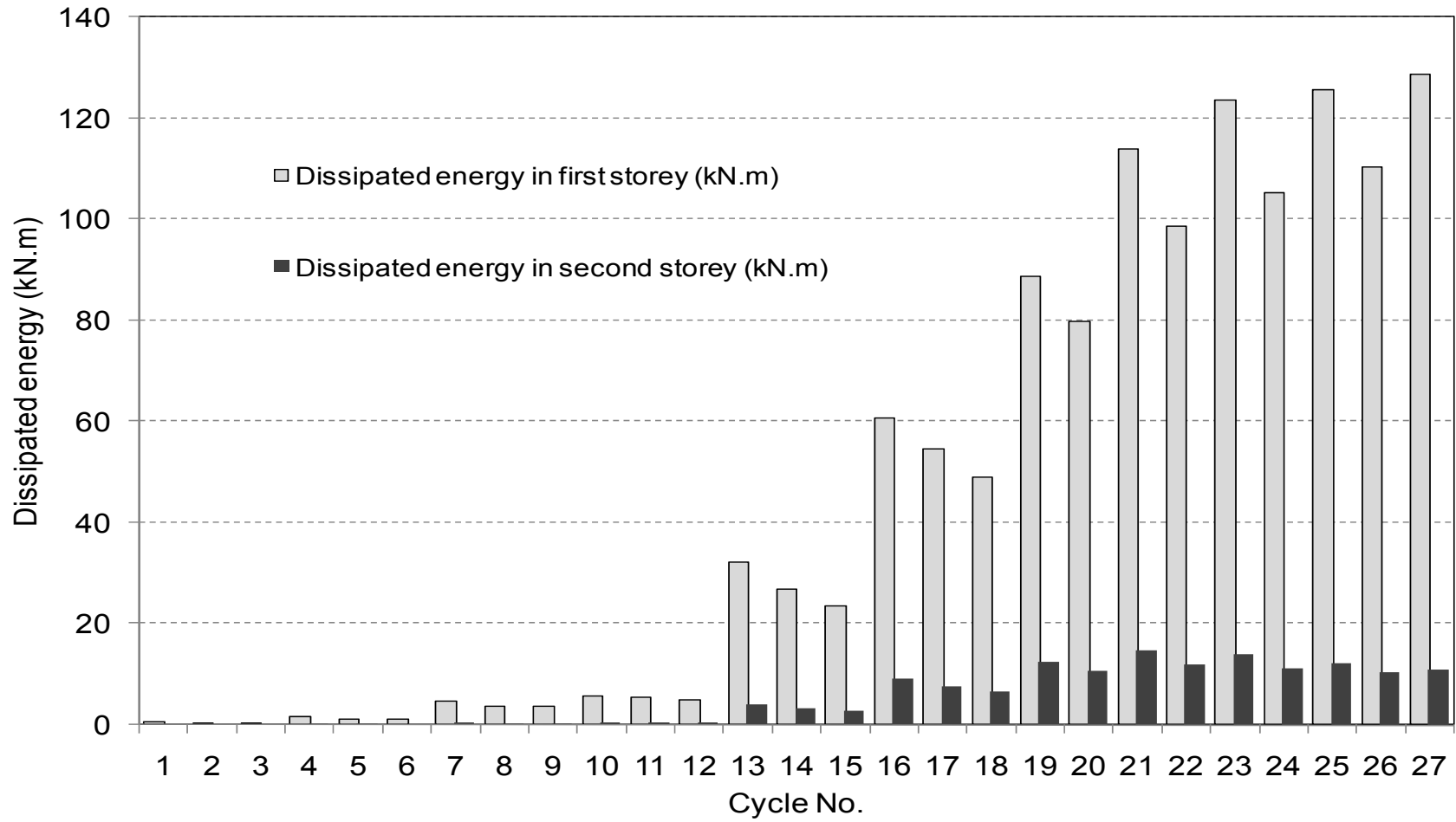


Figure 6.22: Amount of the dissipated energy in each cycle of the RBS test in the first and second storeys

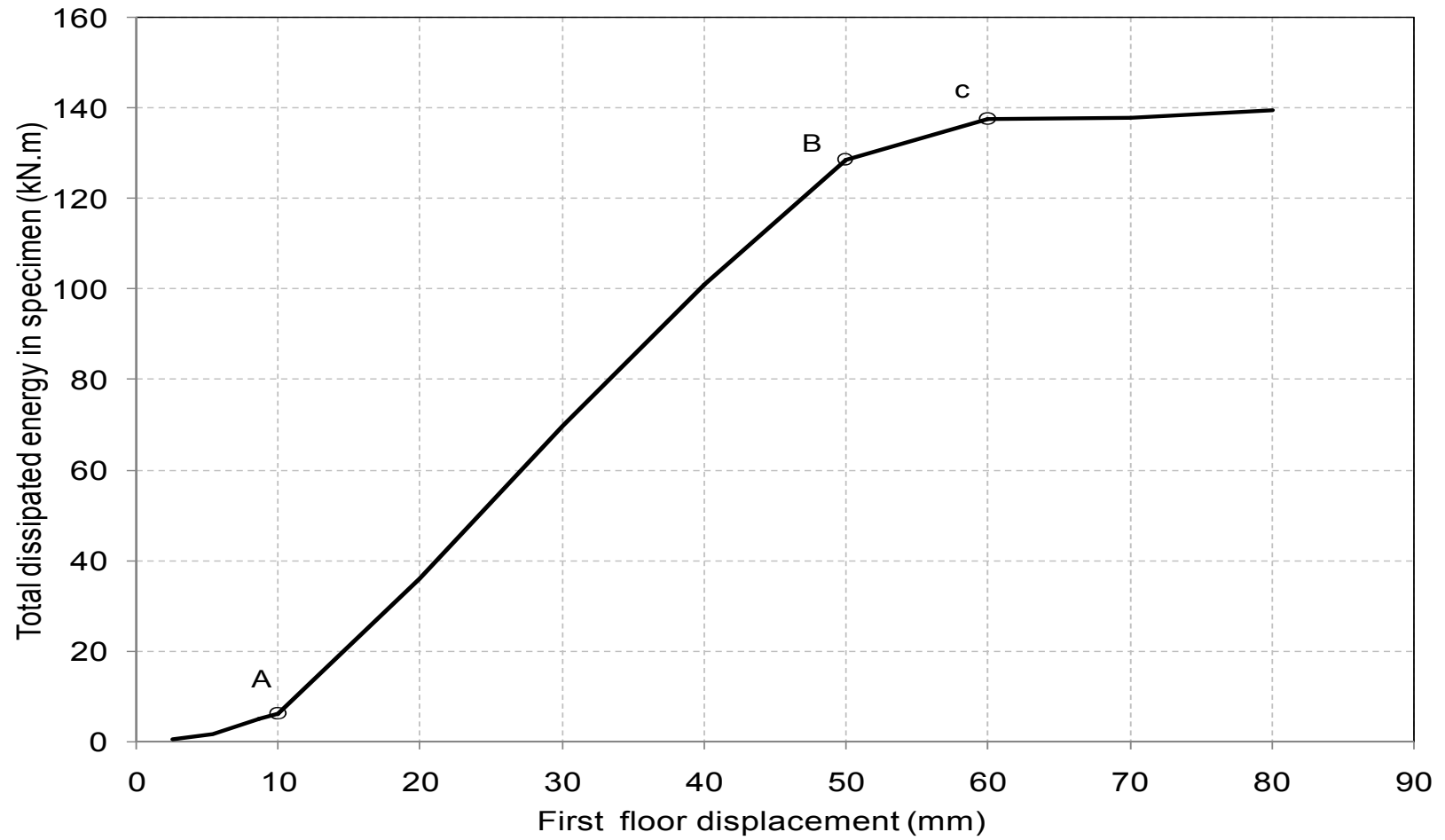


Figure 6.23: Total dissipated energy versus first floor displacement in the RBS test

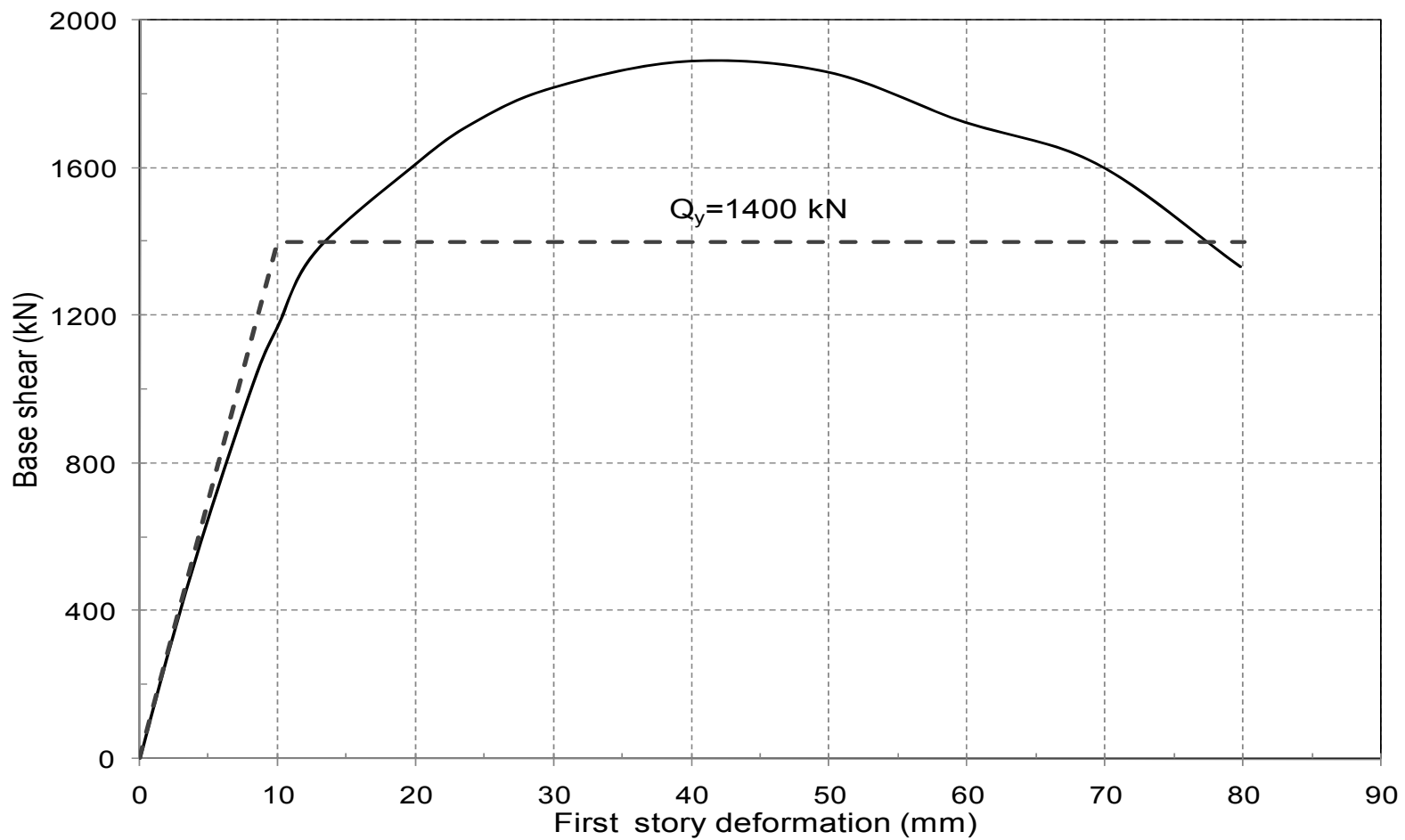


Figure 6.24: Envelope of the hysteretic loops of base shear versus first story deformation in the RBS test

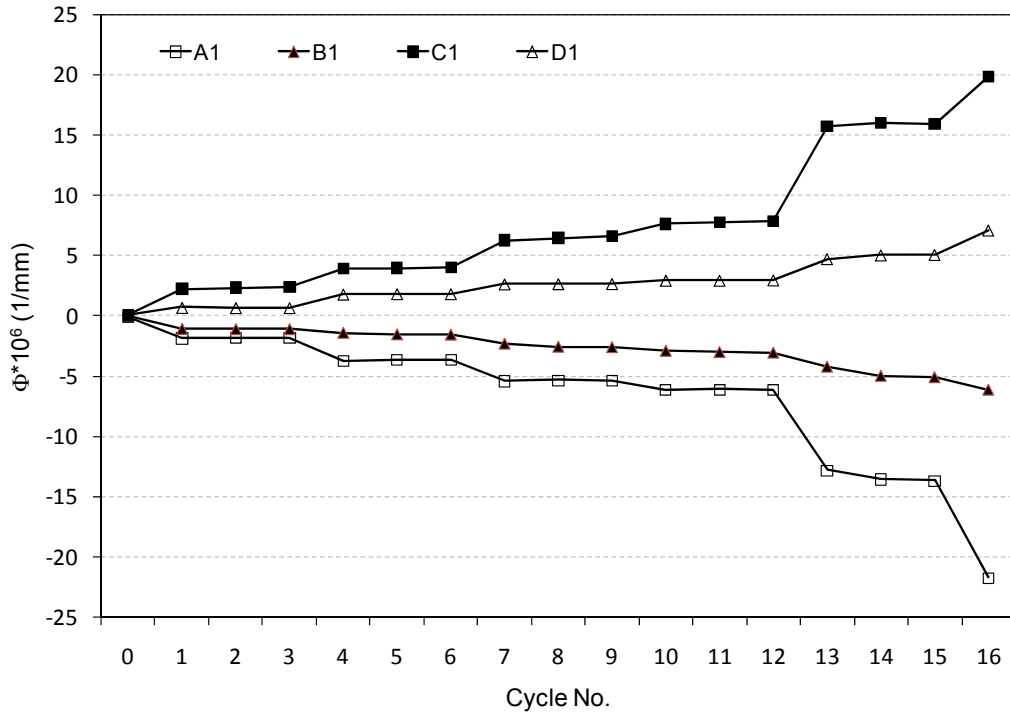


Figure 6.25: The curvature of the north column at four sections in cycles 1 to 16



Figure 6.26: Base of north column in cycle 16⁺ and initiation of new cracks, adjacent to the inner flange of column

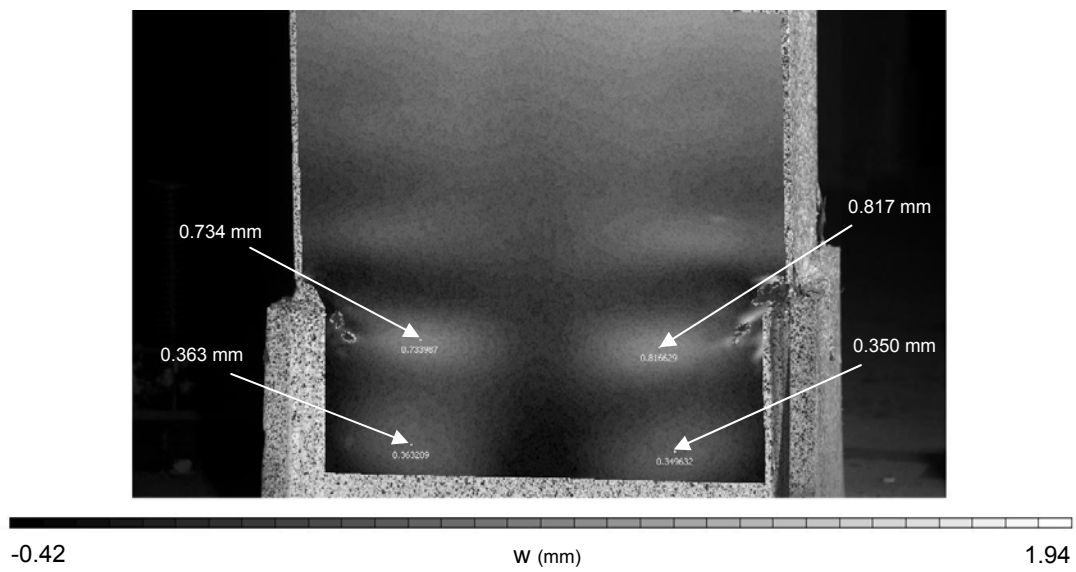
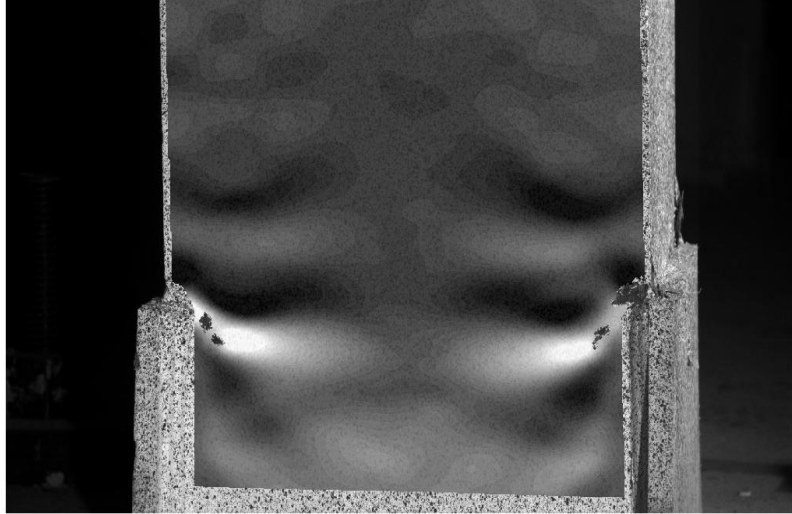


Figure 6.27: Out of flatness deformation of outer flange of north column in cycle 18⁺



-2.1

eyy(%) - Lagrange

4.1

Figure 6.28: Vertical strain distribution in outer flange of the north column in cycle 18⁺



-0.005

e1(%) - Lagrange

0.76

Figure 6.29: Maximum principal strain distribution in concrete at the base of the north column in cycle 4⁻

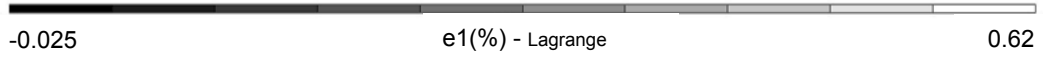
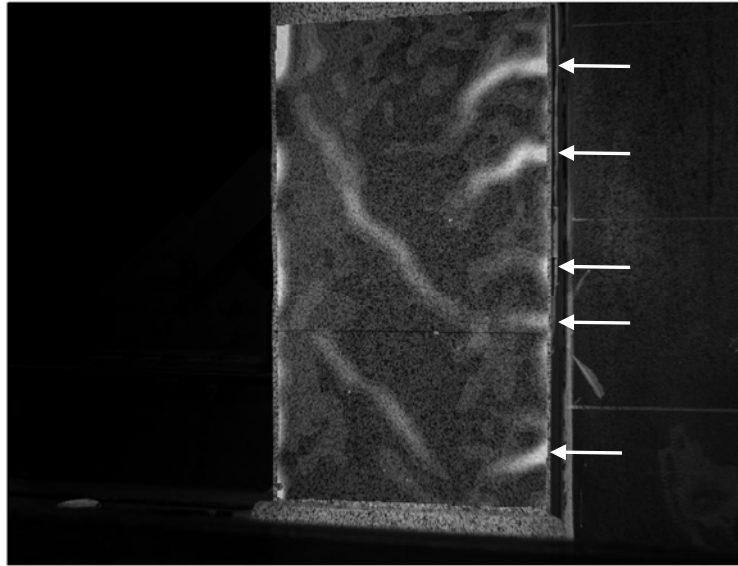


Figure 6.30: Maximum principal strain distribution in cycle 13⁺, showing the locations of the flexural cracks adjacent to the inner flange of column

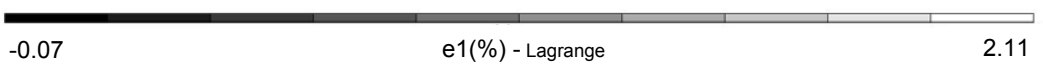


Figure 6.31: Maximum principal strain distribution in cycle 19⁺

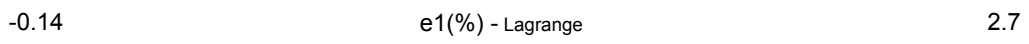


Figure 6.32: Maximum principal strain distribution in cycle 21⁺

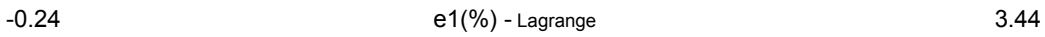


Figure 6.33: Maximum principal strain distribution in cycle 23⁺

7. COMPARISONS AND DISCUSSION OF TEST RESULTS

7.1 Introduction

One of the main differences between the modular test specimen and the RBS test specimen is the method of construction; the frame connections are shear connections in the modular specimen and moment-resisting connections in the RBS specimen. The comparison of the results of these two tests shows that the modular construction scheme did not affect the results greatly. The detail of the links in the columns was similar in the first story of both specimens. The benchmark test specimen (Deng et al. 2008) had different detailing in the columns, as, unlike the modular and RBS test specimens, it did not have the longitudinal rebars at the bases of columns. The spacing of the links was 50 mm close to the base of the columns in the modular and RBS test specimens, while it was 80 mm in the benchmark test. In other words, the concrete at the bases of the PEC columns in the modular and RBS test specimens was more confined with a lower stress level compared to the benchmark test specimen, resulting in better overall performance.

In this chapter, some key results of the benchmark test, modular test and RBS test, such as typical hysteretic loops, the envelope of the hysteretic loops, frame connection rotation, and ductility and energy dissipation capacity, are compared. Also, the crack depth in the concrete portion of the columns is studied to properly identify the effective moment of inertia of the columns. At the end of this chapter, the results of the RBS test are used to compare the accuracy of the constructed P-M interaction diagrams and the interaction formula in CSA standard S16-09 (CSA 2009).

7.2 Typical hysteretic loops

In Figure 7.1, the hysteretic loops of cycles with a maximum first-story deflection of close to 50 mm are plotted for the three tests. The first story of the benchmark test specimen

experienced 49 mm deformation in cycle 26, while in the modular test, the deformation of the first story reached 51 mm in cycle 24 and in RBS test, the first story deformation reached 50 mm in cycle 22. In all three tests, the outer flanges at the bases of the columns tore completely in these cycles.

The slopes of the hysteretic loops in the pinched part, where the tension field in the infill plate of the first story was reorienting so that the only lateral load resisting part of the system was the boundary frame, are similar. Considering the similar situation at the bases of the columns, i.e., the completely torn outer flanges, the only significant difference between the frames of the three test specimens was the frame connection type. It is an indication that the connection type had a negligible effect on the stiffness of the frames at this stage.

As the test specimens approached their maximum deformations in the above-mentioned cycles, the modular and RBS specimens showed similar load versus deformation behaviors, with very close maximum base shear values. The small differences can be attributed to the additional two cycles that the modular specimen had undergone that could have caused more damage in the modular specimen. The benchmark test specimen reached a smaller maximum base shear of around 80 percent of that of the other two tests, which was mainly due to the excessive concrete crushing at the bases of the columns as well as the broken links in this region (Deng et al. 2008).

During the unloading of the test specimens, the hysteretic loops of all three specimens had the same slope (145 kN/mm). A linear numerical analysis, which will be discussed in the next section, showed that the contribution of the frame in the initial stiffness of the steel plate shear wall was approximately 15 percent. As the outer flanges of columns in all three specimens were completely torn at the base, the lateral stiffness of the frames were affected and reduced compared to the initial stages of the tests; thus, it can be

concluded that the stiffness of the specimens in the unloading stage of the above-mentioned cycles was mostly provided by the infill plates.

Figure 7.2 depicts the hysteretic loops of cycles during which the maximum base shears were attained in the three tests. The hysteretic loop of the benchmark test has higher slopes in the pinched part and the unloading part. The higher stiffness of the benchmark test (28 kN/mm) compared to the other two test specimens (18 kN/mm) in the pinched part is attributed to the surrounding frame stiffness. The slope of the unloading part of the hysteretic loop of the benchmark test (175 kN/mm) is also higher than that of the other two tests (165 kN/mm) and the higher frame stiffness is the main cause of the difference.

7.3 Envelope of the hysteretic loops and ductility

Figure 7.3 shows the envelopes of the hysteretic loops of the first story of the three specimens. The initial parts of the envelopes of the modular test and the benchmark test coincide and have the same slope (i.e., the same initial stiffness). The RBS test showed a smaller initial stiffness. As the initial stiffness of steel plate shear walls is provided primarily by the infill plates, the difference between the envelope curves of the RBS test specimen and the benchmark and modular test specimens lies in the infill plate behavior. The path of the curve in the initial part of the tests, where specimens were behaving relatively elastically, was found to be dependent on the shape of the initial out-of-flatness imperfection of the infill plate. Both the modular and the benchmark test specimens had similar infill plate imperfections, i.e., one half-wave, but with different maximum amplitudes. The maximum out-of-flatness values in the benchmark and modular test specimens were 12.6 mm and 38 mm, respectively, measured from the centerlines of the walls. The initial imperfection of the infill plate in the first story of the RBS test specimen included two half-waves, with a maximum out-of-flatness of 15 mm. Figure 7.4 shows the hysteretic loop of cycle 3 of the modular test and RBS test. As the infill plate in the RBS test specimen had to snap to one buckle-wave during the initial cycles, a small plateau

was observed in these hysteretic loops. As can be seen in Figure 7.3, as soon as the infill plate of the first story in all three tests had yielded completely at a base shear of around 1400 kN, the effect of the shape of the initial imperfection faded, and the envelope of the RBS test matched with the envelopes of the other two tests. A linear elastic model was created in SAP2000 (CSI 2010) to examine the initial stiffness of the specimens. As the connection rotations in the beginning of all the tests were close to zero, the frame connections were fixed in the model. The infill plate was modeled as a series of strips and, thus, the effect of the initial imperfection shape was not included in the model. The initial stiffness of the first story of the modeled steel plate shear wall was equal to 158 kN/mm and the stiffness of the first story of the frame alone was 26.5 kN/mm. The results indicated that close to 85 percent of the initial stiffness of the first story of the steel plate shear wall was provided by the presence of the infill plate.

The peak base shears of the modular and RBS test specimens were more than that of the benchmark test specimen, although the expected frame strength was more in the benchmark test compared to the other two specimens. The RBS test specimen attained the maximum base shear among the specimens. The connection type, i.e., RBS moment connection versus shear connection, caused the difference in the strength between the RBS specimen and the modular specimen. The modular test specimen showed higher strength compared to the benchmark test specimen, which was mainly due to the presence of the longitudinal rebars at the bases of the columns in the modular test specimen. The longitudinal rebars reduced the stress level in the concrete and postponed the crushing of concrete in compression. The longitudinal rebars also stopped the growth of the tear in the webs of columns. As shown in Figure 7.3, the peak base shear in the benchmark test was attained at a smaller story deformation compared to the other two tests, as the tear propagated with a higher rate in the outer flanges and web of its columns at the base. Also, the demand on the concrete at the base of the columns was higher in the benchmark test, as there were no longitudinal rebars, which led to crushing

and spalling of concrete in this region at a smaller story deformation compared the other two tests.

In the post-peak stage, the modular and RBS test specimens showed significantly better behavior compared to the benchmark test and the strength degradation happened at a much lower rate compared to the benchmark test. The presence of the longitudinal rebars at the base was found to have a significant impact on the post-peak behavior of the specimens. Tearing of the beam flanges at the first-floor frame connections was detected in the last cycles of the benchmark test, which could have a caused faster strength reduction in the benchmark test.

In Table 7.1, the displacement ductility, R , of the test specimens has been tabulated according to their peak base shears, 90 percent of their peak base shears, 80 percent of peak base shears, and 75 percent of their peak base shears. As all three specimens showed similar behavior up to 1600 kN, as shown in Figure 7.3, the yield displacement, δ_y , and yield base shear, Q_y , were assumed to be the same. The displacement ductility of the specimens at their peak base shears were close to each other. The modular test specimen exhibited the maximum displacement ductility at the peak base shear, which was mainly due to the significant frame connection rotations before the specimen reached its peak base shear; thus, the first story deflection was larger in the modular test compared to the other two specimens, which exhibited smaller frame connection rotations at their peak base shear.

At 90 percent of the peak base shear in the post-peak stage, the displacement ductility of the benchmark test specimen was three quarters of that of the modular test, while the displacement ductility of the RBS test specimen was close to that of the modular test specimen. The main reason for the difference was the longitudinal rebars at the base, which let the modular and RBS test specimens undergo significantly larger displacements than the benchmark test with 10 percent strength degradation.

The modular test was not continued long enough for its ductility to be calculated for 80 percent and 75 percent of the peak base shear in the post-peak stage. The trend of the envelope curves shows that the behavior of the modular test specimen was close to that of the RBS test specimen in this region. The displacement ductilities of the benchmark and RBS test specimens were, respectively, 6.0 and 7.7 at 75 percent of the peak base shear in the post peak stage, or about 1400 kN, i.e., a base shear close to the yield base shear (Q_y).

Figure 7.5 depicts the envelope of the hysteretic loops of the second-story shear versus second-story deformation in the modular and RBS tests. The two specimens showed similar behaviors up to the story shear of 600 kN. The frame connections of the modular test specimen in the second floor rotated for the first time in cycle 13 when the second story shear was 700 kN. The rotation of the frame connections in the second floor increased the ductility of the second story and subsequently, more energy was dissipated in the second story of the modular test specimen compared to the RBS specimen.

In the RBS test specimen, the story shear reduced in the last cycle without any increase in the story deformation compared to the previous cycle, which was mainly due to the formation of a soft story mechanism in the first story as plastic hinges fully developed at the tops of the columns in that story. The complete detachment of the infill plate from the south column of the first story in cycle 26 expedited the formation of the soft story mechanism.

7.4 First floor beam-to-column connection rotations

The rotation of the beam-to-column connections in steel plate shear wall systems has been found to have a significant effect on the behavior of the system. The rotation of the frame connections let the panels deform like a parallelogram, which causes a more uniform tension field stress distribution in the infill plates.

The rotation histories of the first floor frame connections of the modular and RBS test specimens are shown in Figure 7.6. The maximum frame connection rotation range in the modular test (equal to 3.0 degrees) happened in the last cycle and the maximum frame connection rotation in the RBS test happened during cycle 23, with a range of 0.9 degrees. As can be seen in Figures 5.16 and 6.21, the rotations of the side plate at the frame connections in the second floor of the modular specimen were larger than those of the RBS test. The effect of the second floor frame connection rotation can be seen in the hysteretic loops of the second story in Figures 5.12 and 6.17. The second-story deformations in the modular test were almost twice those of the RBS test, even with smaller first floor displacements. By looking at the hysteretic loops of cycles 26 and 27 in these figures, it can be seen that in the modular test, the second story deformation in cycle 27 was larger than that of the cycle 26; however, in the RBS test, the second story deformations were the same in cycles 26 and 27.

7.5 Energy dissipation capacity

One of the most important characteristics of an earthquake load resisting system is its ability to absorb and dissipate the energy that is introduced into the structure by inertial forces during an earthquake. In previous chapters, the energy dissipation capacities of the modular and RBS test specimens have been discussed. The calculated amounts of dissipated energy in all cycles of the three tests are plotted in Figure 7.7. The benchmark test included 30 cycles, whereas the modular and RBS tests included 27 cycles, although the maximum story deformations were higher in the modular and RBS tests.

To better compare the energy dissipation capacities of the specimens, the dissipated energy in the first cycle of each stage of displacement has been plotted versus the first floor displacement in Figure 7.8. The modular test specimen dissipated the most energy with the same story deformation between the three specimens. It was mainly due to the frame connection rotations, which caused the infill plate to dissipate more energy as

there was a more uniform tension field in the infill plate of the modular test specimen. All three specimens dissipated a small amount of energy at displacements of less than 10 mm, which indicates that significant yielding began in all three specimens when the first floor displacement was close to 10 mm. The rate of increase in energy dissipation capacity after 10 mm of floor displacement was almost the same in all three specimens up to the point that the outer flange of the columns started to tear at the base. In the benchmark test, the flange tearing started when the first floor displacement was about 35 mm and after this point the rate of increase of energy dissipation decreased. The flange tearing in the columns of the modular and RBS test specimens started when the first floor displacements were 34 mm and 30 mm, respectively. As can be seen in Figure 7.8, due to the presence of the longitudinal rebars, the initiation of flange tearing did not affect the energy dissipation capacity of these specimens. The outer flanges of the columns tore completely in all three specimens at a floor displacement of close to 50 mm. At this point, part of the web was detected to be torn. The energy dissipation capacity of the benchmark test decreased noticeably at this point, while in the other two specimens, just the rate of increase in energy dissipation decreased. The crushing of concrete was another important parameter influencing the energy dissipation capacity of the specimens. The longitudinal rebars at the bases of the columns postponed the crushing of concrete, which prevented the decline of the energy dissipation capacity for the modular and RBS specimens in the last cycles of these tests.

7.6 Effective moment of inertia of PEC columns

The locations of the neutral axis at column sections A1, B1 and C1 (see Figures 4.12 and 4.13) were determined in both the modular and RBS test specimens in cycle 13, while the base shear was approximately 1400 kN. As mentioned in Chapters 5 and 6, the infill plate of the first story of both the specimens yielded completely when the base shear reached 1400 kN and no local buckling was observed in the flanges of columns. In the first half of cycle 13, the whole cross section of the north column was in compression (i.e., the

neutral axis was out of the cross section at all three sections). This indicates that the effective moment of inertia, I_e , was equal to the moment of inertia of the uncracked cross section. In steel units, this moment of inertia is:

$$I_e = I_s + \frac{1}{n} I_c \quad (7.1)$$

where I_s and I_c are, respectively, the moment of inertia of the steel and concrete parts of the cross section of the PEC column, and n is the ratio of the moduli of elasticity of steel to concrete, which was equal to 9.6 in both the modular and RBS tests.

In the second half of cycle 13, where the north column was subjected to smaller compressive forces, the depth of the crack was observed to be very close to one-half of the column depth (i.e., 125 mm); thus, by assuming that the center of the gravity of the cracked section is on the neutral axis in the mid-height of the section, the effective moment of inertia (I_e) can be estimated for this case as follows:

$$I_e = I_s + \frac{1}{2n} I_c \quad (7.2)$$

By referring to Equation (2.13), which was proposed by Tremblay et al. (2000b) to find the axial strength of PEC columns, the effective moment of inertia (I_e) can be calculated by the following equation:

$$I_e = I_s + \frac{1}{n} \left(\frac{0.6 I_c}{1 + D/T} \right) \quad (7.3)$$

In Table 7.2, the effective moments of inertia resulting from Equations (7.1), (7.2) and (7.3) and the corresponding flexibility parameters, i.e., column flexibility parameter (ω_n) and end-panel flexibility parameter (ω_L) in the top and bottom stories of the test specimens, are tabulated. The ratio D/T in Equation (7.3) was assumed to be equal to 0.35, as at least 65 percent of the compressive axial force in the column was introduced

by the over-turning moment and thus only a maximum of 35 percent of the axial load could have had long-term induced effect on the columns. The flexibility parameters calculated using the effective moment of inertia of column from Equation (7.3) are the largest, but they are very close to the values from the observed cracked cross section and thus the Equation (7.3) can be used as a conservative method of calculation of the effective moment of inertia of PEC columns. The resulting flexibility parameters, ω_h and ω_L , are within the allowed values in CSA S16-09 (CSA 2009).

7.7 Combination of axial compression and bending

In the design of the RBS connections, the PEC column under the side plate at the first floor had to be checked to make sure that the induced moment by the plasticized RBS connection would not cause failure of the PEC column in this region. For this purpose, the axial force and bending moment (P-M) interaction diagram of the PEC column was constructed by assuming a linear strain distribution in the section. The resulting interaction diagram is shown in Figure 7.9. The Canadian steel design standard, CSA S16-09 (CSA 2009), provides an interaction equation, Equation (2.22), and the related diagram is also plotted in Figure 7.9. According to the method proposed by Qu and Bruneau (2010), the moment induced by the RBS connection on the PEC column of the first story was found approximately equal to 160 kN. The axial compression at the top of the PEC column in the first story was approximately 2200 kN during cycle 16, where the plastic hinge fully developed within the RBS cut region. The corresponding point has been shown in Figure 7.9. As mentioned in Chapter 6, no column failure was detected in cycle 16 at the top of the columns of the first story of the RBS specimen. It can be seen that the method in CSA S16-09 (CSA 2009) is very conservative. However, the interaction diagram constructed by assuming a linear strain distribution predicts the failure of the PEC column under combined axial force and bending moment more realistically, since the moment and axial force combination at this stage had not yet caused failure of the cross section.

Table 7.1: Displacement ductility (R) of the first story of the test specimens at different load levels at the post-peak stage

	Benchmark test	Modular test	RBS test
δ_y	10	10	10
Q_y	1400	1400	1400
$\delta_{(p)*}$	35	43	40
$Q_{(p)}$	1817	1830	1890
$R_{(p)}$	3.5	4.3	4.0
$\delta_{(0.9p)*}$	48	64	62
$Q_{(0.9p)}$	1635	1647	1701
$R_{(0.9p)}$	4.8	6.4	6.2
$\delta_{(0.8p)*}$	56	-	73
$Q_{(0.8p)}$	1454	1464	1512
$R_{(0.8p)}$	5.6	-	7.3
$\delta_{(0.75p)*}$	60	-	77
$Q_{(0.75p)}$	1363	1373	1418
$R_{(0.75p)}$	6.0	-	7.7

* p: peak, 0.9p: 90% peak, 0.8p: 80% peak, 0.75p: 75% peak

Table 7.2: Effective moments of inertia of PEC columns of the modular and RBS test specimens and corresponding flexibility parameters

	Equation (7.1)	Equation (7.2)	Equation (7.3)
I_s ($\times 10^6$ mm ⁴)	54.2	54.2	54.2
I_c ($\times 10^6$ mm ⁴)	271.3	271.3	271.3
I_e ($\times 10^6$ mm ⁴)	82.5	68.3	66.8
ω_h	2.20	2.30	2.32
ω_L (top panel)	2.13	2.19	2.20
ω_L (bottom panel)	1.85	1.94	1.95

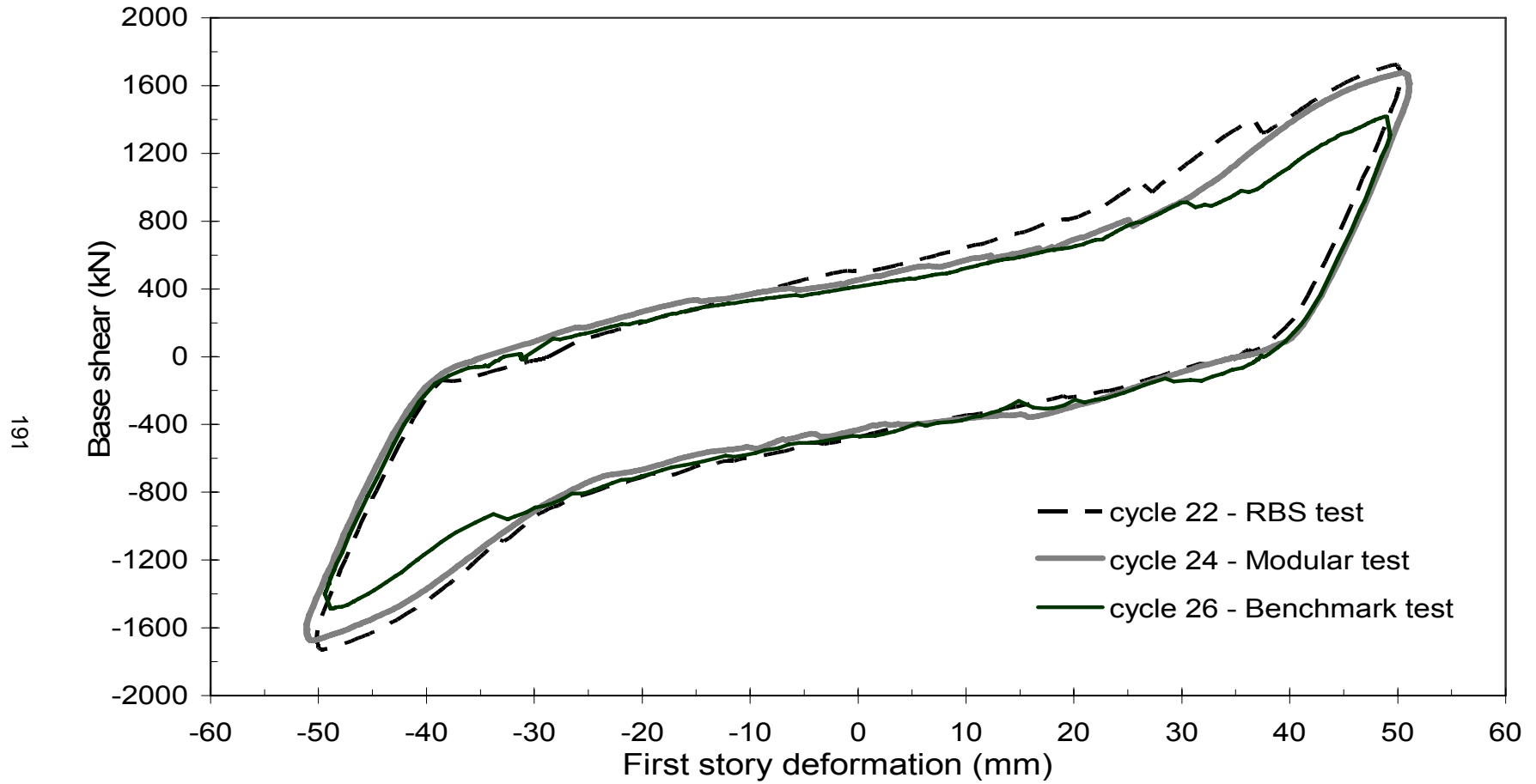


Figure 7.1: Hysteretic loops of cycles with story deformations of close to 50 mm

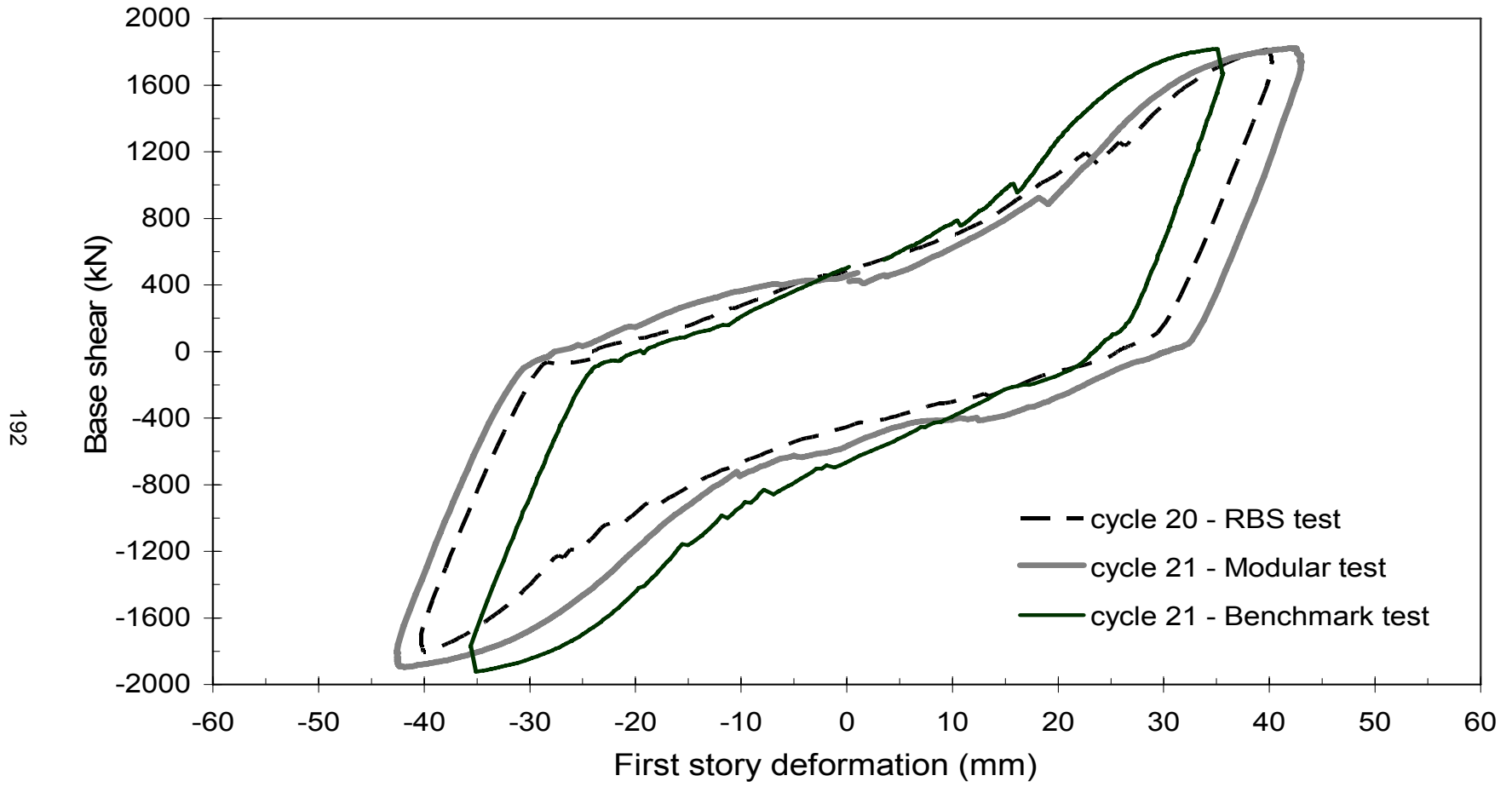


Figure 7.2: Hysteretic loops of cycles with the peak base shear

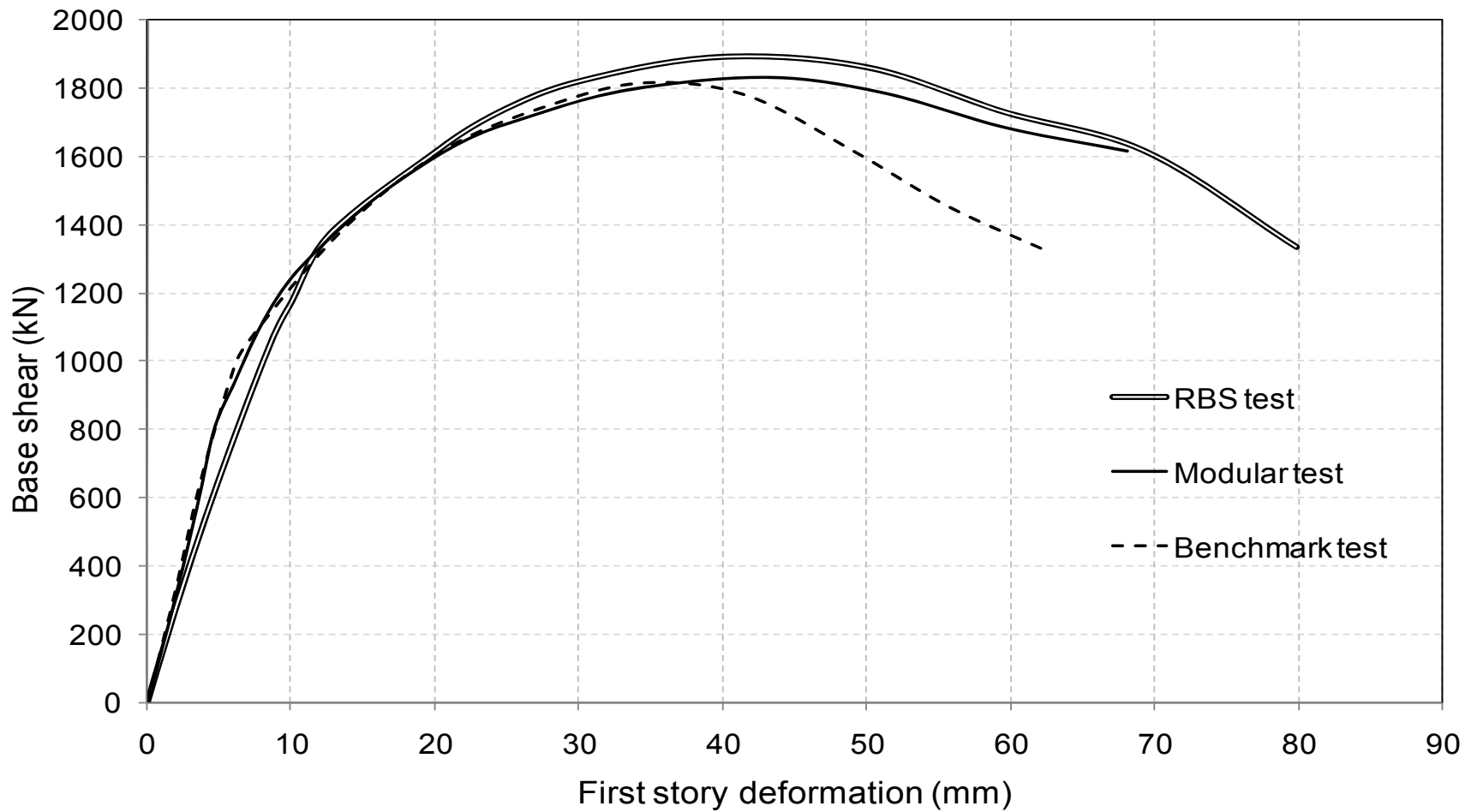


Figure 7.3: Envelope of hysteretic loops of first story of three test specimens

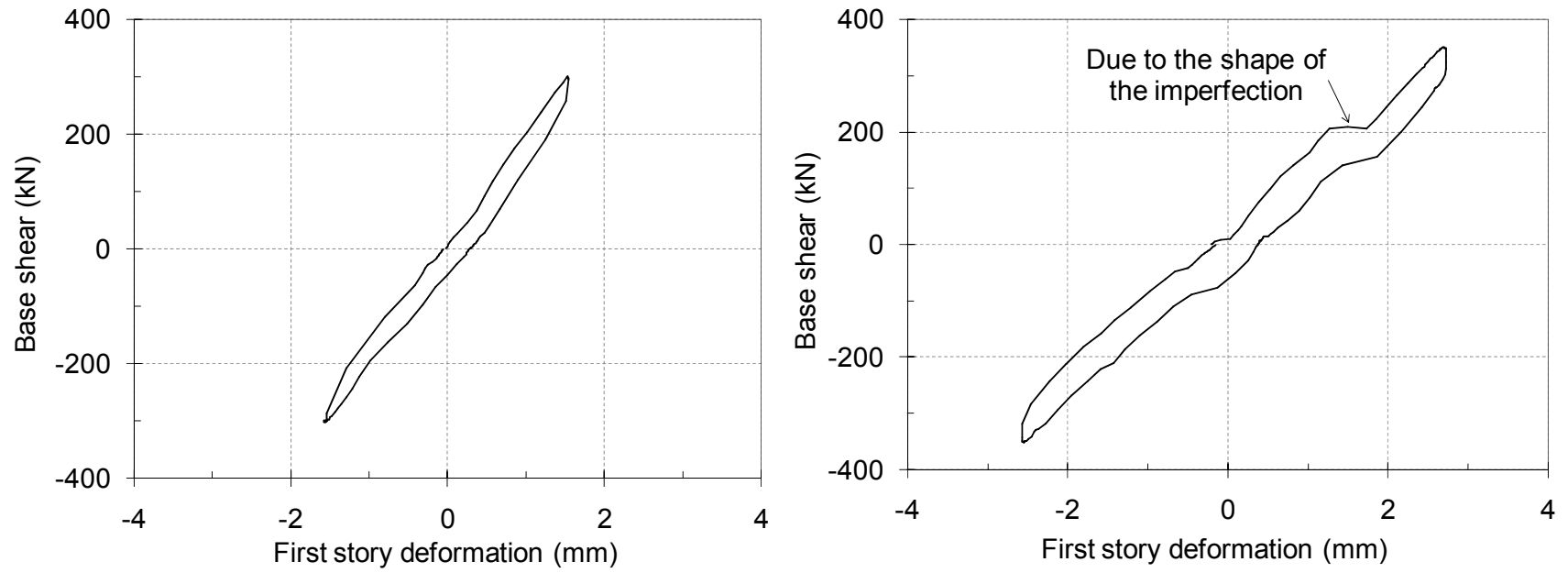


Figure 7.4: Hysteretic loop of cycle 3 of the modular test (left) and RBS test (right)

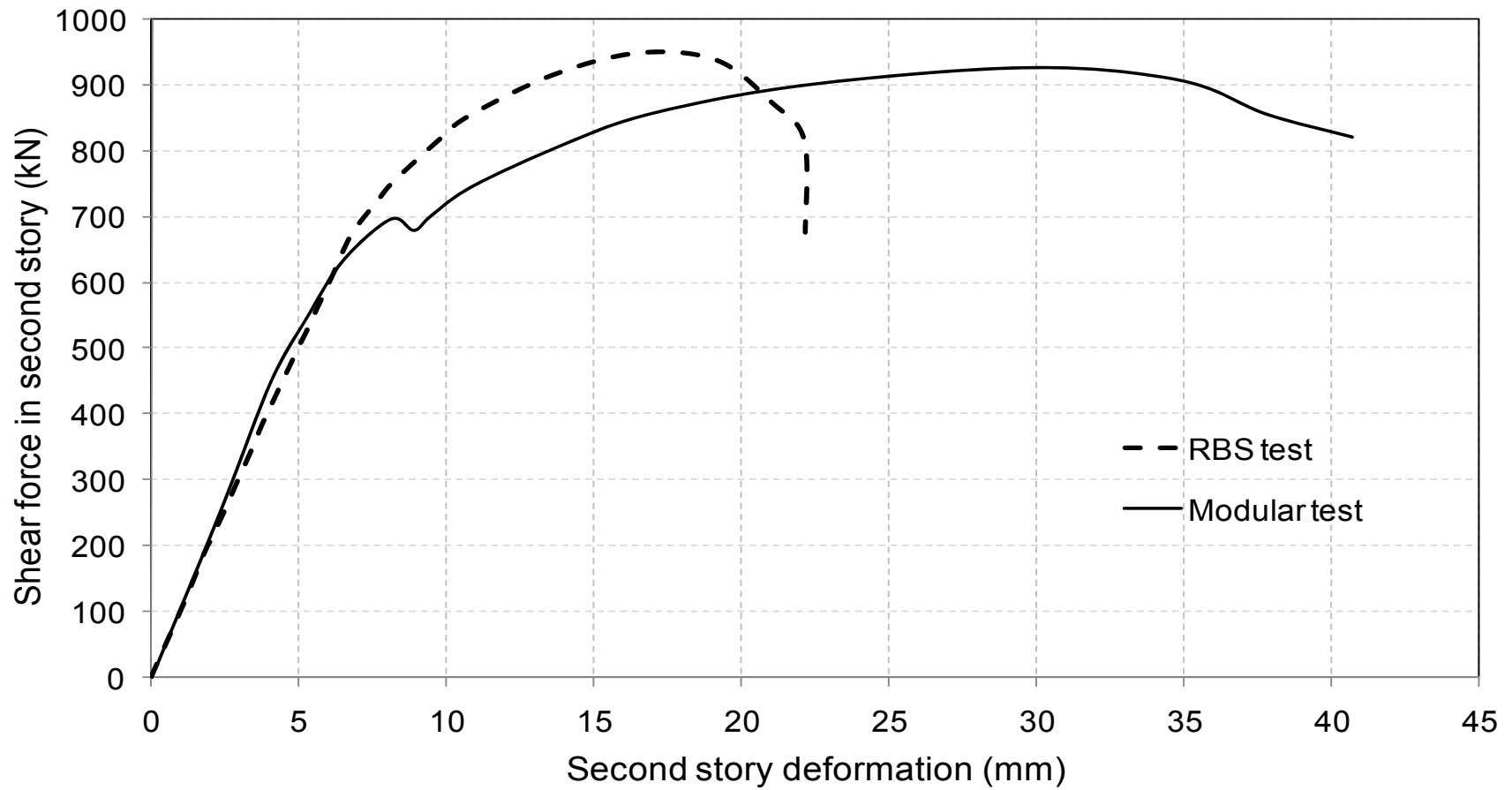


Figure 7.5: Envelope of the hysteretic loops of the second story of the modular and RBS tests

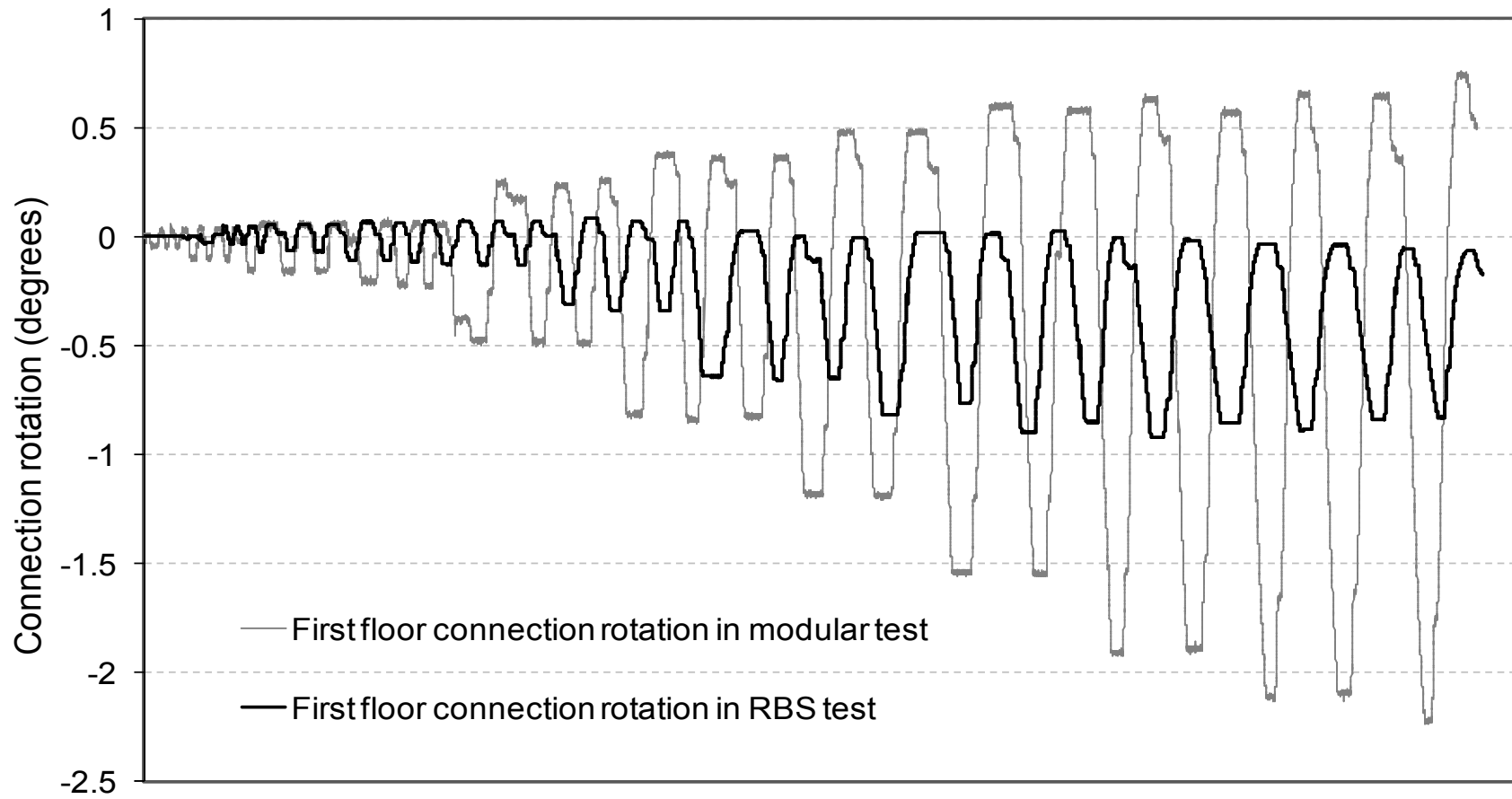


Figure 7.6: Rotation of the frame connection in the first floor during the modular and RBS tests

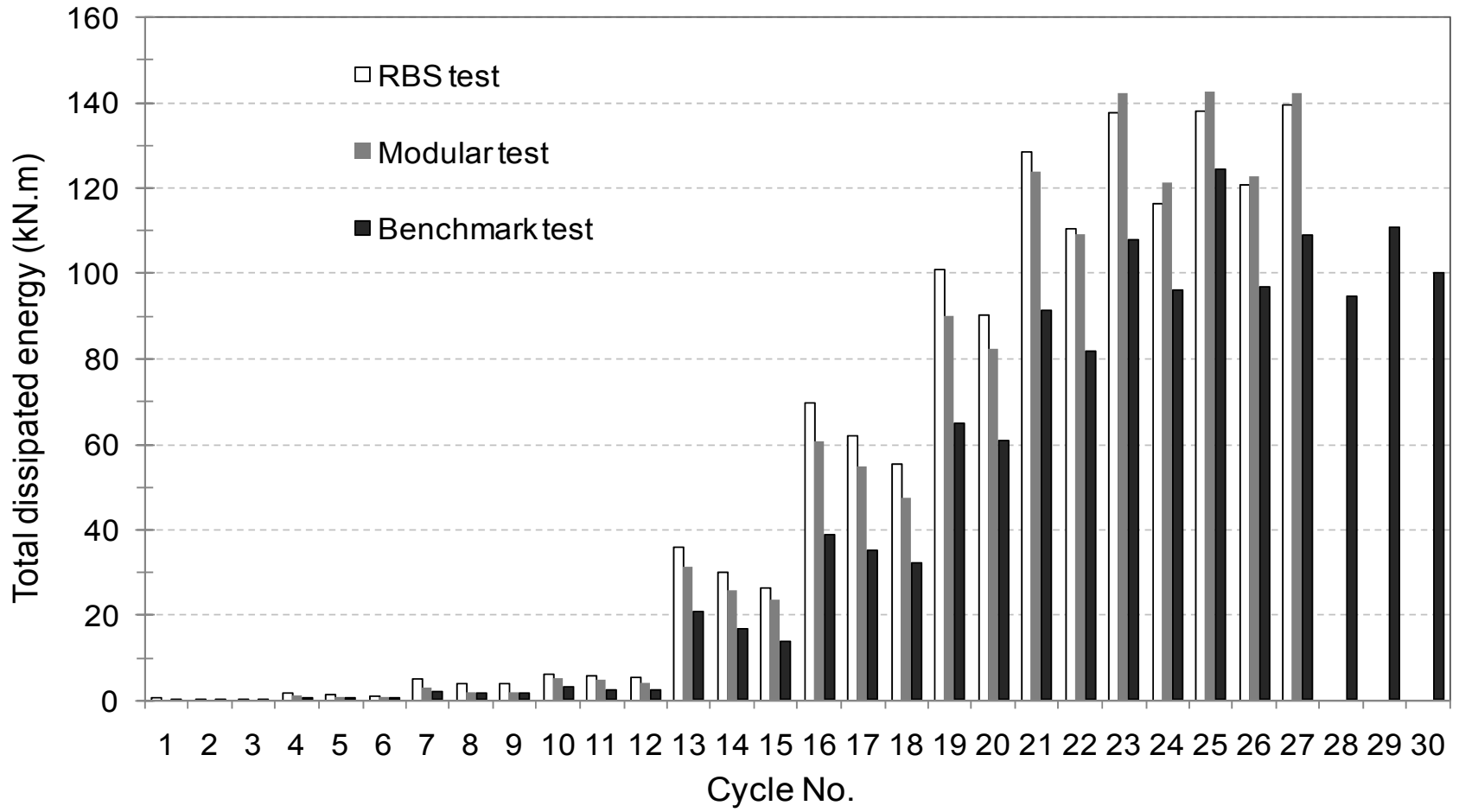


Figure 7.7: Total amount of the dissipated energy in each cycle during the benchmark, modular and RBS tests

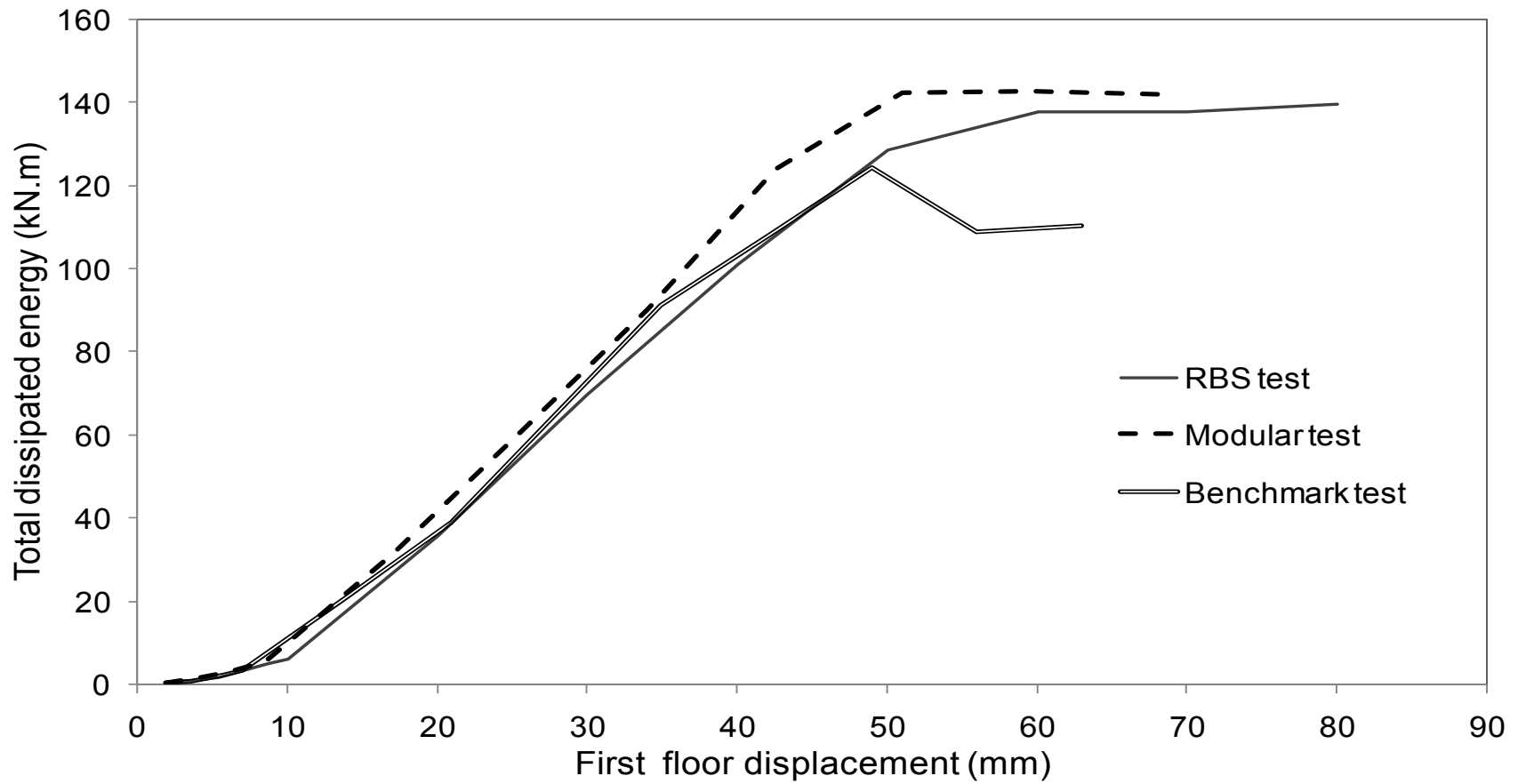


Figure 7.8: Total dissipated energy versus first floor displacement in the benchmark, modular and RBS tests

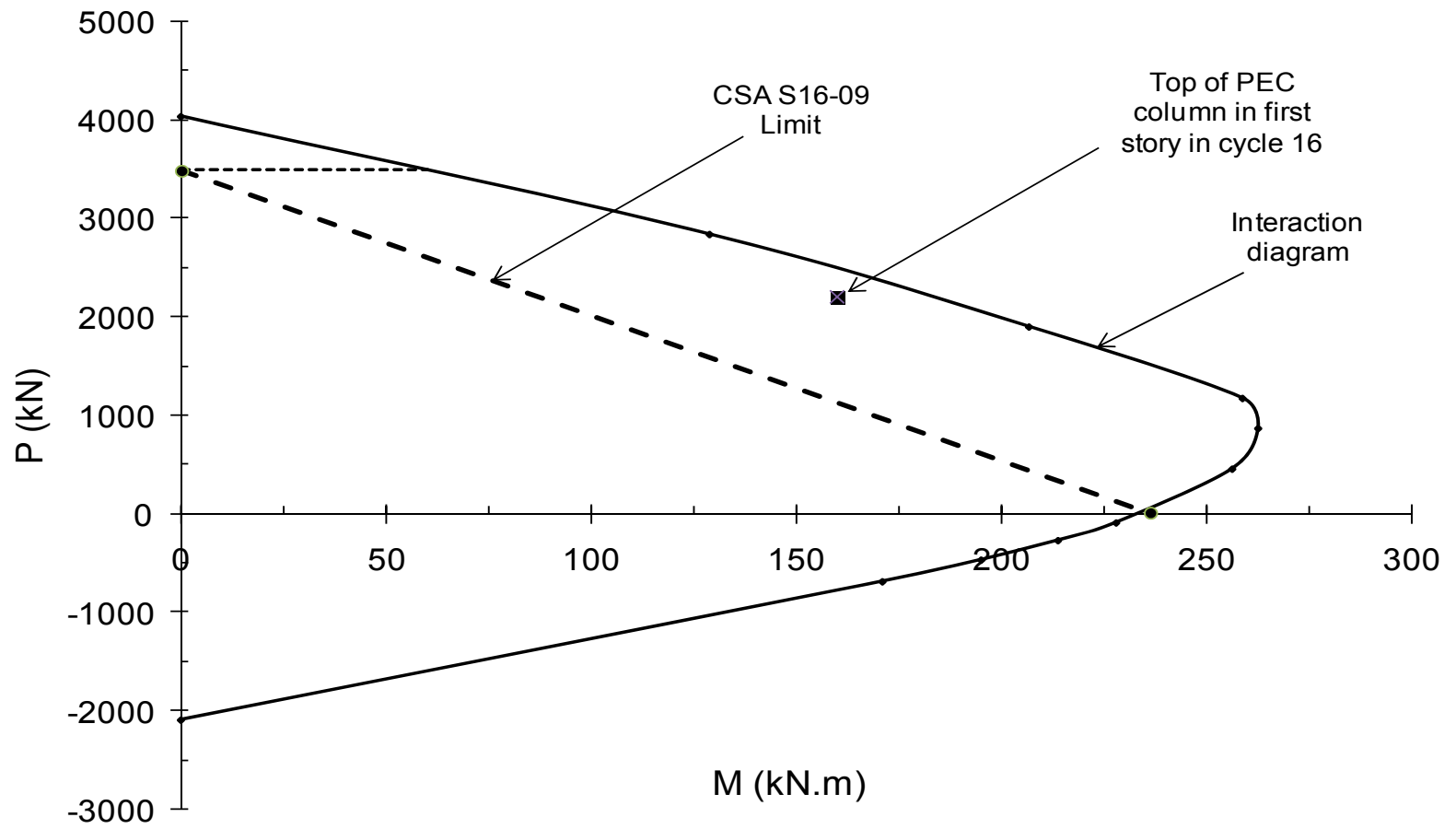


Figure 7.9: P-M interaction diagram for strong-axis bending of PEC column at top of the first story

8. SUMMARY, CONCLUSIONS AND RECOMMENDATIONS

8.1 Summary

This research consisted of two parts. Since the boundary frame members play an important role in steel plate shear wall systems by providing proper anchorage to the infill plate, the first part of this research was focused on the column flexibility parameter, ω_h , and the development of a suitable flexibility parameter to determine the minimum required flexural stiffness of end beams in the top and bottom stories of steel plate shear walls. An analytical study was done to develop the end-panel flexibility parameter, ω_L . In order to determine the upper limit of ω_L , an extensive parametric numerical study was conducted. The numerical study covered various parameters like panel aspect ratio (L / h), infill plate thickness and size effect. In order to investigate the effect of the beam-to-column connection rigidity on both ω_h and ω_L , a numerical study was conducted on full-scale models with various panel aspect ratios and infill plate thicknesses.

The second part of this research consisted of an experimental study on the behavior of two large-scale two-story steel plate shear walls with partially encased composite (PEC) columns with built-up H-shaped steel sections. The main objective of the experimental program was to study the behavior of PEC columns in the steel plate shear wall system, where columns are subjected to concurrent axial force and bending moment. The test specimens were subjected to both gravity loads and lateral loads. The lateral loads were gradually increased according to the instructions of ATC-24 (ATC 1992) until the specimens failed. Out of 27 cycles that were applied to each specimen, 15 cycles were in the inelastic range. Both specimens exhibited large initial stiffness and good ductility and energy dissipation characteristics. In the post-peak stage, the strength degradation was gradual and the behavior of both specimens at large deformations was stable. The PEC columns in both specimens failed at their base in a ductile manner.

Another objective of the experimental program was to examine the modular construction method in one of the specimens and the RBS connections in the other specimen. No severe problem was detected in the connections and infill plate until the last cycles of the modular test. The presence of the shear connections in the modular test specimen helped the infill plate of the second story enter the inelastic range and thus engaged more in the energy dissipation of the specimen. The fish plates were not damaged, which means that the infill plate could be replaced easily after the occurrence of a severe earthquake. The presence of the RBS connections in the RBS test specimen improved the overall behavior of the specimen as it postponed the formation of plastic hinges at the top of the PEC columns in the first story and thus the formation of a soft story mechanism. The location of the plastic hinge center within the cut was monitored. It was observed that a plastic hinge formed within the RBS cut closer to the column than the cut centerline.

8.2 Conclusions

8.2.1 Flexibility parameters in steel plate shear wall systems

The end-panel flexibility parameter, ω_L , can be calculated by using Equation (3.10) or its simplified formula in Equation (3.11). To find the maximum value of ω_L , the uniformity of the tension field in the end-panels was quantified with parameter C_3 . For panels with the same ω_L values, panels with larger aspect ratio had more uniform tension fields. As the same value for ω_L can be obtained from different combinations of end-beam and column stiffness, it was seen that it is better to use a larger end-beam stiffness than a larger column stiffness.

From the results of the finite element analysis, it was concluded that limiting ω_L to 2.0, will limit the parameter C_3 to -20% and limiting ω_L to 2.5, would limit the parameter C_3 to -40%. As the bottom story carries the base shear and its performance is crucial to the overall behavior of the system, it is proposed that ω_L be limited to 2.0; however, as the

top story is far less influential on the overall behaviour of the system, a maximum value of 2.5 is recommended for ω_L there. In order to avoid obtaining negative moments of inertia for end-beams, a lower limit equal to $0.84 \omega_h$ was defined for ω_L .

Changing the frame connection type from pinned to fixed led to a less uniform tension field in the middle panels, and for panels with an aspect ratios of 1.0, the targeted non-uniformity parameter for middle panels (i.e., C_2) was exceeded. In the bottom and top panels, for panels with an aspect ratio of 0.5, the rigidity of the frame connections led to a more uniform tension field, but for larger aspect ratios, the tension field was less uniform in panels with rigid connections and high ω_L values. In all cases, the non-uniformity parameter of end-panels (i.e., C_3) remained less than the proposed upper limits. Also, it was shown that frame connection rigidity reduces the dependence of C_3 on ω_L for all panel aspect ratios.

8.2.2 Tests of shear walls with PEC columns

The modular steel plate shear wall with PEC columns exhibited excellent performance under the quasi-static cyclic loads. As shown in Figures 5.10 and 5.11, the hysteretic loops of the first and second stories of the specimen were stable and fairly wide.

The initial stiffness of the modular specimen was high (180 kN/mm) and similar to that of the benchmark test, which implied that the type of frame connection had almost no effect on the initial stiffness of the steel plate shear walls. High stiffness is important, as it limits the lateral deformation of the structure due to gravity loads combined with frequent lateral loads like wind.

The frame connections of the module specimen rotated substantially, which helped increase the uniformity of the tension field in the infill plates, especially in the infill plate of the second story. This increased the amount of dissipated energy in the second story. As shown in Figure 5.19, the energy dissipation capacity of the modular specimen increased as the lateral deformation of the specimen increased throughout the test.

The displacement ductility of the modular specimen at its peak strength was 4.25 and when the specimen reached 90 percent of its peak strength in the post-peak stage, its ductility was 6.5. The PEC columns fractured in a ductile manner at their base due to the presence of longitudinal reinforcing bars in the columns. Although the specimen suffered from several regions of tearing in the infill plate and the complete tearing of the outer flanges of the columns, there was no sudden decrease in the strength of the specimen. This means that the specimen was highly redundant and capable of changing the load path in case of local failures. The above-mentioned qualities make this specimen configuration an excellent option for resisting lateral loads.

The steel plate shear wall with PEC columns and RBS connections showed good overall performance under quasi-static cyclic lateral load. As shown in Figure 6.15, the hysteretic loops of the first story were stable and wide. The post-peak strength degradation was gradual. The initial stiffness was relatively high (140 kN/mm), although the shape of the imperfection of the infill plate affected the initial stiffness of the RBS test specimen.

The RBS test specimen exhibited good post-peak performance and ductility. The displacement ductility of the specimen when it reached its peak strength was 4.0 and at 90% of the peak strength in the post-peak stage, the ductility of the specimen was 6.2.

The amount of energy dissipated by the RBS specimen increased as the deformations increased throughout the test, as shown in Figure 6.23. The plastic hinge did not form at the center of the RBS cut, but rather it was located within the RBS cut closer to the column face. Despite the infill plate of the first story detaching from the south column completely and the outer flanges of the columns tearing completely at the base, there was no sudden change in the strength of the wall, which indicates the high redundancy of the system. The specimen possessed all the characteristics of an efficient lateral load resisting system.

The results of the 3D camera system, as shown in Figures 6.29 to 6.33, show that the failure of the PEC columns at the base was gradual and the crushing of concrete happened in cycle 21, after the specimen reached its maximum strength in cycle 19.

A linear elastic model created with SAP2000 showed that the initial stiffness of the first story of the steel plate shear wall was 158 kN/mm. The results of this model also indicated that the initial stiffness of the first story of the frame was 26.5 kN/mm. This indicates that the contribution of the frame in the overall lateral stiffness of the test specimens was approximately 15 percent in the initial stage. The contribution of the frame in the overall lateral stiffness of the system reduced as tests progressed and the columns suffered from tearing of their flanges and crushing of concrete at their base.

In both the above-mentioned experiments, the presence of the longitudinal rebars at the bases of the columns improved the local performance of the columns at the plastic hinge region as well as the overall behavior of the specimens, as compared to the benchmark test of Deng et al. (2008). A stress concentration was observed in the concrete at the end of the longitudinal rebars, which was because of the sudden change of the stiffness of columns. The outer flanges of the columns buckled in this region during both tests and in the modular test, the concrete crushed in this region. It is recommended that the link spacing be reduced in this region to improve the performance of this region. As an alternative solution, the longitudinal rebars should be continued to the first floor beam-to-column connection and be discontinued behind the side plate of the connection.

The link spacing at the bases of the columns was reduced from 80 mm in the benchmark test to 50 mm in these tests, which improved the performance of the region significantly. The eventual formation of the plastic hinges at the tops of the columns in the first story of the RBS specimen in cycle 25 was triggered by the crushing of the concrete at the bases of the columns, which reduced the stiffness of the columns at the base and redistributed the base moments to the tops of the columns. The use of a more ductile concrete, like

fiber-reinforced concrete, at the bases of the PEC columns may help postpone the crushing of concrete and improve the ductility of the hinge region.

The importance of the frame connection rotation was proved in this experimental program, as it postponed the formation of the plastic hinges at the tops of the columns in the first story in both tests. The frame connections of the modular specimen rotated in both floors, which led to more energy dissipation in the modular test as the infill plate in the second story of the modular specimen was more engaged compared to the RBS test specimen. As discussed in Chapter 3, the rigidity of the frame connections increases the non-uniformity of the stress distribution in infill panels and it was observed during both tests that the rotation of the frame connections increased the energy dissipation capacity of the specimens significantly. The main reason for the significant increase of the energy dissipation capacity was the uniform stress distribution across the infill plate of the first story which led to yielding of all parts of the infill plate.

8.3 Recommendations

8.3.1 Design

The formation of plastic hinges at the base of PEC columns is required to fully utilize the infill plate, so PEC column bases should be highly ductile. The link spacing of 50 mm in the test (i.e., $s / b = 0.2$) worked well in the plastic hinge region. In the benchmark test, a larger link spacing ($s / b = 0.32$) was used in this region and necking and rupture of some links was observed. It is recommended that the link spacing be limited to no greater than $s / b = 0.2$ at the bases of the PEC columns. As the formation of hinges at the bases of the columns can cause large bending moments at the tops of the columns in the first story, it is also recommended that the link spacing be limited to $s / b = 0.2$ at the tops of the columns in the first story to reduce the chance of a soft story mechanism forming.

The Use of longitudinal reinforcement at the bases of the PEC columns is strongly recommended, as it affects the performance of the columns in several ways. Longitudinal rebars reduce the demands on both the concrete and steel flanges of the columns and thus delay crushing of concrete and flange tearing. Even after the tearing of the column flanges starts, the longitudinal rebars start to play the role of the torn flange and thus the tear growth is controlled and the compressive concrete adjacent to the inner flanges of columns does not crush prematurely.

The location of discontinuity of the longitudinal rebars is a point of weakness, as the stiffness of column changes rapidly and a high stress concentration was observed there. It is recommended that either the link spacing in this region be decreased or the longitudinal rebars be terminated behind the side plates of the column at the first floor connection. A link spacing of 160 mm (i.e., $s/d = 0.64$) was used in both test specimens where the rebars were terminated, but a maximum spacing of $s/d = 0.3$ is recommended for design if the bars are not a full story in height and terminated within the joint region.

The steel flanges of the columns at the base tore in the post-peak stage in both the modular and RBS specimens as well as in the benchmark test (Deng et al. 2008). The tear development in the webs of the columns should be avoided, as it affects the column capacity and overall behavior of the system. It is not recommended that a thicker flange plate or flange stiffeners be used in the desired hinge region, as they may only force the plastic hinge to a higher level, increasing the demand on the columns. Rather, use of a thicker web or stiffening the web of the column with doubler plates and use of longitudinal rebars at the bases of the columns is recommended for increasing hinge ductility. Without the presence of the longitudinal rebars, tearing of the flange should be considered the ultimate limit state.

The use of the modular construction method was successful as the modular test specimen showed excellent behavior. The good overall behavior of the modular

specimen was mainly due to the rotation of the frame connections. In design of the modular specimen, the bolted connections were all designed as bearing connections, although they were pretensioned in accordance with seismic code requirements. The pretensioning of the bolts in the connection of the beams to the columns increases the initial stiffness of the system. In design of the beam-to-column connections, the buckling of the shear tab, which was part of the fish plate in the test specimens, was the governing parameter. It is therefore recommended that the fish plate be stiffened in frame connection locations, or double-sided beam-to-column connections be used.

For rehabilitation of an existing steel plate shear wall or design of a new one, the use of RBS connections is a viable option to increase the ductility of the structure. In the design stage, it is recommended that the assumed location of the plastic hinge be taken as the quarter point of the RBS cut portion closer to the column face, as was recommended for conventional steel plate shear walls by Qu and Bruneau (2010).

Based on the RBS specimen, where the infill plate detached from the south column along the weld line during the test, it is recommended when thin infill plates are being used (3.0 mm in these tests) that the welds be inspected over their full length to ensure their integrity. Alternatively, thicker fish plates should be used to connect the infill plates to the surrounding beams and columns instead of welding them directly to the frame members. The use of fish plates also facilitates the replacement of the damaged infill plate after the occurrence of a severe earthquake. The infill plate can either be welded or preferably bolted to the fish plate. By bolting, the minimum warping will be created in the infill plate.

8.3.2 Future research

The formation of the plastic hinges at the bases of the columns of any lateral load resisting system is expected, and thus the behavior of the PEC columns in the plastic hinge regions requires further study. A parametric study including the flange slenderness, link spacing, longitudinal reinforcement, and concrete type and strength would help to

better understand the behavior and design considerations of PEC columns in plastic hinge locations.

The lateral load regime (ATC-24, 1992) used in this experimental study is mainly used for components of steel structures. As there is no such protocol for composite steel–concrete structures, it is recommended that additional study be carried out on the behavior of steel plate shear walls with PEC column subjected to other lateral load regimes.

Another concern with the ATC-24 (1992) protocol is that it is very dependent on the yield deformation selected, and different assumptions of this value usually lead to results that are difficult to compare to other test results with different yield deformations. It is recommended that a study be conducted on the outcome of other loading protocols like the SAC protocol (Clark et al., 1997), which do not rely on the yield deformation.

In ATC-24, there is no specific requirement with regard to the largest amplitude applied in the cyclic tests. Most cyclic tests are terminated at 75 to 90 percent of the peak capacity, which does not permit an evaluation of important deterioration characteristics in large story deflections, before collapse. It is recommended that tests be continued, if possible, to larger amplitudes. In the numerical studies, with the current hardware and software capabilities, this can be achieved.

It is also recommended that a few pseudo-dynamic tests be conducted to see the time effect on the response of this kind of the structure, especially because it contains concrete.

LIST OF REFERENCES

Astaneh-Asl, A, and Zhao, Q. (2002). "Cyclic behavior of steel shear wall systems." *Proc., Structural Stability Research Council Annual Stability Conference*, Seattle, WA.

ASTM. (2002). *C469-02, Standard test method for static modulus of elasticity and poisson's ratio of concrete in compression*. American Society for Testing and Materials, Philadelphia, PA.

ASTM. (2005). *A370-05, Standard test methods and definitions for mechanical testing of steel products*. American Society for Testing and Materials, Philadelphia, PA.

ATC. (1992). *Guidelines for cyclic seismic testing of components of steel structures. Report 24*, Applied Technology Council, Redwood City, CA.

AWS. (1977). *Surface Roughness Guide for Oxygen Cutting, AWS C4.1-77*. American Welding Society, Opa-Locka, FL.

Begum, M., Driver, R. G., and Elwi, A. E. (2007). "Finite-element modeling of partially encased composite columns using the dynamic explicit method." *Journal of Structural Engineering, ASCE*, 133 (3), 326-334.

Behbahanifard, M. R., Grondin, G. Y., and Elwi, A. E. (2003). "Experimental and numerical investigation of steel plate shear wall." *Structural Engineering Report No. 254*, Dept. of Civil and Environmental Engineering, University of Alberta, Edmonton, AB.

Berman, J. W., and Bruneau, M. (2004). "Steel plate shear walls are not plate girders." *AISC Engineering Journal*, Third Quarter, 95-106.

Berman, J. W., and Bruneau, M. (2005). "Experimental investigation of light-gauge steel plate shear walls." *Journal of Structural Engineering, ASCE*, 131(2), 259-267.

Bouchereau, R., and Toupin, J. D. (2003). "Étude du comportement en compression-flexion des poteaux mixtes partiellement enrobés." *Report EPM/CGS-2003-03*, Dept. Of Civil Engineering, École Polytechnique, Montreal (in French).

Chicoine, T., Tremblay, R., and Massicotte, B. (2001). "Finite element modeling of the experimental response of partially encased composite columns." *EPM/GCS No. 2001-06*, Dept. of Civil, Geological and Mining Engineering, Ecole Polytechnique, Montreal, QC.

Chicoine, T., Tremblay, R., Massicotte, B., Ricles, J., and Lu, L. W. (2002a). "Behaviour and strength of partially encased composite columns with built up shapes." *Journal of Structural Engineering, ASCE*, 128 (3), 279-288.

Chicoine, T., Massicotte, B., and Tremblay, R. (2002b). "Finite element modelling and design of partially encased composite columns." *Steel & Composite Structures*, 2 (3), 171-194.

Chicoine, T., Massicotte, B., and Tremblay, R. (2003). "Long-term behaviour and strength of partially encased composite columns with built up shapes." *Journal of Structural Engineering, ASCE*, 129 (2), 141-150.

Clark, P., Frank, K., Krawinkler, H., and Shaw, R. (1997). "Protocol for fabrication, inspection, testing and documentation of beam-column connection tests and other experimental specimens." *SAC steel project background document. Report No. SAC/BD-97/02*.

CSA. (1994). *CAN/CSA S136-94, Cold formed steel structural members*. Canadian Standards Association, Rexdale, ON.

CSA. (2001). *CAN/CSA S16-01, Limit states design of steel structures*. Canadian Standards Association, Rexdale, ON.

CSA. (2004). *CAN/CSA A23.2-04, Methods of test and standard practices of concrete*. Canadian Standards Association, Rexdale, ON.

CSA. (2009). *CAN/CSA S16-09, Limit states design of steel structures*. Canadian Standards Association, Rexdale, ON.

CSI. (2010). *SAP2000, Version 14*, Computers and Structures Inc., Berkeley, CA.

Deng, X., Dastfan, M., and Driver, R. G. (2008). "Behaviour of steel plate shear walls with composite columns." *Proc., American Society of Civil Engineers Structures Congress*, Vancouver, BC.

Deng, X., and Driver, R. G. (2007). "Steel plate shear walls with partially encased composite columns." *Proc., Structural Stability Research Council Annual Stability Conference*, New Orleans, LA, 437-453.

Driver, R. G., Kulak, G. L., Kennedy, D. J. L., and Elwi, A. E. (1997). "Seismic behavior of steel plate shear walls." *Structural Engineering Report No. 215*, Dept. of Civil and Environmental Engineering, University of Alberta, Edmonton, AB.

Elgaaly, M., Caccese, V., and Du, C. (1993). "Post-buckling behavior of steel plate shear walls under cyclic loads." *Journal of Structural Engineering, ASCE*, 119(2), 588-605.

Engelhardt, M. D., Winneberger, T., Zekany, A. J., and Potyraj, T. J. (1996). "The dogbone connection, Part II", *Modern Steel Construction, AISC*, Chicago, IL.

Fillion, I. (1998). "Étude expérimentale des poteaux mixtes avec section d'acier en I de classe 4." *Report EPM/GCS-98-06*, Dept. of Civil Engineering, École Polytechnique, Montreal, QC (in French).

Grubbs, K. V. (1997). "The effect of the dogbone connection on the elastic stiffness of steel moment frames." *M.Sc. Thesis*, The University of Texas at Austin, Austin, TX.

HKS. (2000). *ABAQUS/Standard user's manual, Version 5.8-19*, Hibbitt, Karlsson and Sorensen, Inc.

HKS. (2003). *ABAQUS/Explicit user's manual, Version 6.3*, Hibbitt, Karlsson and Sorensen, Inc.

HKS. (2004). *ABAQUS/CAE user's manual, Version 6.5*, Hibbitt, Karlsson and Sorensen, Inc.

Kuhn, P., Peterson, J. P., and Levin, L. R. (1952). "A Summary of diagonal tension, Part I: Methods of analysis." *Technical Note 2661*, National Advisory Committee for Aeronautics, Washington, DC.

Maranda, R. (1999). "Analyses par éléments finis de poteaux mixtes avec sections d'acier en I de classe 4." *Report n°. EPM/GCS-1998-11*, Dept. of Civil, Geological and Mining Engineering, Ecole Polytechnique, Montreal, QC.

Montgomery, C. J., and Medhekar, M. (2001). "Discussion on unstiffened steel plate shear wall performance under cyclic loading." *Journal of Structural Engineering, ASCE*, 127(8), page 973.

Moore, K. S., Malley, J. O., and Engelhardt, M. D., (1999). "Design of reduced beam section (RBS) moment frame connections," *Steel Tips*, Structural Steel Educational Council, Moraga, CA.

NBCC. (1995). *National Building Code of Canada*. National Research Council of Canada, Ottawa, ON.

Prickett, B. S., and Driver, R. G. (2006). "Behavior of partially encased composite columns made with high performance concrete." *Structural Engineering Report No. 262*, Dept. of Civil and Environmental Engineering, University of Alberta, Edmonton, AB.

Qu, B., Bruneau, M., Lin, C. H., and Tsai, K. C. (2008). "Testing of full-scale two-story steel Plate shear wall with reduced beam section connections and composite floors." *Journal of Structural Engineering, ASCE*, 134(3), 364-372.

Qu, B., and Bruneau, M. (2010). "Capacity design of intermediate horizontal boundary elements of steel plate shear walls." *Journal of Structural Engineering, ASCE*, 136(6), 665-675.

Sabouri-Ghomi, S. (2001). *Lateral load resisting systems: An introduction to steel plate shear walls*. Angizeh Publication Inc., Tehran, IRAN (in Persian).

Tremblay, R., Chicoine, T., Massicotte, B., Ricles, J., and Lu, L. W. (2000a). "Compressive strength of large scale partially-encased composite stub columns." *Proc., 2000 SSRC Annual Technical Session & Meeting*, Memphis, TN, 262-272.

Tremblay, R., Chicoine, T., and Massicotte, B. (2000b). "Design equation for the axial load capacity of partially encased non-compact columns." *Proc., Composite Construction in Steel and Concrete IV, ASCE*, Reston, VA, 506-517.

Tremblay, R., Massicotte, B., Fillion, I., and Maranda, R. (1998). "Experimental study on the behaviour of partially encased composite columns made with light welded H steel shapes under compressive axial loads." *Proc., 1998 SSRC Annual Technical Meeting*, Atlanta, GA, 195-204.

Tremblay, R., Tirca, L., Bouchereau, R., Toupin, J. D., and Massicotte, B. (2003). "Flexural demand on partially-encased composite columns in multi-story concentrically braced steel frames." *Proc., STESSA 2003 Behavior of Steel Structures in Seismic Areas*, Naples, Italy, 479-485.

Vincent, R., and Tremblay, R. (2001). "An innovative partially encased composite column system for high-rise buildings." *Proc., North American Conference on Steel Construction*, Fort Lauderdale, FL, 30-3-30-17.

Wagner, H. (1931). "Flat sheet metal girders with very thin metal web, Part III: Sheet metal girders with spars resistant to bending – The stress in uprights – Diagonal tension fields." *Technical Memorandum No. 606*, National Advisory Committee for Aeronautics, Washington, DC.

APPENDIX A. SHOP DRAWINGS OF TEST SPECIMENS

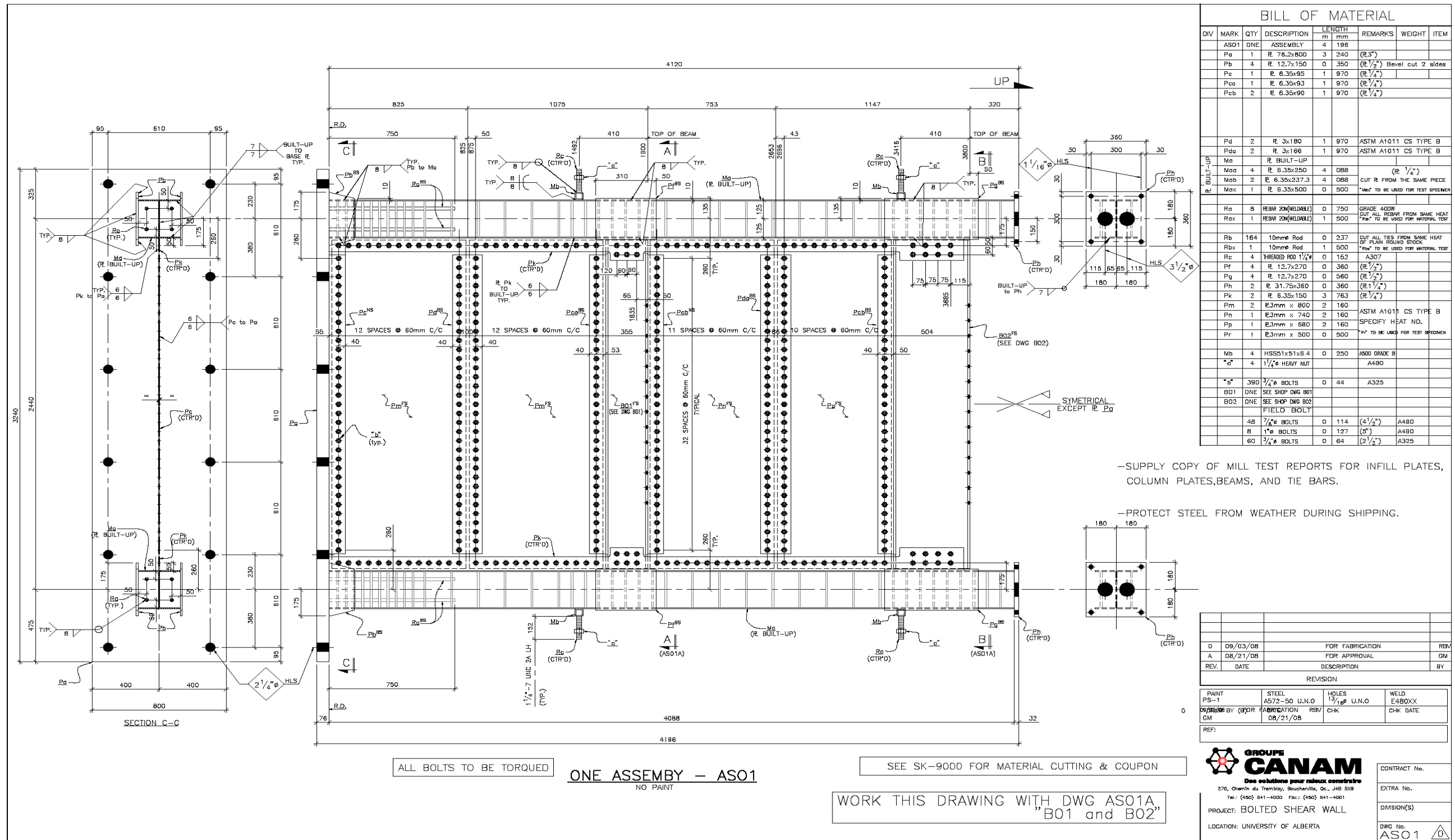

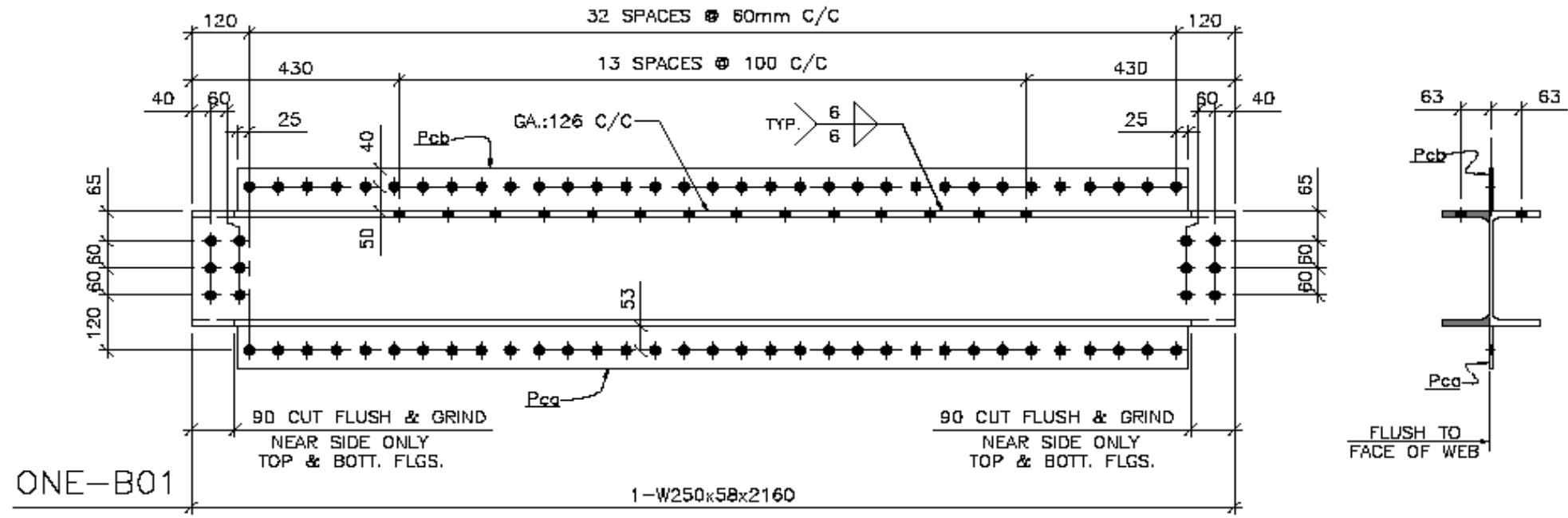


Figure A.1: Details of the assembled modular test specimen

DIV	MARK	QTY	DESCRIPTION	LENGTH	REMARKS	WEIGHT	ITEM	DIV	MARK	QTY	DESCRIPTION	LENGTH	REMARKS	WEIGHT	ITEM
			BEAM												
	B01	1	W250x58	2	160										
	B01X	1	W250x58	1	000	CUT BEAMS FROM SAME PIECE "B01X" TO BE USED FOR TEST SPECIMEN									

CONTRACT No.	EXTRA No.	DWG. NO B01
PROJECT: BOLTED SHEAR WALL		DMSIDN
 CANAM <small>Des solutions pour votre construction</small> <small>270, Chemin du Tremblay, Baieville, Qc., J4B 0Z8</small> <small>Tel: (468) 641-4000 Fax: (468) 641-4001</small>		

DET. (B)	DATE: 08/21/08	CHK.	CHK. DATE
PAINT PS-1	STEEL A572-50	HOLES 13/16"	WELD E480XX
REF	REVISION		
	REV.	DATE	DESCRIPTION
	△	08/21/08	FOR APPROVAL
	△	09/03/08	FOR FABRICATION
	△		
	△		
	△		



WORK THIS DRAWING WITH DWG AS01

Figure A.3: Details of the first-floor beam in the modular test specimen

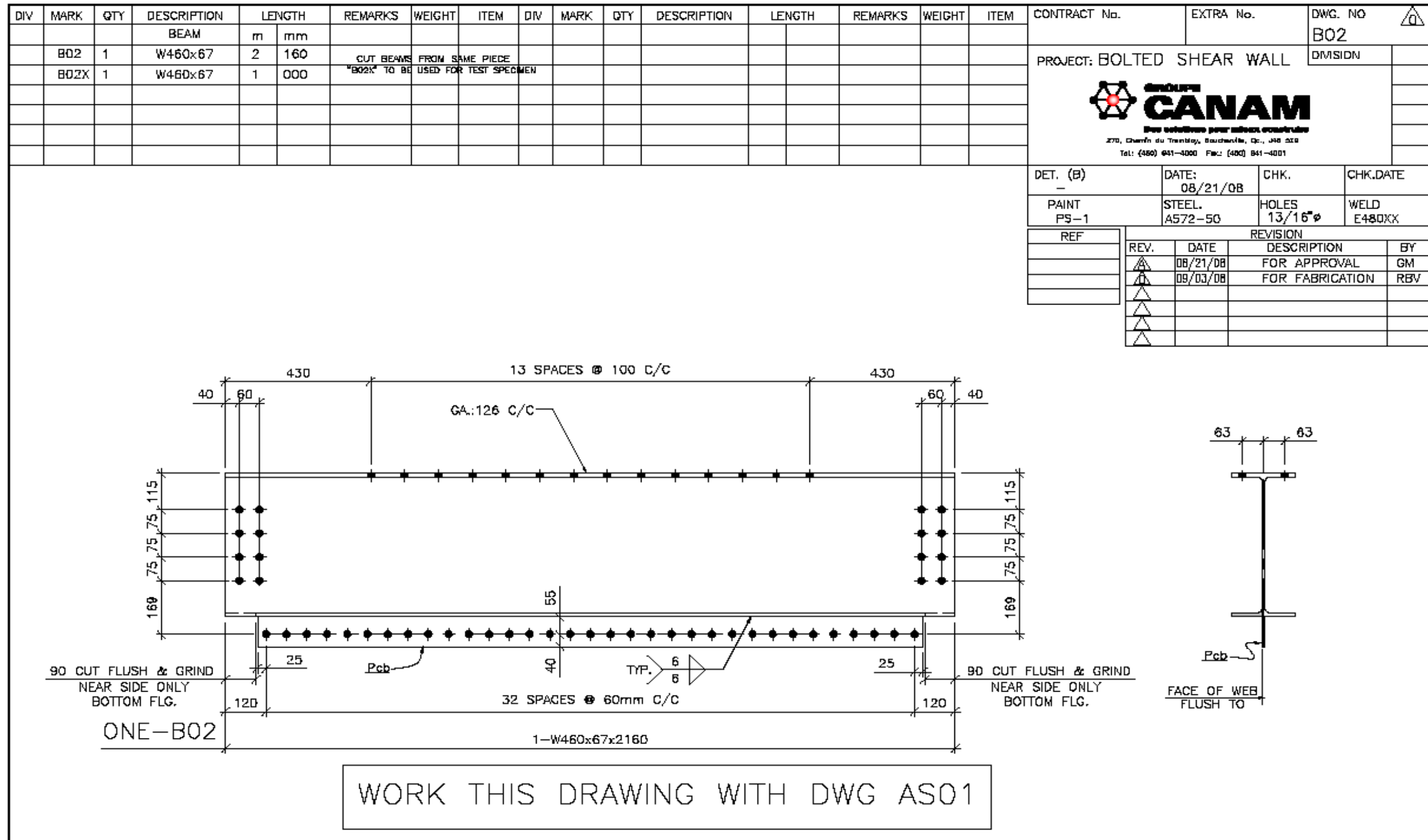


Figure A.4: Details of the second-floor beam in the modular test specimen

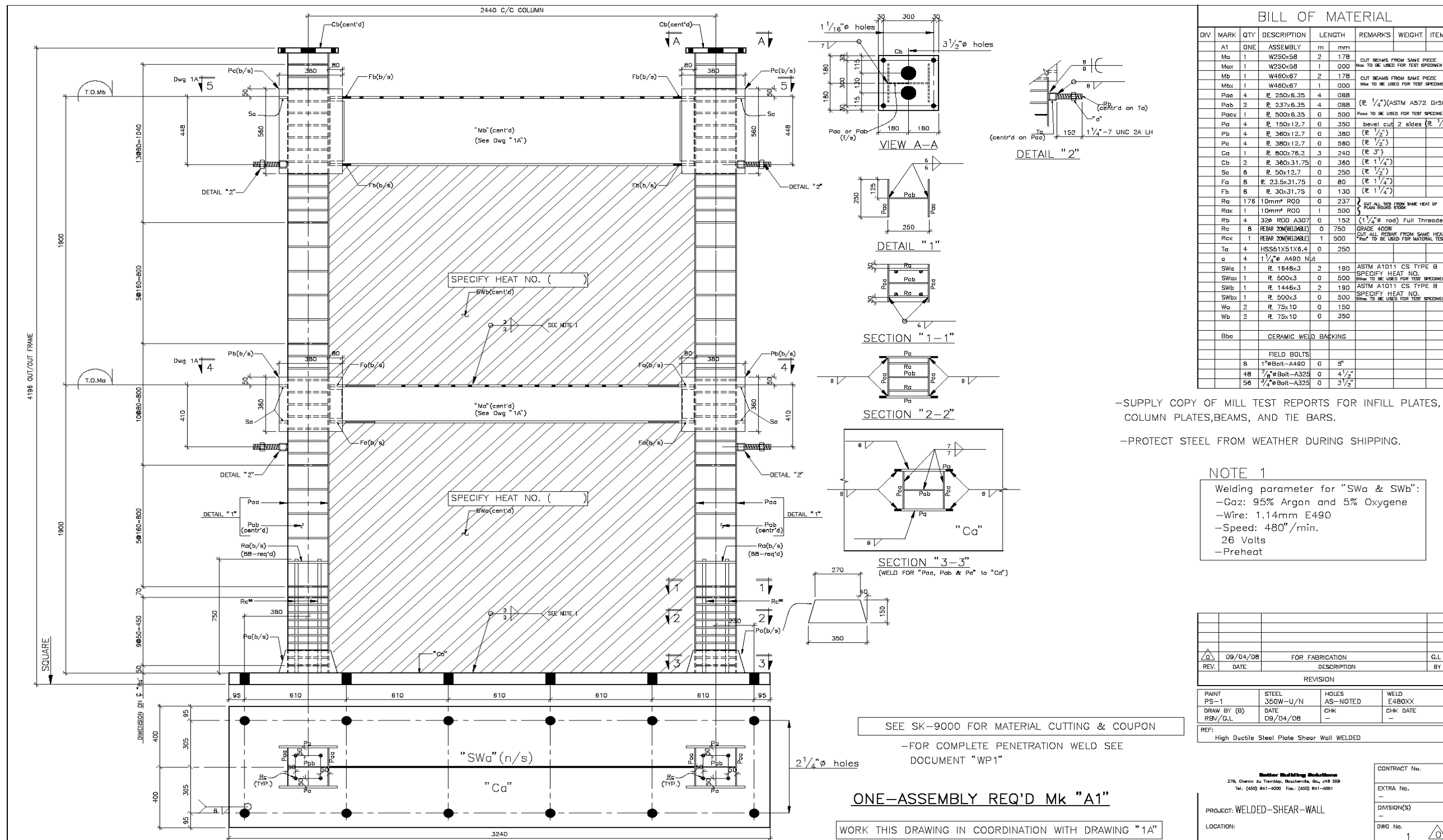


Figure A.6: Elevation view and details of the RBS test specimen

APPENDIX B. ANCILLARY TEST RESULTS

B.1 Steel

In this part of the appendix, further information regarding the results of the tension coupon tests on the infill plate, column plate, and flange and web of floor beams is provided. The stress vs. strain curves for coupons taken from the same material are grouped in one diagram.

Figures B.1 to B.6 are related to the modular test specimen and Figures B.7 to B.13 are related to the RBS test specimen.

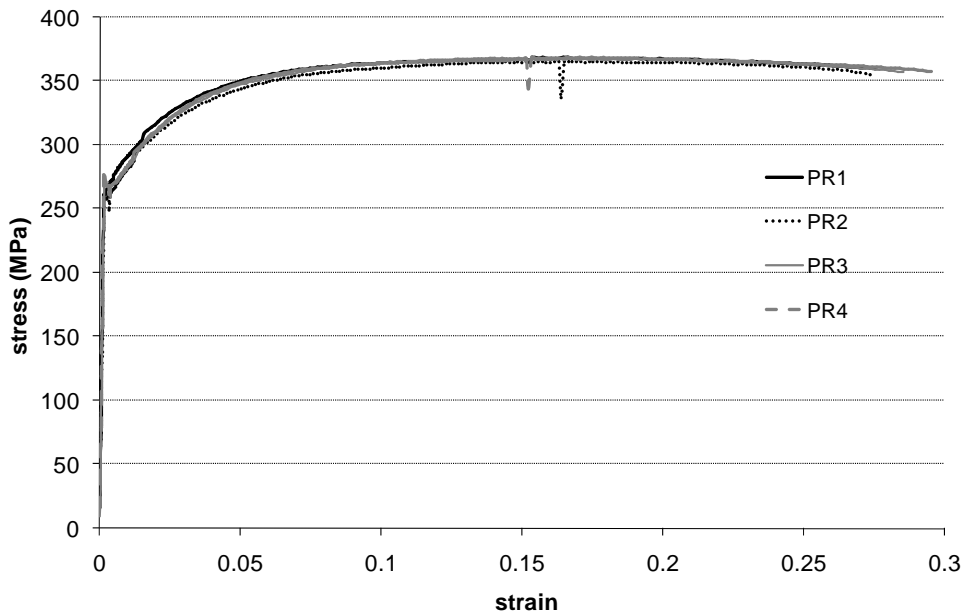


Figure B.1: Stress vs. strain curves of coupons from the infill plate of the modular test specimen

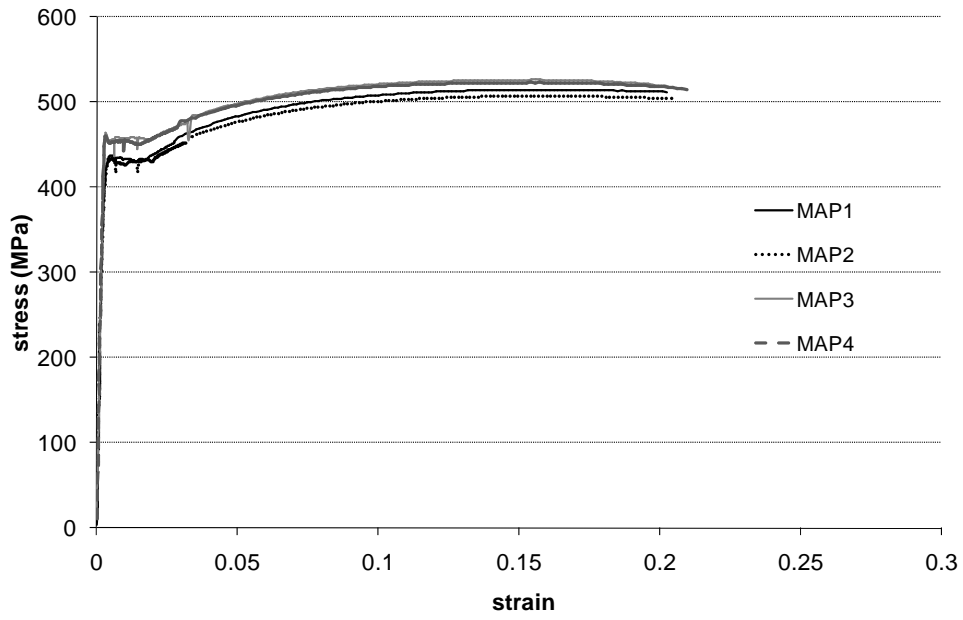


Figure B.2: Stress vs. strain curves of coupons from the column plates of the modular test specimen

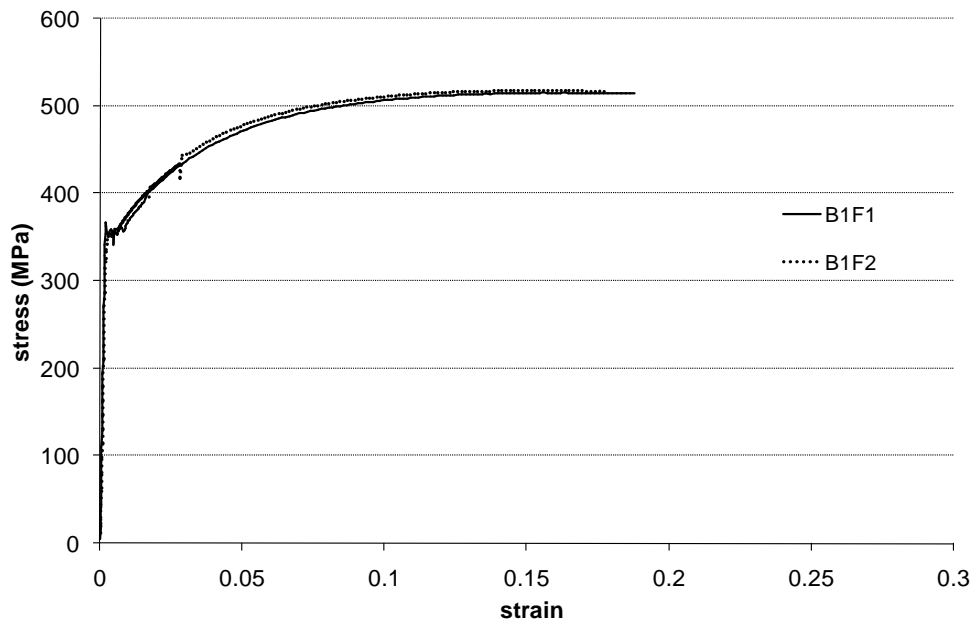


Figure B.3: Stress vs. strain curves of coupons from the flanges of the first floor beam of the modular test specimen

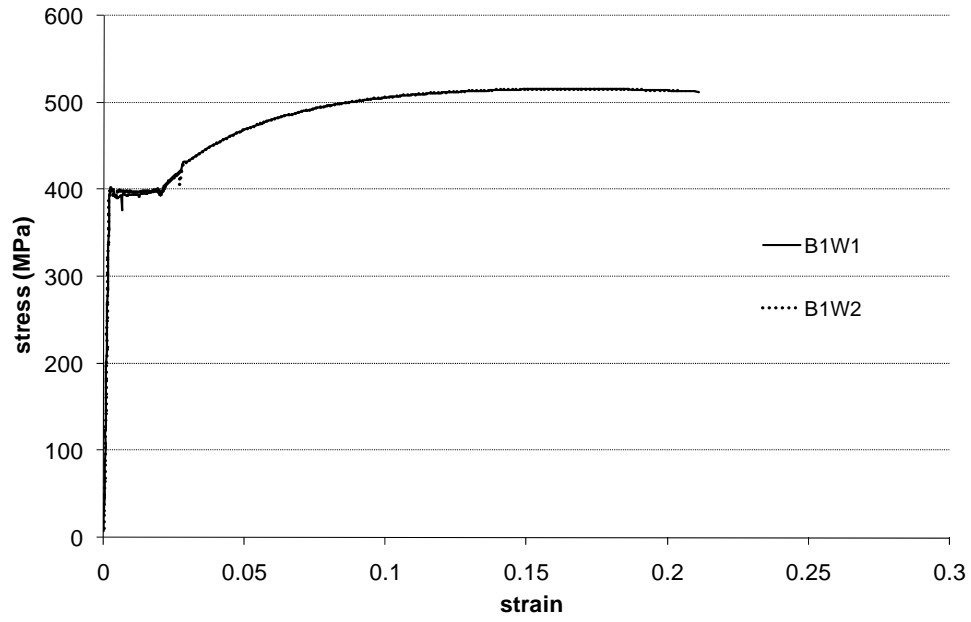


Figure B.4: Stress vs. strain curves of coupons from the web of the first floor beam of the modular test specimen

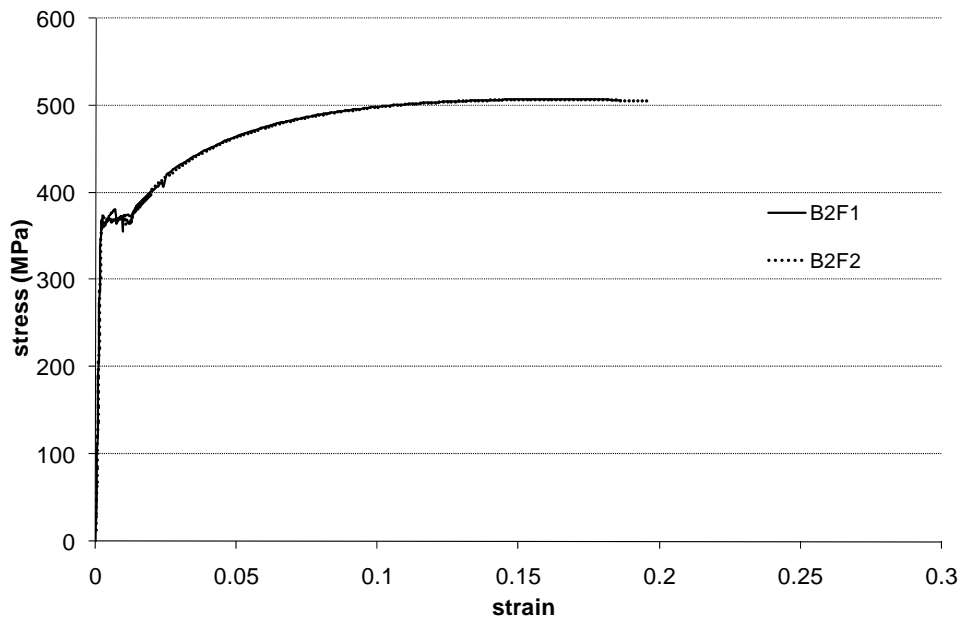


Figure B.5: Stress vs. strain curves of coupons from the flanges of the second floor beam of the modular test specimen

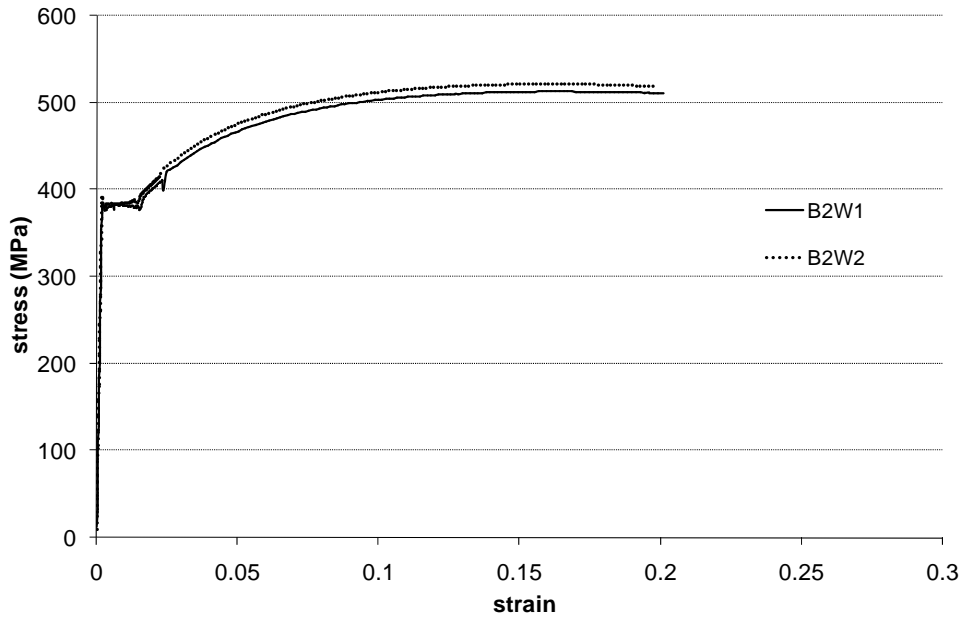


Figure B.6: Stress vs. strain curves of coupons from the web of the second floor beam of the modular test specimen

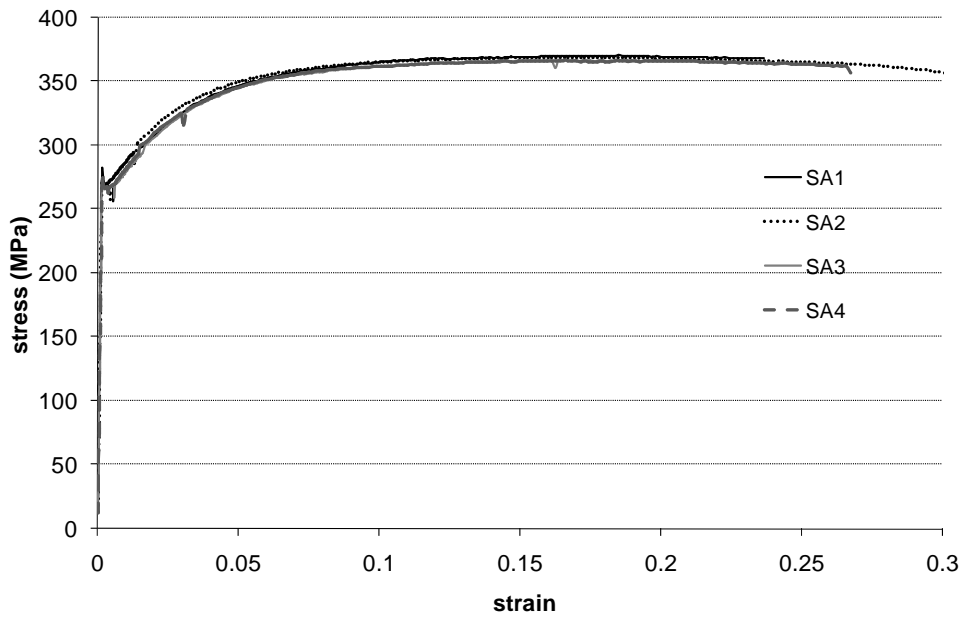


Figure B.7: Stress vs. strain curves of coupons from the infill plate in the first story of the RBS test specimen

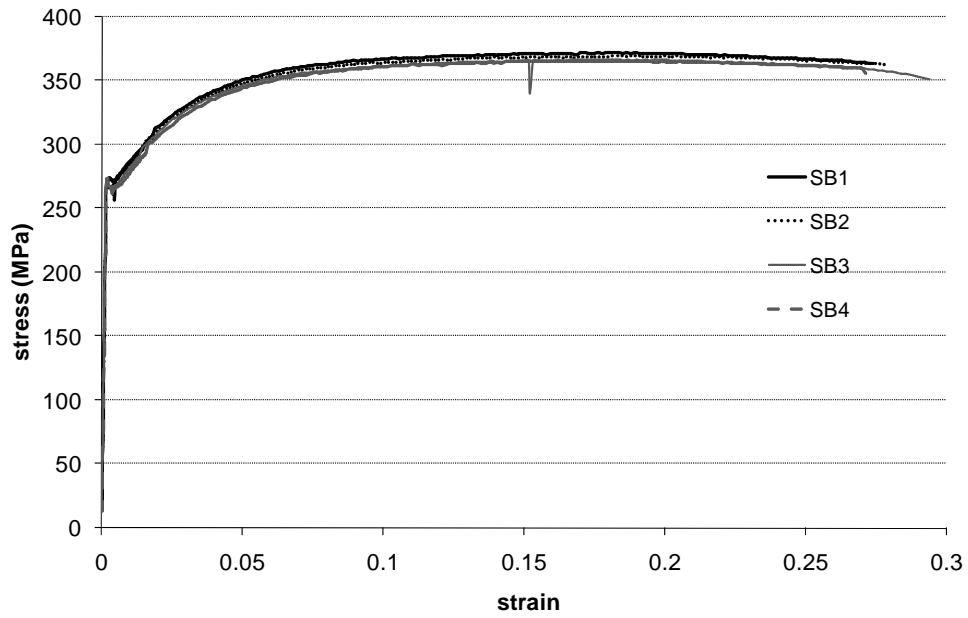


Figure B.8: Stress vs. strain curves of coupons from the infill plate in the second story of the RBS test specimen

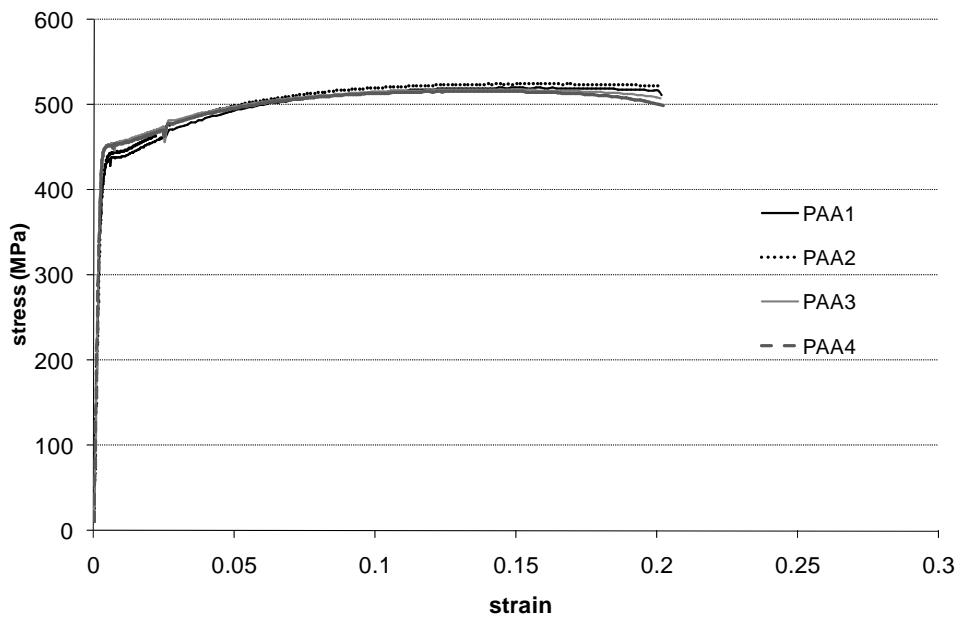


Figure B.9: Stress vs. strain curves of coupons from the column plates of the RBS test specimen

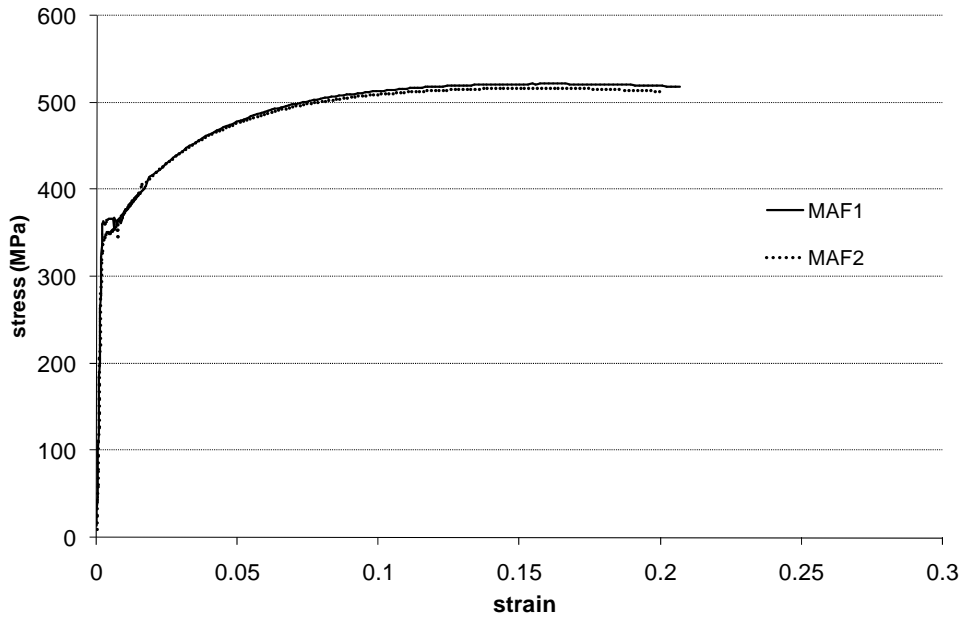


Figure B.10: Stress vs. strain curves of coupons from the flanges of the first floor beam of the RBS test specimen

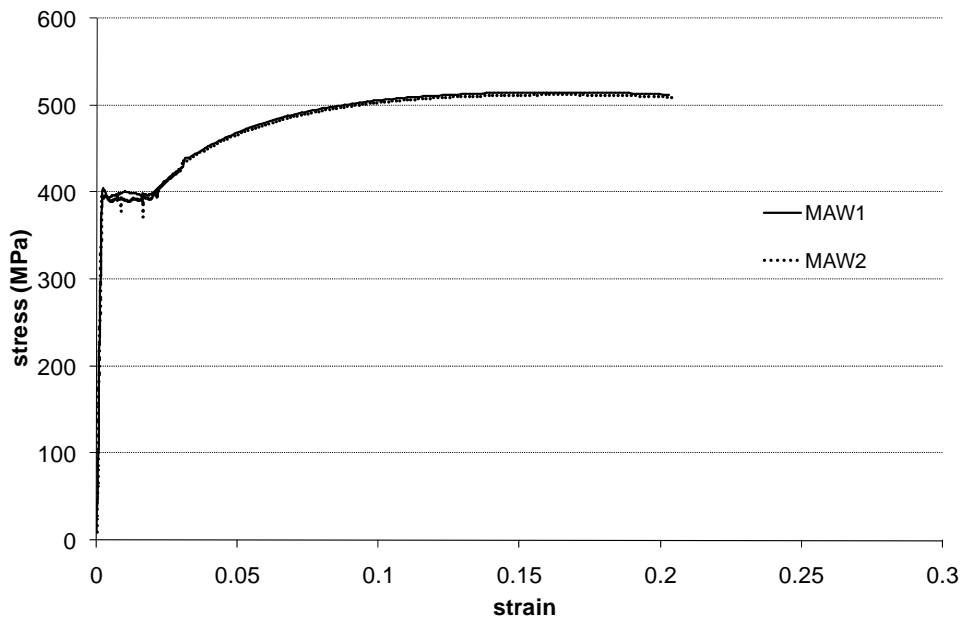


Figure B.11: Stress vs. strain curves of coupons from the web of the first floor beam of the RBS test specimen

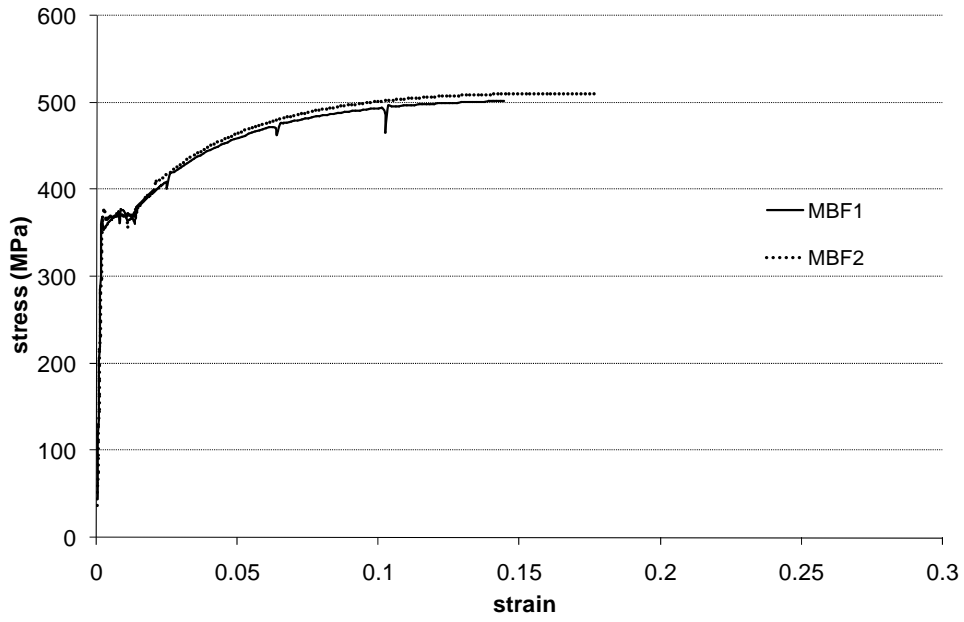


Figure B.12: Stress vs. strain curves of coupons from the flanges of the second floor beam of the RBS test specimen

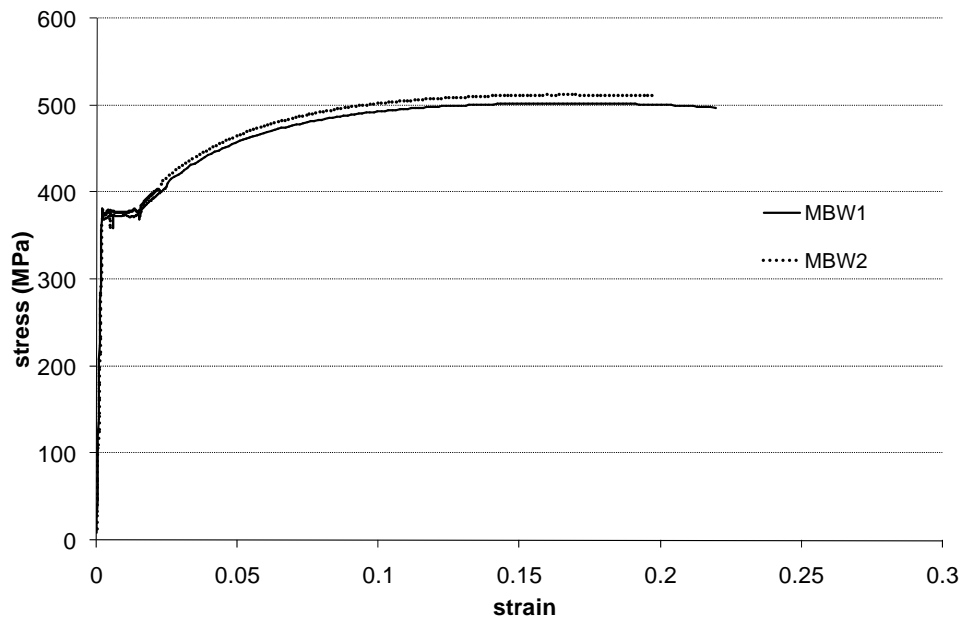


Figure B.13: Stress vs. strain curves of coupons from the web of the second floor beam of the RBS test specimen

B.2 Concrete

Table B.1: Material properties of concrete in first story of PEC columns in the modular and RBS test specimens

Slump	120		mm	
Concrete density in 7 days				
Cylinder number	mass (kg)	volume (m ³)	density (kg/m ³)	
1	13.04	0.0053	2460	
2	13.10	0.0053	2472	
mean			2466	
7 days compressive strength (Jan. 23rd, 2008)				
Cylinder number	Load (kN)	Area (mm ²)	Strength (MPa)	Failure type
1	677.5	18146	37.3	split & cone
2	639.5	18146	35.2	split & cone
3	662.5	18146	36.5	split & cone
4	699.0	18146	38.5	split & cone
mean			36.9	
28 days compressive strength (Feb. 13th, 2008)				
Cylinder number	Load (kN)	Area (mm ²)	Strength (MPa)	Failure type
1	957.0	18146	52.7	split & cone
2	954.5	18146	52.6	split & cone
3	978.0	18146	53.9	split & cone
mean			53.1	
7 days compressive strength / 28 days compressive strength =			69.5%	
Test day (modular test) compressive strength (Aug. 2009)				
Cylinder number	Load (kN)	Area (mm ²)	Strength (MPa)	Failure type
1	929.5	18146	51.2	split & cone
2	955.5	18146	52.7	split & cone
3	938.5	18146	51.7	split & cone
mean			51.9	
Test day (RBS test) compressive strength (Feb. 2010)				
Cylinder number	Load (kN)	Area (mm ²)	Strength (MPa)	Failure type
1	902	18146	49.7	split & cone
2	888	18146	48.9	split & cone
3	890	18146	49.0	split & cone
mean			49.2	
Test day (modular) tensile strength (Aug. 2009)				
Cylinder number	Load (kN)	Strength (MPa)*		
1	237	3.4		
2	221	3.1		
mean		3.3		
Test day (RBS) tensile strength (Feb. 2010)				
Cylinder number	Load (kN)	Strength (MPa)*		
1	237	3.3		
2	233	3.3		
mean		3.3		

* $f_t = 2P/\pi DL$

Table B.2: Material properties of concrete in second story of PEC columns in the modular and RBS test specimens

Slump	110		mm	
Concrete density in 7 days				
Cylinder number	mass (kg)	volume (m ³)	density (kg/m ³)	
1	13.08	0.0053	2468	
2	13.02	0.0053	2457	
mean			2462	
7 days compressive strength (Jan. 29th, 2008)				
Cylinder number	Load (kN)	Area (mm ²)	Strength (MPa)	Failure type
1	676	18146	37.3	split & cone
2	669	18146	36.9	split & cone
3	676	18146	37.3	split & cone
4	707.5	18146	39.0	split & cone
mean			37.6	
28 days compressive strength (Feb. 19th, 2008)				
Cylinder number	Load (kN)	Area (mm ²)	Strength (MPa)	Failure type
1	908	18146	50.0	split & cone
2	951	18146	52.4	split & cone
3	893	18146	49.2	split & cone
mean			50.6	
7 days compressive strength / 28 days compressive strength =			74.3%	
Test day (modular test) compressive strength (Aug. 2009)				
Cylinder number	Load (kN)	Area (mm ²)	Strength (MPa)	Failure type
1	873	18146	48.1	split & cone
2	748	18146	41.2	split & cone
3	785	18146	43.3	split & cone
mean			44.2	
Test day (RBS test) compressive strength (Feb. 2010)				
Cylinder number	Load (kN)	Area (mm ²)	Strength (MPa)	Failure type
1	789	18146	43.5	split & cone
2	799	18146	44.0	split & cone
3	793	18146	43.7	split & cone
mean			43.7	
Test day (modular) tensile strength (Aug. 2009)				
Cylinder number	Load (kN)	Strength (MPa)*		
1	219	3.1		
2	213.5	3.0		
mean		3.1		
Test day (RBS) tensile strength (Feb. 2010)				
Cylinder number	Load (kN)	Strength (MPa)*		
1	214	3.0		
2	217	3.1		
mean		3.0		

* $f_t = 2P/\pi DL$